Three Tales of Death: New Pathways in the Induction, Inhibition and Execution of Apoptosis

Inaugural-Dissertation

zur Erlangung des Doktorgrades

der Mathematisch-Naturwissenschaftlichen Fakultät

der Heinrich-Heine-Universität Düsseldorf

vorgelegt von

Philip Böhler

aus Bonn

Düsseldorf, Juni 2019

aus dem Institut für Molekulare Medizin I

der Heinrich-Heine-Universität Düsseldorf

Gedruckt mit der Genehmigung der

Mathematisch-Naturwissenschaftlichen Fakultät der

Heinrich-Heine-Universität Düsseldorf

Berichterstatter:

1. Prof. Dr. Sebastian Wesselborg

2. Prof. Dr. Henrike Heise

Tag der mündlichen Prüfung: 29. Oktober 2019

"Where the first primal cell was, there was I also.
Where man is, there am I.
When the last life crawls under freezing stars, there will I be."

— DEATH, in: *Mort*, by Terry Pratchett

"Right away I found out something about biology:
it was very easy to find a question that was very interesting,
and that nobody knew the answer to."

— Richard Feynman, in: *Surely You're Joking, Mr. Feynman!*

Acknowledgements (*Danksagung*)

Viele Menschen haben zum Gelingen meiner Forschungsarbeit und dieser Dissertation beigetragen, und nicht alle können hier namentlich erwähnt werden. Dennoch möchte ich einige besonders hervorheben.

An erster Stelle möchte ich Professor Sebastian Wesselborg danken, der diese Dissertation als Erstgutachter betreut hat und der mir die Möglichkeit gab, die dazugehörigen experimentellen Arbeiten am Institut für Molekulare Medizin durchzuführen. Er und Professor Björn Stork, dem ich für die herzliche Aufnahme in seine Arbeitsgruppe danke, legten durch die richtige Mischung aus aktiver Förderung und dem Freiraum zur Umsetzung eigener wissenschaftlicher Ideen die ideale Grundlage für die Forschungsprojekte, aus denen diese Dissertation entstand.

Professorin Henrike Heise, die sich freundlicherweise zur Betreuung dieser Dissertation als Zweitgutachterin bereiterklärt hat, gilt ebenfalls mein herzlicher Dank.

Allen Mitgliedern des Instituts für Molekulare Medizin und des Instituts für Molekulare Radioonkologie danke ich für die schöne gemeinsame Zeit nicht nur im Labor. Ich freue mich, dass hieraus auch viele persönliche Freundschaften erwachsen sind.

Professor Peter Proksch und seiner Arbeitsgruppe, insbesondere Marian Frank und Hendrik Niemann, danke ich für ihren Anstoß des Phomoxanthon-Projekts und für ihre Beiträge dazu, sowie für die unermüdliche Bereitstellung immer neuer Chargen für unsere Experimente.

I would also like to express my thanks to Professor Andreas Reichert and his research group, especially to Ruchika Anand and Arun Kondadi, for their invaluable support with the experiments on mitochondria.

Professor Hans Reinke und Gabi Schoder danke ich für ihre wertvollen Beiträge zum BMAL1-Projekt.

Ein großer Dank gilt meinen Eltern, die schon in frühen Jahren meine Neugier und meinen Forschergeist unterstützt und gefördert haben und die mir in allen Lebenslagen stets zur Seite standen.

Zu guter Letzt und ganz besonders danke ich Marta. Unsere gemeinsamen Stunden am Durchflusszytometer waren der Beginn von mehr als nur einer wunderbaren Freundschaft. Ich bin glücklich und dankbar, dass Du mein Leben bereicherst.

Summary

Death is not always a matter of accident. In many multicellular lifeforms including humans, the death of cells that have become unnecessary or even dangerous to the organism takes place through a regulated process termed *apoptosis*. This dissertation is based on three research projects that contributed to the understanding of three aspects of apoptosis: its induction, inhibition and execution (**Figure 1**). To tell these "three tales of death" in the proper context, the reader is provided with a short introduction to apoptosis with a focus on those aspects.

The first project investigated the induction of apoptosis by the mycotoxin phomoxanthone A (PXA). It was shown that this small molecule targets the mitochondria and disrupts their form and function in multiple ways: it elicits a strong mitochondrial release of Ca^{2+}, depolarises the mitochondria, inhibits the respiratory chain, and rapidly collapses the mitochondrial network into fragments. Cytochrome c, which is normally a component of the respiratory chain, is released from these damaged mitochondria and triggers the assembly of the apoptosome, thus leading to apoptosis. In the second project, a new regulatory feature was identified in the PI3K/PDK1/AKT signalling pathway that contributes to the inhibition of apoptosis. Through the newly found feedback loop in this pathway, inhibition or genetic deletion of AKT or PDK1 leads to an increase in PI3K expression that depends on the transcription factor FOXO1. The third project was concerned with the execution of apoptosis. During this final phase of the process, the cell and its components are disassembled and prepared for disposal and recycling. The transcription factor BMAL1, which is a component of the circadian clock that regulates day/night cycles in healthy cells, was characterised as one of the cellular components that are specifically targeted and degraded by the effectors of apoptosis. Through this mechanism, apoptosis inactivates the cellular circadian clock.

Taken together, the findings of these three research projects and the corresponding publications may have implications for basic research on mitochondrial morphology and the circadian clock, and for clinical research on anticancer regimens that target the PI3K/PDK1/AKT pathway to induce cancer cell apoptosis.

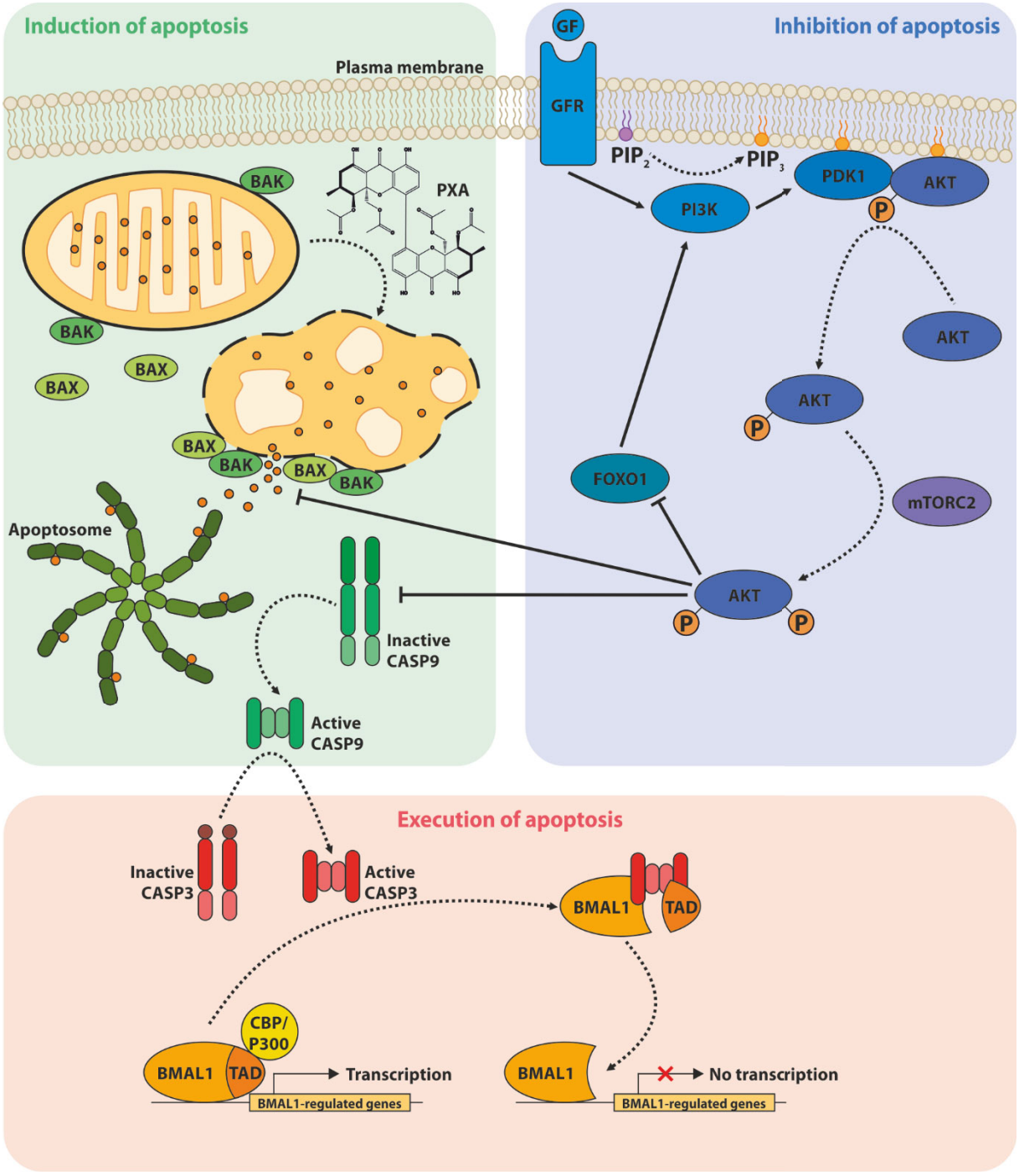

Figure 1: Graphical summary. Apoptosis can be triggered by many stimuli including the mycotoxin phomoxanthone A (**PXA**; green panel). While PXA damages the mitochondria directly, induction of apoptosis almost always involves mitochondrial outer membrane permeabilization (**MOMP**) via recruitment of **BAX** and its association with **BAK** to form pores that allow the release of cytochrome c (**CYCS**). Release of CYCS results in assembly of the **apoptosome**, which activates the initiator caspase **CASP9**. This is prevented by the pathways of the inhibition of apoptosis, which include **PI3K/PDK1/AKT** signalling (blue panel). Initiation of this pathway can be caused by the binding of growth factors (**GF**) to growth factor receptors (**GFR**), resulting in the conversion of **PIP_2** into **PIP_3** by class 1 **PI3K**. Inactive AKT as well as PDK1 are recruited to PIP_3, and AKT is activated via phosphorylation by PDK1 and **mTORC2**. Active AKT inhibits MOMP and CASP9, and it also negatively regulates itself via a feedback loop involving **FOXO1**. If the signals in favour of initiation of apoptosis exceed those in favour of inhibition of apoptosis, the cell enters the phase of the execution of apoptosis (red panel). In this phase, executioner caspases such as **CASP3** facilitate the controlled demolition of the cell by cleaving various substrate proteins. These include the transcription factor **BMAL1**, whose transactivation domain (**TAD**) is cleaved off by CASP3. This renders BMAL1 unable to recruit the coactivators **CBP** and **P300** and thus disables BMAL1-regulated gene transcription.

Summary in German (*Zusammenfassung*)

Der Tod ist nicht immer eine Frage des Zufalls. In vielen mehrzelligen Lebewesen einschließlich des Menschen erfolgt der Tod einzelner Zellen, die für den Organismus unnötig oder gar gefährlich geworden sind, durch eine sorgfältig regulierte Form des Zelltodes, die als *Apoptose* bezeichnet wird. Die vorliegende Arbeit basiert auf drei Forschungsprojekten, die verschiedene Aspekte der Apoptose untersuchten: ihre Einleitung (Induktion), ihre Hemmung (Inhibition) und ihre Ausführung (Exekution). Zudem beinhaltet die Arbeit eine umfassende Einleitung mit Schwerpunkten auf diesen drei Aspekten.

Das erste Forschungsprojekt untersuchte die Induktion der Apoptose durch das Mykotoxin Phomoxanthon A (PXA). Es wurde gezeigt, dass PXA die Form und Funktion der Mitochondrien in vielfältiger Weise beeinträchtigt: es setzt mitochondriales Ca^{2+} frei, depolarisiert die Mitochondrien, inhibiert die Atmungskette und führt zum Zusammenbruch der mitochondrialen Netzwerkstruktur. Dadurch kommt es zu einer Freisetzung mitochondrialer Bestandteile einschließlich Cytochrom c ins Zytoplasma, wodurch in betroffenen Zellen Apoptose induziert wird. Im Rahmen des zweiten Forschungsprojekts wurde eine neue regulatorische Komponente des PI3K/PDK1/AKT-Signalwegs identifiziert, der zur Inhibition der Apoptose beiträgt und somit bei Dysregulation ein hohes onkogenes Potenzial birgt. Mehrere experimentelle Krebsmedikamente sind daher gegen Komponenten dieses Signalwegs gerichtet. Eine Inhibition von AKT führt jedoch über eine durch FOXO1-vermittelte Rückkopplung zu einer verstärkten Expression von PI3K. Das dritte Forschungsprojekt beschäftigte sich mit der finalen Phase der Apoptose, während der die Zelle und ihre Komponenten systematisch abgebaut werden. Die Ergebnisse dieses Projekts demonstrieren, dass die Effektoren der Apoptose sich hierbei auch gezielt gegen den Transkriptionsfaktor BMAL1 richten, welcher in gesunden Zellen ein Bestandteil der zirkadianen Uhr der Zelle ist. Die Apoptose inaktiviert damit die zelluläre innere Uhr.

Im Anschluss an die fachliche Einleitung, die Übersicht über die drei Forschungsprojekte und die daraus hervorgegangenen Fachpublikationen folgt eine Diskussion deren möglicher Bedeutung für die Grundlagenforschung zu mitochondrialer Morphologie, zur inneren Uhr und zur Apoptose sowie für die klinische Forschung zu PI3K/PDK1/AKT-Inhibitoren in der Krebstherapie.

Abbreviations

ACINUS	apoptotic chromatin condensation inducer in the nucleus
AIF	apoptosis-inducing factor
AKT	protein kinase B
ANT	adenine nucleotide translocator
APAF1	apoptotic protease-activating factor 1
ATP	adenosine triphosphate
BAD	BCL2-associated agonist of cell death
BAK	BCL2 antagonist/killer
BAX	BCL2-associated X protein
BCL2	B-cell lymphoma 2
BH	BCL2 homology
BID	BH3-interacting domain death agonist
BIK	BCL2-interacting killer
BIM	BCL2-interacting mediator of cell death
BIR	baculovirus IAP repeat
BIRC	BIR-containing protein
BMAL1	aryl hydrocarbon receptor nuclear translocator-like protein 1
CAD	caspase-activated DNase
CARD	caspase activation and recruitment domain
CASP	caspase
CBP	CREB-binding protein
CJ	cristae junction
CTL	cytotoxic T lymphocyte
CYCS	cytochrome c
CYPD	cyclophilin D
DD	death domain
DED	death effector domain
DISC	death-inducing signalling complex
DRP1	dynamin-1-like protein
EIF	eukaryotic translation initiation factor
ER	endoplasmic reticulum
ETC	electron transport chain
FADD	FAS-associated death domain protein
FASL	FAS ligand
FLIP	FLICE-like inhibitory protein
FOXO	forkhead box protein O
GDP	guanosine diphosphate
GF	growth factor
GFR	growth factor receptor
GPCR	G-protein coupled receptor
GRASP65	Golgi reassembly-stacking protein 1
GSK3B	glycogen synthase kinase-3β
GTP	guanosine triphosphate
IAP	inhibitor of apoptosis
IBM	IAP-binding motif
ICAD	caspase-activated DNase
IMM	inner mitochondrial membrane
IMS	mitochondrial intermembrane space
JAK	Janus kinase
JNK	Jun N-terminal kinase
LPC	lysophosphatidylcholine
MAC	mitochondrial apoptosis-induced channel
MHC	major histocompatibility complex
MICOS	mitochondrial contact site and cristae organizing system
MLC	myosin light chain
MOMP	mitochondrial outer membrane permeabilisation
mPT	mitochondrial permeability transition
mPTP	mitochondrial permeability transition pore
MST1	serine/threonine-protein kinase 4
mTORC2	mammalian target of rapamycin complex 2
NK cell	natural killer cell
OMI	serine protease HTRA2, mitochondrial
OMM	outer mitochondrial membrane
OPA1	optic atrophy protein 1 / dynamin-like 120 kDa protein, mitochondrial
OxPhos	oxidative phosphorylation
P300	histone acetyltransferase p300
PDK1	3-phosphoinositide-dependent protein kinase 1
PH	pleckstrin homology
PI	phosphatidylinositol
PI3K	phosphatidylinositol-3-kinase
PIP_2	phosphatidylinositol-4,5-bisphosphate
PIP_3	phosphatidylinositol-3,4,5-trisphosphate
PS	phosphatidylserine
PUMA	p53 up-regulated modulator of apoptosis
PXA	phomoxanthone A
RING	really interesting new protein
ROCK1	Rho-associated protein kinase 1
RTK	receptor tyrosine kinase
SMAC	second mitochondria-derived activator of caspase
STAT	signal transducer and activator of transcription
TAD	transactivation domain
tBID	truncated BH3-interacting domain death agonist
TNF	tumour necrosis factor
TNFRSF	tumour necrosis factor receptor superfamily
TNFSF	tumour necrosis factor superfamily
TRAIL	TNF-related apoptosis-inducing ligand
UTP	uridine triphosphate
VDAC	voltage-gated ion channel
XIAP	X-linked inhibitor of apoptosis protein
$\Delta\Psi_m$	mitochondrial inner membrane potential

1. Introduction

1.1. Background and scope of this dissertation

1.1.1. Apoptosis – cellular self-destruction

As iconically remarked by DEATH himself in Terry Pratchett's *Mort*, death always accompanies life. In complex multicellular life forms such as humans, the death of individual cells can and must happen without eventually causing the death of the entire organism. Life has thus evolved to accommodate death. In an average adult human body, billions of cells die every day – an amount equivalent to about 0.5% of the body's cells.[1] The reasons for the death of these cells are diverse: some die because they have become a threat to the body, such as damaged, degenerated or infected cells. Others are removed simply because they are no longer required yet occupy scarce resources that could be put to better use.

The body removes such unwanted cells through *apoptosis*, a process of programmed, purposeful cell death. Apoptosis has crucial functions in embryonic development, in cell recycling, and in the defence against viral infections and cancer. It is thus involved in many diseases: on the one hand, inhibition of apoptosis is one of the ways through which many viruses and cancer cells can evade the body's immune system; on the other hand, excessive apoptosis is implicated in many autoimmune disorders.[2] Therefore, research on apoptosis remains an important and highly active field of study. The goal of the three research projects – the "three tales of death" – on which this dissertation is mainly based was to expand the understanding of three major aspects of apoptosis: its induction, inhibition, and execution.

Programmed cell death was first characterized in detail in 1972, and the term "apoptosis", which is derived from the Greek word for the "falling off" of leaves from a tree, was coined to refer to this phenomenon.[3] At this time, it became increasingly clear that apoptosis is a guided, active process that is distinct from accidental cell death, which is termed *necrosis*. Necrosis is usually the result of acute cell damage or injury and leads to swelling and ultimately to rupture and lysis of the affected cells. This causes the release of the cells' contents into the surrounding tissue, often resulting in an inflammatory reaction and further tissue damage. In contrast, apoptotic cells maintain membrane integrity throughout the whole process. Instead of rupturing, these cells disintegrate into many small vesicles termed

apoptotic bodies, which are readily removed by phagocytes.[4] Apoptosis has often been compared to controlled demolition of a building: both are ordered processes serving the disposal and recycling of unneeded or damaged structures while minimising damage to the surrounding structures.[5]

1.1.2. First tale – induction of apoptosis: characterisation of phomoxanthone A (PXA) as a mitochondrial toxin

The reasons for cell death are diverse, ranging from lack of nutrients to viral infection. Cell death by apoptosis can be induced by different extrinsic and intrinsic stimuli, which are initially processed by different pathways that only converge at a later stage. Extrinsic pro-apoptotic stimuli mainly originate from the body's immune system, since it is the task of immune cells to identify and remove threats such as infected or malignant cells. Intrinsic pro-apoptotic stimuli can be diverse and result mainly from excessive or irreversible damage to crucial elements of the cell. A classical and frequently mentioned example of an intrinsic pro-apoptotic stimulus is irreparable DNA damage.[6] However, other forms of cell damage can also cause intrinsic apoptosis, such as endoplasmic reticulum (ER) stress, oxidative stress, or direct damage to the mitochondria. Regardless of the stimulus, the mitochondria are at the centre of intrinsic apoptosis since they contain many factors that, if released, induce or facilitate apoptosis. The goal of the first project described in this dissertation was the identification of the mechanism by which the mycotoxin phomoxanthone A (PXA) induces apoptosis. PXA was identified as a mitochondrial toxin that causes the release of pro-apoptotic factors by direct damage to the mitochondria.[7–9]

1.1.3. Second tale – inhibition of apoptosis: feedback loop in the PI3K/PDK1/AKT pathway

The induction of apoptosis sets in motion a self-reinforcing chain reaction of events that can escalate quickly. Therefore, these events are tightly controlled to prevent accidental apoptosis initiation. Cells employ diverse checks and balances to negatively regulate apoptosis as long as there is no clear signal in its favour. Dysregulation of these checks and balances can inhibit apoptosis despite a strong pro-apoptotic stimulus, leading to cell immortalisation and thus to cancer. A major cell signalling pathway that regulates apoptosis by translating survival signals from outside the cell into anti-apoptotic effects inside the cell is the so-called PI3K/PDK1/AKT pathway, named after the three major enzymes

involved.[10–12] The goal of the second main project described in this dissertation was the identification of new signalling axes in this pathway, specifically of a negative feedback loop through which downstream targets of PDK1 can repress the expression of their upstream regulator PI3K.[13] Additionally, a side project dealt with a potential clinical application of the inhibition of apoptosis in the protection of transplanted corneal tissue from graft rejection and stress-induced apoptosis.[14]

1.1.4. Third tale – execution of apoptosis: identification of BMAL1 as a caspase substrate

During apoptosis, the contents of the cell including proteins and DNA are actively degraded in a controlled manner. This degradation process is guided, and to a large part carried out, by members of a class of enzymes termed *caspases*, which is short for **c**ysteine **asp**art**ases** or **c**ysteine-dependent **asp**artate-directed prote**ases**. Caspases are thus proteases relying on a cysteine residue in their active centre to catalyse the cleavage of substrate proteins C-terminally of aspartate residues. However, caspases do not cleave randomly after any aspartate, but rely on specific recognition sequences in their substrate proteins. To date, almost 1,000 caspase substrate proteins are known, yet only a minority of these have been confirmed in vivo, and for even fewer of them a physiological function of the cleavage has been described.[15] The goal of the third main project described in this dissertation was the identification of the protein BMAL1 (ARNTL) as a new *bona fide* caspase substrate.[16]

Together, the projects and the corresponding manuscripts on which this dissertation is based have contributed to expanding the understanding of the induction, inhibition and execution of apoptosis. The following chapters will thus provide a brief introduction to apoptosis with special focus on these three fields to help in accessing and interpreting the presented results.

1.2. Hallmarks of apoptosis

1.2.1. Cell contraction and membrane blebbing

Apoptosis was first identified as a distinct type of cell death by the morphological features of apoptotic cells: the disintegration into discrete apoptotic bodies, which is preceded by contraction and *blebbing*, the formation of small protrusions termed *blebs*, of the cell's plasma membrane.[3,5] In the early stages after cell contraction and rounding, the formation of the first blebs is referred to as surface blebbing,

whereas at later stages, dynamic blebbing leads to much more severe changes in cell shape. Eventually, long protrusions of the plasma membrane are formed, such as the so-called *apoptopodia*.[17] All of these changes in plasma membrane morphology result from a remodelling of the cell's actin-myosin cytoskeleton, which, like most effects of apoptosis, is orchestrated by caspases. The architecture of the actin-myosin cytoskeleton is generally regulated by a family of GTPases termed *Rho GTPases*, which in turn are regulated by the *Rho-associated protein kinase 1* (ROCK1). In apoptotic cells, an isoform of ROCK1 is cleaved by caspases, resulting in loss of its auto-inhibitory domain and thus constitutive ROCK1 activation. Cleaved ROCK1 then proceeds to phosphorylate myosin light chain (MLC) filaments of the cell's cytoskeleton to generate the contractile force that causes membrane blebbing (**Figure 2**).[5,18] In addition, the cell retracts from surrounding cells and tissue due to caspase-dependent detachment of focal adhesion sites and cell-cell adhesion sites.[5]

1.2.2. Disintegration of the nucleus

The actin cytoskeleton is connected to the nuclear envelope, and apoptotic ROCK1 activation thus exerts considerable stress on the nucleus that literally tears it apart.[5,19] To facilitate this, the nuclear architecture is additionally weakened by caspase-mediated cleavage of the nuclear lamina (**Figure 2**).[20] While lamin cleavage alone is not sufficient to disrupt the nucleus, it may weaken its structure sufficiently to allow actin filament contraction to achieve this. Once the nucleus has fragmented, the nuclear fragments are transported to the membrane blebs in the plasma membrane via the cytoskeletal microtubule system.[21] Inside the membrane blebs, the nuclear fragments are sealed and shed off in the form of apoptotic bodies.

1.2.3. Chromatin condensation

Similarly to nuclear disintegration, apoptotic chromatin condensation has also been shown to be mediated by caspases, specifically through cleavage of the proteins *apoptotic chromatin condensation inducer in the nucleus* (ACINUS)[22] and *serine/threonine-protein kinase 4* (STK4 / MST1), although it was later shown that ACINUS is dispensable for chromatin condensation .[5,23] Additionally, both chromatin condensation and DNA fragmentation can be induced by apoptotic release of the protein *apoptosis-inducing factor* (AIF) from the mitochondria.[24,25] However, the exact mechanism of apoptotic chromatin condensation has remained elusive so far.

1.2.4. Organelle fragmentation

Just as the nucleus disintegrates into fragments, other cellular organelles also undergo apoptotic fragmentation. This affects especially the mitochondria, the *endoplasmic reticulum* (ER), and the Golgi apparatus (Golgi). While mitochondrial fragmentation and its role in apoptosis will be discussed in chapter 1.5.7 in much more detail, the fragmentation of ER and Golgi will be discussed here. Apoptotic fragmentation of the Golgi is facilitated by the caspase-mediated cleavage of the *Golgi reassembly-stacking protein 1* (GORASP1 / GRASP65) and *golgin subfamily B member 1* (GOLGB1 / giantin), which are responsible for the stacking of the Golgi membrane into the typical cisternal structure, and the *golgin subfamily A member 3* (GOLGA3 / Golgin-160), which also has a suspected role in Golgi structure (**Figure 2**).[26-28] Unlike nuclear disintegration, the fragmentation of the Golgi is independent of the apoptotic remodelling of the cytoskeleton.[29] In addition, cellular vesicle trafficking is shut down during apoptosis via caspase-mediated cleavage of *syntaxin-5* (STX5), which mediates vesicle transport from the ER to the Golgi, and *Rab GTPase-binding effector protein 1* (RABEP1 / rabaptin-5), which is involved in endosome trafficking, and *general vesicular transport factor p115* (USO1), which contributes to Golgi fragmentation after its cleavage.[28,30,31] Apoptotic remodelling of the ER is less well-understood but is still a phenomenon that clearly plays an important role in apoptotic body formation. It is probably an active yet caspase-independent process which results in the relocalisation of ER fragments from the perinuclear area to the plasma membrane and finally into apoptotic bodies.[32]

1.2.5. DNA fragmentation

Membrane blebbing and actin-myosin remodelling also play a role during the final steps of another classical hallmark of apoptosis: the condensation and fragmentation of genomic DNA, which is eventually relocalised into membrane blebs and packaged into apoptotic bodies.[33] Chromatin condensation (also called *pyknosis*) and DNA fragmentation were among the earliest apoptotic markers discovered.[34] Just like membrane blebbing, apoptotic DNA fragmentation is largely guided by caspases, yet since these are proteases, they cannot cut DNA directly. Instead, caspases activate the aptly named *caspase-activated DNase* (CAD / DFFB) by cleaving the *inhibitor* of *caspase-activated DNase* (ICAD / DFFA).[35–37] As an endonuclease, CAD consequently proceeds to cleave the genomic DNA (**Figure 2**).

The cleavage takes place at the internucleosomal linkers, i.e. exposed parts of DNA that are not wound around histones. This creates DNA fragments with a length of about 180 nucleotides or multiples thereof, resulting in a typical "DNA ladder" pattern when separated by gel electrophoresis.[34]

1.2.6. Shutdown of transcription and translation

The fragmentation of nuclear DNA during apoptosis not only facilitates its packaging into apoptotic bodies, but it also serves a crucial protective function that becomes especially important in the case of viral infection and carcinogenesis: the shutdown of gene transcription and translation. In addition to the CAD-mediated cleavage of DNA, apoptosis also causes the caspase-mediated cleavage of factors involved in these processes. This includes the cleavage of several transcription factors, such as *activating protein 2α* (TFAP2A), *B transcription factor 3* (BTF3), *nuclear factor of activated T-cells 1 & 2* (NFATC1 & NFATC2), *nuclear factor kappa-light-chain-enhancer of activated B cells* (NF-κB p65 / RELA), and *specificity protein 1* (SP1), as well as several others.[5,38] Many *eukaryotic translation initiation factors* (EIFs) are also cleaved by caspases, such as EIF2A, EIF3A, EIF4B, EIF4E, EIF4G1, and EIF4H (**Figure 2**). In addition, several components of the ribosomal translation machinery are cleaved, such as the *60S acidic ribosomal protein P0* (RPP0) and the *ribosomal protein S6 kinases* (RPS6Ks).[5,38,39] The involvement of caspases in the shutdown of transcription factors is especially interesting in the context of one of the research projects on which this dissertation is based, since it adds the transcription factor BMAL1 (ARNTL) to this list.[16]

1.2.7. Release of "find me" and "eat me" signals

Apoptotic cells communicate with their environment to facilitate their rapid removal by means of phagocytosis: they release *"find me" signals* that attract phagocytes, and they present *"eat me" signals* on their plasma membrane that enable recognition and subsequent engulfment by the phagocyte.[40,41] The most well-known and well-understood "eat me" signal to date is *phosphatidylserine* (PS).[42] This phospholipid is normally retained on the cytoplasmic side of the plasma membrane but becomes exposed on the outside in apoptotic cells (**Figure 2**).[43] The localisation of PS depends on two types of enzymes: *flippases*, which transport PS to the cytoplasmic side of the membrane, and *scramblases*, which transport PS non-specifically in either direction. Upon apoptosis induction, flippases are inactivated and

scramblases are activated. Both of these events depend on caspase-mediated cleavage of the respective enzyme.[44–46] In opposite to "eat me" signals, the "find me" signals released by apoptotic cells do not stay bound to the plasma membrane but instead spread out into the surrounding tissue to attract phagocytes. However, there are some molecules that can serve as either of these signals depending on whether they remain membrane-bound or are released, such as *lysophosphatidylcholine* (LPC).[47–49] In general, "find me" signals are chemically diverse and include, in addition to lipids such as LPC, proteins such as dimerised *40S ribosomal protein S19* (dRPS19), peptides such as *endothelial monocyte-activating polypeptide II* (EMAP II), and nucleotides such as ATP and UTP, to name but a few.[50,51] Just like the exposure of "eat me" signals, the release of "find me" signals depends at least partially on caspase activity.[49]

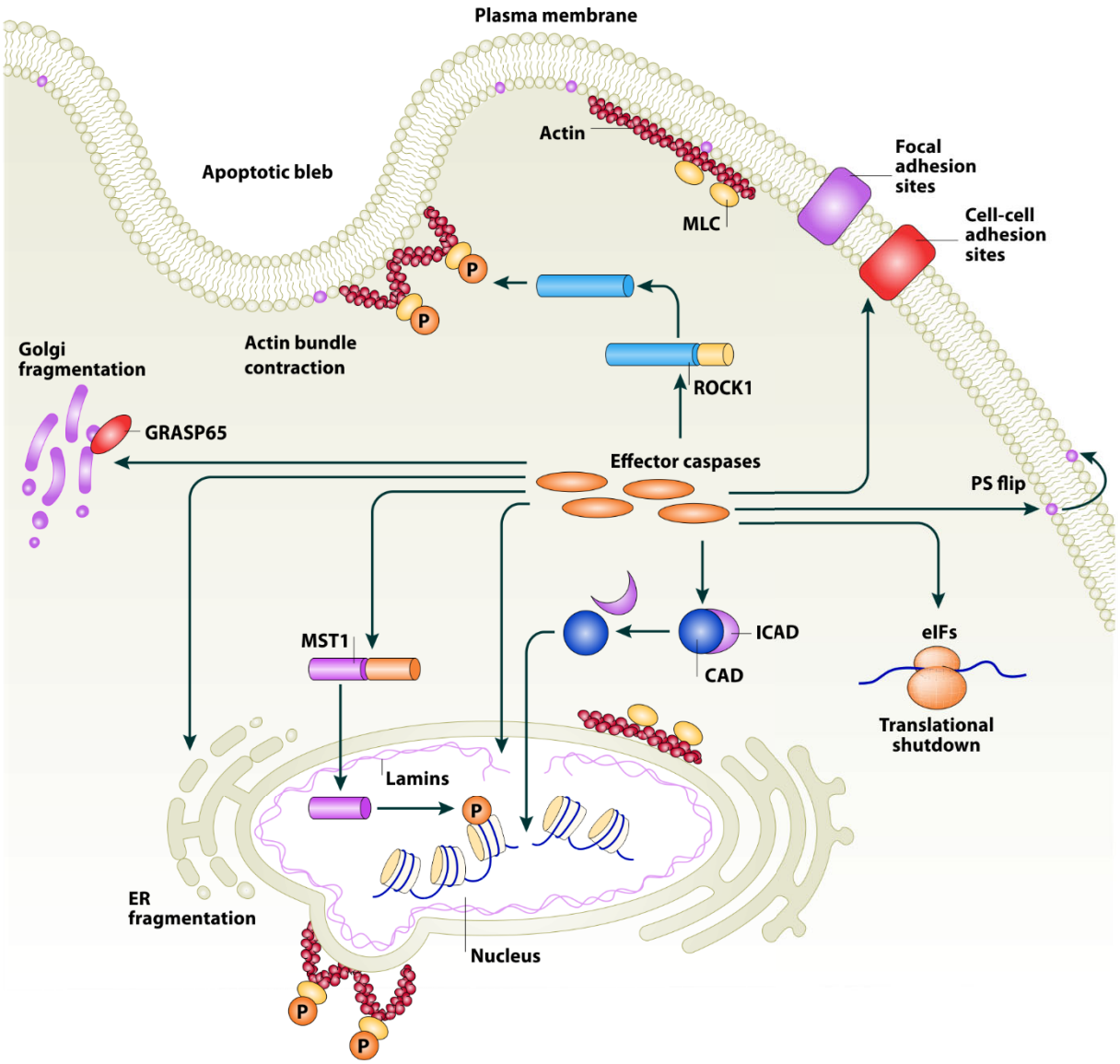

Figure 2: Hallmarks of apoptosis. During apoptosis, the **effector caspases** mediate the controlled demolition of the cell in a multitude of ways. The plasma membrane contracts and forms so-called **apoptotic blebs** due to remodelling of the actin–myosin cytoskeleton. This is in part due to excessive **actin bundle contraction** caused by the phosphorylation of **MLC** by constitutively active caspase-cleaved **ROCK1**. Cleavage of the nuclear **lamins** by caspases facilitates the apoptotic disintegration of the **nucleus**. The kinase **MST1** contributes to chromatin condensation if it is cleaved by caspases, and cleavage of **ICAD** releases its inhibition of the DNase **CAD**, leading to apoptotic DNA fragmentation. Aside from the nucleus, other organelles also disintegrate during apoptosis: while the role of caspases in **ER fragmentation** is still unclear, their role in **Golgi fragmentation** is exerted through cleavage of Golgi-stacking proteins such as **GRASP65**. Another consequence of apoptosis is a transcriptional and **translational shut down** of the cell, which is in part due to the caspase-mediated cleavage of eukaryotic translation initiation factors (**EIFs**). The cell retracts from the surrounding tissue due to caspase-dependent detachment of **focal adhesion sites** and cell-cell adhesion sites. Finally, to facilitate its rapid removal through phagocytosis, the cell releases "find me" signals and exposes "eat me" signals such as phosphatidylserine (**PS**).

1.3. Caspases, the executioners of programmed cell death

1.3.1. Discovery and classification of caspases

The caspases (**c**ysteine **asp**art**ases**) are a class of endoproteases that are centrally involved in the initiation and execution of apoptosis. They are directly or indirectly responsible for virtually all of the hallmarks of apoptosis described in the previous chapters. The potential role of caspases in apoptosis was first noticed in 1993 when human *caspase-1* (CASP1, originally called *interleukin-1 converting enzyme* (ICE)), the only caspase known at that time, was identified as an orthologue of the *C. elegans* protein CED-3, which plays a crucial role in programmed cell death during the embryonic development of this species.[52,53] Since then, fourteen caspases numbered CASP1 to CASP14 have been identified in mammals, and either eleven or twelve of these are expressed in humans; the *CASP12* gene is a non-functional pseudogene in most individuals, and CASP11 and CASP13 are expressed only in non-human animals.[54–56] While the caspases have been numbered in the order of their discovery, they are classified according to their function: as either inflammatory caspases (CASP1, CASP4, CASP5 and CASP12) or apoptotic caspases, the latter of which are further divided into *initiator caspases* (CASP2, CASP8, CASP9 and CASP10) and *executioner caspases* (CASP3, CASP6 and CASP7; also called *effector caspases*).[57] Human CASP14 appears to play a role in neither inflammation nor apoptosis but in terminal keratinocyte differentiation.[58,59]

1.3.2. Initiator caspases and executioner caspases

The division of the apoptotic caspases into initiator caspases and executioner caspases is based on their respective role in the *caspase cascade*, the consecutive activation of caspases by other caspases: initiator caspases start the caspase cascade in response to pro-apoptotic stimuli by cleaving and thus activating the executioner caspases, which then go on to cleave hundreds of different substrate proteins.[60] Both initiator and executioner caspases are synthesised as *pro-caspases*: inactive zymogens that are constitutively expressed to enable their rapid activation. During their activation in apoptotic cells, all pro-caspases are cleaved by another caspase.[61] However, this cleavage is neither sufficient nor necessary to activate the initiator caspases, which can become partially activated by a process termed *proximity-induced activation*. In this process, the initiator caspases are recruited to adaptor proteins via homotypic

binding of protein interaction domains collectively known as *death folds*.[62,63] Homologous death folds are present both in the adaptor proteins and in the respective initiator caspases. The initiator caspases of the extrinsic apoptotic pathway (CASP8 and CASP10) interact with their adaptor proteins via two death folds termed *death effector domains* (DEDs) and assemble into a caspase-activating complex termed the *death-inducing signalling complex* (DISC). Correspondingly, the main initiator caspase of the intrinsic apoptotic pathway, CASP9, interacts with its adaptor proteins via a single death fold termed *caspase activation and recruitment domain* (CARD) to assemble into the *apoptosome*.[5,64–66] Both the DISC and the apoptosome facilitate the proximity-induced activation of the respective initiator caspases, presumably by enabling their dimerisation. Although the molecular mechanism is still not understood in detail, it is believed that this dimerisation leads to conformational changes in the caspase molecule that stabilise its catalytic centre in an active conformation, and that subsequent cleavage of the caspase molecule only serves further conformational stabilisation.[63,67,68] In the case of executioner caspases, however, the mechanism of activation is much better understood: here, the required conformational changes are blocked by steric hindrance, and cleavage by an initiator caspase enables these changes and leads to activation of the executioner caspase (**Figure 3**).[60]

1.3.3. Caspase structure and mechanism

Despite their different roles, all caspases share similar structures: as inactive pro-caspases, they all consist of an N-terminal pro-domain followed by the actual caspase domain. The pro-domain of executioner caspases is only a short peptide, whereas it is much longer in initiator caspases and inflammatory caspases since it contains their death folds. During their activation, caspases are cleaved at two sites, resulting in detachment of the pro-domain and separation of the caspase domain into a large and a small subunit that undergo a conformational rearrangement to form a fully active caspase dimer-of-heterodimers (**Figure 3**).[5,57,61] All activated caspases are cysteine aspartases, i.e. they depend on a cysteine in the catalytic triad of their reactive centre to cleave their substrate proteins by hydrolysis of the peptide bond C-terminal of an aspartate residue (or, in very rare cases, a glutamate residue).[69] However, caspases do not cleave randomly after any aspartate but instead are highly selective for specific sites in specific proteins. This is achieved by the presence of recognition sequences in the

substrate proteins that consist of at least four amino acid residues N-terminal of the cleavage site. According to convention, these residues are labelled P4 to P1, with P1 marking the residue after which the caspase cleaves.[15] Correspondingly, the substrate binding groove of the caspase that houses its catalytic centre contains four binding pockets termed sub-sites and labelled S1 to S4. Each amino acid residue in the substrate protein's recognition sequence thus binds specifically to the corresponding sub-site in the caspase.[60,68] While the binding pocket for the P1 residue is conserved among all known caspases, the binding pockets for the other three residues show some variation. Most caspases seem to slightly prefer a glutamate at the P3 position, but this is not a strict requirement, and the preference for residues P2 and P4 is even more variable. This enables different caspases to recognise different sequences and thus to cleave different sites in different proteins.

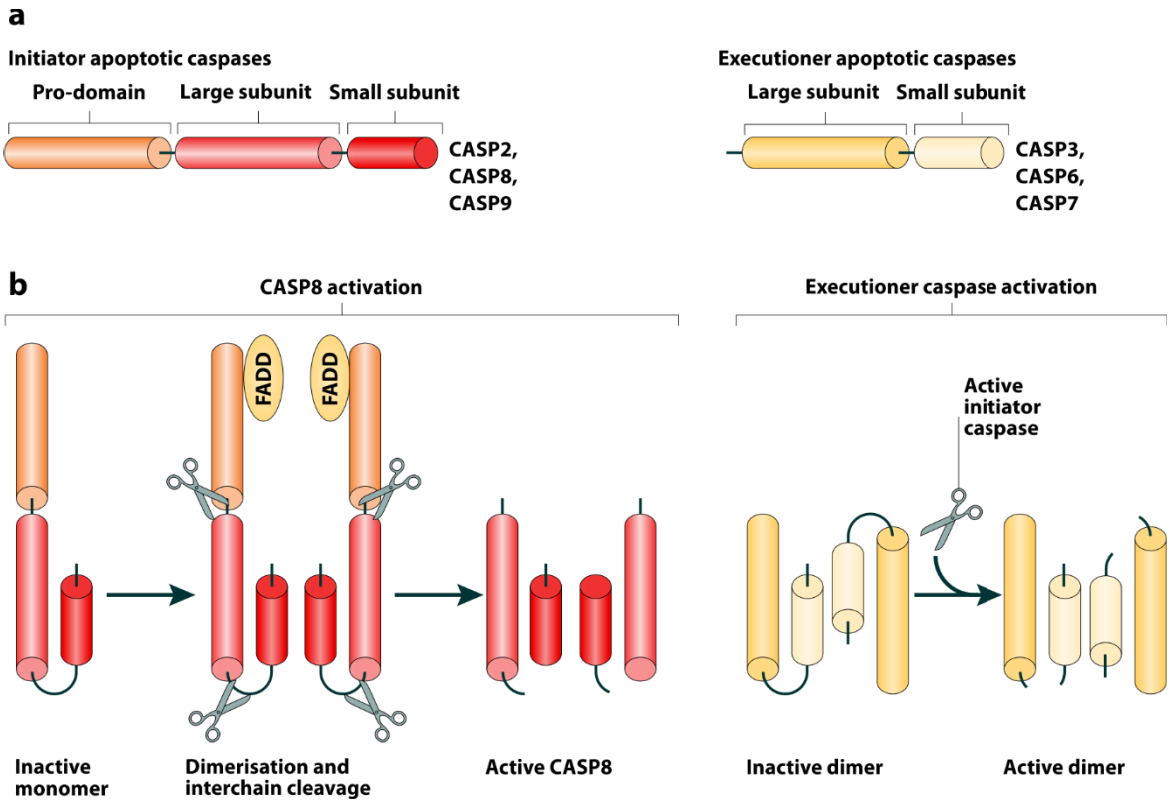

Figure 3: Caspase classification, structure, and activation. (a) The apoptotic caspases are divided into **initiator apoptotic caspases**, which consist of a long **pro-domain**, a **large subunit** and a **small subunit**, and executioner apoptotic caspases, which have the same basic structure but in which the pro-domain is negligibly short. **(b)** In a non-apoptotic cell, initiator caspases exist as **inactive monomers**. A pro-apoptotic stimulus triggers their proximity-induced activation via recruitment to their respective adaptor proteins. For example, in the case of **CASP8 activation**, the death folds in the pro-domain of this initiator caspase bind to corresponding domains of the FAS-associated death domain protein (**FADD**). This enables the **dimerization and interchain cleavage** that produces fully **active CASP8**, which consists of a dimer-of-heterodimers. **Executioner caspase activation** occurs in a similar manner but with some important differences: it does not rely on proximity-induced activation and autocatalytic cleavage but requires an active initiator caspase that cleaves the pre-formed **inactive dimer** to produce the **active dimer**.

1.3.4. Substrate specificity of caspases

Aside from the classification of caspases according to their function (initiator, executioner or inflammatory), they have also been classified into three groups according to their preferred recognition sequence: group I caspases (CASP1, CASP4, CASP5, and CASP13), which slightly prefer bulky hydrophobic amino acids at the P4 position and preferentially recognise the sequence (W/L)EHD; group II caspases (CASP2, CASP3 and CASP7), which strongly prefer an aspartate at the P4 position and preferentially recognise the sequence DExD; and group III caspases (CASP6, CASP8, CASP9, and CASP10), which prefer branched chain aliphatic amino acids at the P4 position and preferentially recognize the sequence (I/V/L)E(H/T)D.[70–73] This classification is based on known recognition sequences in proven caspase substrates, and the discovery of new substrates thus enabled a more detailed and specific definition of the recognition sequences of individual caspases, such as the sequence VExD for CASP6 and the sequence DxxD for CASP3.[72] However, whenever the concept of such recognition sequences is considered, three points have to be kept in mind: first, that these sequences are merely approximations of the actual chemical requirements, which may well tolerate different residues; second, that it is common for different caspases to cleave at the same sites due do overlaps in their specificities, and that probably no sequence is exclusively recognised by only one caspase; and third, that a recognition sequence is not the only prerequisite for cleavage, but that other factors also play a role, such as the amino acid residue after the cleavage site (P1') or the position of the site in the substrate protein's tertiary structure.[69] Nevertheless, the substrate specificity of different caspases is thought to reflect their function at least partially: the recognition sequence of group III, which contains mainly initiator caspases, is found in many other caspases, and the recognition sequence of group II caspases, which contains mainly executioner caspases, is found in many of the other proteins that are cleaved during cell death.[71]

1.3.5. Caspase substrate proteins

Caspase substrate proteins are numerous and highly diverse: almost 1,000 proteins have been shown to be cleaved by caspases at least in vitro, and the comprehensive caspase substrate database *Cascleave* contains entries for 562 cleavage sites in 370 proteins that are considered to be *bona fide* caspase

substrates.[15,72] One such *bona fide* caspase substrate protein, BMAL1, was identified in one of the three studies this dissertation is based on.[16] The cleavage of caspase substrates is responsible for almost all features associated with apoptotic cells, from DNA fragmentation to phagocytosis, as described in chapter 1.2.[34,49] However, not every cleavage event is actually relevant to the process of apoptosis. Many caspase substrate proteins are so-called bystander substrates, meaning that they contain a recognition sequence that is sufficient for cleavage, but that no relevant effect of this cleavage could be observed.[38,69,73] Examples of such presumed bystander substrates are the proteins *DNA topoisomerase 1* (TOP1), *protein O-GlcNAcase* (MGEA5), and *signal recognition particle 72 kDa protein* (SRP72).[38] Of those caspase substrates whose cleavage has been shown to fulfil a physiological function, most are inactivated by cleavage, as could be expected. However, some proteins are also activated by cleavage, such as most notably the caspases themselves. Other proteins undergo a change in function after caspase-mediated cleavage, such as some members of the BCL2 protein family (discussed in detail in chapter 1.5.5), the cleavage of some of which turns them from anti-apoptotic into pro-apoptotic proteins.[38,74,75]

1.3.6. Roles of caspases beyond apoptosis

Apoptosis is not the only type of programmed cell death. Two related but distinct death pathways have been characterised recently: *necroptosis* (programmed necrosis) and *pyroptosis* (inflammatory cell death). One central characteristic that these programmed cell death pathways share with apoptosis is their regulation by caspases.[76] Necroptosis is thought to be an "emergency self-destruct" mechanism that is used by the cell if induction of apoptosis fails. While apoptosis depends on caspase activity, necroptosis depends on the lack thereof. Specifically, the initiator caspase CASP8 is thought to decide whether an extrinsic pro-apoptotic stimulus leads to apoptosis (if CASP8 can be activated) or necroptosis (if CASP8 remains inactive).[77,78] Pyroptosis, a highly pro-inflammatory form of programmed cell death that can be initiated in response to infection, is regulated by the inflammatory caspases CASP1, CASP4, and CASP5 (in mice: CASP11).[79] Aside from cell death and inflammation, caspases may also play roles in tissue regeneration, cell proliferation, and cell differentiation.[80–83] One example for this is CASP2, which is now recognised to have a complex function in the response to DNA damage and aberrant cell division.[84–86]

1.4. Extrinsic apoptosis pathways

1.4.1. Induction of extrinsic apoptosis

Apoptosis can be induced via either the *extrinsic pathway* or the *intrinsic pathway*, both of which converge in the activation of executioner caspases. The extrinsic pathway plays a role mainly in the regulation and execution of immune cell function. Extrinsic apoptosis is mediated through the binding of specific ligands to corresponding *death receptors*, which are displayed on the target cell's surface.[87] Death-inducing ligands are displayed or secreted mainly by immune cells, such as *cytotoxic T lymphocytes* (CTLs, also called CD8+ T cells or killer T cells) and *natural killer cells* (NK cells), but other types of cells may also do so under specific circumstances.

A classic example of extrinsic apoptosis is one of the ways by which immune cells eliminate pathogen-infected cells: on the surface of most cells, proteins of the *major histocompatibility complex I* (MHC-I) display antigenic peptides that result from the proteasomal degradation of proteins inside the cell.[88,89] While the presentation of normal self-antigens leads to immune tolerance, infected or malignant cells often display peptides derived from pathogens or oncogenes, which can be recognised by CTLs. If antigen presentation via MHC-I is suppressed by the infected or malignant cell, the absence of self-antigen presentation can be recognised by NK cells. In both cases, either CTLs or NK cells can then induce apoptosis in the affected cell.[90–96]

Extrinsic apoptosis also plays a crucial role in the selection and regulation of immune cells, particularly B and T lymphocytes (**Figure 4**). During their development, these cells undergo an extensive and strict selection process both to ensure their functionality as well as to remove potentially autoreactive cells that might cause an autoimmune response. Those B or T lymphocytes that retain strongly autoreactive receptors are eliminated by a process termed clonal deletion, which involves induction of extrinsic apoptosis in autoreactive cells before they maturate and leave the primary lymphoid organs.[63,97–99] Similarly, effector lymphocytes that enter immunologically privileged tissues, such as the eye or the gonads, are rapidly eliminated by extrinsic apoptosis, which is induced via the expression of specific death-inducing ligands on the surface of cells in these tissues.[100] Finally, extrinsic apoptosis contributes to the self-regulation and self-limitation of an immune response. Activated B and T lymphocytes become

more sensitive to apoptosis-inducing stimuli, so they can easily be disposed of after they have served their purpose. This process is called *activation-induced cell death* (AICD) and involves the increased expression of death receptors on the lymphocytes' surfaces, making them more susceptible to ligand-induced extrinsic apoptosis.[101–106]

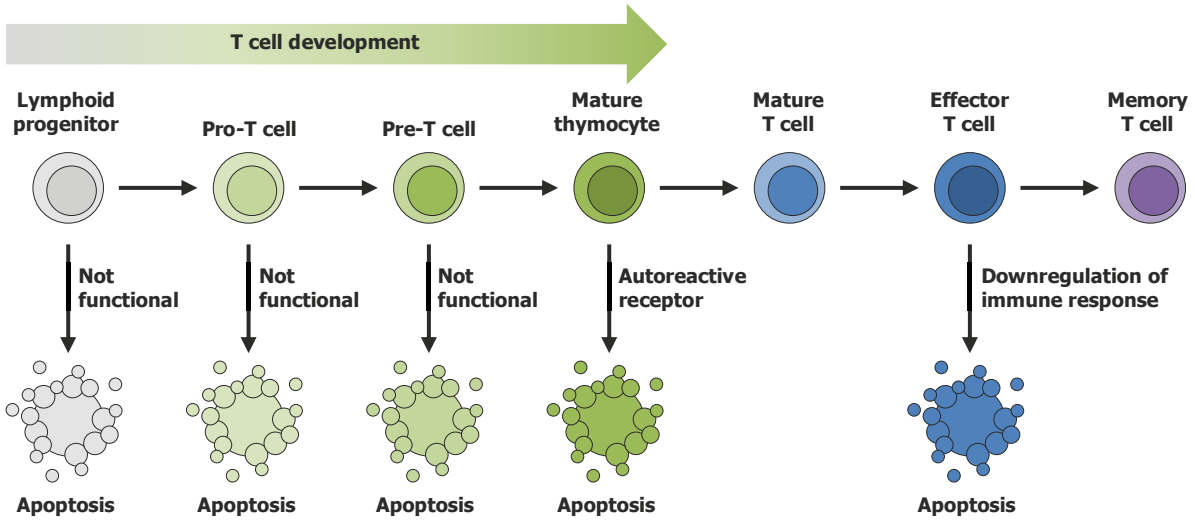

Figure 4: Role of apoptosis in the development and regulation of T cells. During the development of common lymphoid progenitor cells (grey) into T cells, the intermediate stages (green) are subject to strict quality control, resulting in apoptosis of non-functional cells. Mature thymocytes (dark green) undergo apoptosis if they are potentially autoreactive. During an immune response, mature T cells (blue) become activated and turn into effector T cells (dark blue). When the immune response is over, most of these are disposed of by apoptosis, and only a few survive as memory T cells (purple).

1.4.2. Death receptors and death-inducing ligands

Extrinsic apoptosis is mediated by the death receptors, which are members of the *tumour necrosis factor receptor superfamily* (TNFRSF) that comprises at least 26 known members, and their corresponding ligands, which are members of the *tumour necrosis factor superfamily* (TNFSF) that comprises at least 19 known members.[107,108] All members of the TNFRSF and of the TNFSF form homotrimers when the respective ligands bind to their corresponding receptors, although other forms of multimers have also been proposed for some members. However, not all of these ligands or receptors are involved in apoptosis. The eponymous founding members of the two superfamilies, the cytokine *tumour necrosis factor* (TNF, formerly called TNFα) and its corresponding receptors (TNF receptors; TNFRSF1A and TNFRSF1B), were discovered when the release of TNF from immune cells in response to bacterial endotoxins was correlated with tumour necrosis.[87,109] However, TNF itself can not only induce apoptosis

but also inflammation, necroptosis or even cell survival and proliferation, depending on the downstream processing of its signal, which in turn depends on the cell type and the physiological context.[76,78,110,111] The major apoptosis-inducing members of the TNFSF and the TNFRSF that are best studied to date are the *Fas ligand* (FASL, also known as FASLG, CD95L, CD178, or APO-1L) and the corresponding receptor *FAS* (also known as FasR, CD95, APO-1, or TNFRFS6) as well as the *TNF-related apoptosis-inducing ligand* (TRAIL, also known as TNFSF10, CD253, or APO2L) and the corresponding two TRAIL receptors TRAIL-RI (TNFSF10A, also known as DR4) and TRAIL-RII (TNFSF10B, also known as DR5). Like most TNFSF members, FASL and TRAIL can be expressed either in a membrane-bound form that is displayed on the surface of the cell expressing it, or in a soluble form that is released by the cell and acts as a cytokine. FASL is the death-inducing ligand mainly involved in lymphocyte regulation and lymphocyte-induced apoptosis as described in the previous chapter, and it is displayed and released mainly by lymphocytes.[105,106] However, only its membrane-bound form can induce apoptosis.[112] TRAIL, on the other hand, is active in both the membrane-bound as well as the soluble form, although the former is more active that the later.[113] Membrane-bound TRAIL is displayed on the surface of some NK cells to induce apoptosis in their target cells.[94] In a more general context, TRAIL appears to play a role in immune surveillance and immune-mediated tumour suppression.[113] A particularly interesting feature of TRAIL, as opposed to other apoptosis-inducing members of the TNFSF, is that it appears to be able to induce apoptosis specifically in malignant cells while sparing healthy cells.[114] This feature has been the subject of extensive research including several clinical trials. However, to date, the reason for this specificity is still not fully understood, and no statistically significant anticancer activity could be shown for any of the TRAIL-receptor agonists tested in clinical trials so far.[113,115,116]

1.4.3. Activation of caspases in extrinsic apoptosis

All receptors of the TNFRSF that are involved in apoptosis, including the TNF receptor TNFRSF1A, the FASL receptor TNFRSF6, and the two TRAIL receptors TNFSF10A and TNFSF10B, contain an intracellular domain called the *death domain* (DD). Upon ligand binding to the receptor, the resulting receptor trimerisation leads to conformational changes in the DDs that enable the recruitment of the

FAS-associated death domain protein (FADD) to the DDs. FADD is an adaptor protein that in turn recruits the initiator caspases of the extrinsic pathway, CASP8 and CASP10, via homotypic interaction between the *death effector domains* (DEDs) of FADD and of the respective caspase (**Figure 5**). For some death receptors such as TNFRSF1A, this step requires an additional adapter protein, *TNF receptor-associated death domain protein* (TRADD), to lead to apoptosis induction. As described in chapter 1.3.2, these interactions result in the assembly of the caspase-activating death-inducing signalling complex (DISC). This leads to activation of the extrinsic initiator caspases CASP8 and CASP10, which go on to cleave and thus activate executioner caspases such as CASP3 and CASP7.[5,63] The function of CASP8 and CASP10 is largely homologous and redundant, which is exemplified by the fact that many animals such as mice do not express CASP10.[117] Nevertheless, in humans, CASP8 and CASP10 produce different cleavage patterns in some of their substrates and may thus be not entirely redundant.[118] An interesting feature of the extrinsic apoptosis pathway is the *FLICE-like inhibitory protein* (FLIP, also known as CFLAR), which is a CASP8 homolog that lacks the catalytic cysteine and is therefore inactive. Like CASP8, FLIP can be recruited to the DED of FADD, where it can form heterodimers with CASP8. While it was long thought that FLIP acts exclusively as an inhibitor of CASP8 in this way, it has now been understood that different isoforms of FLIP can have either inhibitory or inducing functions and play a crucial role in the cell fate decision between apoptosis and necroptosis.[119–122] In some cell types, extrinsic apoptosis can also induce intrinsic apoptosis to enhance the strength of the apoptotic response. This is achieved via the activating, CASP8-mediated cleavage of the pro-apoptotic protein *BH3-interacting domain death agonist* (BID).[123] Cleaved, truncated BID (tBID) promotes intrinsic apoptosis, as described in more detail in chapter 1.5.6.

1.4.4. Granzyme B

Aside from death receptor signalling, CTLs and NK cells can also induce apoptosis in their target cells via direct injection of pro-apoptotic factors. Induction of apoptosis by this mechanism is not considered part of the extrinsic pathway since it bypasses death receptor signalling and initiator caspases and directly activates executioner caspases, but it is nevertheless an *extrinsic* form of apoptosis induction. To achieve this, the CTLs or NK cells release the contents of lytic granules onto the target cells. These

granules contain two decisive factors: *perforin* (PRF1), which inserts itself into the target cell's membrane, where it oligomerises to form pores, and *granzyme B* (GZMB), which is an enzyme with caspase-like activity, although it is not a caspase itself. Granzyme B directly cleaves and thus activates the executioner caspases CASP3 and CASP7.[5]

1.5. Intrinsic apoptosis pathways

1.5.1. Causes for the initiation of intrinsic apoptosis

While extrinsic apoptosis is induced via outside signals from other cells, intrinsic apoptosis is usually induced by events inside the affected cell itself. The best-understood cause for intrinsic apoptosis is irreparable DNA damage, such as induced by ionising radiation or some anti-cancer drugs.[6,124–126] However, while often used as a textbook example, this is by far not the only inducer. Other factors that can lead to induction of intrinsic apoptosis include hypoxia[127], hyperthermia[128], nutrient withdrawal[129], osmotic stress[130], growth factor deprivation or inhibition of survival signalling[11,131,132], infection of the cell with certain viruses or cytotoxic pathogens[133–135], activation of certain oncogenes such as MYC[136,137], persistently high levels of Ca^{2+} in the cytoplasm[138], ER stress[139,140], oxidative stress[141,142], mitochondrial damage or dysfunction leading to cristae disruption[143,144], certain neuropathologies or factors that lead to neural excitotoxicity[138,145], various factors during embryonic development[146,147], and the previously mentioned crosstalk from the extrinsic apoptotic pathway via tBID (chapter 1.5.6)[123,144]. Two of the three studies on which this dissertation is based deal with the induction of apoptosis: the mycotoxin PXA induces intrinsic apoptosis via mitochondrial stress and cristae disruption; the PI3K/PDK1/AKT pathway is involved in growth factor-dependent inhibition of apoptosis.[7,13] Mitochondria and their role in intrinsic apoptosis will thus be in the focus of the following chapters, while the regulation and inhibition of apoptosis with a focus on PI3K/PDK1/AKT signalling will be discussed in chapters 1.6.3 and 1.6.4.

1.5.2. Induction of intrinsic apoptosis

Just as the initiation of extrinsic apoptosis relies on recruitment of inactive procaspases into the DISC complex via homotypic binding to the death folds of adapter proteins, a very similar process takes place during the initiation of intrinsic apoptosis: here, the main intrinsic initiator caspase CASP9 and the

adapter protein *apoptotic protease-activating factor 1* (APAF1) bind via homotypic interaction of their death folds, the CARDs.[61,148] This interaction requires a crucial previous step: the assembly of multiple APAF1 molecules into the multimeric initiation complex of intrinsic apoptosis, the apoptosome, which in humans consists of seven APAF1 subunits. The shape of this complex resembles a seven-spoked wheel, with the APAF1 molecules as the spokes and CASP9 at the central hub (**Figure 5**).[149] The apoptosome activates CASP9 via proximity-induced activation, as described in chapter 1.3.2.[67,68] Apoptosome assembly depends on two additional factors: first, APAF1 is an ATPase that requires ATP to polymerize.[149,150] Second, while APAF1 is always present in the cell's cytoplasm, it normally remains in an inactive state, where its N-terminal CARD is hidden between two C-terminal beta propellers. To become active, APAF1 has to undergo a conformational change in which the CARD is displaced by another protein. This displacement, leading to induction of intrinsic apoptosis, is achieved by the protein *cytochrome c* (CYCS).[63] While cytochrome c is well-known for its function as an electron carrier in the mitochondrial respiratory chain (electron transport chain, ETC), it attains a new and completely different function when it is released from the mitochondria.[151–154] The release of cytochrome c from the mitochondria is both a necessary as well as a usually sufficient step in the induction of apoptosome-mediated intrinsic apoptosis.

1.5.3. The role of mitochondria in intrinsic apoptosis

The mitochondria are double-membraned organelles, comprising two functionally and structurally distinct membranes: the *inner mitochondrial membrane* (IMM; also known as mitochondrial inner membrane, MIM) and the outer mitochondrial membrane (OMM; also known as mitochondrial outer membrane, MOM).[155] The well-known function of the mitochondria as the powerhouse of the cell due to their large-scale production of ATP relies on the process of *oxidative phosphorylation* (OxPhos), which takes place at the IMM.[156,157] However, ATP production is by far not the only function of the mitochondria – they are also at the centre of the induction of intrinsic apoptosis.[158] The fact that intrinsic apoptosis is also known as the mitochondrial pathway of apoptosis demonstrates this importance. The *mitochondrial intermembrane space* (IMS) between the two membranes, IMM and OMM, houses many pro-apoptotic factors which, if released into the cytosol, can induce or enhance apoptosis (**Figure 5**).[159]

Aside from the above-mentioned CYCS, these factors also include SMAC (DIABLO)[160,161], OMI (HTRA2)[162–165], endonuclease G (ENDOG)[25,166], and apoptosis-inducing factor (AIF).[24,25] Most of these proteins play a different role in the intact mitochondria of healthy cells: cytochrome c is an electron carrier in the ETC, shuttling electrons from complex III to complex IV[153]; AIF is an oxidoreductase that also plays a role in OxPhos[24]; OMI may have a function as a mitochondrial chaperone.[167] Upon their release from the mitochondria and into the cytosol, these proteins undergo a fundamental change of function: AIF, as already discussed in chapter 1.2.3, causes chromatin condensation and DNA fragmentation.[24,25] Both OMI and SMAC bind and inhibit the *inhibitor of apoptosis* (IAP) proteins (described in more detail in chapter 1.6.1) and thus release their inhibition of caspases. Finally, cytochrome c binds to APAF1 proteins and thus enables them to oligomerise and assemble into the apoptosome, as described in the previous chapter. The release of all of these mitochondrial pro-apoptotic factors takes place through the process of *mitochondrial outer membrane permeabilisation* (MOMP).[159]

1.5.4. Mitochondrial outer membrane permeabilisation (MOMP)

The OMM, unlike the IMM, is not a strict diffusion barrier but is rather highly permeable to small hydrophilic molecules such as salts, nucleotides, and citric acid cycle intermediates. Channel proteins in the OMM, termed *voltage-gated ion channels* (VDACs), which are a subclass of the *porin* family of proteins, allow the passive diffusion of such and other molecules up to 5 kDa in size in either direction and are thus essential to the function of mitochondria in metabolism.[168–170] However, larger molecules such as most proteins can normally not pass the OMM in an uncontrolled fashion. During induction of intrinsic apoptosis, this changes dramatically: mitochondrial outer membrane permeabilisation (MOMP), resulting from the formation of very larges pore complexes in the OMM about 25–100 nm in diameter, enables the efflux of large molecules including cytochrome c and other pro-apoptotic factors.[154,159] MOMP is a highly coordinated and strictly regulated process that is largely mediated by two proteins, *BCL2-associated X protein* (BAX) and *BCL2 antagonist/killer* (BAK), as described in detail in a recent review article by Cosentino & García-Sáez.[171] Both BAX and BAK can shuttle between the cytosol and the OMM. In healthy, non-apoptotic cells, BAX is primarily cytosolic and BAK is primarily associated with the OMM. BAX and BAK each contain a hydrophobic groove that “hides”

their C-terminal transmembrane domain that enables insertion into the OMM. Activation of BAX, described in detail in the next chapter, displaces this domain and results in further structural changes that lead to the translocation of BAX to the OMM. There, activated BAX proteins dimerise with each other. A similar process leads to the dimerisation of BAK.[172,173] The resulting homodimers of either two BAX or two BAK proteins then oligomerise, i.e. they form oligomers of homodimers. Whether BAK and BAX can also form functional heterodimers with each other and whether the oligomers of dimers can contain a mixture of BAX and BAK or consist exclusively of either of the two is, as of 2017, still subject to ongoing debate.[171,174,175] In any case, the resulting oligomers assemble into ring-shaped structures that bend, stress and finally disrupt the OMM to form the *mitochondrial apoptosis-induced channel* (MAC) through which the pro-apoptotic factors are released. The pore that causes MOMP – not without reason often likened to Pandora's box – has been opened.[171,176–178]

1.5.5. Regulation of MOMP by BCL2 family proteins

The MOMP-mediating proteins BAX and BAK are members of a larger protein family, the BCL2 family. The complex interplay between the various members of this family regulates the cellular decision for or against MOMP. All eighteen known BCL2 family proteins contain one or more *Bcl-2 homology* (BH) domains, numbered BH1 to BH4, that are crucial for their mutual interaction. However, the individual functions of the BCL2 family members are quite different, so that they can be divided along two lines: first, into pro- and anti-apoptotic members, the former of which promote MOMP and the latter of which inhibit it; second, into multi-BH-domain proteins that contain several different BH domains and can localise to the OMM, and BH3-only proteins that contain only a BH3 domain and cannot localise to the OMM. While the BH3-only proteins are exclusively pro-apoptotic, the multi-BH-domain proteins comprise both pro- and anti-apoptotic members.[5,179,180] Both BAX and BAK are pro-apoptotic multi-BH-domain proteins. In contrast, the eponymous founding member of the BCL2 family, the protein *apoptosis regulator BCL-2* (BCL2; originally short for *B-cell lymphoma 2*) that should not be confused with the entire BCL2 family since it bears the same name, is an anti-apoptotic multi-BH-domain protein. As its name suggests, it was first discovered in a type of malignant B-cells.[181,182] In these cells, a chromosomal translocation event resulted, among other effects, in the overexpression of

BCL2 and thus in a strong inhibition of MOMP and, consequently, of apoptosis. This causal relation between BCL2 dysregulation and cell immortalisation defined BCL2 as a *bona fide* oncogene and thus moved it into the spotlight of research as a potential target in cancer therapy, as excellently summarised in a recent review by Ashkenazi and co-workers.[183] The anti-apoptotic function of the BCL2 protein results from its antagonism to the pro-apoptotic, i.e. MOMP-promoting, BCL2 family members. For this antagonism, several mechanistic models have been proposed.[171,179] While some of these models assume that anti-apoptotic BCL2 proteins inhibit BAX/BAK indirectly by sequestering their activators, the pro-apoptotic BH3-only proteins[184], other models propose that anti-apoptotic BCL2 proteins inhibit BAX/BAK directly by preventing pore formation until BH3-only proteins displace them.[185] A unified model has been proposed that attempts to reconcile these two opposing hypotheses.[186] In any case, BH3-only proteins act as the tip of the balance that decides for or against BAX/BAK pore formation, MOMP, and intrinsic apoptosis (**Figure 5**).

1.5.6. Induction of MOMP by BH3-only proteins

When a BH3-only protein binds either BAX/BAK via interaction of its BH3 domain with the hydrophobic groove, it displaces and thus releases the C-terminal transmembrane domain of BAX/BAK. This structural change is the activating event that enables dimerisation and persistent insertion of BAX/BAK into the OMM and thus triggers MOMP. In healthy, non-apoptotic cells, the numbers of BH3-only proteins are low. However, many of the pro-apoptotic stimuli described in chapter 1.5.1 lead to an increase in BH3-only protein levels via transcriptional upregulation: for example, DNA damage can upregulate NOXA (PMAIP1)[187] and *p53 up-regulated modulator of apoptosis* (PUMA; also known as *BCL2 binding component 3*, BBC3)[188] via the transcription factor *tumour suppressor p53* (TP53)[6]; ER stress can upregulate BIM (BCL2L11) via the transcription factor *C/EBP-homologous protein* (CHOP; also known as *DNA damage-inducible transcript 3 protein*, DDIT3)[139]; and growth factor deprivation can upregulate BIM via the transcription factor *forkhead box protein O3* (FOXO3).[189] In addition, active BH3-only protein levels can also be increased post-translationally. The prime example for this mechanism is the cleavage of BID by CASP8 that creates the more active tBID, as already briefly mentioned in chapter 1.4.3. As a result of this cleavage, tBID associates with BAX/BAK by binding its

hydrophobic BH3-binding pocket, thus facilitating BAX/BAK oligomerisation and MOMP (**Figure 5**).[123,190–194] In addition, tBID and some other BH3-only proteins such as *Bcl-2-interacting killer* (BIK) can also directly affect the inner mitochondrial membrane by inducing cristae disruption, a potentially pro-apoptotic event that can result in the release of cytochrome c and that is discussed in more detail in the following chapter.[144,159,176,195] Another pro-apoptotic BH3-only protein whose levels can be increased post-translationally is the *Bcl2-associated agonist of cell death* (BAD). While BAD is normally bound and thus inhibited by 14-3-3 proteins, this binding depends on BAD being phosphorylated at specific sites. The phosphatase calcineurin can dephosphorylate BAD and thus release it from inhibition by 14-3-3 proteins, which enables it to interact with other pro-apoptotic BCL2 family proteins and thus induce MOMP.[138,196]

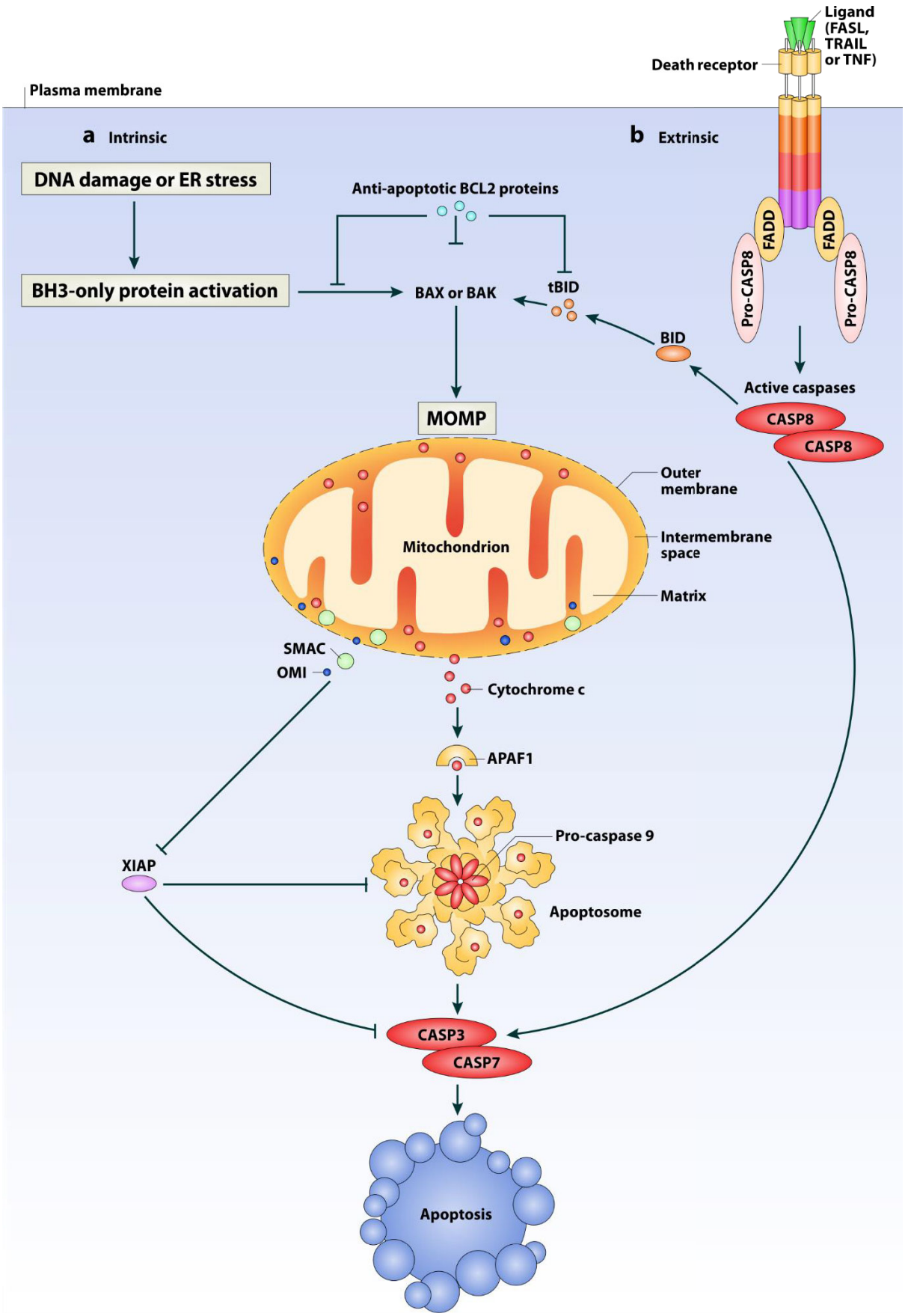
Ligand (FASL, TRAIL or TNF)
Death receptor
Plasma membrane
a Intrinsic
b Extrinsic
DNA damage or ER stress
Anti-apoptotic BCL2 proteins
BH3-only protein activation
BAX or BAK
tBID
BID
FADD
FADD
Pro-CASP8
Pro-CASP8
Active caspases
CASP8
CASP8
MOMP
Outer membrane
Intermembrane space
Matrix
Mitochondrion
SMAC
OMI
Cytochrome c
APAF1
Pro-caspase 9
Apoptosome
XIAP
CASP3
CASP7
Apoptosis

Figure 5: Induction of extrinsic and intrinsic apoptosis. (a) The induction of intrinsic apoptosis usually begins with one of several types of cellular stress or damage, including but not limited to **DNA damage or ER stress**, resulting in **BH3-only protein activation**. **(b)** The induction of extrinsic apoptosis also leads to activation of a specific BH3-only protein, **tBID**. It begins with the binding of a death-inducing ligand such as **FASL, TRAIL or TNF** to a corresponding **death receptor** on the **plasma membrane**, resulting in receptor trimerization, recruitment of the adaptor protein FADD, and consequent recruitment and proximity-induced activation of the initiator caspase CASP8. This activated caspase then cleaves **BID** and thus converts it into its active form tBID. The BH3-only proteins, which aside from tBID also include NOXA, PUMA, BIM, and BIK, are a type of pro-apoptotic BCL2 proteins. Two other types of BCL2 proteins compete for binding to BH3-only proteins: the **anti-apoptotic BCL2 proteins** on the one hand, and the pro-apoptotic multi-BH-domain proteins **BAX** and **BAK** on the other hand. If sufficiently many BH3-only proteins bind to BAX and BAK oligomerise to form large pore complexes in the outer mitochondrial membrane, leading to mitochondrial outer membrane permeabilisation (**MOMP**). A mitochondrion that undergoes MOMP releases many of its content proteins that are normally attached to its **matrix** or contained in its **intermembrane space**, including **SMAC**, **OMI**, and **cytochrome c** (CYCS). Upon their release, these mitochondrial proteins attain a pro-apoptotic function: SMAC and OMI counteract the anti-apoptotic function of **XIAP** and other so-called inhibitor of apoptosis (IAP) proteins, and CYCS binds **APAF1** to assemble into the **apoptosome**, a protein megacomplex that catalyses the conversion of **pro-caspase 9** into active CASP9. The initiator caspases CASP9 and CASP8 then go on to activate executioner caspases such as **CASP3** and **CASP7** that catalyse the final stage of **apoptosis**.
Note: The structure of the apoptosome in this figure may not accurately represent its actual stoichiometric composition.

1.5.7. Mitochondrial morphology and apoptosis

While the apoptotic loss of OMM integrity due to MOMP has been established as a key event in the induction of intrinsic apoptosis, the apoptotic events taking place at the IMM are less well-understood. The IMM is normally a tight diffusion barrier between the mitochondrial matrix and the IMS. Its surface, which is much larger than that of the surrounding OMM, is extensively folded into multiple invaginations termed cristae. The cristae are the sites at which cellular respiration through the ETC and ATP synthesis through OXPHOS take place, where the IMM potential ($\Delta\Psi_m$) is generated, and where most of the mitochondrial pro-apoptotic factors are contained.[155–157,197] Several functional and morphological changes that affect the IMM have been associated with apoptosis. Among these are mitochondrial fragmentation, loss of the $\Delta\Psi_m$, loss of IMM integrity, and cristae disruption (also called cristae remodelling). However, whether these changes are causes or effects of apoptosis (or possibly both) is not in all cases entirely clear.[198,199] For example, mitochondria have been observed to fragment at the same time or just before cytochrome c release, and this fragmentation has been linked to BAX/BAK.[200,201] It has been suggested that mitochondrial fission contributes to BAX/BAK-mediated MOMP and, conversely, that BCL2 family proteins such as BAX/BAK can also regulate mitochondrial fission.[201-203] However, while mitochondrial fragmentation clearly enhances apoptosis, it alone is neither sufficient nor necessary to induce apoptosis in humans[200,201,204,205], although it may be in other species

such as *C. elegans* and *D. melanogaster*.[206,207] Similarly, cristae disruption has also been linked to apoptosis, but the question as to whether it is cause or effect still remains. The width of the openings that connect the cristae with the IMS, the so-called *cristae junctions* (CJs), are regulated by the *mitochondrial contact site and cristae organizing system* (MICOS) as well as by the protein *dynamin-like 120 kDa protein, mitochondrial* (OPA1, originally short for *optic atrophy protein 1*), which also plays a role in mitochondrial fission and fusion.[208-210] Aside from its other roles in mitochondrial function, OPA1 is believed to act as the gatekeeper of CJs by keeping them tight and thus reducing the efflux of pro-apoptotic factors from the cristae.[195,205,209,211] Whether MICOS plays a relevant or a dispensable role in this process is subject to debate.[209,212] Several pro-apoptotic proteins interfere with OPA1, resulting in the release of cytochrome c from the cristae, probably through CJ widening and ultimately cristae disruption.[155,195,211,213] Among these proteins are several BH3-only BCL2 family members, such as BIK[214], BNIP3[215], BIM[216], and BID.[155,159,195,216] BID, for example, translocates to the mitochondria after CASP8-mediated cleavage into its active form, *truncated BID* (tBID; also referred to as *cleaved BID*, cBID), as discussed in the previous chapter. Inside the mitochondria, tBID disrupts the OPA1 oligomers that maintain the CJs in a tight conformation.[155,195] However, and seemingly paradoxically, other reports observed only a subtle effect of BH3-only proteins on the CJs, without CJ widening or cristae disruption.[159,216] To make matters more complex, it has also been reported that cristae remodelling happens downstream of caspase activation, i.e. that it is an effect rather than a cause of apoptosis.[158,159] On the other hand, cristae remodelling has been reported as a sufficient cause to induce apoptosis.[143,155] These apparent paradoxes might be resolved by the hypothesis that cristae remodelling may well be a sufficient cause for apoptosis, but not a necessary one. Cristae remodelling downstream of caspase activation, i.e. as an effect of apoptosis, might thus serve as an apoptotic amplifier.

1.5.8. The mitochondrial membrane potential $\Delta\Psi_m$ and apoptosis

The shape of the mitochondria in general and of the cristae in particular is closely connected to the mitochondrial inner membrane potential ($\Delta\Psi_m$). While polarised mitochondria normally maintain an elongated tubular shape, depolarized segments are separated from the mitochondrial network via fission, with excessive depolarisation resulting in excessive fission and hence fragmentation of the network.[198]

Just like mitochondrial fragmentation and cristae disruption, loss of $\Delta\Psi_m$ has been linked to apoptosis.[199,217] As a cause for apoptosis, loss of $\Delta\Psi_m$ alone is probably not sufficient in most cases: dissipation of $\Delta\Psi_m$ by protonophores, which also results in mitochondrial fragmentation, is reversible if the protonophore is removed, allowing both $\Delta\Psi_m$ as well as the mitochondrial network to recover without inducing apoptosis.[201] It has also been shown that the release of cytochrome c from the mitochondria does not necessarily coincide with loss of $\Delta\Psi_m$, and that apoptotic depolarisation of the mitochondria happens downstream of cytochrome c release and caspase activation.[199,218] As an effect of apoptosis, loss of $\Delta\Psi_m$ is well known to occur following MOMP, through both caspase-dependent and caspase-independent means.[159] Caspase-dependent loss of $\Delta\Psi_m$ is at least partially the result of caspase-mediated cleavage of the protein *NADH-ubiquinone oxidoreductase 75 kDa subunit* (NDUFS1), which is a core subunit of complex I of the ETC.[219] Caspase-independent loss of $\Delta\Psi_m$ following MOMP is partially attributed to the release of cytochrome c from the cristae, but it probably also depends on further events such as the caspase-independent apoptotic loss of the activity of complexes I and IV of the ETC. However, the reasons for this are still poorly understood.[159] In addition, loss of $\Delta\Psi_m$ can also occur upstream of apoptosis induction, although not as a cause but rather as a side effect of other apoptosis-inducing events.

1.5.9. The mitochondrial permeability transition pore (mPTP) and apoptosis

One potentially pro-apoptotic event that also causes loss of $\Delta\Psi_m$ is the persistent opening of the *mitochondrial permeability transition pore* (mPTP or MPTP; also referred to as PTP, PTPC, or sometimes mTP or *mitochondrial megachannel*, MMC). The mPTP is a protein channel complex in the IMM that usually remains closed in healthy mitochondria. With an estimated pore radius of 1.4 nm, it allows free diffusion of molecules up to about 1.5 kDa in size in either direction.[220] Persistent mPTP opening, called *mitochondrial permeability transition* (mPT, MPT or PT), thus leads to equilibration of all ion gradients between mitochondrial matrix and intermembrane space, resulting in loss of $\Delta\Psi_m$.[170,220,221] While the mPTP may be able to "flicker" between open and closed states even in healthy mitochondria, persistent opening in the form of mPT occurs only in response to certain types of cellular stress, such as high cytosolic Ca^{2+}, oxidative stress, or high matrix pH.[220,222] To make matters more

complex, loss of $\Delta\Psi_m$ is not only a necessary consequence of mPT, but can also contribute to mPT as an upstream event, although it alone is probably not sufficient.[220] The mPTP has been, and still is, subject to extensive controversy, ranging from its role in apoptosis to even its molecular identity. It has long been thought that the mPTP consists of three core proteins: VDAC located in the OMM, the *adenine nucleotide translocato*r (ANT) located in the IMM, and *cyclophilin D* (CYPD; also known as *peptidylprolyl isomerase D*, PPID) located in the mitochondrial matrix. In this model, VDAC and ANT form the mPTP megachannel whereas CYPD serves as a regulator of mPTP opening, and the mPTP would bypass both the IMM and OMM and thus directly connect the mitochondrial matrix to the cytosol.[170] However, this model has been increasingly challenged during recent years, with current studies instead pointing at a central involvement of the mitochondrial F_1F_O ATP synthase in mPTP formation, while a central role of VDAC and ANT was excluded by genetic knockout studies.[220,223-225] Even CYPD, which clearly is an important mPTP regulator, may not be required for mPTP function per se.[220,222,226-228] Regarding the role of the mPTP in apoptosis, it was originally thought that mPT was a critical event or even the point of no return for apoptosis.[229] It has long been thought that mPT is both sufficient and necessary to induce MOMP, which went so far that both phenomena have even been repeatedly confused or considered as equivalent.[159,170] It may thus be necessary to clarify that mPT and MOMP are two completely distinct events. Both involve the opening of a pore in the mitochondria (the mPTP and the BAX/BAK pore, respectively), and both play a role in intrinsic apoptosis, but this is where the similarities end (**Table 1**).[230] It has been suggested that mPT may cause MOMP by leading to swelling of the matrix and consequently to rupture of the OMM.[151,158,221] However, genetic knockout studies have demonstrated that the MOMP mediators BAX and BAK, while completely dispensable for mPT per se, are crucially required for mPT-dependent OMM rupture and cell death.[220,231] In addition, MOMP can be caused by many other factors that do not involve or depend on mPT, and mPT can also occur as a consequence rather than a cause of MOMP.[151,158,170,221] While it was long thought that mPT, through MOMP, necessarily leads to apoptosis, more recent evidence suggests that whether mPT-induced cell death is apoptotic or rather necrotic may depend on a variety of factors, such as the availability of ATP or the interaction of BAX and BAK. The exact role of mPT in apoptosis thus remains unclear.[151,220,231]

Table 1: Summary of essential differences between the mitochondrial permeability transition pore (**mPTP**) and the **BAX/BAK pore**, also known as mitochondrial apoptosis-induced channel (**MAC**).

Pore	mPTP	BAX/BAK pore (MAC)
Event	mPT	MOMP
Diameter	~3 nm [Ref. 220]	~25–100 nm [Ref. 178]
Permeant molecule size	up to 1.5 kDa [Ref. 220]	at least 100 kDa [Ref. 176]
Membrane	IMM	OMM
Role in intrinsic apoptosis	unclear	sufficient
Constituent proteins	possibly F_1F_O ATPase, others	BAX / BAK

1.6. Negative regulation of apoptosis

1.6.1. Intracellular regulation of apoptosis by IAP proteins

Since the process of apoptosis, once started, irrevocably condemns the affected cell to death, its initiation underlies strict negative regulation. This and the following chapters will deal with these regulatory mechanisms, some of which act from inside the cell and others from the outside. Among the most well-understood and probably most important cell-internal regulators are the anti-apoptotic members of the BCL2 protein family, which prevent MOMP, as well as the aptly named *inhibitor of apoptosis* proteins (IAPs), which inhibit caspases.[60] Since the role of BCL2 proteins has already been extensively discussed in chapter 1.5.5, the current chapter will focus on the role of IAPs. The IAPs are a family of anti-apoptotic proteins that are often dysregulated in cancer cells and promote their survival.[232] All IAPs contain one to three *baculovirus IAP repeat* (BIR) domains and are thus also known as *BIR-containing proteins* (BIRCs or sometimes BIRPs).[233,234] The BIR domains are central to the function of the IAPs since they facilitate their interaction with other proteins, including caspases. However, of the eight human IAPs that are known today, only three have been shown to inhibit caspases directly: BIRC2 (cIAP1), BIRC3 (cIAP2), and BIRC4 (XIAP, X-linked inhibitor of apoptosis protein), the last of which has been studied most extensively. All of these three IAPs contain three BIR domains in their N-terminal part, two of which belong to the type II BIR class, which is distinguished from other BIR domains by the presence of a specific hydrophobic cleft. This cleft can bind corresponding *IAP-binding motifs* (IBMs) in target proteins such as the caspase CASP9. Binding of XIAP to the IBM of CASP9 via its BIR3 domain (i.e. its third BIR domain) sterically blocks the homodimerisation interface of CASP9.[232,234-236] Since CASP9 depends on dimerisation for activation, as discussed in chapter 1.3.2, this

prevents CASP9 activation. However, IAPs interact with other caspases using different mechanisms. The inhibition of CASP3 and CASP7 by XIAP has been shown to require not only the BIR3 domain but additionally a small segment N-terminal of the BIR2 domain. For these two caspases, the direct inhibitory mechanism is completely different from that for CASP9 and does not depend on inhibition of dimerisation, but rather on blockade of the active site of an already activated, functional caspase dimer.[232,235] In addition to these direct inhibitory mechanisms shown for XIAP, this and other caspase-binding IAPs such as cIAP1 and cIAP2 can also inhibit caspases indirectly.[232,235] For this, they depend on their C-terminal *really interesting new protein* (RING) domain in addition to their N-terminal BIR domains. The RING domain is an E3 ubiquitin ligase domain that enables those IAPs that possess one to ubiquitinate their target proteins, either leading to their proteasomal degradation or inhibiting them in other ways.[232] The role of IAPs in apoptosis regulation can thus probably best be described as an intracellular fail-safe mechanism that prevents the activation of a few caspases from spiralling out of control. To overcome this inhibition, MOMP causes the release of two pro-apoptotic factors that inhibit IAPs: SMAC (DIABLO)[160,161] and OMI (HTRA2)[162–165], both of which contain an IBM and thus serve as competitive inhibitors of IAPs by displacing them from caspases.

1.6.2. Extracellular regulation of apoptosis and cell survival by growth factors

Aside from IAPs and anti-apoptotic BCL2 proteins, negative regulation of apoptosis also relies on a broad range of signalling pathways that are often collectively referred to as *survival signalling*. This umbrella term encompasses several related and interconnected signalling pathways that generally promote cell survival, proliferation and, if dysregulated, carcinogenesis. While acting inside the cell, these pathways are directly regulated by signals from outside the cell, which are mainly hormones or growth factors such as insulin, insulin-like growth factors (IGFs), epidermal growth factor (EGF) and vascular endothelial growth factors (VEGFs). Most cells require constant signals from other cells in this form to survive, and competition for growth factors is one of the mechanisms by which the human body ensures that only fit and necessary cells survive while damaged, aged and superfluous cells are weeded out.[132] For example, the withdrawal of survival signals plays a central role in the reduction of the immune cell population after a successful immune response.[105] The bridge between the extracellular signal and

the intracellular pathways in survival signalling are often *receptor tyrosine kinases* (RTKs).[237-239] Binding of a ligand on the extracellular domain of these receptors triggers autophosphorylation of tyrosine residues on their intracellular domain, leading to the recruitment and activation of further intracellular signalling proteins, many of which are protein kinases. Another type of receptors that play an important role in survival and growth factor signalling are the *G-protein coupled receptors* (GPCRs), which transmit an extracellular signal to an intracellular G-protein by exchanging a GDP bound to it with a GTP, resulting in the G-protein's release from the receptor.[240] Among the most important RTK- and GPCR-regulated anti-apoptotic pathways are the signalling axes of RAS/RAF/MEK/ERK[241], JAK/STAT[242], and PI3K/PDK1/AKT[12], the last of which has been in the focus of one of the projects on which this dissertation is based.[13] The following chapter will thus highlight the features of this pathway as an example of anti-apoptotic survival signalling.

1.6.3. Activation of AKT by the PI3K/PDK1/AKT signalling pathway

The induction of virtually all growth factor receptors leads to the activation of *phosphatidylinositol-3-kinases* (PI3Ks).[132] The PI3Ks are a family of lipid kinases that phosphorylate *phosphoinositides*, a class of lipid second messengers, at the 3′ position of their inositol ring.[10,131,243] PI3Ks are divided into three or sometimes four classes, and the class I PI3Ks are the ones that are mainly involved in PI3K/PDK1/AKT signalling. In vivo, class I PI3Ks exclusively phosphorylate phosphatidylinositol-4,5-bisphosphate ($PI(4,5)P_2$) to generate phosphatidylinositol-3,4,5-trisphosphate ($PI(3,4,5)P_3$ or PIP_3), whereas in vitro, they have also been observed to phosphorylate phosphatidylinositol (PI) and phosphatidylinositol-4-phosphate (PI(4)P or PIP).[10,244,245] Class I PI3Ks are opposed by the phosphatase PTEN (originally short for *phosphatase and tensin homolog*) which dephosphorylates $PI(3,4,5)P_3$ at the 3′ position and thus converts it back to $PI(4,5)P_2$. Phosphoinositides serve as membrane anchors for proteins that contain a corresponding binding domain, and different phosphoinositides can be bound by different domains with different affinities. One such domain that binds $PI(3,4,5)P_3$ with high affinity is the *pleckstrin homology* (PH) domain, which is present in both PDK1 and AKT. The induction of growth factor signalling, via class I PI3K activation, $PI(3,4,5)P_3$ production and PH domain binding, thus recruits both PDK1 and AKT to the plasma membrane and brings them into close proximity of each

other.[12,246] Both PDK1 (*3-phosphoinositide-dependent protein kinase 1*, also known as PDPK1) and AKT (named after the *AKT8 murine leukaemia virus* in which it was first discovered; also known as *protein kinase B* (PKB) or rarely *related to A- and C-kinase* (RAC)) are protein kinases or, more specifically, serine/threonine kinases. The PI3K-mediated recruitment of AKT and PDK1 to the plasma membrane not only brings them into proximity but also induces conformational changes in AKT that make it accessible for phosphorylation by PDK1 at a specific threonine residue. This phosphorylation contributes to the activation of AKT. However, to become fully activated, AKT has to be phosphorylated at two specific amino acid residues: one in the activation loop of its catalytic centre and one in its C-terminal hydrophobic domain. In the AKT isoform AKT1, these residues are T308 and S473.[12] While phosphorylation of T308 is carried out by PDK1, the kinase primarily responsible for phosphorylation of S473 is the *mammalian target of rapamycin complex 2* (mTORC2). Just as in the case of PDK1, the phosphorylation of AKT by mTORC2 can be enhanced by growth factor-induced binding of both to $PI(3,4,5)P_3$, but in the case of mTORC2, this is not strictly required.[12] Once AKT has been fully activated, it can go on to phosphorylate its downstream substrates, which play roles in many diverse cellular events including but by far not limited to apoptosis.

1.6.4. Inhibition of apoptosis by AKT signalling

Of the literally hundreds of known AKT substrate proteins (comprehensively compiled by Cell Signaling Technology® Ref. 247), many play a role in apoptotic or anti-apoptotic signalling. One of the first recognised AKT substrates with a role in apoptosis was the pro-apoptotic BCL2 family protein BAD (see also chapter 1.5.4). Phosphorylation of BAD by AKT results in its inactivation via sequestration by 14-3-3 proteins.[132,248] The same is true for another pro-apoptotic BCL2 family protein, BIM.[249] Conversely and more indirectly, AKT protects the anti-apoptotic BCL2 family protein MCL1 (BCL2L3) from proteasomal degradation. This is achieved by AKT-mediated inhibitory phosphorylation of *glycogen synthase kinase-3β* (GSK3B), which is thus prevented from phosphorylating MCL1.[250] The pro-apoptotic BCL2 family member PUMA is negatively regulated by AKT in a similar, GSK3B-dependent manner.[251] Additionally, AKT-mediated phosphorylation of the anti-apoptotic BCL2 family protein BCL-X_L or its pro-apoptotic alternative splice form BCL-X_S

(BCL2L1) might reduce VDAC-dependent mitochondrial apoptosis.[252] In humans, another pro-apoptotic AKT substrate is the key initiator caspase of the intrinsic pathway, CASP9, although its inhibition by AKT alone cannot prevent apoptosis.[132,253,254] A completely different kind of apoptosis-regulating AKT substrate proteins are the transcription factors of the *forkhead box O* (FOXO) family, particularly FOXO1 (FKHR), FOXO3 (FKHRL1), and FOXO4 (AFX).[255-260] These three FOXO transcription factors are crucial tumour suppressors that can induce cellular growth arrest and apoptosis.[261] However, phosphorylation by AKT marks them for binding by 14-3-3 proteins that facilitate their export from the nucleus and thus inhibit their activity. Another tumour suppressor that is inhibited by AKT in a similar way is the *programmed cell death protein 4* (PDCD4), which is normally present in the nucleus but is exported to the cytosol upon phosphorylation by AKT.[262] AKT also inhibits the potentially pro-apoptotic crucial tumour suppressor and transcription factor p53 (TP53) by stabilising phosphorylation of the ubiquitin ligase MDM2, which then carries on to ubiquitinate p53 and thus marks it for proteasomal degradation.[263,264] It has also been suggested that AKT stabilises the IAP protein XIAP (discussed in chapter 1.6.1) in a similar manner, however the respective article has been retracted.[265] In a related matter, the same research group has also suggested that the mitochondrial XIAP inhibitor OMI (HTRA2) that is released upon MOMP is also phosphorylated by AKT, resulting in its inhibition, yet the respective article has also been retracted.[266] More robust evidence has been presented for the involvement of AKT in the potentially pro-apoptotic *Jun N-terminal kinase* (JNK) signalling pathway. Not only does AKT negatively regulate the *mitogen-activated protein kinase kinase kinase 5* (MAP3K5, also known as ASK1), an upstream positive regulator of JNK[267,268], but it also inhibits the protein *plenty of SH3 domains* (POSH, also known as SH3RF1), a scaffolding protein that contributes to JNK activation.[269] AKT also interferes with the induction of extrinsic apoptosis by negatively regulating the pro-apoptotic, long isoform of FLIP (CFLAR; discussed in chapter 1.4.3) as well as the *prostate apoptosis response 4 protein* (PAR4, also known as PAWR) that normally enhances extrinsic apoptosis induction.[270,271] During the execution stage of apoptosis, AKT can interfere with apoptotic chromatin condensation (discussed in chapter 1.2.3) by inhibiting the protein ACINUS. This is done both directly by phosphorylating ACINUS itself as well as indirectly by phosphorylating the protein *zyxin* (ZYX), which then binds and inhibit ACINUS.[272,273] Out of all of these and other AKT substrates

with a role in cell survival and apoptosis, it is still not entirely clear whether some of them are redundant, however it is believed that not the effect of AKT on a few specific substrates but rather on most or all of them together is responsible for its inhibition of apoptosis.[132]

1.7. Aims of the projects described this dissertation

The goal of all projects on which this dissertation is based was the identification of new pathways in apoptosis signalling. Three main projects emerged:

1. The identification of the mechanism by which the mycotoxin phomoxanthone A causes induction of apoptosis
2. The discovery of a feedback loop in the PI3K/PDK1/AKT signalling axis and its role in the inhibition of apoptosis
3. The characterisation of BMAL1 as a caspase substrate and the role of its cleavage during the execution of apoptosis

These three and other projects resulted in several manuscripts, all but one of which have already been published. The manuscript texts have thus been added as a supplement to this dissertation.

2. Manuscripts

2.1. Manuscripts on which this dissertation is based

The full original texts of these manuscripts can be found in the appendix to this dissertation.

2.1.1. The mycotoxin phomoxanthone A disturbs the form and function of the inner mitochondrial membrane

Böhler P[*], Stuhldreier F[*], Anand R, Kondadi AK, Schlütermann D, Berleth N, Deitersen J, Wallot-Hieke N, Wu W, Frank M, Niemann H, Wesbuer E, Barbian A, Luyten T, Parys JB, Weidtkamp-Peters S, Borchardt A, Reichert AS, Peña-Blanco A, García-Sáez AJ, Itskanov S, van der Bliek AM, Proksch P, Wesselborg S[*], Stork B[*]. *Cell Death & Disease* (2018) **9**:286, doi: 10.1038/s41419-018-0312-8

The author of this dissertation conceived and oversaw the project, planned, designed and carried out the majority of the experiments, and independently researched and wrote the manuscript. Total contribution: about 45%

2.1.2. Phomoxanthone A − from mangrove forests to anticancer therapy

Frank M, Niemann H, Böhler P, Stork B, Wesselborg S, Lin W, Proksch P. *Current Medicinal Chemistry* (2015) **22**:3523, doi: 10.2174/0929867322666150716115300

The author of this dissertation contributed several ideas and suggestions to the project and carried out all in vivo experiments. Total contribution: about 10%

2.1.3. Pro-apoptotic and immunostimulatory tetrahydroxanthone dimers from the endophytic fungus *Phomopsis longicolla*

Rönsberg D, Debbab A, Mándi A, Vasylyeva V, Böhler P, Stork B, Engelke L, Hamacher A, Sawadogo R, Diederich M, Wray V, Lin W, Kassack MU, Janiak C, Scheu S, Wesselborg S, Kurtán T, Aly AH, Proksch P. *The Journal of Organic Chemistry* (2013) **78**:12409, doi: 10.1021/jo402066b

The author of this dissertation contributed several ideas and suggestions to the project and carried out the in vivo experiments on apoptosis. Total contribution: about 5%

[*] These authors contributed equally to the manuscript.

2.1.4. PDK1 controls upstream PI3K expression and PIP_3 generation

Dieterle AM*, Böhler P*, Keppeler H, Alers S, Berleth N, Drießen S, Hieke N, Pietkiewicz S, Löffler AS, Peter C, Gray A, Leslie NR, Shinohara H, Kurosaki T, Engelke M, Wienands J, Bonin M, Wesselborg S, Stork B. *Oncogene* (2014) **33**:3043, doi: 10.1038/onc.2013.266

The author of this dissertation contributed several ideas and suggestions to the project, independently planned, designed and carried out the experiments on which figures 3b & 3c and figures 4b–d are based, and wrote parts of the manuscript. Total contribution: about 30%

2.1.5. Efficient and safe gene delivery to human corneal endothelium using magnetic nanoparticles

Czugala M, Mykhaylyk O, Böhler P, Onderka J, Stork B, Wesselborg S, Kruse FE, Plank C, Singer BB, Fuchsluger TA. *Nanomedicine* (2016) **11**:1787, doi: 10.2217/nnm-2016-0144

The author of this dissertation contributed several ideas and suggestions to the project, independently planned, designed and carried out the experiments on which figure 3b is based, and contributed to data evaluation and to writing the manuscript. Total contribution: about 15%

2.1.6. CASP3 inactivates BMAL1 by cleaving off its transactivation domain at D585

Böhler P, Peter C, Friesen O, Berleth N, Deitersen J, Schlütermann D, Stuhldreier F, Wu W, Dibner C, Schoder G, Reinke H, Stork B. *Manuscript prepared for publication.*

The author of this dissertation conceived and oversaw the project, planned, designed and carried out the majority of the experiments, and independently researched and wrote the manuscript. Total contribution: about 60%

* These authors contributed equally to the manuscript.

2.2. Manuscripts beyond the scope of this dissertation

The author contributed to these publications; however, they are beyond the scope of this dissertation

2.2.1. SIRT4 interacts with OPA1 and regulates mitochondrial quality control and mitophagy

Lang A, Anand R, Altinoluk-Hambüchen S, Ezzahoini H, Stefanski A, Iram A, Bergmann L, Urbach J, Böhler P, Hänsel J, Franke M, Stühler K, Krutmann J, Scheller J, Stork B, Reichert AS, Piekorz RP. *Aging* (2017) **9**:2163, doi: 10.18632/aging.101307

The author of this dissertation contributed several ideas and suggestions to the project and assisted in designing the experiments on which figures 6–8 are based. Total contribution: about 5%

2.2.2. Systematic analysis of ATG13 domain requirements for autophagy induction

Wallot-Hieke N, Verma N, Schlütermann D, Berleth N, Deitersen J, Böhler P, Stuhldreier F, Wu W, Seggewiß S, Peter C, Gohlke H, Mizushima N, Stork B. *Autophagy* (2018) **14**:743, doi: 10.1080/15548627.2017.1387342

The author of this dissertation contributed several ideas and suggestions to the project, provided experimental support and assisted in data evaluation. Total contribution: about 5%

2.2.3. Targeting urothelial carcinoma cells by combining cisplatin with a specific inhibitor of the autophagy-inducing class III PtdIns3K complex

Schlütermann D, Skowron MA, Berleth N, Böhler P, Deitersen J, Stuhldreier F, Wallot-Hieke N, Wu W, Peter C, Hoffmann MJ, Niegisch G, Stork B. Urologic Oncology (2018) **36**:160, doi: 10.1016/j.urolonc.2017.11.021

The author of this dissertation contributed several ideas and suggestions to the project, provided experimental support and assisted in data evaluation. Total contribution: about 5%

2.2.4. Deubiquitinase inhibition by WP1130 leads to ULK1 aggregation and blockade of autophagy

Drießen S, Berleth N, Friesen O, Löffler AS, Böhler P, Hieke N, Stuhldreier F, Peter C, Schink KO, Schultz SW, Stenmark H, Holland P, Simonsen A, Wesselborg S, Stork B. *Autophagy* (2015) **11**:1458, doi: 10.1080/15548627.2015.1067359

The author of this dissertation contributed several ideas and suggestions to the project, provided experimental support and assisted in data evaluation. Total contribution: about 5%

2.2.5. Expression of a ULK1/2 binding-deficient ATG13 variant can partially restore autophagic activity in ATG13-deficient cells

Hieke N, Löffler AS, Kaizuka T, Berleth N, Böhler P, Drießen S, Stuhldreier F, Friesen O, Assani K, Schmitz K, Peter C, Diedrich B, Dengjel J, Holland P, Simonsen A, Wesselborg S, Mizushima N, Stork B. *Autophagy* (2015) **11**:1471, doi: 10.1080/15548627.2015.1068488

The author of this dissertation contributed several ideas and suggestions to the project, provided experimental support and assisted in data evaluation. Total contribution: about 5%

2.2.6. Callyspongiolide, a cytotoxic macrolide from the marine sponge *Callyspongia* sp.

Pham CD, Hartmann R, Böhler P, Stork B, Wesselborg S, Lin W, Lai D, Proksch P. *Organic Letters* (2014) **16**:266, doi: 10.1021/ol403241v

The author of this dissertation contributed several ideas and suggestions to the project and carried out the in vivo experiments on viability. Total contribution: about 5%

3. Discussion

Understanding the mechanisms through which apoptosis can be induced, inhibited or executed is crucial for the development of new strategies in the fight against many diseases such as autoimmune disorders and cancer. The projects presented in this dissertation contributed to the knowledge of these three aspects of apoptosis signalling in several ways.

Both the inhibition and induction of apoptosis are at the core of cancer treatment: while inhibition of apoptosis is a crucial event during cellular carcinogenesis, overcoming this inhibition and inducing apoptosis is the goal of most anti-cancer drugs. Many recently developed anti-cancer drugs are small molecule inhibitors, i.e. they interact directly and specifically with certain proteins that are the products of oncogenes. Among these small molecules are the BCL2 inhibitor venetoclax (ABT-199), the PI3K inhibitor idelalisib (GS-1101), and the AKT inhibitor MK-2206.[274-276] A successful therapy employing such small molecules depends critically on understanding the signalling pathways their target proteins are part of. As we have demonstrated in one of our own studies, this is especially true for the PI3K/PDK1/AKT signalling pathway.[13] Several anti-cancer drugs that are currently under development or already in clinical use are inhibitors of one or more components of this pathway.[246,277] In our own studies, we used the AKT inhibitor MK-2206, the PDK1 inhibitors BX795 and BX912, and the PI3K inhibitors LY294002, GDC-0941, TGX-221, and IC8711 to dissect this pathway.[13] Our results were concordant with the high selectivity and specificity of these compounds, yet they also demonstrated that inhibition of some individual components of this pathway may not be sufficient: inhibiting either AKT or PDK1 alone resulted in suppression of the negative feedback mechanisms through which they repress the expression of their upstream regulator PI3K, thus leading to the upregulation of PI3K signalling that may result in resistance to drugs that target its downstream effectors.[13] This logic is reflected by the results of clinical trials on inhibitors of PI3K/PDK1/AKT signalling: while several specific PI3K inhibitors, such as idelalisib, duvelisib, and copanlisib, have entered routine clinical use in cancer therapy during the last years, not a single PDK1 or AKT inhibitor has demonstrated sufficient efficacy and safety in clinical trials to gain approval for the treatment of cancer.[244,277,278]

The search for novel anti-cancer drugs to complement or replace existing drugs thus remains an ongoing effort, and countless chemical compounds are under investigation as such potential drugs. Aside from synthetic drug candidates, these compounds also include several natural products, which have been proven to be a rich source of potential drugs in the past. Anti-cancer drugs derived from natural products include daunorubicin (from *Streptomyces peucetius*), mitomycin C (from *Streptomyces caespitosus* and *Streptomyces lavendulae*), paclitaxel (from *Taxus brevifolia*), sirolimus (from *Streptomyces hygroscopicus*), and vinblastine and vincristine (both from *Catharanthus roseus*).[279,280] The mechanism of action of these compounds is highly diverse, ranging from DNA damage over cytoskeleton disruption to the specific inhibition of enzymes, yet the goal is always the same: to induce apoptosis. A promising new pro-apoptotic compound with a novel mechanism of action has been found with the mycotoxin phomoxanthone A (PXA) from the fungus *Phomopsis longicolla*. PXA was in the focus of several publications included in this dissertation.[7–9] Essentially nothing was known about the biological activity of PXA prior to these studies except that it had a strong broadband antibiotic activity. The results of a 2013 study to which the author of this dissertation contributed show that PXA induces apoptosis in a number of haematological cancer cell lines including the highly apoptosis-resistant Burkitt lymphoma cell line DG75.[9] As published previously and as also confirmed by our own experiments (unpublished data), DG75 cells are deficient or near-deficient for the pro-apoptotic BCL2 family members BAX and BAK (described in chapter 1.5.4).[281,282] The fact that PXA can nevertheless induce apoptosis in these cells could probably be attributed to its mechanism of action, which directly damages the mitochondria and may thus bypass the BAX/BAK-dependence of intrinsic apoptosis induction. While this potential ability makes PXA a promising tool to induce apoptosis in BAX/BAK-deficient cancer cells, its broad range of toxicity may be an obstacle to this application. Preliminary data from our 2013 study suggest that PXA may be more toxic towards cancer cells than non-cancer cells.[9] However, since the experiments leading to these results were performed by different research groups using different test methods and different lots of PXA, whose instability in solution was not known at the time, further experiments will be required to thoroughly test this assumption. An alternative approach would be to modify PXA in a way that allows it to target cancer cells directly as well as to improve its stability.

Attempts to modify PXA chemically while preserving or even enhancing its activity are currently ongoing, and first results have been published in one of the studies on which this dissertation is based.[8]

Aside from the potential use of PXA or one of its derivatives as a chemotherapeutic drug, a more direct application of this compound is in the research on apoptosis and mitochondrial dynamics. As described in chapter 1.5, mitochondrial function in general and mitochondrial dynamics in particular lie at the heart of apoptosis. Mitochondrial fragmentation and cristae disruption might be both cause and effect of apoptosis and have received increased research interest during the last years.[155,197,209,211] Our studies on PXA have shown that mitochondrial fragmentation and cristae disruption can be induced within a few minutes or even seconds and independent of the canonical fission regulators DRP1 and OPA1, resulting in exclusive fragmentation of the inner mitochondrial membrane.[7] These results challenge the view that mitochondrial fragmentation is necessarily an active, guided process, and they demonstrate that exclusive fragmentation of the inner mitochondrial membrane without fragmentation of the outer mitochondrial membrane is possible in higher animals despite the lack of a known inner membrane fission machinery. Further studies might address the open questions that are posed by these results: What is the molecular target of PXA? What is the order of events in mitochondrial fragmentation, cristae disruption, and apoptosis induction? What is the mechanism of exclusive inner mitochondrial membrane fragmentation in higher animals? Especially regarding this last question, PXA might prove to be a useful research tool.

Apoptosis, whether induced by PXA, by inhibitors of PI3K/PDK1/AKT signalling, or by any of the other stimuli summarised in chapters 1.4.1 and 1.5.1, always has the goal of executing cell death in a controlled manner. The shutdown of gene transcription, as described in chapter 1.2.6, is an integral part of the execution of apoptosis. In another one of the studies on which this dissertation is based, we have shown that apoptosis inactivates the transcription factor BMAL1 (ARNTL) via cleavage by the executioner caspase CASP3.[16] The cellular function of BMAL1 that is best known is its role in the mammalian circadian clock. This intricate molecular machinery generates the 24-hour rhythms that guide the life of nearly all mammals including humans. Since it regulates many diverse bodily functions from metabolism to sleep and social behaviour, it comes as no surprise that the circadian clock in general

and BMAL1 in particular can also play a role in oncogenesis.[283,284] However, BMAL1 itself is usually not considered an oncogene but a tumour suppressor.[285] Why, then, should the anti-cancer protein BMAL1 be inactivated by the anti-cancer process of apoptosis? The answer may lie in the role of BMAL1 in another cyclical cellular process: not the circadian cycle, but the cell cycle. These two cycles influence each other[286], and cell cycle arrest is a possible response to DNA damage to prevent uncontrolled cell proliferation and oncogenesis. BMAL1 depletion can result in a decrease in the levels of several cell cycle regulators that coincides with an increased sensitivity to anticancer drugs and apoptosis induction.[287,288] Therefore, apoptotic inactivation of BMAL1 by CASP3 might contribute to shifting the cellular DNA damage response away from cell cycle arrest and towards cell death, thus constituting a positive feedback mechanism that enhances the execution of apoptosis.

In summary, the projects and publications that form the foundation of this dissertation shed new light on three aspects of apoptosis: first, anticancer drugs that target the oncoproteins AKT and PDK1 might trigger a feedback mechanism resulting in increased PI3K expression that contributes to inhibition of apoptosis; second, mitochondrial inner membrane fragmentation and cristae disruption caused by the mycotoxin PXA result in BAX/BAK-independent induction of apoptosis; and third, the transcription factor BMAL1 and thus the circadian clock is inactivated by CASP3 during the execution of apoptosis.

4. References

1 Green DR. *Means to an end: apoptosis and other cell death mechanisms*. Cold Spring Harbor Laboratory Press, 2010.

2 Strasser A, Cory S, & Adams JM. (2011) Deciphering the rules of programmed cell death to improve therapy of cancer and other diseases. *EMBO J* **30**:3667. doi:10.1038/emboj.2011.307

3 Kerr JF, Wyllie AH, & Currie AR. (1972) Apoptosis: a basic biological phenomenon with wide-ranging implications in tissue kinetics. *Br J Cancer* **26**:239.

4 Arandjelovic S & Ravichandran KS. (2015) Phagocytosis of apoptotic cells in homeostasis. *Nat Immunol* **16**:907. doi:10.1038/ni.3253

5 Taylor RC, Cullen SP, & Martin SJ. (2008) Apoptosis: controlled demolition at the cellular level. *Nat Rev Mol Cell Biol* **9**:231. doi:10.1038/nrm2312

6 Roos WP, Thomas AD, & Kaina B. (2016) DNA damage and the balance between survival and death in cancer biology. *Nat Rev Cancer* **16**:20. doi:10.1038/nrc.2015.2

7 Böhler P, Stuhldreier F, Anand R, et al. (2018) The mycotoxin phomoxanthone A disturbs the form and function of the inner mitochondrial membrane. *Cell Death Dis* **9**:286. doi:10.1038/s41419-018-0312-8

8 Frank M, Niemann H, Böhler P, et al. (2015) Phomoxanthone A — from mangrove forests to anticancer therapy. *Curr Med Chem* **22**:3523. doi:10.2174/0929867322666150716115300

9 Rönsberg D, Debbab A, Mándi A, et al. (2013) Pro-apoptotic and immunostimulatory tetrahydroxanthone dimers from the endophytic fungus *Phomopsis longicolla*. *J Org Chem* **78**:12409. doi:10.1021/jo402066b

10 Vanhaesebroeck B, Stephens L, & Hawkins P. (2012) PI3K signalling: the path to discovery and understanding. *Nat Rev Mol Cell Biol* **13**:195. doi:10.1038/nrm3290

11 Hemmings BA & Restuccia DF. (2012) PI3K-PKB/Akt pathway. *Cold Spring Harb Perspect Biol* **4**:a011189. doi:10.1101/cshperspect.a011189

12 Manning BD & Toker A. (2017) AKT/PKB signaling: navigating the network. *Cell* **169**:381. doi:10.1016/j.cell.2017.04.001

13 Dieterle AM, Böhler P, Keppeler H, et al. (2014) PDK1 controls upstream PI3K expression and PIP3 generation. *Oncogene* **33**:3043. doi:10.1038/onc.2013.266

14 Czugala M, Mykhaylyk O, Böhler P, et al. (2016) Efficient and safe gene delivery to human corneal endothelium using magnetic nanoparticles. *Nanomedicine* **11**:1787. doi:10.2217/nnm-2016-0144

15 Crawford ED & Wells JA. (2011) Caspase substrates and cellular remodeling. *Annu Rev Biochem* **80**:1055. doi:10.1146/annurev-biochem-061809-121639

16 Böhler P, Peter C, Friesen O, et al. CASP3 inactivates BMAL1 by cleaving off its transactivation domain at D585. *Manuscript prepared for publication.*

17 Tixeira R, Caruso S, Paone S, et al. (2017) Defining the morphologic features and products of cell disassembly during apoptosis. *Apoptosis* **22**:475. doi:10.1007/s10495-017-1345-7

18 Coleman ML, Sahai EA, Yeo M, et al. (2001) Membrane blebbing during apoptosis results from caspase-mediated activation of ROCK I. *Nat Cell Biol* **3**:339. doi:10.1038/35070009

19 Croft DR, Coleman ML, Li S, et al. (2005) Actin-myosin–based contraction is responsible for apoptotic nuclear disintegration. *J Cell Biol* **168**:245. doi:10.1083/jcb.200409049

20 Rao L, Perez D, & White E. (1996) Lamin proteolysis facilitates nuclear events during apoptosis. *J Cell Biol* **135**:1441. doi:10.1083/jcb.135.6.1441

21 Moss DK, Betin VM, Malesinski SD, et al. (2006) A novel role for microtubules in apoptotic chromatin dynamics and cellular fragmentation. *J Cell Sci* **119**:2362. doi:10.1242/jcs.02959

22 Sahara S, Aoto M, Eguchi Y, et al. (1999) Acinus is a caspase-3-activated protein required for apoptotic chromatin condensation. *Nature* **401**:168. doi:10.1038/43678

23 Joselin AP, Schulze-Osthoff K, & Schwerk C. (2006) Loss of Acinus inhibits oligonucleosomal DNA fragmentation but not chromatin condensation during apoptosis. *J Biol Chem* **281**:12475. doi:10.1074/jbc.M509859200

24 Susin SA, Lorenzo HK, Zamzami N, et al. (1999) Molecular characterization of mitochondrial apoptosis-inducing factor. *Nature* **397**:441. doi:10.1038/17135

25 Arnoult D, Gaume B, Karbowski M, et al. (2003) Mitochondrial release of AIF and EndoG requires caspase activation downstream of Bax/Bak-mediated permeabilization. *EMBO J* **22**:4385. doi:10.1093/emboj/cdg423

26 Mancini M, Machamer CE, Roy S, et al. (2000) Caspase-2 is localized at the Golgi complex and cleaves Golgin-160 during apoptosis. *J Cell Biol* **149**:603. doi:10.1083/jcb.149.3.603

27 Lane JD, Lucocq J, Pryde J, et al. (2002) Caspase-mediated cleavage of the stacking protein GRASP65 is required for Golgi fragmentation during apoptosis. *J Cell Biol* **156**:495. doi:10.1083/jcb.200110007

28 Lowe M, Lane JD, Woodman PG, et al. (2004) Caspase-mediated cleavage of syntaxin 5 and giantin accompanies inhibition of secretory traffic during apoptosis. *J Cell Sci* **117**:1139. doi:10.1242/jcs.00950

29 Mukherjee S, Chiu R, Leung S-M, et al. (2007) Fragmentation of the Golgi apparatus: an early apoptotic event independent of the cytoskeleton. *Traffic* **8**:369. doi:10.1111/j.1600-0854.2007.00542.x

30 Cosulich SC, Horiuchi H, Zerial M, et al. (1997) Cleavage of Rabaptin-5 blocks endosome fusion during apoptosis. *EMBO J* **16**:6182. doi:10.1093/emboj/16.20.6182

31 Chiu R, Novikov L, Mukherjee S, et al. (2002) A caspase cleavage fragment of p115 induces fragmentation of the Golgi apparatus and apoptosis. *J Cell Biol* **159**:637. doi:10.1083/jcb.200208013

32 Lane JD, Allan VJ, & Woodman PG. (2005) Active relocation of chromatin and endoplasmic reticulum into blebs in late apoptotic cells. *J Cell Sci* **118**:4059. doi:10.1242/jcs.02529

33 Zamzami N & Kroemer G. (1999) Condensed matter in cell death. *Nature* **401**:127. doi:10.1038/43591

34 Wyllie AH. (1980) Glucocorticoid-induced thymocyte apoptosis is associated with endogenous endonuclease activation. *Nature* **284**:555. doi:10.1038/284555a0

35 Liu X, Zou H, Slaughter C, et al. (1997) DFF, a heterodimeric protein that functions downstream of caspase-3 to trigger DNA fragmentation during apoptosis. *Cell* **89**:175. doi:10.1016/S0960-9822(98)79298-X

36 Enari M, Sakahira H, Yokoyama H, et al. (1998) A caspase-activated DNase that degrades DNA during apoptosis, and its inhibitor ICAD. *Nature* **391**:43. doi:10.1038/34112

37 Halenbeck R, MacDonald H, Roulston A, et al. (1998) CPAN, a human nuclease regulated by the caspase-sensitive inhibitor DFF45. *Curr Biol* **8**:537. doi:10.1016/s0960-9822(98)79298-x

38 Fischer U, Jänicke RU, & Schulze-Osthoff K. (2003) Many cuts to ruin: a comprehensive update of caspase substrates. *Cell Death Differ* **10**:76. doi:10.1038/sj.cdd.4401160

39 Lüthi AU & Martin SJ. (2007) The CASBAH: a searchable database of caspase substrates. *Cell Death Differ* **14**:641. doi:10.1038/sj.cdd.4402103

40 Peter C, Wesselborg S, & Lauber K, in: *Phagocytosis of Dying Cells: From Molecular Mechanisms to Human Diseases* (eds Dmitri Krysko & Peter Vandenabeele), p. 63. Springer, 2009.

41 Lauber K & Wesselborg S, in: *Apoptosis and Cancer Therapy: From Cutting-edge Science to Novel Therapeutic Concepts* (eds Klaus-Michael Debatin & Simone Fulda), Ch. 24, p. 625. WILEY-VCH Verlag, 2006.

42 Segawa K & Nagata S. (2015) An apoptotic 'eat me' signal: phosphatidylserine exposure. *Trends Cell Biol* **25**:639. doi:10.1016/j.tcb.2015.08.003

43 Fadok VA, Voelker DR, Campbell PA, et al. (1992) Exposure of phosphatidylserine on the surface of apoptotic lymphocytes triggers specific recognition and removal by macrophages. *J Immunol* **148**:2207.

44 Martin SJ, Finucane DM, Amarante-Mendes GP, et al. (1996) Phosphatidylserine externalization during CD95-induced apoptosis of cells and cytoplasts requires ICE/CED-3 protease activity. *J Biol Chem* **271**:28753. doi:10.1074/jbc.271.46.28753

45 Suzuki J, Fujii T, Imao T, et al. (2013) Calcium-dependent phospholipid scramblase activity of TMEM16 protein family members. *J Biol Chem* **288**:13305. doi:10.1074/jbc.M113.457937

46 Segawa K, Kurata S, Yanagihashi Y, et al. (2014) Caspase-mediated cleavage of phospholipid flippase for apoptotic phosphatidylserine exposure. *Science* **344**:1164. doi:10.1126/science.1252809

47 Mueller RB, Sheriff A, Gaipl US, et al. (2007) Attraction of phagocytes by apoptotic cells is mediated by lysophosphatidylcholine. *Autoimmunity* **40**:342. doi:10.1080/08916930701356911

48 Peter C, Waibel M, Keppeler H, et al. (2012) Release of lysophospholipid 'find-me' signals during apoptosis requires the ATP-binding cassette transporter A1. *Autoimmunity* **45**:568. doi:10.3109/08916934.2012.719947

49 Lauber K, Bohn E, Kröber SM, et al. (2003) Apoptotic cells induce migration of phagocytes via caspase-3-mediated release of a lipid attraction signal. *Cell* **113**:717. doi:10.1016/s0092-8674(03)00422-7

50 Peter C, Wesselborg S, & Lauber K. (2010) Molecular suicide notes: last call from apoptosing cells. *J Mol Cell Biol* **2**:78. doi:10.1093/jmcb/mjp045

51 Peter C, Wesselborg S, Herrmann M, et al. (2010) Dangerous attraction: phagocyte recruitment and danger signals of apoptotic and necrotic cells. *Apoptosis* **15**:1007. doi:10.1007/s10495-010-0472-1

52 Thornberry NA, Bull HG, Calaycay JR, et al. (1992) A novel heterodimeric cysteine protease is required for interleukin-1 beta processing in monocytes. *Nature* **356**:768. doi:10.1038/356768a0

53 Yuan J, Shaham S, Ledoux S, et al. (1993) The *C. elegans* cell death gene ced-3 encodes a protein similar to mammalian interleukin-1β-converting enzyme. *Cell* **75**:641. doi:10.1016/0092-8674(93)90485-9

54 Saleh M, Vaillancourt JP, Graham RK, et al. (2004) Differential modulation of endotoxin responsiveness by human caspase-12 polymorphisms. *Nature* **429**:75. doi:10.1038/nature02451

55 Stowe I, Lee B, & Kayagaki N. (2015) Caspase-11: arming the guards against bacterial infection. *Immunol Rev* **265**:75. doi:10.1111/imr.12292

56 Koenig U, Eckhart L, & Tschachler E. (2001) Evidence that caspase-13 is not a human but a bovine gene. *Biochem Biophys Res Commun* **285**:1150. doi:10.1006/bbrc.2001.5315

57 McIlwain DR, Berger T, & Mak TW. (2013) Caspase functions in cell death and disease. *Cold Spring Harb Perspect Biol* **5**:a008656. doi:10.1101/cshperspect.a008656

58 Denecker G, Ovaere P, Vandenabeele P, et al. (2008) Caspase-14 reveals its secrets. *J Cell Biol* **180**:451. doi:10.1083/jcb.200709098

59 Pistritto G, Jost M, Srinivasula SM, et al. (2002) Expression and transcriptional regulation of caspase-14 in simple and complex epithelia. *Cell Death Differ* **9**:995. doi:10.1038/sj.cdd.4401061

60 Riedl SJ & Shi Y. (2004) Molecular mechanisms of caspase regulation during apoptosis. *Nat Rev Mol Cell Biol* **5**:897. doi:10.1038/nrm1496

61 Kumar S. (2006) Caspase function in programmed cell death. *Cell Death Differ* **14**:32. doi:10.1038/sj.cdd.4402060

62 Lahm A, Paradisi A, Green DR, et al. (2003) Death fold domain interaction in apoptosis. *Cell Death Differ* **10**:10. doi:10.1038/sj.cdd.4401203

63 Boatright KM & Salvesen GS. (2003) Mechanisms of caspase activation. *Curr Opin Cell Biol* **15**:725. doi:10.1016/j.ceb.2003.10.009

64 Kischkel FC, Hellbardt S, Behrmann I, et al. (1995) Cytotoxicity-dependent APO-1 (Fas/CD95)-associated proteins form a death-inducing signaling complex (DISC) with the receptor. *EMBO J* **14**:5579.

65 Muzio M, Chinnaiyan AM, Kischkel FC, et al. (1996) FLICE, a novel FADD-homologous ICE/CED-3–like protease, is recruited to the CD95 (Fas/APO-1) death-inducing signaling complex. *Cell* **85**:817. doi:10.1016/s0092-8674(00)81266-0

66 Chinnaiyan AM, O'Rourke K, Tewari M, et al. (1995) FADD, a novel death domain-containing protein, interacts with the death domain of fas and initiates apoptosis. *Cell* **81**:505. doi:10.1016/0092-8674(95)90071-3

67 Shi Y. (2004) Caspase activation: revisiting the induced proximity model. *Cell* **117**:855. doi:10.1016/j.cell.2004.06.007

68 Fuentes-Prior P & Salvesen GS. (2004) The protein structures that shape caspase activity, specificity, activation and inhibition. *Biochem J* **384**:201. doi:10.1042/BJ20041142

69 Timmer JC & Salvesen GS. (2007) Caspase substrates. *Cell Death Differ* **14**:66. doi:10.1038/sj.cdd.4402059

70 Thornberry NA, Rano TA, Peterson EP, et al. (1997) A combinatorial approach defines specificities of members of the caspase family and granzyme B. *J Biol Chem* **272**:17907. doi:10.1074/jbc.272.29.17907

71 Nicholson DW. (1999) Caspase structure, proteolytic substrates, and function during apoptotic cell death. *Cell Death Differ* **6**:1028. doi:10.1038/sj.cdd.4400598

72 Song J, Tan H, Shen H, et al. (2010) Cascleave: towards more accurate prediction of caspase substrate cleavage sites. *Bioinformatics* **26**:752. doi:10.1093/bioinformatics/btq043

73 Poręba M, Stróżyk A, Salvesen GS, et al. (2013) Caspase substrates and inhibitors. *Cold Spring Harb Perspect Biol* **5**:a008680. doi:10.1101/cshperspect.a008680

74 Cheng EH, Kirsch DG, Clem RJ, et al. (1997) Conversion of Bcl-2 to a Bax-like death effector by caspases. *Science* **278**:1966.

75 Clem RJ, Cheng EH-Y, Karp CL, et al. (1998) Modulation of cell death by Bcl-x_L through caspase interaction. *PNAS* **95**:554.

76 Wallach D, Kang TB, Dillon CP, et al. (2016) Programmed necrosis in inflammation: toward identification of the effector molecules. *Science* **352**:aaf2154. doi:10.1126/science.aaf2154

77 Pasparakis M & Vandenabeele P. (2015) Necroptosis and its role in inflammation. *Nature* **517**:311. doi:10.1038/nature14191

78 Weinlich R, Oberst A, Beere HM, et al. (2017) Necroptosis in development, inflammation and disease. *Nat Rev Mol Cell Biol* **18**:127. doi:10.1038/nrm.2016.149

79 Jorgensen I, Rayamajhi M, & Miao EA. (2017) Programmed cell death as a defence against infection. *Nat Rev Immunol* **17**:151. doi:10.1038/nri.2016.147

80 Nakajima YI & Kuranaga E. (2017) Caspase-dependent non-apoptotic processes in development. *Cell Death Differ* **24**:1422. doi:10.1038/cdd.2017.36

81 Shalini S, Dorstyn L, Dawar S, et al. (2015) Old, new and emerging functions of caspases. *Cell Death Differ* **22**:526. doi:10.1038/cdd.2014.216

82 Miura M. (2012) Apoptotic and nonapoptotic caspase functions in animal development. *Cold Spring Harb Perspect Biol* **4**:a008664. doi:10.1101/cshperspect.a008664

83 Yi CH & Yuan J. (2009) The Jekyll and Hyde functions of caspases. *Dev Cell* **16**:21. doi:10.1016/j.devcel.2008.12.012

84 Olsson M, Forsberg J, & Zhivotovsky B. (2014) Caspase-2: the reinvented enzyme. *Oncogene* **34**:1877. doi:10.1038/onc.2014.139

85 O'Byrne KJ & Richard DJ. (2017) Nucleolar caspase-2: protecting us from DNA damage. *J Cell Biol* **216**:1521. doi:10.1083/jcb.201704114

86 Fava LL, Schuler F, Sladky V, et al. (2017) The PIDDosome activates p53 in response to supernumerary centrosomes. *Genes Dev* **31**:34. doi:10.1101/gad.289728.116

87 Walczak H. (2013) Death receptor-ligand systems in cancer, cell death, and inflammation. *Cold Spring Harb Perspect Biol* **5**:a008698. doi:10.1101/cshperspect.a008698

88 Neefjes J, Jongsma ML, Paul P, et al. (2011) Towards a systems understanding of MHC class I and MHC class II antigen presentation. *Nat Rev Immunol* **11**:823. doi:10.1038/nri3084

89 Rock KL, Reits E, & Neefjes J. (2016) Present yourself! By MHC class I and MHC class II molecules. *Trends Immunol* **37**:724. doi:10.1016/j.it.2016.08.010

90 Coulie PG, Van den Eynde BJ, van der Bruggen P, et al. (2014) Tumour antigens recognized by T lymphocytes: at the core of cancer immunotherapy. *Nat Rev Cancer* **14**:135. doi:10.1038/nrc3670

91 Warren HS & Smyth MJ. (1999) NK cells and apoptosis. *Immunol Cell Biol* **77**:64. doi:10.1046/j.1440-1711.1999.00790.x

92 Kärre K, Ljunggren HG, Piontek G, et al. (1986) Selective rejection of H-2-deficient lymphoma variants suggests alternative immune defence strategy. *Nature* **319**:675. doi:10.1038/319675a0

93 Kärre K. (2008) Natural killer cell recognition of missing self. *Nat Immunol* **9**:477. doi:10.1038/ni0508-477

94 Murphy K & Weaver C. *Janeway's Immunobiology 9th ed.*, Ch. 3, p. 125. Garland Science/Taylor & Francis, 2017.

95 Murphy K & Weaver C. *Janeway's Immunobiology 9th ed.*, Ch. 9, p. 386. Garland Science/Taylor & Francis, 2017.

96 Vigneron N, Stroobant V, Van den Eynde BJ, et al. (2013) Database of T cell-defined human tumor antigens: the 2013 update. *Cancer Immun* **13**:15.

97 Murphy K & Weaver C. *Janeway's Immunobiology 9th ed.*, Ch. 8, p. 307. Garland Science/Taylor & Francis, 2017.

98 Murphy K & Weaver C. *Janeway's Immunobiology 9th ed.*, Ch. 8, p. 317. Garland Science/Taylor & Francis, 2017.

99 Murphy K & Weaver C. *Janeway's Immunobiology 9th ed.*, Ch. 8, p. 328. Garland Science/Taylor & Francis, 2017.

100 Ferguson TA & Griffith TS. (2006) A vision of cell death: Fas ligand and immune privilege 10 years later. *Immunol Rev* **213**:228. doi:10.1111/j.1600-065X.2006.00430.x

101 Donjerković D & Scott DW. (2000) Activation-induced cell death in B lymphocytes. *Cell Res* **10**:179. doi:10.1038/sj.cr.7290047

102 Green DR, Droin N, & Pinkoski M. (2003) Activation-induced cell death in T cells. *Immunol Rev* **193**:70. doi:10.1034/j.1600-065X.2003.00051.x

103 Murphy K & Weaver C. *Janeway's Immunobiology 9th ed.*, Ch. 15, p. 652. Garland Science/Taylor & Francis, 2017.

104 Murphy K & Weaver C. *Janeway's Immunobiology 9th ed.*, Ch. 15, p. 674. Garland Science/Taylor & Francis, 2017.

105 Murphy K & Weaver C. *Janeway's Immunobiology 9th ed.*, Ch. 11, p. 471. Garland Science/Taylor & Francis, 2017.

106 Bouillet P & O'Reilly LA. (2009) CD95, BIM and T cell homeostasis. *Nat Rev Immunol* **9**:514. doi:10.1038/nri2570

107 Bodmer J-L, Schneider P, & Tschopp J. (2002) The molecular architecture of the TNF superfamily. *Trends Biochem Sci* **27**:19. doi:10.1016/s0968-0004(01)01995-8

108 Locksley RM, Killeen N, & Lenardo MJ. (2001) The TNF and TNF receptor superfamilies. *Cell* **104**:487. doi:10.1016/s0092-8674(01)00237-9

109 Carswell EA, Old LJ, Kassel RL, et al. (1975) An endotoxin-induced serum factor that causes necrosis of tumors. *PNAS* **72**:3666. doi:10.1073/pnas.72.9.3666

110 Kalliolias GD & Ivashkiv LB. (2016) TNF biology, pathogenic mechanisms and emerging therapeutic strategies. *Nat Rev Rheumatol* **12**:49. doi:10.1038/nrrheum.2015.169

111 Brenner D, Blaser H, & Mak TW. (2015) Regulation of tumour necrosis factor signalling: live or let die. *Nat Rev Immunol* **15**:362. doi:10.1038/nri3834

112 LA OR, Tai L, Lee L, et al. (2009) Membrane-bound Fas ligand only is essential for Fas-induced apoptosis. *Nature* **461**:659. doi:10.1038/nature08402

113 von Karstedt S, Montinaro A, & Walczak H. (2017) Exploring the TRAILs less travelled: TRAIL in cancer biology and therapy. *Nat Rev Cancer* **17**:352. doi:10.1038/nrc.2017.28

114 Walczak H, Miller RE, Ariail K, et al. (1999) Tumoricidal activity of tumor necrosis factor-related apoptosis-inducing ligand in vivo. *Nat Med* **5**:157. doi:10.1038/5517

115 Lemke J, von Karstedt S, Zinngrebe J, et al. (2014) Getting TRAIL back on track for cancer therapy. *Cell Death Differ* **21**:1350. doi:10.1038/cdd.2014.81

116 Dimberg LY, Anderson CK, Camidge R, et al. (2013) On the TRAIL to successful cancer therapy? Predicting and counteracting resistance against TRAIL-based therapeutics. *Oncogene* **32**:1341. doi:10.1038/onc.2012.164

117 Jänicke RU, Sohn D, Totzke G, et al. (2006) Caspase-10 in mouse or not? *Science* **312**:1874. doi:10.1126/science.312.5782.1874a

118 Fischer U, Stroh C, & Schulze-Osthoff K. (2006) Unique and overlapping substrate specificities of caspase-8 and caspase-10. *Oncogene* **25**:152. doi:10.1038/sj.onc.1209015

119 Boatright KM, Deis C, Denault JB, et al. (2004) Activation of caspases-8 and -10 by FLIP(L). *Biochem J* **382**:651. doi:10.1042/BJ20040809

120 Ram DR, Ilyukha V, Volkova T, et al. (2016) Balance between short and long isoforms of cFLIP regulates Fas-mediated apoptosis in vivo. *PNAS* **113**:1606. doi:10.1073/pnas.1517562113

121 Hughes MA, Powley IR, Jukes-Jones R, et al. (2016) Co-operative and hierarchical binding of c-FLIP and caspase-8: A unified model defines how c-FLIP isoforms differentially control cell fate. *Mol Cell* **61**:834. doi:10.1016/j.molcel.2016.02.023

122 Oberst A & Green DR. (2011) It cuts both ways: reconciling the dual roles of caspase 8 in cell death and survival. *Nat Rev Mol Cell Biol* **12**:757. doi:10.1038/nrm3214

123 Li H, Zhu H, Xu C-j, et al. (1998) Cleavage of BID by caspase 8 mediates the mitochondrial damage in the fas pathway of apoptosis. *Cell* **94**:491. doi:10.1016/s0092-8674(00)81590-1

124 Kaina B, in: *Encyclopedia of Cancer* (ed M. Schwab), 1136. Springer, 2011.

125 Roos WP & Kaina B. (2013) DNA damage-induced cell death: from specific DNA lesions to the DNA damage response and apoptosis. *Cancer Lett* **332**:237. doi:10.1016/j.canlet.2012.01.007

126 Bieging KT, Mello SS, & Attardi LD. (2014) Unravelling mechanisms of p53-mediated tumour suppression. *Nat Rev Cancer* **14**:359. doi:10.1038/nrc3711

127 Sendoel A & Hengartner MO. (2014) Apoptotic cell death under hypoxia. *Physiology (Bethesda)* **29**:168. doi:10.1152/physiol.00016.2013

128 Ahmed K, Tabuchi Y, & Kondo T. (2015) Hyperthermia: an effective strategy to induce apoptosis in cancer cells. *Apoptosis* **20**:1411. doi:10.1007/s10495-015-1168-3

129 Altman BJ & Rathmell JC. (2012) Metabolic stress in autophagy and cell death pathways. *Cold Spring Harb Perspect Biol* **4**:a008763. doi:10.1101/cshperspect.a008763

130 Burg MB, Ferraris JD, & Dmitrieva NI. (2007) Cellular response to hyperosmotic stresses. *Physiol Rev* **87**:1441. doi:10.1152/physrev.00056.2006

131 Fruman DA & Rommel C. (2014) PI3K and cancer: lessons, challenges and opportunities. *Nat Rev Drug Discov* **13**:140. doi:10.1038/nrd4204

132 Kearney CJ & Martin SJ. (2013) Competition for growth factors: a lot more death with a little less Aktion. *Cell Death Differ* **20**:1291. doi:10.1038/cdd.2013.99

133 Rudel T, Kepp O, & Kozjak-Pavlovic V. (2010) Interactions between bacterial pathogens and mitochondrial cell death pathways. *Nat Rev Microbiol* **8**:693. doi:10.1038/nrmicro2421

134 Ashida H, Mimuro H, Ogawa M, et al. (2011) Cell death and infection: a double-edged sword for host and pathogen survival. *J Cell Biol* **195**:931. doi:10.1083/jcb.201108081

135 Jacotot E, Ravagnan L, Loeffler M, et al. (2000) The HIV-1 viral protein R induces apoptosis via a direct effect on the mitochondrial permeability transition pore. *J Exp Med* **191**:33. doi:10.1084/jem.191.1.33

136 Prendergast GC. (1999) Mechanisms of apoptosis by c-Myc. *Oncogene* **18**:2967. doi:10.1038/sj.onc.1202727

137 Hoffman B & Liebermann DA. (2008) Apoptotic signaling by c-MYC. *Oncogene* **27**:6462. doi:10.1038/onc.2008.312

138 Wang H. (1999) Ca^{2+}-Induced apoptosis through calcineurin dephosphorylation of BAD. *Science* **284**:339. doi:10.1126/science.284.5412.339

139 Hetz C. (2012) The unfolded protein response: controlling cell fate decisions under ER stress and beyond. *Nat Rev Mol Cell Biol* **13**:89. doi:10.1038/nrm3270

140 Tabas I & Ron D. (2011) Integrating the mechanisms of apoptosis induced by endoplasmic reticulum stress. *Nat Cell Biol* **13**:184. doi:10.1038/ncb0311-184

141 Sinha K, Das J, Pal PB, et al. (2013) Oxidative stress: the mitochondria-dependent and mitochondria-independent pathways of apoptosis. *Arch Toxicol* **87**:1157. doi:10.1007/s00204-013-1034-4

142 Orrenius S, Gogvadze V, & Zhivotovsky B. (2007) Mitochondrial oxidative stress: implications for cell death. *Annu Rev Pharmacol Toxicol* **47**:143. doi:10.1146/annurev.pharmtox.47.120505.105122

143 MacVicar T & Langer T. (2016) OPA1 processing in cell death and disease - the long and short of it. *J Cell Sci* **129**:2297. doi:10.1242/jcs.159186

144 Scorrano L, Ashiya M, Buttle K, et al. (2002) A distinct pathway remodels mitochondrial cristae and mobilizes cytochrome c during apoptosis. *Dev Cell* **2**:55. doi:10.1016/s1534-5807(01)00116-2

145 Ankarcrona M, Dypbukt JM, Bonfoco E, et al. (1995) Glutamate-induced neuronal death: A succession of necrosis or apoptosis depending on mitochondrial function. *Neuron* **15**:961. doi:10.1016/0896-6273(95)90186-8

146 Penaloza C, Lin L, Lockshin RA, et al. (2006) Cell death in development: shaping the embryo. *Histochem Cell Biol* **126**:149. doi:10.1007/s00418-006-0214-1

147 Jacobson MD, Weil M, & Raff MC. (1997) Programmed cell death in animal development. *Cell* **88**:347. doi:10.1016/s0092-8674(00)81873-5

148 Li P, Nijhawan D, Budihardjo I, et al. (1997) Cytochrome c and dATP-dependent formation of Apaf-1/Caspase-9 complex initiates an apoptotic protease cascade. *Cell* **91**:479. doi:10.1016/s0092-8674(00)80434-1

149 Yuan S & Akey CW. (2013) Apoptosome structure, assembly, and procaspase activation. *Structure* **21**:501. doi:10.1016/j.str.2013.02.024

150 Acehan D, Jiang X, Morgan DG, et al. (2002) Three-dimensional structure of the apoptosome. *Mol Cell* **9**:423. doi:10.1016/s1097-2765(02)00442-2

151 Green DR. (2005) Apoptotic pathways: ten minutes to dead. *Cell* **121**:671. doi:10.1016/j.cell.2005.05.019

152 Hao Z, Duncan GS, Chang CC, et al. (2005) Specific ablation of the apoptotic functions of cytochrome C reveals a differential requirement for cytochrome C and Apaf-1 in apoptosis. *Cell* **121**:579. doi:10.1016/j.cell.2005.03.016

153 Ow YP, Green DR, Hao Z, et al. (2008) Cytochrome c: functions beyond respiration. *Nat Rev Mol Cell Biol* **9**:532. doi:10.1038/nrm2434

154 Garrido C, Galluzzi L, Brunet M, et al. (2006) Mechanisms of cytochrome c release from mitochondria. *Cell Death Differ* **13**:1423. doi:10.1038/sj.cdd.4401950

155 Pernas L & Scorrano L. (2016) Mito-morphosis: mitochondrial fusion, fission, and cristae remodeling as key mediators of cellular function. *Annu Rev Physiol* **78**:505. doi:10.1146/annurev-physiol-021115-105011

156 Vyas S, Zaganjor E, & Haigis MC. (2016) Mitochondria and cancer. *Cell* **166**:555. doi:10.1016/j.cell.2016.07.002

157 Nunnari J & Suomalainen A. (2012) Mitochondria: in sickness and in health. *Cell* **148**:1145. doi:10.1016/j.cell.2012.02.035

158 Wang C & Youle RJ. (2009) The role of mitochondria in apoptosis*. *Annu Rev Genet* **43**:95. doi:10.1146/annurev-genet-102108-134850

159 Tait SW & Green DR. (2010) Mitochondria and cell death: outer membrane permeabilization and beyond. *Nat Rev Mol Cell Biol* **11**:621. doi:10.1038/nrm2952

160 Du C, Fang M, Li Y, et al. (2000) Smac, a mitochondrial protein that promotes cytochrome c–dependent caspase activation by eliminating IAP inhibition. *Cell* **102**:33. doi:10.1016/s0092-8674(00)00008-8

161 Verhagen AM, Ekert PG, Pakusch M, et al. (2000) Identification of DIABLO, a mammalian protein that promotes apoptosis by binding to and antagonizing IAP proteins. *Cell* **102**:43. doi:10.1016/s0092-8674(00)00009-x

162 Suzuki Y, Imai Y, Nakayama H, et al. (2001) A serine protease, HtrA2, is released from the mitochondria and interacts with XIAP, inducing cell death. *Mol Cell* **8**:613. doi:10.1016/s1097-2765(01)00341-0

163 Hegde R, Srinivasula SM, Zhang Z, et al. (2002) Identification of Omi/HtrA2 as a mitochondrial apoptotic serine protease that disrupts inhibitor of apoptosis protein-caspase interaction. *J Biol Chem* **277**:432. doi:10.1074/jbc.M109721200

164 Martins LM, Iaccarino I, Tenev T, et al. (2002) The serine protease Omi/HtrA2 regulates apoptosis by binding XIAP through a reaper-like motif. *J Biol Chem* **277**:439. doi:10.1074/jbc.M109784200

165 Verhagen AM, Silke J, Ekert PG, et al. (2002) HtrA2 promotes cell death through its serine protease activity and its ability to antagonize inhibitor of apoptosis proteins. *J Biol Chem* **277**:445. doi:10.1074/jbc.M109891200

166 Li LY, Luo X, & Wang X. (2001) Endonuclease G is an apoptotic DNase when released from mitochondria. *Nature* **412**:95. doi:10.1038/35083620

167 Vande Walle L, Lamkanfi M, & Vandenabeele P. (2008) The mitochondrial serine protease HtrA2/Omi: an overview. *Cell Death Differ* **15**:453. doi:10.1038/sj.cdd.4402291

168 Shoshan-Barmatz V & Ben-Hail D. (2012) VDAC, a multi-functional mitochondrial protein as a pharmacological target. *Mitochondrion* **12**:24. doi:10.1016/j.mito.2011.04.001

169 Benz R. (1994) Permeation of hydrophilic solutes through mitochondrial outer membranes: review on mitochondrial porins. *Biochim Biophys Acta* **1197**:167. doi:10.1016/0304-4157(94)90004-3

170 Zamzami N & Kroemer G. (2001) The mitochondrion in apoptosis: how Pandora's box opens. *Nat Rev Mol Cell Biol* **2**:67. doi:10.1038/35048073

171 Cosentino K & García-Sáez AJ. (2017) Bax and Bak pores: are we closing the circle? *Trends Cell Biol* **27**:266. doi:10.1016/j.tcb.2016.11.004

172 Dewson G, Kratina T, Sim HW, et al. (2008) To trigger apoptosis, Bak exposes its BH3 domain and homodimerizes via BH3:groove interactions. *Mol Cell* **30**:369. doi:10.1016/j.molcel.2008.04.005

173 Dewson G, Kratina T, Czabotar P, et al. (2009) Bak activation for apoptosis involves oligomerization of dimers via their alpha6 helices. *Mol Cell* **36**:696. doi:10.1016/j.molcel.2009.11.008

174 Dewson G, Ma S, Frederick P, et al. (2012) Bax dimerizes via a symmetric BH3:groove interface during apoptosis. *Cell Death Differ* **19**:661. doi:10.1038/cdd.2011.138

175 Mikhailov V, Mikhailova M, Degenhardt K, et al. (2003) Association of Bax and Bak homo-oligomers in mitochondria. Bax requirement for Bak reorganization and cytochrome c release. *J Biol Chem* **278**:5367. doi:10.1074/jbc.M203392200

176 Tait SW & Green DR. (2013) Mitochondrial regulation of cell death. *Cold Spring Harb Perspect Biol* **5**:a008706. doi:10.1101/cshperspect.a008706

177 Westphal D, Kluck RM, & Dewson G. (2014) Building blocks of the apoptotic pore: how Bax and Bak are activated and oligomerize during apoptosis. *Cell Death Differ* **21**:196. doi:10.1038/cdd.2013.139

178 Große L, Wurm CA, Brüser C, et al. (2016) Bax assembles into large ring-like structures remodeling the mitochondrial outer membrane in apoptosis. *EMBO J* **35**:402. doi:10.15252/embj.201592789

179 Youle RJ & Strasser A. (2008) The BCL-2 protein family: opposing activities that mediate cell death. *Nat Rev Mol Cell Biol* **9**:47. doi:10.1038/nrm2308

180 Czabotar PE, Lessene G, Strasser A, et al. (2014) Control of apoptosis by the BCL-2 protein family: implications for physiology and therapy. *Nat Rev Mol Cell Biol* **15**:49. doi:10.1038/nrm3722

181 Tsujimoto Y, Finger L, Yunis J, et al. (1984) Cloning of the chromosome breakpoint of neoplastic B cells with the t(14;18) chromosome translocation. *Science* **226**:1097. doi:10.1126/science.6093263

182 Vaux DL, Cory S, & Adams JM. (1988) Bcl-2 gene promotes haemopoietic cell survival and cooperates with c-myc to immortalize pre-B cells. *Nature* **335**:440. doi:10.1038/335440a0

183 Ashkenazi A, Fairbrother WJ, Leverson JD, et al. (2017) From basic apoptosis discoveries to advanced selective BCL-2 family inhibitors. *Nat Rev Drug Discov* **16**:273. doi:10.1038/nrd.2016.253

184 Youle RJ. (2007) Cellular demolition and the rules of engagement. *Science* **315**:776. doi:10.1126/science.1138870

185 Willis SN, Fletcher JI, Kaufmann T, et al. (2007) Apoptosis initiated when BH3 ligands engage multiple Bcl-2 homologs, not Bax or Bak. *Science* **315**:856. doi:10.1126/science.1133289

186 Llambi F, Moldoveanu T, Tait SW, et al. (2011) A unified model of mammalian BCL-2 protein family interactions at the mitochondria. *Mol Cell* **44**:517. doi:10.1016/j.molcel.2011.10.001

187 Oda E. (2000) Noxa, a BH3-only member of the Bcl-2 family and candidate mediator of p53-induced apoptosis. *Science* **288**:1053. doi:10.1126/science.288.5468.1053

188 Nakano K & Vousden KH. (2001) PUMA, a novel proapoptotic gene, is induced by p53. *Mol Cell* **7**:683. doi:10.1016/s1097-2765(01)00214-3

189 Fu Z & Tindall DJ. (2008) FOXOs, cancer and regulation of apoptosis. *Oncogene* **27**:2312. doi:10.1038/onc.2008.24

190 Huang K, Zhang J, O'Neill KL, et al. (2016) Cleavage by caspase 8 and mitochondrial membrane association activate Bid during TRAIL-induced apoptosis. *J Biol Chem* **291**:11843. doi:10.1074/jbc.M115.711051

191 Luo X, Budihardjo I, Zou H, et al. (1998) Bid, a Bcl2 interacting protein, mediates cytochrome c release from mitochondria in response to activation of cell surface death receptors. *Cell* **94**:481. doi:10.1016/s0092-8674(00)81589-5

192 Wei MC, Lindsten T, Mootha VK, et al. (2000) tBID, a membrane-targeted death ligand, oligomerizes BAK to release cytochrome c. *Genes Dev* **14**:2060. doi:10.1101/gad.14.16.2060

193 Lovell JF, Billen LP, Bindner S, et al. (2008) Membrane binding by tBid initiates an ordered series of events culminating in membrane permeabilization by Bax. *Cell* **135**:1074. doi:10.1016/j.cell.2008.11.010

194 Schug ZT, Gonzalvez F, Houtkooper RH, et al. (2011) BID is cleaved by caspase-8 within a native complex on the mitochondrial membrane. *Cell Death Differ* **18**:538. doi:10.1038/cdd.2010.135

195 Frezza C, Cipolat S, Martins de Brito O, et al. (2006) OPA1 controls apoptotic cristae remodeling independently from mitochondrial fusion. *Cell* **126**:177. doi:10.1016/j.cell.2006.06.025

196 Springer JE, Azbill RD, Nottingham SA, et al. (2000) Calcineurin-mediated BAD dephosphorylation activates the caspase-3 apoptotic cascade in traumatic spinal cord injury. *J Neurosci* **20**:7246. doi:10.1523/jneurosci.20-19-07246.2000

197 Cogliati S, Enriquez JA, & Scorrano L. (2016) Mitochondrial cristae: where beauty meets functionality. *Trends Biochem Sci* **41**:261. doi:10.1016/j.tibs.2016.01.001

198 Youle RJ & van der Bliek AM. (2012) Mitochondrial fission, fusion, and stress. *Science* **337**:1062. doi:10.1126/science.1219855

199 Ly JD, Grubb DR, & Lawen A. (2003) The mitochondrial membrane potential ($\Delta\psi_m$) in apoptosis; an update. *Apoptosis* **8**:115. doi:10.1023/a:1022945107762

200 Martinou JC & Youle RJ. (2006) Which came first, the cytochrome c release or the mitochondrial fission? *Cell Death Differ* **13**:1291. doi:10.1038/sj.cdd.4401985

201 Suen DF, Norris KL, & Youle RJ. (2008) Mitochondrial dynamics and apoptosis. *Genes Dev* **22**:1577. doi:10.1101/gad.1658508

202 Autret A & Martin SJ. (2009) Emerging role for members of the Bcl-2 family in mitochondrial morphogenesis. *Mol Cell* **36**:355. doi:10.1016/j.molcel.2009.10.011

203 Montessuit S, Somasekharan SP, Terrones O, et al. (2010) Membrane remodeling induced by the dynamin-related protein Drp1 stimulates Bax oligomerization. *Cell* **142**:889. doi:10.1016/j.cell.2010.08.017

204 Schäfer A & Reichert AS. (2009) Emerging roles of mitochondrial membrane dynamics in health and disease. *Biol Chem* **390**:707. doi:10.1515/BC.2009.086

205 Hoppins S & Nunnari J. (2012) Mitochondrial dynamics and apoptosis—the ER connection. *Science* **337**:1052. doi:10.1126/science.1224709

206 Jagasia R, Grote P, Westermann B, et al. (2005) DRP-1-mediated mitochondrial fragmentation during EGL-1-induced cell death in *C. elegans*. *Nature* **433**:754. doi:10.1038/nature03316

207 Abdelwahid E, Yokokura T, Krieser RJ, et al. (2007) Mitochondrial disruption in *Drosophila* apoptosis. *Dev Cell* **12**:793. doi:10.1016/j.devcel.2007.04.004

208 Pfanner N, van der Laan M, Amati P, et al. (2014) Uniform nomenclature for the mitochondrial contact site and cristae organizing system. *J Cell Biol* **204**:1083. doi:10.1083/jcb.201401006

209 Barrera M, Koob S, Dikov D, et al. (2016) OPA1 functionally interacts with MIC60 but is dispensable for crista junction formation. *FEBS Lett* **590**:3309. doi:10.1002/1873-3468.12384

210 Kozjak-Pavlovic V. (2017) The MICOS complex of human mitochondria. *Cell Tissue Res* **367**:83. doi:10.1007/s00441-016-2433-7

211 Varanita T, Soriano ME, Romanello V, et al. (2015) The OPA1-dependent mitochondrial cristae remodeling pathway controls atrophic, apoptotic, and ischemic tissue damage. *Cell Metab* **21**:834. doi:10.1016/j.cmet.2015.05.007

212 Glytsou C, Calvo E, Cogliati S, et al. (2016) Optic atrophy 1 is epistatic to the core MICOS component MIC60 in mitochondrial cristae shape control. *Cell Rep* **17**:3024. doi:10.1016/j.celrep.2016.11.049

213 Gottlieb E. (2006) OPA1 and PARL keep a lid on apoptosis. *Cell* **126**:27. doi:10.1016/j.cell.2006.06.030

214 Germain M, Mathai JP, McBride HM, et al. (2005) Endoplasmic reticulum BIK initiates DRP1-regulated remodelling of mitochondrial cristae during apoptosis. *EMBO J* **24**:1546. doi:10.1038/sj.emboj.7600592

215 Landes T, Emorine LJ, Courilleau D, et al. (2010) The BH3-only Bnip3 binds to the dynamin Opa1 to promote mitochondrial fragmentation and apoptosis by distinct mechanisms. *EMBO Rep* **11**:459. doi:10.1038/embor.2010.50

216 Yamaguchi R, Lartigue L, Perkins G, et al. (2008) Opa1-mediated cristae opening is Bax/Bak and BH3 dependent, required for apoptosis, and independent of Bak oligomerization. *Mol Cell* **31**:557. doi:10.1016/j.molcel.2008.07.010

217 Gottlieb E, Armour SM, Harris MH, et al. (2003) Mitochondrial membrane potential regulates matrix configuration and cytochrome c release during apoptosis. *Cell Death Differ* **10**:709. doi:10.1038/sj.cdd.4401231

218 Bossy-Wetzel E, Newmeyer DD, & Green DR. (1998) Mitochondrial cytochrome c release in apoptosis occurs upstream of DEVD-specific caspase activation and independently of mitochondrial transmembrane depolarization. *EMBO J* **17**:37. doi:10.1093/emboj/17.1.37

219 Ricci JE, Munoz-Pinedo C, Fitzgerald P, et al. (2004) Disruption of mitochondrial function during apoptosis is mediated by caspase cleavage of the p75 subunit of complex I of the electron transport chain. *Cell* **117**:773. doi:10.1016/j.cell.2004.05.008

220 Bernardi P, Rasola A, Forte M, et al. (2015) The mitochondrial permeability transition pore: Channel formation by F-ATP synthase, integration in signal transduction, and role in pathophysiology. *Physiol Rev* **95**:1111. doi:10.1152/physrev.00001.2015

221 Green DR & Kroemer G. (2004) The pathophysiology of mitochondrial cell death. *Science* **305**:626. doi:10.1126/science.1099320

222 Izzo V, Bravo-San Pedro JM, Sica V, et al. (2016) Mitochondrial permeability transition: New findings and persisting uncertainties. *Trends Cell Biol* **26**:655. doi:10.1016/j.tcb.2016.04.006

223 Bernardi P. (2013) The mitochondrial permeability transition pore: a mystery solved? *Front Physiol* **4**:95. doi:10.3389/fphys.2013.00095

224 Kokoszka JE, Waymire KG, Levy SE, et al. (2004) The ADP/ATP translocator is not essential for the mitochondrial permeability transition pore. *Nature* **427**:461. doi:10.1038/nature02229

225 Baines CP, Kaiser RA, Sheiko T, et al. (2007) Voltage-dependent anion channels are dispensable for mitochondrial-dependent cell death. *Nat Cell Biol* **9**:550. doi:10.1038/ncb1575

226 Baines CP, Kaiser RA, Purcell NH, et al. (2005) Loss of cyclophilin D reveals a critical role for mitochondrial permeability transition in cell death. *Nature* **434**:658. doi:10.1038/nature03434

227 Basso E, Fante L, Fowlkes J, et al. (2005) Properties of the permeability transition pore in mitochondria devoid of Cyclophilin D. *J Biol Chem* **280**:18558. doi:10.1074/jbc.C500089200

228 Nakagawa T, Shimizu S, Watanabe T, et al. (2005) Cyclophilin D-dependent mitochondrial permeability transition regulates some necrotic but not apoptotic cell death. *Nature* **434**:652. doi:10.1038/nature03317

229 Kroemer G, Petit P, Zamzami N, et al. (1995) The biochemistry of programmed cell death. *FASEB J* **9**:1277. doi:10.1096/fasebj.9.13.7557017

230 Kinnally KW & Antonsson B. (2007) A tale of two mitochondrial channels, MAC and PTP, in apoptosis. *Apoptosis* **12**:857. doi:10.1007/s10495-007-0722-z

231 Karch J, Kwong JQ, Burr AR, et al. (2013) Bax and Bak function as the outer membrane component of the mitochondrial permeability pore in regulating necrotic cell death in mice. *eLife* **2**:e00772. doi:10.7554/eLife.00772

232 Silke J & Meier P. (2013) Inhibitor of apoptosis (IAP) proteins-modulators of cell death and inflammation. *Cold Spring Harb Perspect Biol* **5**:a008730. doi:10.1101/cshperspect.a008730

233 Birnbaum MJ, Clem RJ, & Miller LK. (1994) An apoptosis-inhibiting gene from a nuclear polyhedrosis virus encoding a polypeptide with Cys/His sequence motifs. *J Virol* **68**:2521.

234 Salvesen GS & Duckett CS. (2002) IAP proteins: blocking the road to death's door. *Nat Rev Mol Cell Biol* **3**:401. doi:10.1038/nrm830

235 Scott FL, Denault JB, Riedl SJ, et al. (2005) XIAP inhibits caspase-3 and -7 using two binding sites: evolutionarily conserved mechanism of IAPs. *EMBO J* **24**:645. doi:10.1038/sj.emboj.7600544

236 Oberoi-Khanuja TK, Murali A, & Rajalingam K. (2013) IAPs on the move: role of inhibitors of apoptosis proteins in cell migration. *Cell Death Dis* **4**:e784. doi:10.1038/cddis.2013.311

237 Gschwind A, Fischer OM, & Ullrich A. (2004) The discovery of receptor tyrosine kinases: targets for cancer therapy. *Nat Rev Cancer* **4**:361. doi:10.1038/nrc1360

238 Lemmon MA & Schlessinger J. (2010) Cell signaling by receptor tyrosine kinases. *Cell* **141**:1117. doi:10.1016/j.cell.2010.06.011

239 Schlessinger J. (2014) Receptor tyrosine kinases: legacy of the first two decades. *Cold Spring Harb Perspect Biol* **6** doi:10.1101/cshperspect.a008912

240 Hilger D, Masureel M, & Kobilka BK. (2018) Structure and dynamics of GPCR signaling complexes. *Nat Struct Mol Biol* **25**:4. doi:10.1038/s41594-017-0011-7

241 Samatar AA & Poulikakos PI. (2014) Targeting RAS-ERK signalling in cancer: promises and challenges. *Nat Rev Drug Discov* **13**:928. doi:10.1038/nrd4281

242 O'Shea JJ, Schwartz DM, Villarino AV, et al. (2015) The JAK-STAT pathway: impact on human disease and therapeutic intervention. *Annu Rev Med* **66**:311. doi:10.1146/annurev-med-051113-024537

243 Vanhaesebroeck B, Guillermet-Guibert J, Graupera M, et al. (2010) The emerging mechanisms of isoform-specific PI3K signalling. *Nat Rev Mol Cell Biol* **11**:329. doi:10.1038/nrm2882

244 Janku F, Yap TA, & Meric-Bernstam F. (2018) Targeting the PI3K pathway in cancer: are we making headway? *Nat Rev Clin Oncol* **15**:273. doi:10.1038/nrclinonc.2018.28

245 Fruman DA, Chiu H, Hopkins BD, et al. (2017) The PI3K pathway in human disease. *Cell* **170**:605. doi:10.1016/j.cell.2017.07.029

246 Mayer IA & Arteaga CL. (2016) The PI3K/AKT pathway as a target for cancer treatment. *Annu Rev Med* **67**:11. doi:10.1146/annurev-med-062913-051343

247 Cell Signaling Technology®. *PI3K / Akt substrates table*, https://www.cellsignal.com/contents/resources-reference-tables/pi3k-akt-substrates-table/science-tables-akt-substrate (2015) last accessed 2019-04-01.

248 Datta SR, Dudek H, Tao X, et al. (1997) Akt phosphorylation of BAD couples survival signals to the cell-intrinsic death machinery. *Cell* **91**:231. doi:10.1016/s0092-8674(00)80405-5

249 Qi XJ, Wildey GM, & Howe PH. (2006) Evidence that Ser87 of BimEL is phosphorylated by Akt and regulates BimEL apoptotic function. *J Biol Chem* **281**:813. doi:10.1074/jbc.M505546200

250 Maurer U, Charvet C, Wagman AS, et al. (2006) Glycogen synthase kinase-3 regulates mitochondrial outer membrane permeabilization and apoptosis by destabilization of MCL-1. *Mol Cell* **21**:749. doi:10.1016/j.molcel.2006.02.009

251 Ambacher KK, Pitzul KB, Karajgikar M, et al. (2012) The JNK- and AKT/GSK3beta- signaling pathways converge to regulate Puma induction and neuronal apoptosis induced by trophic factor deprivation. *PLoS One* **7**:e46885. doi:10.1371/journal.pone.0046885

252 Wei Z, Qi J, Dai Y, et al. (2009) Haloperidol disrupts Akt signalling to reveal a phosphorylation-dependent regulation of pro-apoptotic Bcl-XS function. *Cell Signal* **21**:161. doi:10.1016/j.cellsig.2008.10.005

253 Cardone MH, Roy N, Stennicke HR, et al. (1998) Regulation of cell death protease caspase-9 by phosphorylation. *Science* **282**:1318. doi:10.1126/science.282.5392.1318

254 McCarthy NJ, Whyte MKB, Gilbert CS, et al. (1997) Inhibition of Ced-3/ICE-related proteases does not prevent cell death induced by oncogenes, DNA damage, or the Bcl-2 homologue Bak. *J Cell Biol* **136**:215. doi:10.1083/jcb.136.1.215

255 Rena G, Guo S, Cichy SC, et al. (1999) Phosphorylation of the transcription factor Forkhead family member FKHR by protein kinase B. *J Biol Chem* **274**:17179. doi:10.1074/jbc.274.24.17179

256 Rena G, Prescott AR, Guo S, et al. (2001) Roles of the forkhead in rhabdomyosarcoma (FKHR) phosphorylation sites in regulating 14-3-3 binding, transactivation and nuclear targetting. *Biochem J* **354**:605. doi:10.1042/bj3540605

257 Brunet A, Bonni A, Zigmond MJ, et al. (1999) Akt promotes cell survival by phosphorylating and inhibiting a forkhead transcription factor. *Cell* **96**:857. doi:10.1016/s0092-8674(00)80595-4

258 Kashii Y, Uchida M, Kirito K, et al. (2000) A member of Forkhead family transcription factor, FKHRL1, is one of the downstream molecules of phosphatidylinositol 3-kinase-Akt activation pathway in erythropoietin signal transduction. *Blood* **96**:941.

259 Kops GJ, de Ruiter ND, De Vries-Smits AM, et al. (1999) Direct control of the Forkhead transcription factor AFX by protein kinase B. *Nature* **398**:630. doi:10.1038/19328

260 Brownawell AM, Kops GJ, Macara IG, et al. (2001) Inhibition of nuclear import by protein kinase B (Akt) regulates the subcellular distribution and activity of the forkhead transcription factor AFX. *Mol Cell Biol* **21**:3534. doi:10.1128/MCB.21.10.3534-3546.2001

261 Coomans de Brachene A & Demoulin JB. (2016) FOXO transcription factors in cancer development and therapy. *Cell Mol Life Sci* **73**:1159. doi:10.1007/s00018-015-2112-y

262 Palamarchuk A, Efanov A, Maximov V, et al. (2005) Akt phosphorylates and regulates Pdcd4 tumor suppressor protein. *Cancer Res* **65**:11282. doi:10.1158/0008-5472.can-05-3469

263 Zhou BP, Liao Y, Xia W, et al. (2001) HER-2/neu induces p53 ubiquitination via Akt-mediated MDM2 phosphorylation. *Nat Cell Biol* **3**:973. doi:10.1038/ncb1101-973

264 Feng J, Tamaskovic R, Yang Z, et al. (2004) Stabilization of Mdm2 via decreased ubiquitination is mediated by protein kinase B/Akt-dependent phosphorylation. *J Biol Chem* **279**:35510. doi:10.1074/jbc.M404936200

265 Dan HC, Sun M, Kaneko S, et al. (2004) Akt phosphorylation and stabilization of X-linked inhibitor of apoptosis protein (XIAP). *J Biol Chem* **279**:5405. doi:10.1074/jbc.M312044200

266 Yang L, Sun M, Sun XM, et al. (2007) Akt attenuation of the serine protease activity of HtrA2/Omi through phosphorylation of serine 212. *J Biol Chem* **282**:10981. doi:10.1074/jbc.M700445200

267 Kim AH, Khursigara G, Sun X, et al. (2001) Akt phosphorylates and negatively regulates apoptosis signal-regulating kinase 1. *Mol Cell Biol* **21**:893. doi:10.1128/MCB.21.3.893-901.2001

268 Zhang R, Luo D, Miao R, et al. (2005) Hsp90-Akt phosphorylates ASK1 and inhibits ASK1-mediated apoptosis. *Oncogene* **24**:3954. doi:10.1038/sj.onc.1208548

269 Lyons TR, Thorburn J, Ryan PW, et al. (2007) Regulation of the pro-apoptotic scaffolding protein POSH by Akt. *J Biol Chem* **282**:21987. doi:10.1074/jbc.M704321200

270 Shi B, Tran T, Sobkoviak R, et al. (2009) Activation-induced degradation of FLIP(L) is mediated via the phosphatidylinositol 3-kinase/Akt signaling pathway in macrophages. *J Biol Chem* **284**:14513. doi:10.1074/jbc.M807918200

271 Goswami A, Burikhanov R, de Thonel A, et al. (2005) Binding and phosphorylation of Par-4 by Akt is essential for cancer cell survival. *Mol Cell* **20**:33. doi:10.1016/j.molcel.2005.08.016

272 Hu Y, Yao J, Liu Z, et al. (2005) Akt phosphorylates acinus and inhibits its proteolytic cleavage, preventing chromatin condensation. *EMBO J* **24**:3543. doi:10.1038/sj.emboj.7600823

273 Chan CB, Liu X, Tang X, et al. (2007) Akt phosphorylation of zyxin mediates its interaction with acinus-S and prevents acinus-triggered chromatin condensation. *Cell Death Differ* **14**:1688. doi:10.1038/sj.cdd.4402179

274 Roberts AW, Stilgenbauer S, Seymour JF, et al. (2017) Venetoclax in patients with previously treated chronic lymphocytic leukemia. *Clin Cancer Res* **23**:4527. doi:10.1158/1078-0432.Ccr-16-0955

275 Fruman DA & Cantley LC. (2014) Idelalisib — a PI3Kδ inhibitor for B-cell cancers. *N Engl J Med* **370**:1061. doi:10.1056/NEJMe1400055

276 Konopleva MY, Walter RB, Faderl SH, et al. (2014) Preclinical and early clinical evaluation of the oral AKT inhibitor, MK-2206, for the treatment of acute myelogenous leukemia. *Clin Cancer Res* **20**:2226. doi:10.1158/1078-0432.Ccr-13-1978

277 Jansen VM, Mayer IA, & Arteaga CL. (2016) Is there a future for AKT inhibitors in the treatment of cancer? *Clin Cancer Res* **22**:2599. doi:10.1158/1078-0432.Ccr-16-0100

278 Nitulescu GM, Margina D, Juzenas P, et al. (2016) Akt inhibitors in cancer treatment: The long journey from drug discovery to clinical use (Review). *Int J Oncol* **48**:869. doi:10.3892/ijo.2015.3306

279 Mann J. (2002) Natural products in cancer chemotherapy: past, present and future. *Nat Rev Cancer* **2**:143. doi:10.1038/nrc723

280 Demain AL & Vaishnav P. (2011) Natural products for cancer chemotherapy. *Microb Biotechnol* **4**:687. doi:10.1111/j.1751-7915.2010.00221.x

281 Brimmell M, Mendiola R, Mangion J, et al. (1998) BAX frameshift mutations in cell lines derived from human haemopoietic malignancies are associated with resistance to apoptosis and microsatellite instability. *Oncogene* **16**:1803. doi:10.1038/sj.onc.1201704

282 Müller A, Gillissen B, Richter A, et al. (2018) Pan-class I PI3-kinase inhibitor BKM120 induces MEK1/2-dependent mitotic catastrophe in non-Hodgkin lymphoma leading to apoptosis or polyploidy determined by Bax/Bak and p53. *Cell Death Dis* **9**:384. doi:10.1038/s41419-018-0413-4

283 Takahashi JS. (2017) Transcriptional architecture of the mammalian circadian clock. *Nat Rev Genet* **18**:164. doi:10.1038/nrg.2016.150

284 Walton ZE, Altman BJ, Brooks DG, et al. (2018) Circadian clock's cancer connections. *Annu Rev Cancer Biol* **2**:133. doi:10.1146/annurev-cancerbio-030617-050216

285 Jiang W, Zhao S, Jiang X, et al. (2016) The circadian clock gene Bmal1 acts as a potential anti-oncogene in pancreatic cancer by activating the p53 tumor suppressor pathway. *Cancer Lett* **371**:314. doi:10.1016/j.canlet.2015.12.002

286 Hunt T & Sassone-Corsi P. (2007) Riding tandem: circadian clocks and the cell cycle. *Cell* **129**:461. doi:10.1016/j.cell.2007.04.015

287 Farshadi E, Yan J, Leclere P, et al. (2019) The positive circadian regulators CLOCK and BMAL1 control G2/M cell cycle transition through Cyclin B1. *Cell Cycle* **18**:16. doi:10.1080/15384101.2018.1558638

288 Elshazley M, Sato M, Hase T, et al. (2012) The circadian clock gene BMAL1 is a novel therapeutic target for malignant pleural mesothelioma. *Int J Cancer* **131**:2820. doi:10.1002/ijc.27598

5. Licensing & Copyright

- **Manuscript "Pro-apoptotic and immunostimulatory tetrahydroxanthone dimers from the endophytic fungus *Phomopsis longicolla*":** Reproduced with permission from Rönsberg et al. (2013) *The Journal of Organic Chemistry* **78**:12409. Copyright 2013 American Chemical Society.
- **Manuscript "PDK1 controls upstream PI3K expression and PIP_3 generation":** Reproduced with permission from Dieterle et al. (2014) *Oncogene* **33**:3043. Copyright 2013 Springer Nature.
- **Manuscript "Efficient and safe gene delivery to human corneal endothelium using magnetic nanoparticles":** Reproduced with permission from Future Medicine Ltd., license number 4601840355923: Future Medicine Ltd., *Nanomedicine*, Marta Czugala et al., Copyright 2015.
- **Manuscript "CASP3 inactivates BMAL1 by cleaving off its transactivation domain at D585":** This manuscript is reproduced in this dissertation with permission from the responsible authors (Böhler P & Stork B). Any reproduction of any parts of this manuscript in any form is not permitted without the explicit consent of these authors. Copyright Böhler et al. 2019.

Appendix

Manuscript "The mycotoxin phomoxanthone A disturbs the form and function of the inner mitochondrial membrane"

Böhler P[*], Stuhldreier F[*], Anand R, Kondadi AK, Schlütermann D, Berleth N, Deitersen J, Wallot-Hieke N, Wu W, Frank M, Niemann H, Wesbuer E, Barbian A, Luyten T, Parys JB, Weidtkamp-Peters S, Borchardt A, Reichert AS, Peña-Blanco A, García-Sáez AJ, Itskanov S, van der Bliek AM, Proksch P, Wesselborg S[*], Stork B[*]. *Cell Death & Disease* (2018) **9**:286, doi: 10.1038/s41419-018-0312-8

[*] These authors contributed equally to the manuscript.

Böhler et al. *Cell Death and Disease* (2018)9:286
DOI 10.1038/s41419-018-0312-8

Cell Death & Disease

ARTICLE Open Access

The mycotoxin phomoxanthone A disturbs the form and function of the inner mitochondrial membrane

Philip Böhler[1], Fabian Stuhldreier[1], Ruchika Anand[2], Arun Kumar Kondadi[2], David Schlütermann[1], Niklas Berleth[1], Jana Deitersen[1], Nora Wallot-Hieke[1], Wenxian Wu[1], Marian Frank[3], Hendrik Niemann[3], Elisabeth Wesbuer[4], Andreas Barbian[4], Tomas Luyten[5], Jan B. Parys[5], Stefanie Weidtkamp-Peters[6], Andrea Borchardt[2], Andreas S. Reichert[2], Aida Peña-Blanco[7], Ana J. García-Sáez[7], Samuel Itskanov[8], Alexander M. van der Bliek[8], Peter Proksch[3], Sebastian Wesselborg[1] and Björn Stork[1]

Abstract

Mitochondria are cellular organelles with crucial functions in the generation and distribution of ATP, the buffering of cytosolic Ca^{2+} and the initiation of apoptosis. Compounds that interfere with these functions are termed mitochondrial toxins, many of which are derived from microbes, such as antimycin A, oligomycin A, and ionomycin. Here, we identify the mycotoxin phomoxanthone A (PXA), derived from the endophytic fungus *Phomopsis longicolla*, as a mitochondrial toxin. We show that PXA elicits a strong release of Ca^{2+} from the mitochondria but not from the ER. In addition, PXA depolarises the mitochondria similarly to protonophoric uncouplers such as CCCP, yet unlike these, it does not increase but rather inhibits cellular respiration and electron transport chain activity. The respiration-dependent mitochondrial network structure rapidly collapses into fragments upon PXA treatment. Surprisingly, this fragmentation is independent from the canonical mitochondrial fission and fusion mediators DRP1 and OPA1, and exclusively affects the inner mitochondrial membrane, leading to cristae disruption, release of pro-apoptotic proteins, and apoptosis. Taken together, our results suggest that PXA is a mitochondrial toxin with a novel mode of action that might prove a useful tool for the study of mitochondrial ion homoeostasis and membrane dynamics.

Introduction

Mitochondria are cellular organelles that are crucial to almost all eukaryotic organisms. Among their most important functions are generation and distribution of ATP, buffering of cytosolic Ca^{2+} and, in animal cells, initiation of apoptosis. Disturbance of these or other functions by mitochondrial toxins can lead to cellular stress and cell death[1,2].

Mitochondria produce ATP through oxidative phosphorylation (OXPHOS), which depends on the electron transport chain (ETC) embedded in the inner mitochondrial membrane (IMM). The ETC pumps protons out of the mitochondrial matrix and into the mitochondrial intermembrane space. This generates a proton gradient (ΔpH_m) and, consequently, a membrane potential ($\Delta\Psi_m$) across the IMM. The $\Delta\Psi_m$ is then used to drive the mitochondrial ATP synthase[3].

To provide all regions within the cell with sufficient ATP, mitochondria often form a network that constantly undergoes balanced fission and fusion. This allows

Correspondence: Sebastian Wesselborg (sebastian.wesselborg@uni-duesseldorf.de) or Björn Stork (bjoern.stork@uni-duesseldorf.de)
[1]Institute of Molecular Medicine I, Medical Faculty, Heinrich Heine University Düsseldorf, 40225 Düsseldorf, Germany
[2]Institute of Biochemistry and Molecular Biology I, Medical Faculty, Heinrich Heine University Düsseldorf, 40225 Düsseldorf, Germany
Full list of author information is available at the end of the article
Philip Böhler, Fabian Stuhldreier, Sebastian Wesselborg, Björn Stork contributed equally to this work.
Edited by G. Raschellà

SPRINGER NATURE CDDpress

remodelling of the network as well as removal and recycling of damaged mitochondria through mitophagy[1,4,5]. Excessive fission can be triggered by mitochondrial toxins that cause loss of $\Delta\Psi_m$, such as the protonophore carbonyl cyanide *m*-chlorophenyl hydrazone (CCCP)[6].

The $\Delta\Psi_m$ also plays a role in the mitochondrial buffering of cytosolic Ca^{2+}. Normally, the cytosol of a typical animal cell contains only a very low Ca^{2+} concentration ($[Ca^{2+}]_{cyt}$, ~0.1 µM), whereas the concentration of Ca^{2+} within the endoplasmic reticulum ($[Ca^{2+}]_{ER}$, > 100 µM) or outside the cell ($[Ca^{2+}]_{ext}$, > 1000 µM) is up to 10,000-fold higher[2]. In response to certain stimuli, Ca^{2+} channels in the ER and/or the plasma membrane open to release Ca^{2+} into the cytosol as a second messenger. Mitochondria contribute to removal of cytosolic Ca^{2+} by uptake into their matrix via $\Delta\Psi_m$-driven Ca^{2+} transporters. After that, a slow, regulated efflux moves the Ca^{2+} out of the matrix and into the cristae, which are folds in the IMM, from where it is slowly released and shuttled back to the ER[2,7–9]. A separate mechanism through which Ca^{2+} can cross the IMM is the mitochondrial permeability transition pore (mPTP), which can open irreversibly in response to severe mitochondrial stress. The mPTP directly connects the mitochondrial matrix with the cytosol to allow the free exchange of molecules up to 1.5 kDa in size, including Ca^{2+}. Irreversible mPTP opening leads to release of mitochondrial Ca^{2+}, loss of $\Delta\Psi_m$, swelling of the matrix and eventually mitochondrial outer membrane permeabilisation (MOMP)[10,11].

In animal cells, MOMP initiates apoptosis. Several proteins normally contained in the cristae attain a pro-apoptotic function if they pass the outer mitochondrial membrane (OMM) and are released into the cytosol. Among these proteins are cytochrome c (CYCS), SMAC (DIABLO) and OMI (HTRA2). Cytosolic CYCS becomes part of the caspase-activating apoptosome complex, while DIABLO and HTRA2 bind and inhibit the inhibitor of apoptosis proteins (IAPs), thus attenuating their inhibition of caspases[1]. MOMP can be caused either passively through rupture of the OMM, such as triggered by the mPTP, or actively through the formation of pores in the OMM by the pro-apoptotic proteins BAK and BAX, which can be induced in response to severe cellular stress[12].

A variety of mitochondrial toxins with different effects and molecular targets is known today[13]. Several of these toxins are natural products, such as the *Streptomyces*-derived ETC inhibitor antimycin A and the ATP synthase inhibitor oligomycin A.

Phomoxanthone A and B (PXA and PXB) are natural products named after the fungus *Phomopsis*, from which they were first isolated, and after their xanthonoid structure (Fig. S1). PXA is a homodimer of two acetylated tetrahydroxanthones symmetrically linked at C-4,4', whereas PXB is structurally almost identical but asymmetrically linked at C-2,4'. Both possess antibiotic activity against diverse organisms from all biological kingdoms. Originally described in 2001, PXA and PXB were tested against the protozoan *Plasmodium falciparum*, the Gram-positive *Mycobacterium tuberculosis*, and three animal cell lines. In all of these organisms, both PXA and PXB showed significant cytotoxic activity, with PXA being more toxic in every case[14]. A later study in different organisms produced similar results, showing that PXA inhibits the growth of the Gram-positive *Bacillus megaterium*, the alga *Chlorella fusca*, and the fungus *Ustilago violacea*[15].

We previously showed that PXA induces apoptosis in human cancer cell lines. Signs of apoptosis were observed as early as after 4 h of treatment with low micromolar doses of PXA[16,17]. However, the mechanism by which PXA causes apoptosis or cytotoxicity in general has never before been investigated.

The aim of this study was to elucidate the mechanism through which PXA exerts its toxicity. Following our initial results, we hypothesised that PXA directly affects the mitochondria and thus investigated its effects on the ETC, $\Delta\Psi_m$, ATP production, Ca^{2+} buffering, and mitochondrial morphology. It appears that PXA is a mitochondrial toxin that specifically affects the IMM, leading to loss of $\Delta\Psi_m$, ETC inhibition, Ca^{2+} efflux, mitochondrial fragmentation, cristae disruption, and finally to the release of mitochondrial pro-apoptotic factors.

Results

PXA induces Ca^{2+} release from an intracellular store

To determine how PXA induces apoptosis, we analysed its effect on cellular Ca^{2+} levels since ionic imbalance can be an apoptotic trigger. Treatment of Ramos cells with PXA resulted in a strong, steady increase of $[Ca^{2+}]_{cyt}$ (Fig. 1a). Interestingly, there was a delay of about 2–5 min between addition of PXA and increase in $[Ca^{2+}]_{cyt}$. Since this pattern of Ca^{2+} release is similar to that caused by the tyrosine phosphatase inhibitor pervanadate (VO_4^{3-}) (Fig. S2a), and since tyrosine phosphatase inhibition can induce apoptosis, we tested the effect of PXA on tyrosine phosphorylation. However, in contrast to pervanadate, we could not detect any effect (Fig. S2b). In a broader picture, PXA had no inhibitory effect on any of 141 protein kinases against which we tested it (Table S1).

We next tried to determine the origin of the released Ca^{2+}. Since PXA increases $[Ca^{2+}]_{cyt}$ even in the absence of extracellular Ca^{2+}, we tested if it releases Ca^{2+} from the ER. Using thapsigargin, which causes a net efflux of Ca^{2+} from the ER, we could induce an increase in $[Ca^{2+}]_{cyt}$ even after PXA-inducible Ca^{2+} stores were depleted

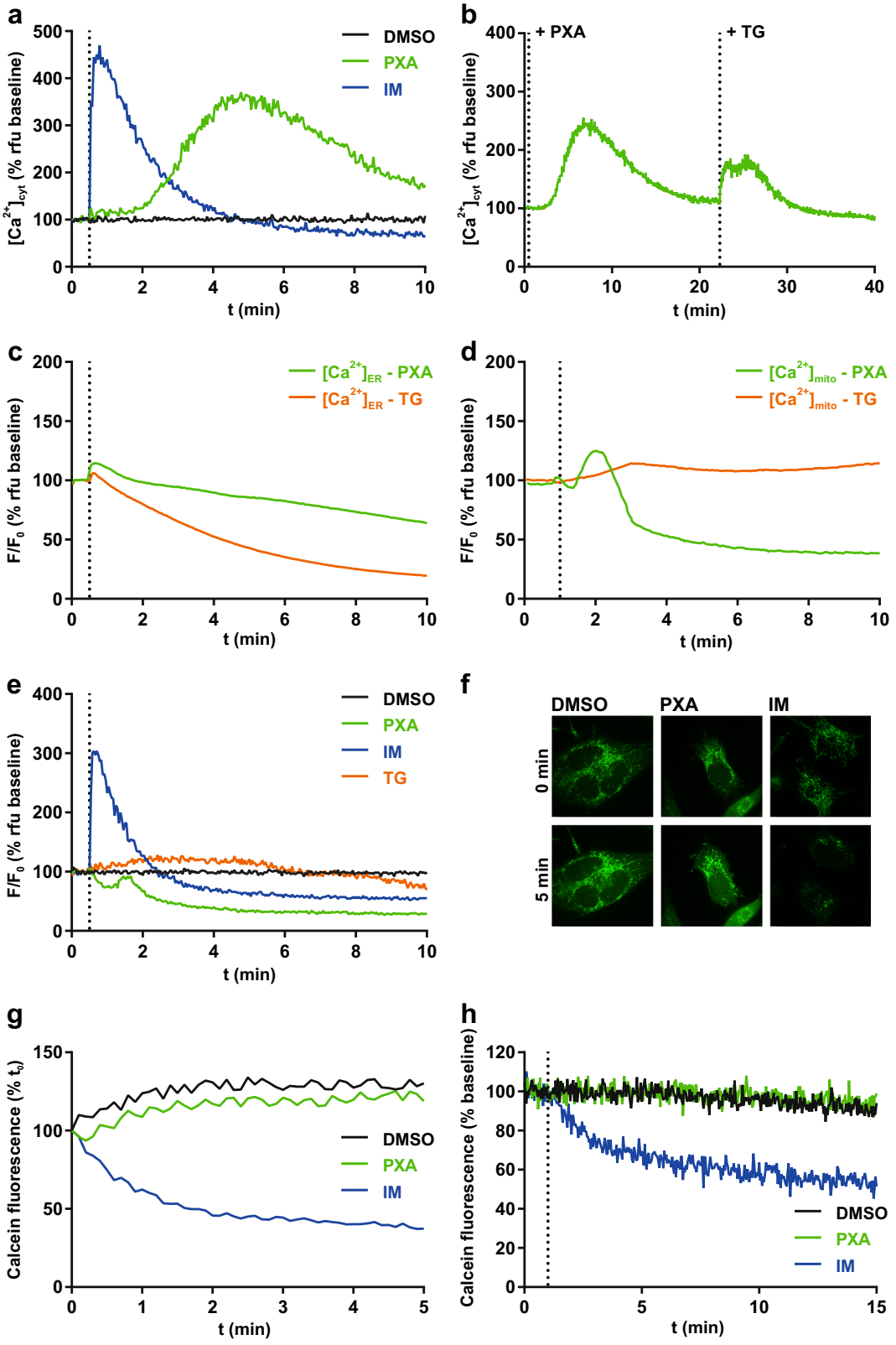

Fig. 1 (See legend on next page.)

Fig. 1 PXA causes an increase of $[Ca^{2+}]_{cyt}$ and a release of $[Ca^{2+}]_{mito}$ but not $[Ca^{2+}]_{ER}$. a Live measurement of the effect of PXA (10 µM) on $[Ca^{2+}]_{cyt}$ in Ramos cells, where DMSO (0.1% v/v) was used as vehicle control and ionomycin (IM; 2 µM) was used as positive control, and **b** live measurement of $[Ca^{2+}]_{cyt}$ after PXA followed by thapsigargin (TG; 10 µM). Measurements were performed by flow cytometry using the Ca^{2+}-sensitive fluorescent probe Fluo-4-AM (Ex 488 nm, Em 530 ± 30 nm) in the absence of extracellular Ca^{2+} by maintaining the cells in Krebs-Ringer buffer containing 0.5 mM EGTA during measurement. **c**, **d** Comparison of the effect of PXA (10 µM) and thapsigargin (TG; 1 µM) on either $[Ca^{2+}]_{ER}$ or $[Ca^{2+}]_{mito}$ as measured by the Ca^{2+}-sensitive fluorescent protein CEPIA targeted to the respective organelle in HeLa cells. All traces were normalised (F/F_0) where F_0 is the starting fluorescence of each trace. **e** Comparison of the effect of PXA (10 µM), ionomycin (IM; 2 µM), and thapsigargin (TG; 1 µM) on $[Ca^{2+}]_{mito}$ in Ramos cells stably transfected with the Ca^{2+}-sensitive ratiometric fluorescent protein mito-Pericam. DMSO (0.1% v/v) was used as vehicle control. F/F_0 is the ratio of fluorescence with excitation at 488 nm (high $[Ca^{2+}]$) to 405 nm (low Ca^{2+}]). **f**, **g** Live imaging and quantification of the effect of PXA (10 µM) on mPTP opening in HeLa cells as measured by mitochondrial calcein fluorescence using the calcein/cobalt quenching method. DMSO (0.1% v/v) was used as vehicle control and ionomycin (IM; 2 µM) was used as positive control. Mitochondrial calcein fluorescence was quantified. **h** Additional live measurement of the effect of PXA on mPTP opening in Ramos cells by the calcein/cobalt quenching method using flow cytometry

(Fig. 1b), suggesting that the Ca^{2+} released by PXA at least partially originates from a source other than the ER.

PXA induces Ca^{2+} release mainly from the mitochondria

To quantify the effect of PXA on Ca^{2+} stores, we used HeLa cells expressing CEPIA Ca^{2+} probes targeted to either the ER or the mitochondria. Although PXA provoked some Ca^{2+} release from the ER, it was much slower and weaker than that evoked by thapsigargin (Fig. 1c). Mitochondria, however, were quickly and severely depleted (Fig. 1d). This effect of PXA on mitochondrial Ca^{2+} was confirmed in Ramos cells, making use of the Ca^{2+} probe Pericam (Fig. 1e).

Mitochondrial Ca^{2+} release caused by PXA is independent from the mPTP

Large-scale Ca^{2+} efflux from the mitochondria can result from persistent opening of the mPTP. We thus tested whether PXA induces mPTP opening by using the cobalt/calcein method, comparing PXA to the mPTP inducer ionomycin (IM). While IM caused a strong decrease in mitochondrial calcein fluorescence as expected, PXA had no observable effect (Fig. 1f, g; Supplementary Movies S1–S3). Similar results were obtained by further live measurement using flow cytometry (Fig. 1h). In addition, we tested whether the mPTP inhibitor cyclosporin A (CsA) can prevent the mitochondrial Ca^{2+} release caused by PXA. We measured mitochondrial Ca^{2+} retention capacity in isolated mitochondria, comparing PXA to IM and CCCP. This was done in either normal isolated mitochondria or mitochondria loaded with Ca^{2+}, and in the presence of either CsA or its derivative cyclosporin H (CsH), which does not affect the mPTP (Fig. 2)[18]. While PXA caused a decrease in calcium green fluorescence, indicating Ca^{2+} release, under every condition, i.e., regardless of Ca^{2+} loading and also in the presence of CsA, IM had an observable effect only in loaded mitochondria, but also regardless of CsA. On the other hand, CCCP caused a release of Ca^{2+} only in the presence of CsH but not CsA, indicating that CCCP-induced Ca^{2+} release does indeed depend on the mPTP, unlike that induced by PXA. Taken together, these results indicate that PXA causes mitochondrial Ca^{2+} release largely independent from the mPTP.

PXA depolarises the mitochondria but does not uncouple cellular respiration

A change in $[Ca^{2+}]_{mito}$ likely correlates with changes in other mitochondrial ion gradients. Uptake of Ca^{2+} into the mitochondrial matrix is driven by $\Delta\Psi_m$. We thus analysed the effect of PXA on $\Delta\Psi_m$. Indeed, PXA caused immediate mitochondrial depolarisation similar to CCCP, both in whole cells and isolated mitochondria (Fig. 3a, b). The EC_{50} for PXA-induced loss of $\Delta\Psi_m$ in Ramos cells was determined to be 1.1 ± 0.3 µM (Fig. S3). The key contributor to $\Delta\Psi_m$ is ΔpH_m, which is maintained via cellular respiration by consumption of O_2. If the PXA-induced loss of $\Delta\Psi_m$ was caused by loss of ΔpH_m downstream of the ETC, as in case of CCCP, it would be accompanied by an increase in respiration to compensate for the loss. Therefore, we measured cellular O_2 consumption upon increasing concentrations of either PXA or CCCP. As expected, CCCP caused a dose-dependent increase in O_2 consumption. However, in contrast to CCCP, PXA caused no increase but rather a slight decrease in O_2 consumption (Fig. 3c). An overview of the kinetics of the effects of PXA on $[Ca^{2+}]_{cyt}$, $[Ca^{2+}]_{mito}$, O_2 consumption and $\Delta\Psi_m$ is presented in Fig. 3d.

PXA inhibits cellular respiration by disrupting the electron transport chain

Since PXA had a moderate inhibitory effect on cellular O_2 consumption under basal conditions, we next measured O_2 consumption after the respiration rate was first increased by CCCP. Here, treatment with PXA caused a strong decrease in O_2 consumption to levels below baseline (Fig. 4a). It thus appeared likely that PXA, unlike CCCP, is not an inducer but rather an inhibitor of cellular respiration and of the ETC. We, therefore, compared PXA to known ETC inhibitors: rotenone (complex I), thenoyltrifluoroacetone (TTFA; complex II), antimycin A (complex III), sodium azide (NaN_3; complex IV) and

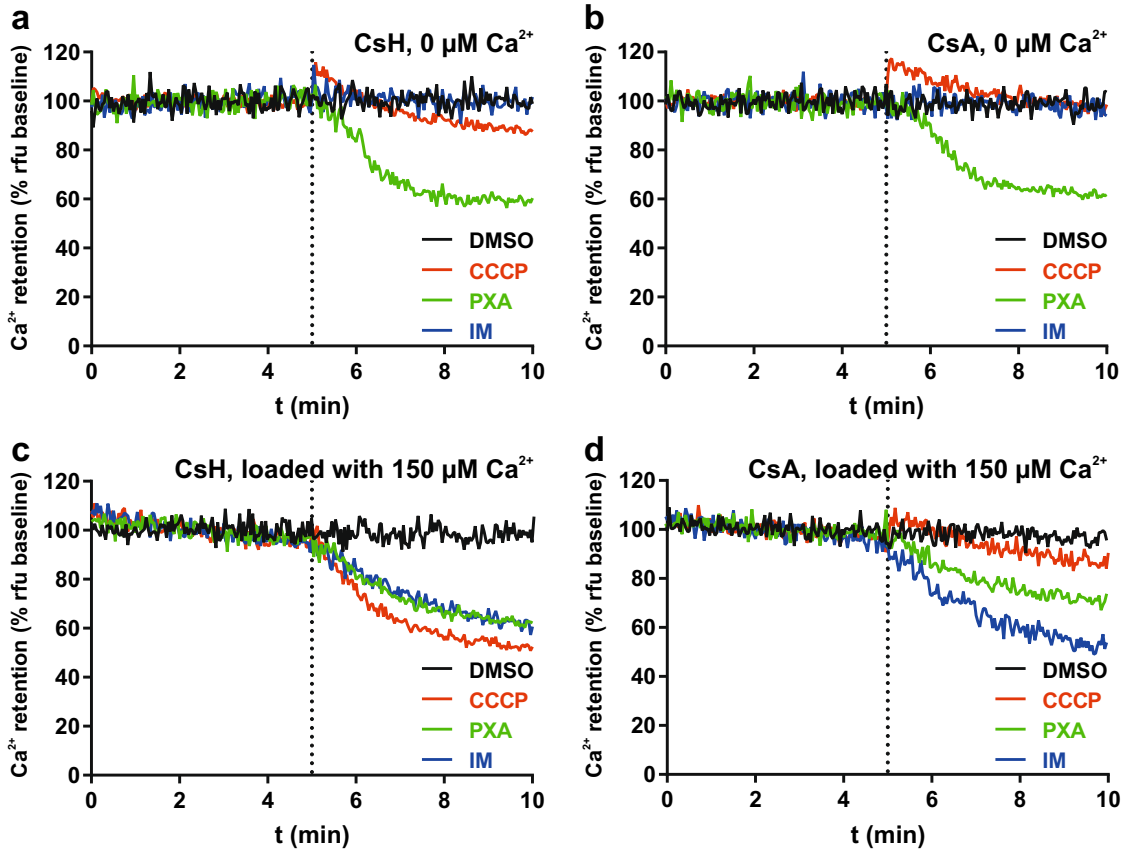

Fig. 2 Live measurement of the effect of PXA on mitochondrial Ca^{2+} retention capacity. Isolated mitochondria were stained with calcium green AM and maintained in the presence of either (**a**, **c**) CsH or (**b**, **d**) CsA, and fluorescence was measured either (**a**, **b**) directly after staining or (**c**, **d**) after first loading the mitochondria with 150 µM Ca^{2+}

oligomycin A (complex V / ATP synthase). In an O_2 consumption assay, PXA caused a strong decrease in cellular respiration, both after CCCP treatment and under basal conditions, similar to that caused by rotenone, antimycin A and azide (Fig. 4b). Oligomycin A expectedly inhibited respiration under basal conditions but not after CCCP treatment since CCCP uncouples respiration from ATP synthesis. TTFA did not have a significant effect, probably because complex II is not involved in respiration if complex I substrates are available[19].

Since a functional ETC is required for ATP synthesis by OXPHOS, we also compared PXA to known ETC inhibitors in this context. Indeed, PXA as well as all tested ETC inhibitors strongly reduced cellular ATP levels if galactose was the only available sugar and ATP had to be synthesised via OXPHOS instead of glycolysis (Fig. 4c). Thus assuming that PXA targets the ETC, we tried to determine if it specifically inhibits one of the ETC complexes. This experiment was performed in permeabilized cells, comparing PXA to rotenone. Succinate, which induces complex II-dependent respiration only if complex I is inhibited, alleviated rotenone-induced inhibition of O_2 consumption but had only a marginal effect in PXA-treated cells. In contrast, duroquinol, which induces complex III-dependent respiration, increased O_2 consumption in both PXA-treated as well as rotenone-treated cells back to levels before inhibition (Fig. 4d). These data suggest that PXA might either affect both complex I and II or the shuttling of electrons between complex I/II and III.

Comparison of PXA with other ETC inhibitors

While PXA inhibits the ETC as well as ATP synthesis, it differs from the other ETC inhibitors used in this study concerning its effects on Ca^{2+} and $\Delta\Psi_m$. Unlike PXA, neither CCCP nor any of the tested ETC inhibitors with the exception of antimycin A caused a noticeable release of Ca^{2+} (Fig. S4a), and that caused by antimycin A was much weaker and had an earlier but slower onset than the one caused by PXA. Similarly, while both CCCP and PXA induced a strong and immediate decrease in $\Delta\Psi_m$, none of the other ETC inhibitors except antimycin A had any effect on $\Delta\Psi_m$, and that of antimycin A was much slower and weaker (Fig. S4b). Since we previously

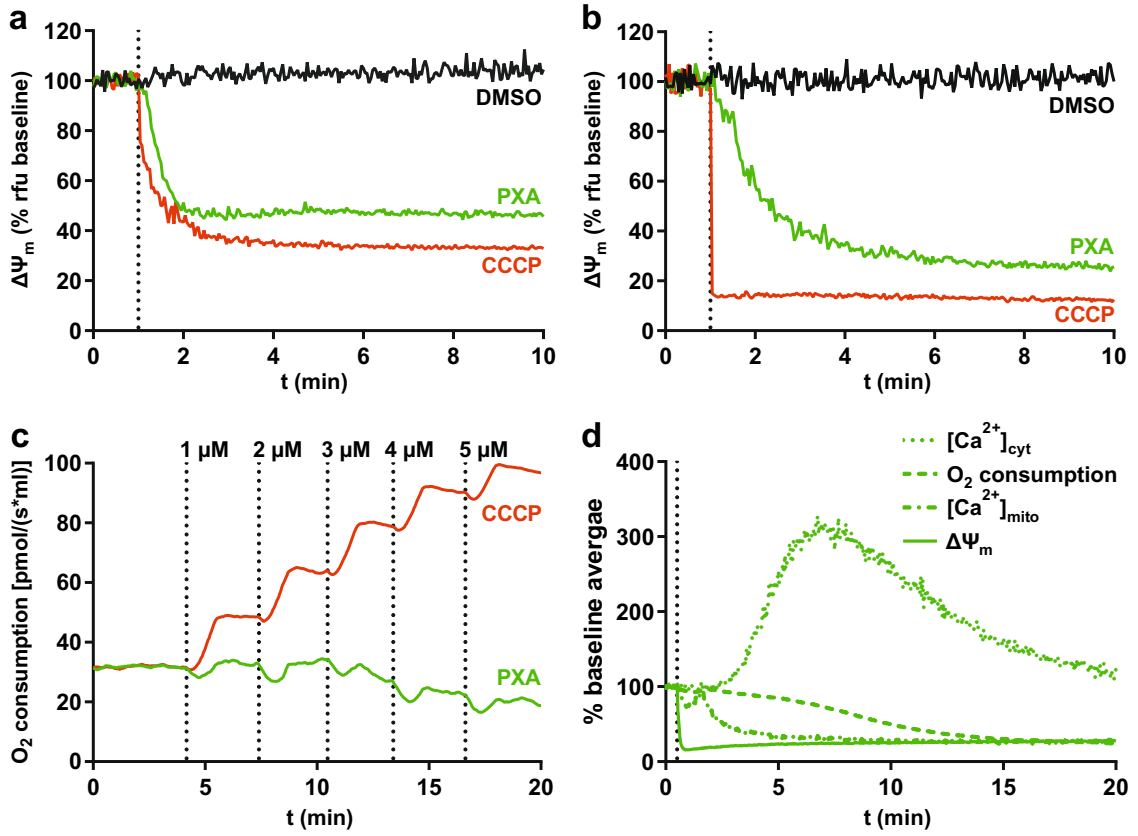

Fig. 3 PXA dissipates the mitochondrial membrane potential ($\Delta\Psi_m$) but does not increase cellular respiration. a Live measurement of the effect of PXA (10 µM) on $\Delta\Psi_m$ in Ramos cells. Measurements were performed by flow cytometry using the $\Delta\Psi_m$-sensitive fluorescent probe TMRE (Ex 488 nm, Em 575 ± 26 nm). A decrease in TMRE fluorescence corresponds to a decrease in $\Delta\Psi_m$. The protonophore carbonyl cyanide *m*-chlorophenyl hydrazone (CCCP; 10 µM) was used as positive control for mitochondrial depolarisation. **b** Live measurement of the effect of PXA (10 µM) $\Delta\Psi_m$ in isolated mitochondria. Measurements were performed by flow cytometry using the $\Delta\Psi_m$-sensitive fluorescent probe TMRM (Ex 488 nm, Em 575 ± 26 nm). The mitochondria were maintained in the presence of 1.6 µM CsH to prevent passive TMRM leakage. **c** Titration of PXA to determine the effect on cellular respiration in Ramos cells as measured by oxygen consumption. CCCP was used as positive control for increase of respiration. Measurement of extracellular [O_2] was performed using an oxygraph. **d** Comparison of the kinetics of the effects of PXA on $[Ca^{2+}]_{cyt}$ (as measured by Fluo-4-AM fluorescence), $[Ca^{2+}]_{mito}$ (as measured by mito-Pericam fluorescence), O_2 consumption (as measured by changes in extracellular [O_2]) and $\Delta\Psi_m$ (as measured by TMRE fluorescence). Graphs were partially adapted from other figures

showed that PXA is cytotoxic and induces apoptosis, we also compared it to CCCP, ETC inhibitors, IM (control for Ca^{2+} release) and staurosporine (control for cytotoxicity/apoptosis) in these regards. PXA, staurosporine and CCCP strongly induced apoptosis, while the ETC inhibitors and IM were much weaker inducers in Ramos cells and did not noticeably induce apoptosis at all in Jurkat cells (Fig. 5a, b). Dependency on OXPHOS for ATP synthesis, which considerably increased the toxicity of the ETC inhibitors, appeared to have no effect on the toxicity of PXA or staurosporine (Fig. 5c, d). These observations indicate that PXA probably causes cytotoxicity in general and apoptosis in particular not via its effects on the ETC, $\Delta\Psi_m$, or $[Ca^{2+}]_{mito}$, but rather that all of these events might have a common cause further upstream.

PXA causes irreversible cleavage of OPA1 mediated by OMA1 but not YME1L1

Several stress conditions including loss of $\Delta\Psi_m$ and low levels of ATP can induce cleavage of the IMM fusion regulator OPA1 by the protease OMA1 (ref. [20]). Additionally, OPA1 is also cleaved by the protease YME1L1, resulting in fragments of different size. We treated MEF cells deficient for either one or both of these proteases with either PXA or CCCP. We observed that PXA, like CCCP, caused stress-induced OPA1 cleavage that was dependent on OMA1, whereas expression of YME1L1 did not have any visible effect on PXA-induced OPA1 cleavage (Fig. 6a). Similarly to their effect in MEF cells, PXA and CCCP-induced cleavage of OPA1 in Ramos and Jurkat cells within minutes. Interestingly, and unlike CCCP, removal of PXA did not enable recovery of the

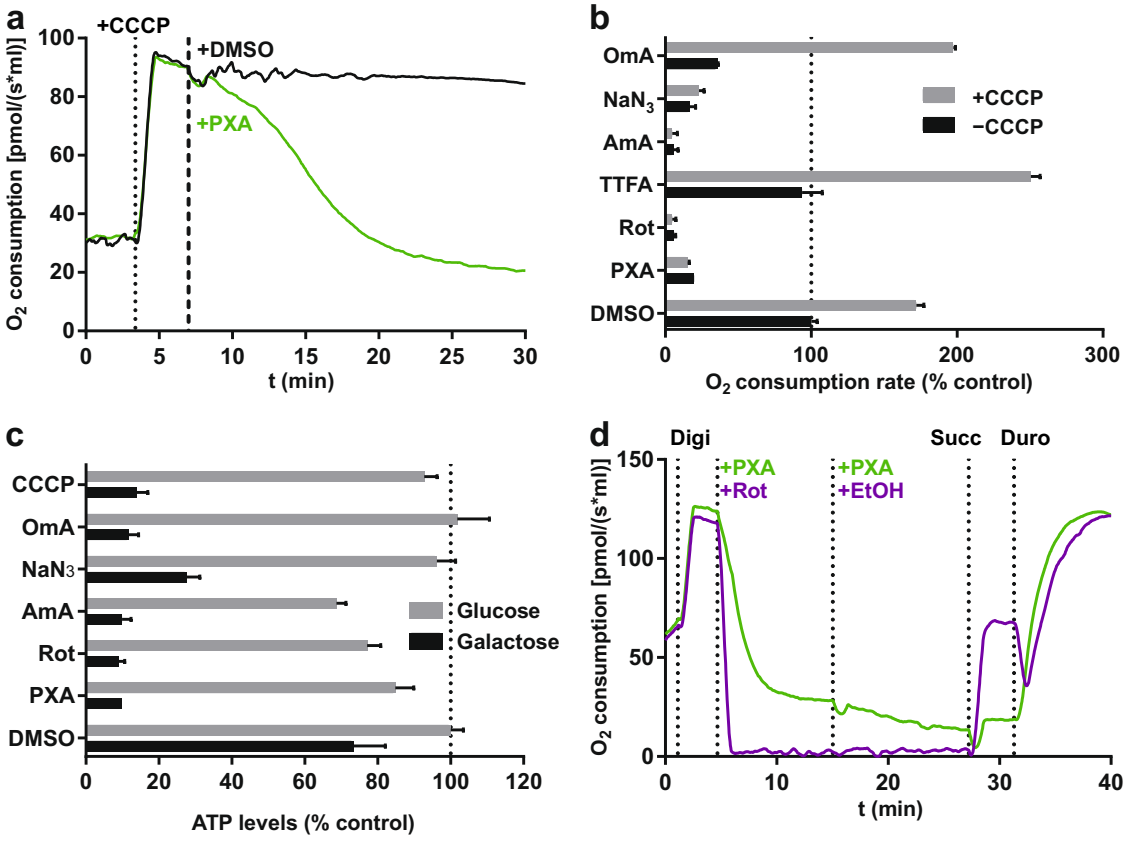

Fig. 4 Effect of PXA on electron transport chain and OXPHOS. a Live measurement of the effect of PXA on uncoupled cellular respiration in intact Ramos cells. Cells were first treated with 1 µM CCCP to uncouple respiration and then with either 10 µM PXA or 0.1% v/v DMSO (vehicle control) to test for inhibition. Measurement of extracellular [O_2] was performed using an oxygraph. **b** Comparative measurements of the effect of PXA and other compounds on basal and uncoupled respiration in Ramos cells. Respiration was uncoupled by CCCP (1 µM). PXA (10 µM) was compared to the complex-specific ETC inhibitors rotenone (Rot; complex I; 10 µM), thenoyltrifluoroacetone (TTFA; complex II; 10 µM), antimycin A (AmA; complex III; 10 µM), azide (NaN_3; complex IV; 1 mM) and oligomycin A (OmA; complex V; 10 µM). Measurement was performed in a microplate reader using the fluorescence-based *MITO-ID® Extracellular O2 Sensor Kit (High Sensitivity)* (Enzo). **c** Comparative measurements of the effect of PXA and other compounds on ATP levels in Ramos cells after 120 min of treatment. PXA (10 µM) was compared to complex-specific ETC inhibitors (see above) as well as CCCP (1 µM). Measurement was performed in a microplate reader using the luminescence-based *Mitochondrial ToxGlo™ Assay* (Promega). Cells were incubated in full growth medium containing either glucose or galactose as the only available sugar. Galactose alone forces the cells to resort exclusively to OXPHOS for ATP synthesis. **d** Live measurement of mitochondrial respiration in Ramos cells permeabilized by digitonin (Digi; 5 µg/ml). The effect of PXA (first 1 µM, then increased to 10 µM as indicated) was compared to that of the known complex I inhibitor rotenone (Rot; 1 µM). To specifically induce complex II and III of the electron transport chain, succinate (Succ; 10 mM) and duroquinol (Duro; 1 mM) were used, respectively. Measurement of extracellular [O_2] was performed using an oxygraph

long OPA1 forms (Fig. 6b). This prompted us to also investigate the effects of removal of PXA on cytotoxicity. Indeed, though PXA was about fivefold less toxic if removed after a few minutes, it still irreversibly primed the cells for death (Fig. 6c). It, thus, appears that at least some of the effects of PXA on the cells are irreversible.

PXA induces fragmentation of the inner but not of the outer mitochondrial membrane independently of OMA1, OPA1 and DRP1

Excessive processing of OPA1 by OMA1 changes mitochondrial cristae morphology, resulting in the release of pro-apoptotic factors such as CYCS and SMAC. We, therefore, investigated the effects of PXA on SMAC localisation and on recruitment of BAX to the OMM. We observed that PXA indeed induced recruitment of GFP-BAX to the mitochondria, with concurrent release of SMAC-mCherry into the cytosol, within about 2–3 h (Fig. 7a and Supplementary Movie S4; quantification shown in Fig. S5). OPA1 processing by OMA1 also prevents IMM fusion and, if excessive, results in mitochondrial fragmentation. Intriguingly, PXA caused rapid fragmentation of the mitochondrial network within minutes (Fig. 7b), and independent of the cells' OMA1 or YME1L1 status (Fig. 7c, left panels; Supplementary Movies S5–S7). The persistence of PXA-induced

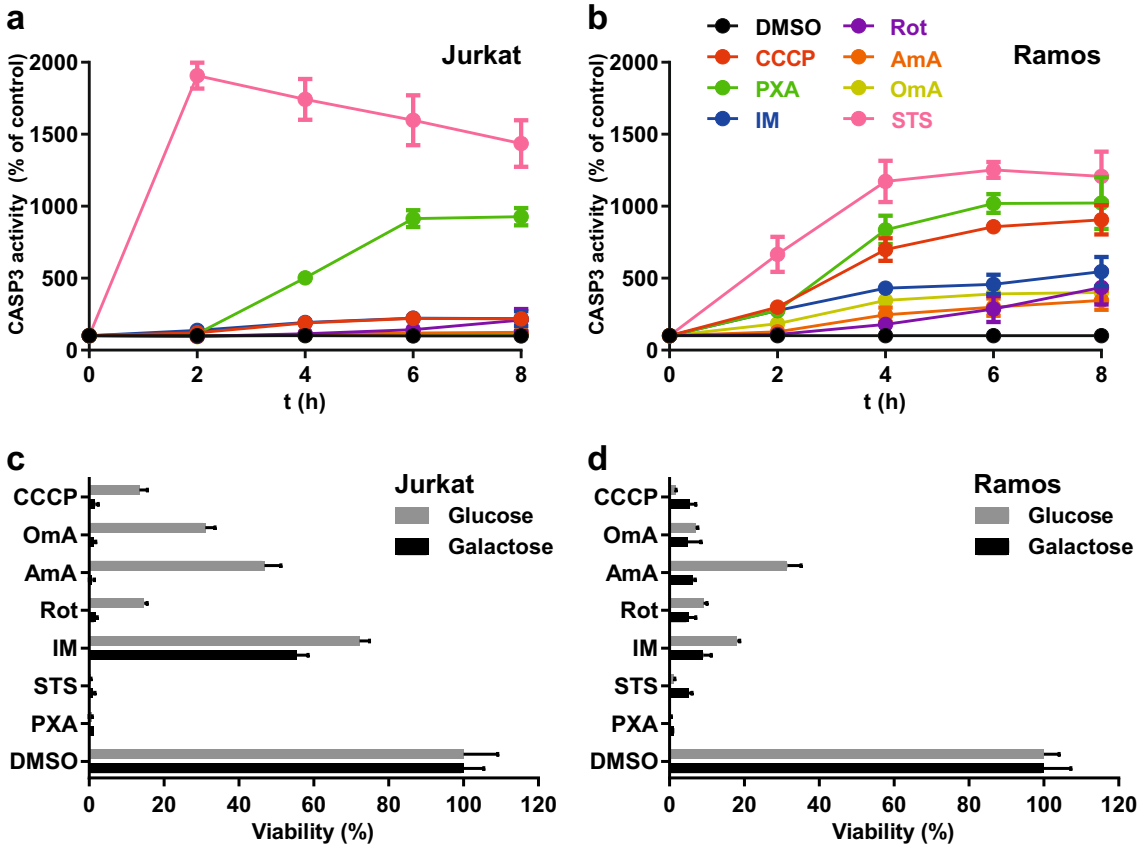

Fig. 5 Comparative measurements of the effect of PXA and other compounds on apoptosis induction and cytotoxicity in Jurkat and Ramos cells. PXA (10 µM) was compared to the protonophore carbonyl cyanide *m*-chlorophenyl hydrazone (CCCP; 10 µM), the Ca^{2+} ionophore ionomycin (IM; 10 µM), the apoptosis inducer staurosporine (STS; 10 µM), and the complex-specific ETC inhibitors rotenone (Rot; complex I; 10 µM), antimycin A (AmA; complex III; 10 µM) and oligomycin A (OmA; complex V; 10 µM). Data shown are the means of three independent experiments; error bars = SD. **a**, **b** Measurement of apoptosis induction based on cleavage of the pro-fluorescent CASP3 substrate Ac-DEVD-AMC, which results in release of AMC (Ex 360 nm, Em 450 nm), as an indicator of apoptosis. **c**, **d** Measurement of cytotoxicity after 24 h of treatment in the presence of either glucose or galactose as the only available sugar. Galactose alone forces the cells to resort exclusively to OXPHOS for ATP synthesis. Measurement was performed in a microplate reader using the MTT viability assay

mitochondrial fragmentation in OMA1-YME1L1 DKO cells indicates that this process is independent of OPA1 cleavage.

Mitochondrial fission is also regulated by the dynamin DRP1, which mediates OMM fission. We, thus, tested the effect of PXA on the mitochondrial morphology in DRP1-deficient MEF cells. Again, fragmentation was observed within minutes after treatment (Fig. 7c, right panel; Supplementary Movie S8). We next used dual staining of both the matrix (via HSP60) as well as the OMM (via TOMM20) to determine whether both or only one of these structures are affected by PXA. CCCP was used as a positive control for fragmentation. As expected, CCCP could not induce fragmentation in DRP1-KO cells, and in WT cells it induced fragmentation of both the IMM and OMM together (Fig. 8a, b). In contrast, in the WT cells treated with PXA, fragmentation was much stronger and resulted in smaller fragments. More intriguingly, in DRP1-KO cells treated with PXA, only the matrix appeared to have fragmented, whereas the OMM appeared to have shrunken around the matrix fragments but otherwise remained connected (Fig. 8a, b). This effect could also be observed in cells deficient for both DRP1 and OPA1 (Fig. S6) demonstrating that PXA acts independently of canonical regulators of mitochondrial fission. Finally, a close examination of the mitochondrial ultrastructure by transmission electron microscopy (TEM) revealed that PXA causes OMA1-independent disruption of mitochondrial matrix morphology, complete loss of cristae, and condensation of IMM structures at the OMM (Fig. 8c).

Taken together, our results show that PXA disturbs mitochondrial form and function in several ways. Some effects, such as the rapid inhibition of both $\Delta\Psi_m$ and the ETC at the same time, the delayed release of mitochondrial Ca^{2+}, and the fragmentation of the inner but not the

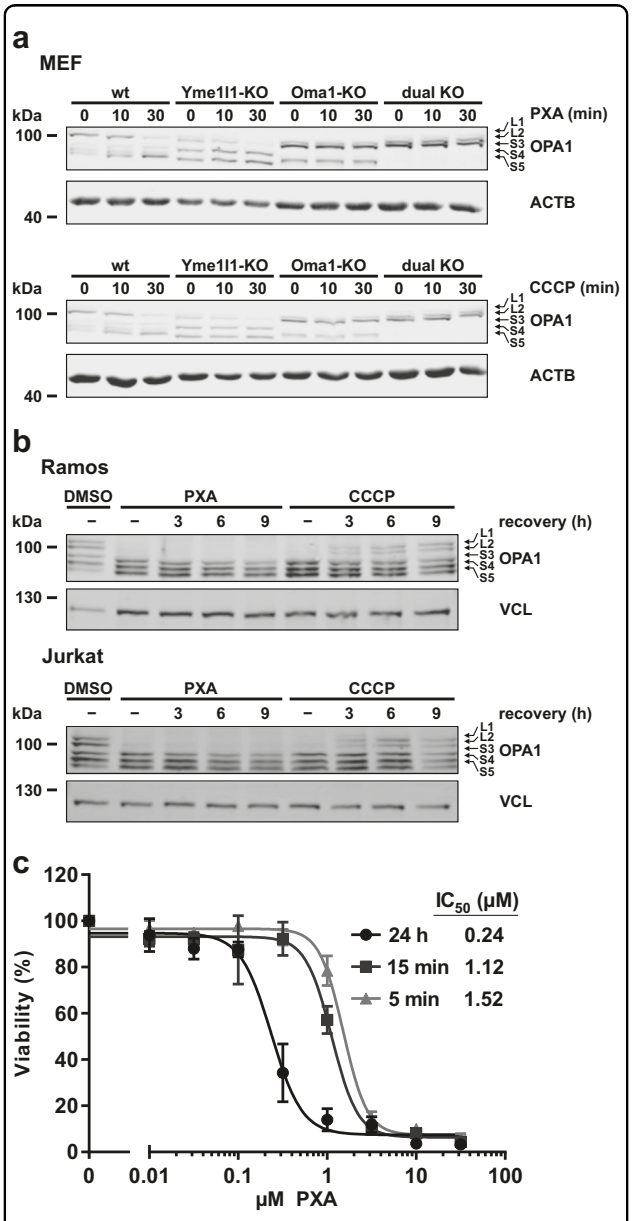

Fig. 6 PXA causes irreversible OMA1-dependent OPA1 processing and primes cells for death. a Effect of PXA (10 μM) and of the protonophore carbonyl cyanide *m*-chlorophenyl hydrazone (CCCP; 10 μM) on OPA1 processing in cells deficient for the OPA1 protease OMA1 and/or YME1L1. Proteins were detected by immunoblot. Beta-actin (ACTB) was used as loading control. **b** Examination of the recovery of long OPA1 forms in Ramos or Jurkat cells after 5 min of treatment with either PXA (10 μM) or CCCP (10 μM) followed by removal of the substance and a recovery period of up to 9 h. Proteins were detected by immunoblot. Vinculin (VCL) was used as loading control. **c** Comparison of the effect of PXA on cell viability if the stimulus was removed after treatment. Measurement was performed in a microplate reader using the MTT viability assay. Data shown are the means of three independent experiments; error bars = SD

outer mitochondrial membrane, are unique and indicate a mode of action that is distinct from all other compounds to which it was compared in this study.

Discussion

The mycotoxin PXA is a toxic natural product whose mechanism of action has so far remained elusive. We provide evidence that PXA disrupts mitochondrial function and causes IMM fragmentation and cristae disruption independently of DRP1 and OPA1, leading to the release of pro-apoptotic factors and ultimately to apoptosis.

PXA, just like CCCP, dissipates $\Delta\Psi_m$ within seconds. In the case of CCCP, respiration increases to compensate this, whereas PXA has the opposite effect and blocks respiration. Conversely, respiration is also blocked by ETC inhibitors, yet in contrast to PXA, these do not strongly affect $\Delta\Psi_m$. This suggests an entirely different mode of action for PXA. Additionally, unlike any of these compounds, PXA causes a strong mitochondrial release of Ca^{2+} and rapid fragmentation of the IMM but not the OMM.

Release of mitochondrial Ca^{2+} and loss of $\Delta\Psi_m$ can be results of persistent mPTP opening, yet we showed that PXA does not strongly affect the mPTP. Since mitochondrial ion gradients are interdependent through various antiporters that are generally linked to $\Delta\Psi_m$ (ref. [2]), one might assume that loss of $\Delta\Psi_m$ disturbs these gradients sufficiently to induce a net Ca^{2+} efflux from the mitochondria. For CCCP, contradictory results have been reported—in some cases it caused Ca^{2+} release[21], in some cases it did not[22]. We observed no effect of CCCP and most ETC inhibitors on $[Ca^{2+}]_{cyt}$, and in fact both ETC-deficient (ρ^0) mitochondria[23] and depolarised mitochondria[24] can still facilitate a net uptake of Ca^{2+}. It, thus, appears that the mitochondrial Ca^{2+} release induced by PXA is not necessarily a result of its effects on the ETC and $\Delta\Psi_m$, but rather that all of these effects might have a common cause.

The delay between addition of PXA and the first observable increase in $[Ca^{2+}]_{cyt}$ and decrease in $[Ca^{2+}]_{mito}$ contrasts with the immediate change in $\Delta\Psi_m$ (Fig. 3d). This discrepancy could possibly be explained by the hypothesis that mitochondria release Ca^{2+} mainly into the cristae, and that the cristae junctions may function as bottlenecks for mitochondrial Ca^{2+} transport[8,25]. Cristae junctions are regulated by OPA1, which is cleaved by OMA1 in response to mitochondrial stress, leading to cristae disruption[26]. We not only showed that OPA1 is irreversibly cleaved by OMA1 upon PXA treatment, but that PXA also causes cristae disruption independently of OMA1. Thus, PXA-induced cristae disruption might cause the release of Ca^{2+} from the cristae and thus eventually into the cytosol. In addition, irreversible cristae

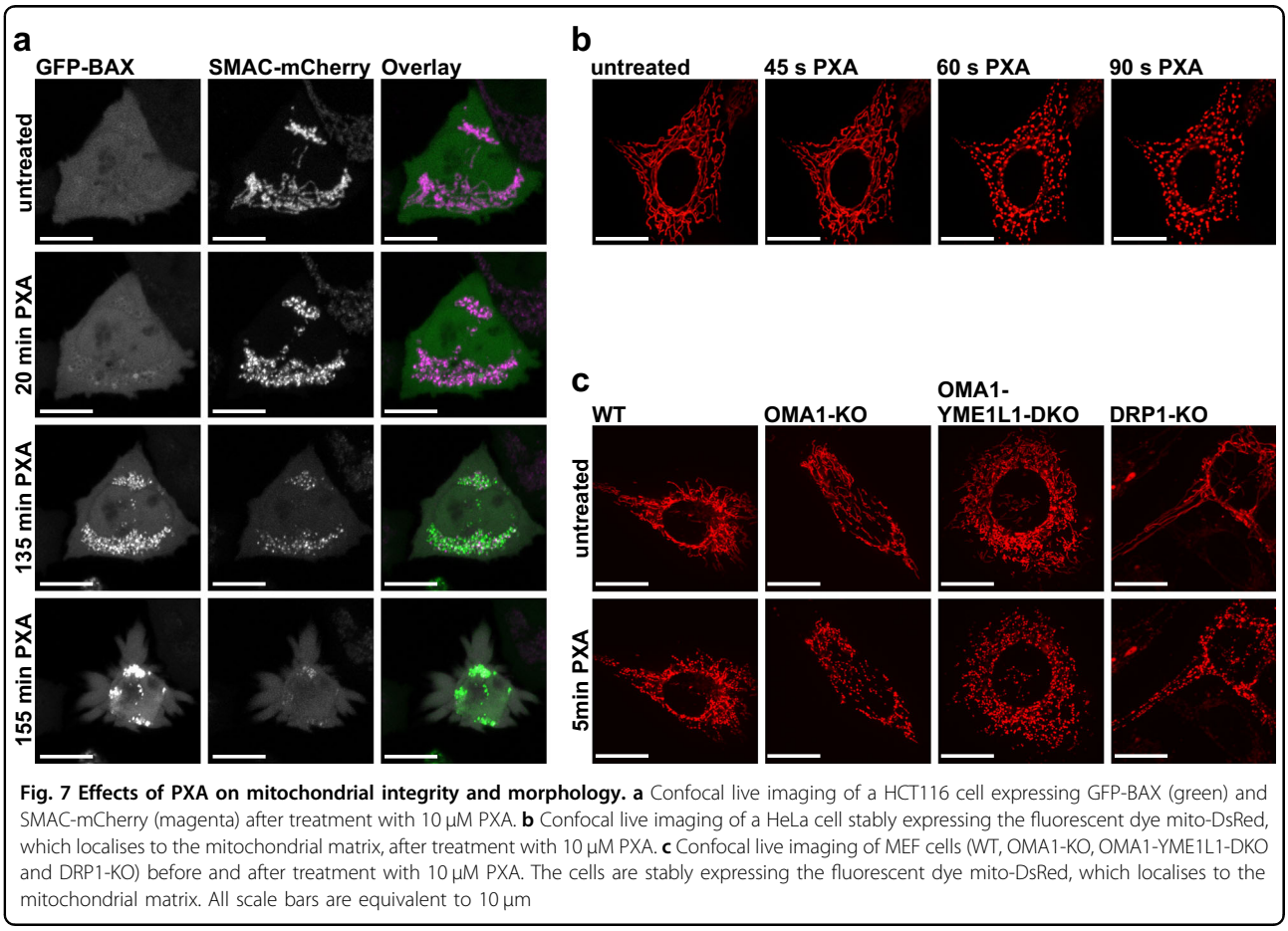

Fig. 7 Effects of PXA on mitochondrial integrity and morphology. a Confocal live imaging of a HCT116 cell expressing GFP-BAX (green) and SMAC-mCherry (magenta) after treatment with 10 µM PXA. **b** Confocal live imaging of a HeLa cell stably expressing the fluorescent dye mito-DsRed, which localises to the mitochondrial matrix, after treatment with 10 µM PXA. **c** Confocal live imaging of MEF cells (WT, OMA1-KO, OMA1-YME1L1-DKO and DRP1-KO) before and after treatment with 10 µM PXA. The cells are stably expressing the fluorescent dye mito-DsRed, which localises to the mitochondrial matrix. All scale bars are equivalent to 10 µm

disruption could well be a sufficient condition for the release of pro-apoptotic factors and thus the induction of apoptosis[26–28].

OPA1 also affects the fragmentation of mitochondrial network structures, which can be induced by PXA as well as CCCP. In the case of CCCP, this is commonly explained by the excessive activation of DRP1 after increased OPA1 processing by OMA1, which in turn is a response to several kinds of cellular stress including impaired ATP production and loss of $\Delta\Psi_m$ (ref. [4,6,20,29–32]). Since PXA dissipates $\Delta\Psi_m$, inhibits ATP production and consequently induces OMA1-mediated OPA1 cleavage, one might assume that it induces fragmentation via the same mechanism, yet we observed PXA-induced fragmentation events that were independent of DRP1, OMA1 and even OPA1.

Mitochondrial fragmentation independent of DRP1 is an unusual phenomenon but has been reported in cells undergoing apoptosis after pro-apoptotic factors had already been released[33,34]. In the case of PXA, however, fragmentation occurs within minutes after treatment, whereas pro-apoptotic factors are released only after several hours. In addition, whereas both the OMM and IMM are divided together during DRP1-dependent fragmentation, PXA can cause exclusive fragmentation of the IMM while the OMM remains intact. This is surprising since no active mechanism for exclusive IMM fission is known in higher eukaryotes, and there are only few reports documenting this phenomenon[6,35,36].

The OMA1-processed short OPA1 forms play a role in IMM fission and cristae morphology[5,29,35]. However, since PXA-induced IMM fragmentation and cristae disruption are independent of both OMA1 and OPA1, this implies that OPA1 may well be an IMM fission regulator but not necessarily a fission executor. It has been recently proposed that OPA1 is dispensable for cristae junction biogenesis but may still be required for cristae junction remodelling[37]. Our results suggest that excessive OPA1 processing may be sufficient but not necessary for inner membrane remodelling and cristae disruption and for the consequent release of pro-apoptotic factors.

The independence of PXA-induced IMM fragmentation from DRP1, OMA1 and OPA1, as well as its very fast onset, suggest that it might not depend on the fission/fusion machinery at all, but could work via a completely separate mechanism. Since no such mechanism is known

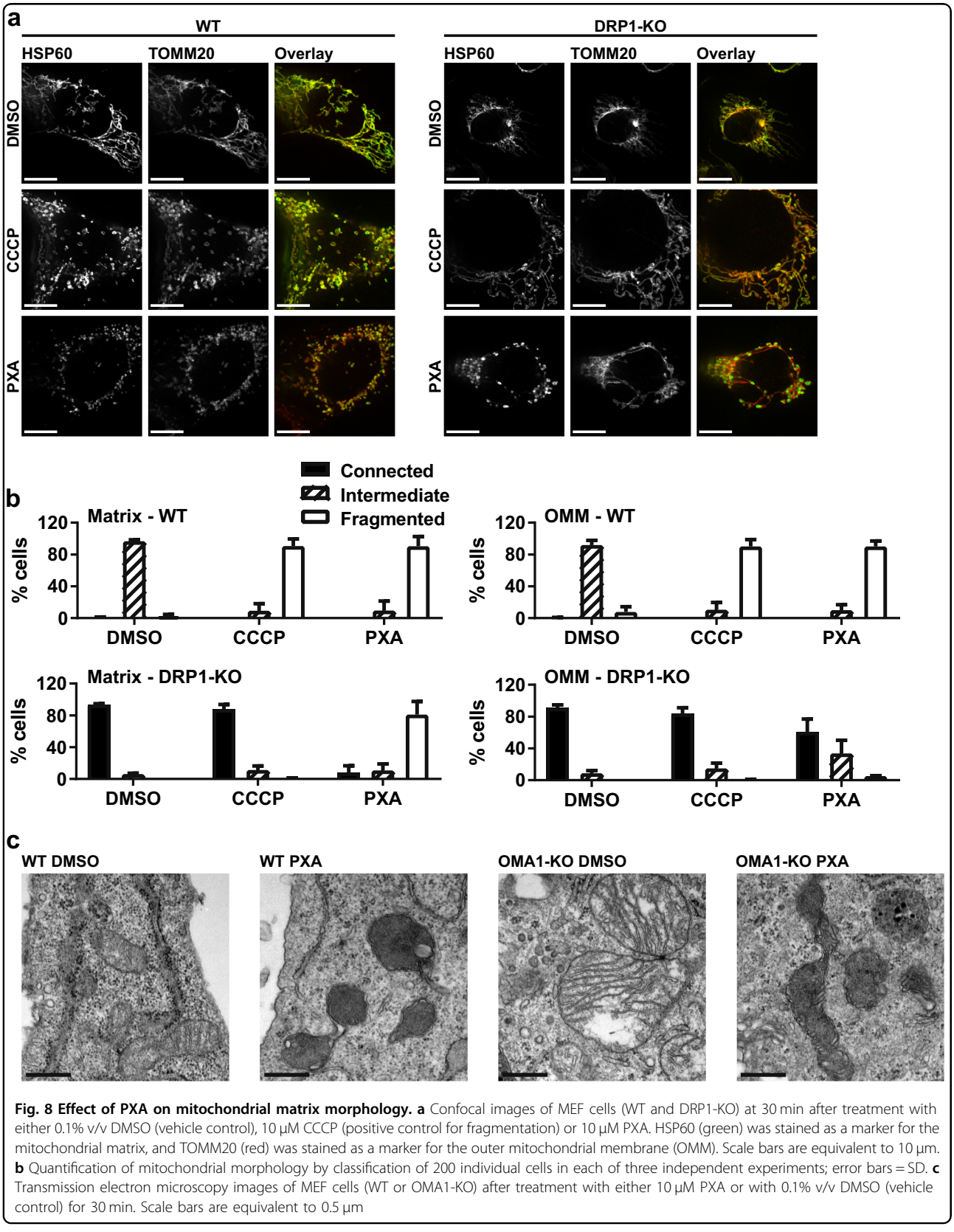

Fig. 8 Effect of PXA on mitochondrial matrix morphology. a Confocal images of MEF cells (WT and DRP1-KO) at 30 min after treatment with either 0.1% v/v DMSO (vehicle control), 10 µM CCCP (positive control for fragmentation) or 10 µM PXA. HSP60 (green) was stained as a marker for the mitochondrial matrix, and TOMM20 (red) was stained as a marker for the outer mitochondrial membrane (OMM). Scale bars are equivalent to 10 µm. **b** Quantification of mitochondrial morphology by classification of 200 individual cells in each of three independent experiments; error bars = SD. **c** Transmission electron microscopy images of MEF cells (WT or OMA1-KO) after treatment with either 10 µM PXA or with 0.1% v/v DMSO (vehicle control) for 30 min. Scale bars are equivalent to 0.5 µm

in higher eukaryotes, any attempt at explaining this effect remains speculative. One explanation could be a change in IMM fluidity or matrix architecture, causing an immediate and strong retraction of the IMM. This could result from interference with the tethering of IMM and OMM at mitochondrial contact sites. If this is the case, a possible mechanistic target of PXA could be the mitochondrial phospholipid cardiolipin, which is present almost exclusively in the IMM and especially at mitochondrial contact sites[38,39]. Cardiolipin serves as a membrane anchor for many proteins that are implicated in mitochondrial contact site formation, mitochondrial ultrastructure and the ETC, such as MIC27 (APOOL)[40,41], F_1F_O ATP synthase[41,42], CYCS[41], and ETC complexes III and IV[41,43,44]. A disruptive interaction between PXA and either cardiolipin or cardiolipin-binding proteins might thus explain several of the effects induced by PXA.

In summary, we identified PXA as a mitochondrial toxin with a mode of action distinct from known ETC inhibitors, OXPHOS uncouplers, and ionophores. Its effects, such as the rapid inhibition of both ETC and $\Delta\Psi_m$, the release of mitochondrial Ca^{2+}, and the induction of DRP1- and OPA1-independent cristae disruption and fission of the inner but not the outer mitochondrial membrane, might render it a useful tool in studying these phenomena. Further studies may reveal the molecular target of PXA and the mechanisms through which it induces mitochondrial Ca^{2+} release and IMM fission.

Material and methods

Cell lines and cell culture

Jurkat cells were obtained from DSMZ (#ACC-282). Ramos cells were kindly provided by Michael Engelke (Institute of Cellular and Molecular Immunology, University Hospital Göttingen, Göttingen, Germany). HeLa cells stably expressing mito-DsRed were kindly provided by Aviva M. Tolkovsky (Department of Clinical Neurosciences, University of Cambridge, England, UK) and have been described previously[45]. MEF cells deficient for OMA1 and/or YME1L1 as well as the corresponding wild-type cells were generated by Ruchika Anand and kindly provided by Thomas Langer (Institute for Genetics, University of Cologne, Germany) and have been described previously[29]. MEF cells deficient for DRP1 as well as the corresponding wild-type cells used for live imaging were kindly provided by Hiromi Sesaki (Department of Cell Biology, Johns Hopkins University, Baltimore, MD, USA) and have been described previously[33]. MEF cells deficient for DRP1 used for imaging of fixed cells were generated using the CRISPR/Cas9 system as described previously[46]. The DNA target sequence for the guide RNA was 5'-CAGTGGGAAGAGCTCAGTGC-3'. HCT116 cells were kindly provided by Frank Essmann (Interfaculty Institute of Biochemistry, Eberhard Karls University Tübingen, Germany). Transient expression of SMAC-mCherry and GFP-BAX was achieved by lipofection at 70–80% confluence using Lipofectamine 2000 (Life Technologies, Darmstadt, Germany). Cells were incubated with 0.15 µl Lipofectamine 2000, 50 ng pcDNA3-Smac(1-60)mCherry (Addgene ID 40880; this plasmid was kindly provided by Stephen Tait (Beatson Institute, University of Glasgow, Scotland, UK) and has been described previously[47]), and 50 ng pGFP-Bax (kindly provided by Nathan R. Brady, Department of Molecular Microbiology and Immunology, Johns Hopkins University, Baltimore, MD, USA) per well in glass bottom 8-well chambers (Ibidi, Planegg, Germany) for 16 h. HeLa cells used for Ca^{2+} measurements were cultured in Dulbecco's modified Eagle's medium supplemented with 10% fetal calf serum (FCS) and 4 mM L-glutamine, 100 U/ml penicillin and 100 µg/ml streptomycin at 37 °C and 5% CO_2. They were authenticated using autosomal STR profiling performed by the University of Arizona Genetics Core and they fully matched the DNA fingerprint present in reference databases. Cell lines stably expressing either mito-DsRed (except HeLa; see above) or ratiometric mito-Pericam were generated by retroviral transfection using the Platinum-E (Plat-E) packaging cell line (kindly provided by Toshio Kitamura, Institute of Medical Science, University of Tokyo, Japan) and the retroviral vectors pMSCVpuro-mito-DsRed1 (Addgene ID 87379) or pMSCVpuro-mito-Pericam (Addgene ID 87381). The medium used for the cultivation of Jurkat cells and Ramos cells was RPMI 1640 medium, and the medium used for cultivation of HCT116 cells was McCoy's 5A medium. All other cells were cultivated in high-glucose Dulbecco's Modified Eagle's medium (DMEM). All media were supplemented with 10% FCS, 100 U/ml penicillin, and 100 µg/ml streptomycin. All cell lines were maintained at 37 °C and 5% CO_2 in a humidity-saturated atmosphere.

Reagents

Phomoxanthone A was isolated and purified as described previously[16]. We found that PXA becomes unstable if dissolved in dimethyl sulfoxide (DMSO) and readily isomerises into the essentially non-toxic compound dicerandrol C (data not shown), in a process similar to the one previously described for the structurally related secalonic acids[48]. However, PXA is barely soluble in EtOH and not soluble in H_2O. Therefore, PXA was prepared in small lyophilised aliquots and only dissolved in DMSO immediately before usage.

The tyrosine phosphatase inhibitor pervanadate (VO_4^{3-}) was freshly prepared by mixing 30 mM sodium orthovanadate with 60 mM H_2O_2 in phosphate-buffered saline (PBS) and incubating at room temperature (RT) in the dark for 10 min; sodium orthovanadate was purchased from Sigma (Munich, Germany), #450243; IM from

Sigma, #I9657; thapsigargin (TG) from Sigma, #T9033; carbonyl cyanide *m*-chlorophenyl hydrazone (CCCP) from Sigma, #C2759; rotenone from Sigma, #45656; thenoyltrifluoroacetone (TTFA) from Sigma, #88300; antimycin A from Sigma, #A8674; sodium azide (NaN_3) from Sigma, #S2002; oligomycin A from Toronto Research Chemicals (Toronto, Canada), #O532970; staurosporine (STS) from LC Laboratories (Woburn, MA, USA), #9300. All cell culture reagents were purchased from Life Technologies, and all other reagents where no manufacturer is explicitly mentioned were purchased from Carl Roth GmbH (Karlsruhe, Germany).

Replicates and statistical analysis

Experiments were replicated at least three times, and representative data are shown. Error bars indicate standard deviation. All statistical analysis was performed using Prism v7.01 (GraphPad Software, La Jolla, CA, USA).

In vitro kinase activity screening

The effect of PXA on the activity of 141 protein kinases was assessed by the International Centre for Kinase Profiling (Dundee, Scotland, UK) using a radioactive filter binding assay with ^{33}P ATP[49,50].

Live measurement of $[Ca^{2+}]_{cyt}$ by Fluo-4-AM

Cells were stained by incubation in growth medium containing 1 µM Fluo-4-AM (Life Technologies; #F14201), 0.005% w/v Pluronic F-127 (Sigma, #540025), 10 mM HEPES and 5% v/v FCS at 30 °C. After 25 min, an equal volume of full growth medium was added, the temperature was increased to 37 °C, and the cells were incubated for another 10 min. After that, the cells were washed and resuspended in Krebs-Ringer buffer (10 mM HEPES pH 7.0, 140 mM NaCl, 4 mM KCl, 1 mM $MgCl_2$, 10 mM glucose) supplemented with 1 mM $CaCl_2$. The cells were kept at RT in the dark until measurement. Just before measurement, the cells were washed and resuspended in Krebs-Ringer buffer supplemented with 0.5 mM EGTA. Fluo-4-AM fluorescence was measured live using an LSRFortessa flow cytometer (BD, Franklin Lakes, NJ, USA) recording fluorescence in the FITC channel (Ex 488 nm, Em 530 ± 30 nm). For each sample, after at least 30 s of baseline measurement, the stimulus was added and measurement was continued for at least 10 min.

Live measurement of $[Ca^{2+}]_{mito}$ and $[Ca^{2+}]_{ER}$ by CEPIA

Measurements of $[Ca^{2+}]_{mito}$ and $[Ca^{2+}]_{ER}$ in HeLa single cells were performed as described previously[51,52], using the genetically-encoded Ca^{2+} indicators CEPIA3mt (Addgene ID 58219) and G-CEPIA1er (Addgene ID 58215), respectively, which were developed by Dr. M. Iino (The University of Tokyo, Japan)[53]. The constructs were introduced into HeLa cells utilising the X-tremeGENE HP DNA transfection reagent (Roche, Mannheim, Germany) according to the manufacturer's protocol. The $[Ca^{2+}]$ measurements were performed 48 h after transfection using a Zeiss Axio Observer Z1 Inverted Microscope equipped with a 20 × air objective and a high-speed digital camera (Axiocam Hsm, Zeiss, Jena, Germany). Changes in fluorescence were monitored in the GFP channel (Ex 480 nm, Em 520 nm). Extracellular Ca^{2+} was chelated with 3 mM EGTA, and PXA (10 µM) or thapsigargin (1 µM) were added as indicated on the figures. All traces were normalised (F/F_0) where F_0 is the starting fluorescence of each trace.

Live measurement of $[Ca^{2+}]_{mito}$ by ratiometric mito-Pericam

Ramos cells stably transfected with ratiometric mito-Pericam as described above were used for this measurement. Ratiometric mito-Pericam is a Ca^{2+}-sensitive fluorescent protein and was described previously[54,55]. An increase in $[Ca^{2+}]$ causes a shift of the Pericam excitation maximum from ~410 to ~495 nm while the emission peak remains at ~515 nm. Pericam fluorescence was measured live using an LSRFortessa flow cytometer recording fluorescence in both the FITC channel (Ex 488 nm, Em 530 ± 30 nm) and the AmCyan channel (Ex 405 nm, Em 525 ± 50 nm). For each sample, after at least 30 s of baseline measurement, the stimulus was added and measurement was continued for at least 10 min. The ratio of fluorescence with excitation at 488 to 405 nm was calculated.

Live measurement of mPTP opening by cobalt-calcein assay

This method was adapted from previously published protocols[10,18,56]. The cells were stained by incubation in Krebs-Ringer buffer supplemented with 1 mM $CaCl_2$, 1 mM $CoCl_2$, and 1 µM calcein-AM (Life Technologies, #65-0853-78) at 37 °C for 30 min. After that, the cells were washed and maintained in Krebs-Ringer buffer supplemented with 1 mM $CaCl_2$ and 1.6 µM cyclosporin H (CsH) to prevent passive efflux of calcein. For live measurement by confocal microscopy, imaging and quantification were performed using a Perkin Elmer Spinning Disc microscope with a 60× objective (oil-immersion and NA = 1.49) at an excitation wavelength of 488 nm. The videos were obtained at 1000 × 1000 pixel resolution with a Hamamatsu C9100 camera. Additional live measurement by flow cytometry was performed using an LSRFortessa flow cytometer recording fluorescence in the FITC channel (Ex 488 nm, Em 530 ± 30 nm). For each sample, after at least 30 s of baseline measurement, the stimulus was added and measurement was continued for at least 10 min.

Isolation of live mitochondria

Adherent cells were harvested by a cell scraper. All cells were pelletised by centrifugation at 600 rcf, resuspended in ice-cold mitochondria isolation buffer (210 mM mannitol, 70 mM sucrose, 1 mM K_2EDTA, 20 mM HEPES), and passed through a 23 G needle ten times. The resulting suspension was centrifuged at 600 rcf and the supernatant was transferred to a new tube and centrifuged at 6500 rcf and 4 °C for 15 min. The resulting mitochondrial pellet was resuspended in sodium-free mitochondrial respiration buffer MiR05 (0.5 mM EGTA, 3 mM $MgCl_2$, 60 mM lactobionic acid, 20 mM taurine, 10 mM KH_2PO_4, 20 mM HEPES, 110 mM D-sucrose, 0.1% w/v fatty-acid-free bovine serum albumin [BSA]) supplemented with 10 mM succinate and 5 mM malate.

Live measurement of mitochondrial Ca^{2+} retention capacity by calcium green

Live mitochondria isolated as described above were stained by incubation in MiR05 buffer supplemented with 10 mM succinate, 5 mM malate, and 1 µM calcium green AM (Life Technologies, #C3012) for 20 min on a shaker at 37 °C. Before measurement, the mitochondria were pelletised at 6500 rcf for 5 min, washed and resuspended in MiR05 supplemented with 10 mM succinate, 5 mM malate, and 5 µM of either CsH or CsA. In experiments where the mitochondria were loaded with Ca^{2+} before measurement, this was achieved by incubation in MiR05 additionally supplemented with 150 µM $CaCl_2$ on a shaker at 37 °C for 10 min after the first washing step and followed by a second washing step.

Measurement of mitochondrial membrane potential by TMRE and TMRM

For measurement in whole cells, the cells were stained by incubation in full growth medium containing 100 nM tetramethylrhodamine ethyl ester (TMRE; AAT Bioquest, Sunnyvale, CA, USA; #22220) and 10 mM HEPES at 37 °C in the dark for 15 min. After that, the cells were washed and resuspended in full growth medium containing 10 mM HEPES and were incubated at 37 °C in the dark for another 15 min. The cells were maintained at these conditions until measurement. For measurement in live mitochondria, these were isolated as described above, resuspended in sodium-free mitochondrial respiration buffer MiR05 supplemented with 10 mM succinate, 5 mM malat, and 1 mM ADP, stained with 50 nM tetramethylrhodamine methyl ester (TMRM; Life Technologies, #T668) at 37 °C for 15 min, and washed and resuspended in MiR05 additionally supplemented with 1.6 µM cyclosporin H (CsH) to prevent passive TMRM leakage. For live measurement, TMRE or TMRM fluorescence was measured using an LSRFortessa flow cytometer recording fluorescence in the PE channel (Ex 488 nm, Em 575 ± 26 nm). For each sample, after at least 30 s of baseline measurement, the stimulus was added and measurement was continued for at least 10 min. For the titration of the EC_{50} for mitochondrial depolarisation, TMRE fluorescence was measured using a Synergy Mx microplate reader (BioTek, Bad Friedrichshall, Germany) recording fluorescence at Ex 549 ± 9 nm, Em 575 ± 9 nm. TMRE fluorescence was measured right before and 10 min after addition of PXA. EC_{50} values were calculated using Prism v7.01.

Live O_2 respirometry measurements

This method was adapted from previously published protocols[19,57]. All measurements were performed using an OROBOROS Oxygraph-2k (Oroboros Instruments, Innsbruck, Austria). For measurement of total cellular respiration, intact cells (2×10^6 cells/ml) were used and maintained in full growth medium supplemented with 20 mM HEPES during measurement. For direct measurement of mitochondrial respiration, digitonin-permeabilised cells (2×10^6 cells/ml) were used and maintained in mitochondrial respiration buffer MiR05 during measurement. To induce respiration, 10 mM glutamate, 5 mM malate, 1 mM ADP, and 5 µg/ml digitonin were added. The following complex-specific ETC inducers were used: For complex II, 10 mM succinate (from Sigma, #S3674); for complex III, 1 mM tetramethylhydroquinone / duroquinol (from TCI Germany, Eschborn, Germany; #T0822); for complex IV, 50 µM tetramethyl-*p*-phenylenediamine (TMPD; from Sigma, #87890) supplemented with 200 µM ascorbate.

Fluorimetric O_2 consumption assay

This measurement was performed using the *MITO-ID® Extracellular O2 Sensor Kit (High Sensitivity)* (Enzo Life Sciences, Lörrach, Germany; #51045) according to manufacturer's instructions. Fluorescence was measured using a Synergy Mx microplate reader (Ex 340–400 nm, Em 630–680 nm; time-resolved fluorescence, delay time 30 µs, integration time 100 µs).

Measurement of cellular ATP levels

This measurement was performed using the *Mitochondrial ToxGlo™ Assay* (Promega, Mannheim, Germany; #G8000) according to manufacturer's instructions. Since most cancer cells prefer ATP synthesis by glycolysis over OXPHOS if glucose is present, this experiment was conducted in the presence of either glucose or galactose as the only available sugar, the latter of which reduces the net ATP yield of glycolysis to zero and forces the cells to resort to OXPHOS for ATP production[58,59].

Fluorimetric caspase-3 activity assay

Caspase-3 activity was measured as described previously[60]. Briefly, cells were harvested by centrifugation at

600 rcf and lysed with 50 µl of ice-cold lysis buffer (20 mM HEPES, 84 mM KCl, 10 mM, $MgCl_2$, 200 µM EDTA, 200 µM EGTA, 0.5% NP-40, 1 µg/ml leupeptin, 1 µg/ml pepstatin, 5 µg/ml aprotinin) on ice for 10 min. Cell lysates were transferred to a black flat-bottom microplate and mixed with 150 µl of ice-cold reaction buffer (50 mM HEPES, 100 mM NaCl, 10% sucrose, 0.1% CHAPS, 2 mM $CaCl_2$, 13.35 mM DTT, 70 µM Ac-DEVD-AMC). The kinetics of AMC release were monitored by measuring AMC fluorescence intensity (Ex 360 nm, Em 450 nm) at 37 °C in intervals of 2 min over a time course of 150 min, using a Synergy Mx microplate reader. The slope of the linear range of the fluorescence curves (Δrfu/min) was considered as corresponding to caspase-3 activity.

Measurement of cell viability by MTT assay

Cell viability was determined by the ability to convert the yellow MTT substrate (Roth, #4022) into a blue formazan product. MTT solution (5 mg/ml MTT in PBS) was added to cells to a final concentration of 1 mg/ml, and the cells were then incubated at 37 °C for 60 min and pelletised at 600 rcf. The supernatant was discarded and replaced with DMSO. After the formazan crystals were fully dissolved, absorption was measured (test wavelength 570 nm, reference wavelength 650 nm). Reference absorbance was subtracted from test absorbance. Cell-free medium samples were considered as having 0% viability and the average of the control samples was considered as having 100% viability. IC_{50} values were calculated using Prism v7.01.

Immunoblotting

Cells were harvested by centrifugation at 11,000 rcf in 4 °C for 10 s, quick-frozen in liquid nitrogen, thawed on ice, incubated in lysis buffer (20 mM Tris-HCl, 150 mM NaCl, 1% v/v Triton X-100, 0.5 mM EDTA, 1 mM Na_3VO_4, 10 mM NaF, 2.5 mM $Na_4P_2O_7$, 0.5% sodium deoxycholate, protease inhibitor (Sigma, #P2714)) for 30 min and vortexed repeatedly. The cell lysates were then cleared from cell debris by centrifugation at 20,000 rcf for 15 min. Sodium dodecyl sulfate-polyacrylamide gel electrophoresis and western blot were performed according to standard protocol. The antibodies used for protein detection were mouse anti-phospho-tyrosine (Merck-Millipore, Darmstadt, Germany; clone 4G10, #05-1050); rabbit anti-OPA1 (described previously[37]); mouse anti-ACTB (Sigma; clone AC-74, #A5316); and mouse anti-VCL (Sigma; clone hVIN-1, #V9131).

Confocal microscopy

Live imaging of HCT116 cells transiently expressing GFP-BAX and SMAC-mCherry was performed using a Zeiss LSM 710 ConfoCor3 microscope (Carl Zeiss, Jena, Germany) with a C-Apochromat × 40 N.A. 1.2 water immersion objective (Zeiss). Excitation light came from argon ion (488 nm) and DPSS (561 nm) lasers. The cells were maintained in full growth medium at 37 °C and 5% CO_2 during imaging. Images were recorded every 5 min and were processed with Fiji[61]. For each time frame, the standard deviation (SD) of the fluorescence intensity was measured for each channel. A low SD was considered as corresponding to homogenous distribution, whereas a high SD was considered as corresponding to accumulation.

Live imaging of HeLa cells stably expressing mito-DsRed was performed using a Cell Observer SD Dual Cam spinning disc confocal microscope (Zeiss) equipped with a C-Apochromat 63×, N.A. of 1.45 oil-immersion objective. Excitation light came from an argon ion (488 nm) and DPSS (561 nm) laser. The cells were maintained in full growth medium supplemented with 10 mM HEPES at 37 °C during imaging. Images were recorded every 5 s.

Live imaging of MEF cells stably expressing mito-DsRed was performed using a Perkin Elmer Spinning Disc microscope with a 60 × objective (oil-immersion and NA = 1.49) at an excitation wavelength of 561 nm. The videos were obtained at 1000 × 1000 pixel resolution with a Hamamatsu C9100 camera. The cells were maintained in full growth medium supplemented with 10 mM HEPES at 37 °C during imaging.

For imaging of fixed HeLa and MEF cells, the cells were seeded on glass coverslips and grown to 60–90% confluence prior to experiments. Cells were treated with either 10 µM PXA, 10 µM CCCP or 0.1% v/v DMSO for 30 min, and were fixed by incubation with pre-warmed 4% paraformaldehyde in PBS at 37 °C for 10 min. Coverslips were then washed once with PBS, followed by incubation with PBS supplemented with 0.5% Triton X-100 for 10 min at RT. The coverslips were washed three times for 3–5 min with PBS supplemented with 0.2% Tween-20 (PBS-T). The coverslips were then incubated at RT for 30 min with blocking buffer (PBS-T supplemented with 0.2% fish gelatin and 5% goat serum) in a humidified box, followed by 1 h incubation with primary antibodies (anti-HSP60 clone N-20, #sc-1052 and anti-TOMM20 clone FL-145, #sc-11415 both from Santa Cruz, Dallas, TX, USA) diluted in blocking buffer. The coverslips were then washed three times with PBS-T, and incubated with blocking buffer for 30 min before adding secondary antibodies (Alexa Fluor 488-labelled donkey anti-goat and Alexa Fluor 594-labelled donkey anti-rabbit). Immunofluorescence images were acquired with a Marianas spinning disc confocal microscope (Intelligent Imaging Innovations, Denver, CO, USA).

Transmission electron microscopy

TEM samples were fixed for a minimum of 4 h in 2.5% v/v glutaraldehyde (GA) and 4% w/v paraformaldehyde

(PFA) in 0.1 M cacodylate buffer (pH 7.4) at 4 °C. Then, samples were incubated in 1% osmium tetroxide in 0.1 M cacodylate buffer for 2 h. Dehydration was achieved using acetone (50%, 70%, 90% and 100%) and block contrast was applied (1% phosphotungstic acid/0.5% uranylacetate in 70% acetone). A SPURR embedding kit (Serva, Heidelberg, Germany) was used to embed samples, which were polymerised overnight at 70 °C, before cutting into 80 nm sections using an Ultracut EM UC7 (Leica, Wetzlar, Germany). Images were captured using an H600 TEM (Hitachi, Tokyo, Japan) at 75 kV.

Acknowledgements
We thank Michael Engelke for providing Ramos B lymphocytes, Hiromi Sesaki for providing wild-type and DRP1-KO MEFs, Frank Essmann for providing HCT116 cells, and Aviva M. Tolkovsky for providing mito-DsRed-expressing HeLa cells. We are furthermore indebted to Thomas Langer for providing wild-type, OMA1-KO, YME1L1 KO and OMA1/YME1L1 DKO MEFs. We thank Stephen Tait for providing the plasmid pcDNA3-Smac(1-60)mCherry, Nathan R. Brady for providing the plasmid pGFP-Bax, and Toshio Kitamura for providing Plat-E cells. This study was supported by the Deutsche Forschungsgemeinschaft STO 864/3-1, STO 864/4-1, STO 864/5-1 (to B.S.), GRK 2158 (to P.P., to S.W. and to B. S.), and SFB 974 Project B09 (to A.S.R.), the Research Committee of the Medical Faculty of the Heinrich Heine University Düsseldorf 22/2015 (to B.S.) and 02/2015 (to A.S.R and R.A.) and 37/2015 (to A.K.K), and the Düsseldorf School of Oncology (to S.W. and B.S.; funded by the Comprehensive Cancer Centre Düsseldorf/Deutsche Krebshilfe and the Medical Faculty of the Heinrich Heine University Düsseldorf).

Author details
[1]Institute of Molecular Medicine I, Medical Faculty, Heinrich Heine University Düsseldorf, 40225 Düsseldorf, Germany. [2]Institute of Biochemistry and Molecular Biology I, Medical Faculty, Heinrich Heine University Düsseldorf, 40225 Düsseldorf, Germany. [3]Institute of Pharmaceutical Biology and Biotechnology, Faculty of Mathematics and Natural Sciences, Heinrich Heine University Düsseldorf, 40225 Düsseldorf, Germany. [4]Institute of Anatomy I, Medical Faculty, Heinrich Heine University Düsseldorf, 40225 Düsseldorf, Germany. [5]Laboratory of Molecular and Cellular Signaling, Department of Cellular and Molecular Medicine, KU Leuven, 3000 Leuven, Belgium. [6]Center for Advanced Imaging, Faculty of Mathematics and Natural Sciences, Heinrich Heine University Düsseldorf, 40225 Düsseldorf, Germany. [7]Interfaculty Institute of Biochemistry, Eberhard Karls University Tübingen, 72076 Tübingen, Germany. [8]Department of Biological Chemistry, David Geffen School of Medicine at UCLA, Los Angeles, CA 90095, USA

Conflict of interest
The authors declare that they have no conflict of interest.

Supplementary Information accompanies this paper at (https://doi.org/10.1038/s41419-018-0312-8).

Received: 1 December 2017 Accepted: 4 January 2018
Published online: 19 February 2018

References

1. Vyas, S., Zaganjor, E. & Haigis, M. C. Mitochondria and Cancer. *Cell* **166**, 555–566 (2016).
2. Rizzuto, R., De Stefani, D., Raffaello, A. & Mammucari, C. Mitochondria as sensors and regulators of calcium signalling. *Nat. Rev. Mol. Cell Biol.* **13**, 566–578 (2012).
3. Nunnari, J. & Suomalainen, A. Mitochondria: in sickness and in health. *Cell* **148**, 1145–1159 (2012).
4. Mishra, P. & Chan, D. C. Metabolic regulation of mitochondrial dynamics. *J. Cell Biol.* **212**, 379–387 (2016).
5. Youle, R. J. & van der Bliek, A. M. Mitochondrial fission, fusion, and stress. *Science* **337**, 1062–1065 (2012).
6. van der Bliek, A. M., Shen, Q., Kawajiri, S. Mechanisms of mitochondrial fission and fusion. *Cold Spring Harb. Perspect. Biol.* **5**, a011072 (2013).
7. Demaurex, N., Poburko, D. & Frieden, M. Regulation of plasma membrane calcium fluxes by mitochondria. *Biochim. Biophys. Acta* **1787**, 1383–1394 (2009).
8. Palty, R. et al. NCLX is an essential component of mitochondrial Na+/Ca2+ exchange. *Proc. Natl Acad. Sci. USA* **107**, 436–441 (2010).
9. Jiang, D., Zhao, L. & Clapham, D. E. Genome-wide RNAi screen identifies Letm1 as a mitochondrial Ca2+/H+ antiporter. *Science* **326**, 144–147 (2009).
10. Bonora, M. et al. Comprehensive analysis of mitochondrial permeability transition pore activity in living cells using fluorescence-imaging-based techniques. *Nat. Protoc.* **11**, 1067–1080 (2016).
11. Rao, V. K., Carlson, E. A. & Yan, S. S. Mitochondrial permeability transition pore is a potential drug target for neurodegeneration. *Biochim. Biophys. Acta* **1842**, 1267–1272 (2014).
12. Chipuk, J. E. & Green, D. R. Dissecting p53-dependent apoptosis. *Cell Death Differ.* **13**, 994–1002 (2006).
13. Wallace, K. B. & Starkov, A. A. Mitochondrial targets of drug toxicity. *Annu. Rev. Pharmacol. Toxicol.* **40**, 353–388 (2000).
14. Isaka, M. et al. Phomoxanthones A and B, novel xanthone dimers from the endophytic fungus *Phomopsis* Species. *J. Nat. Prod.* **64**, 1015–1018 (2001).
15. Elsässer, B. et al. X-ray structure determination, absolute configuration and biological activity of phomoxanthone A. *Eur. J. Org. Chem.* **2005**, 4563–4570 (2005).
16. Rönsberg, D. et al. Pro-apoptotic and immunostimulatory tetrahydroxanthone dimers from the endophytic fungus *Phomopsis longicolla*. *J. Org. Chem.* **78**, 12409–12425 (2013).
17. Frank, M. et al. Phomoxanthone A - from mangrove forests to anticancer therapy. *Curr. Med. Chem.* **22**, 3523–3532 (2015).
18. Petronilli, V. et al. Transient and long-lasting openings of the mitochondrial permeability transition pore can be monitored directly in intact cells by changes in mitochondrial calcein fluorescence. *Biophys. J.* **76**, 725–734 (1999).
19. Salabei, J. K., Gibb, A. A. & Hill, B. G. Comprehensive measurement of respiratory activity in permeabilized cells using extracellular flux analysis. *Nat. Protoc.* **9**, 421–438 (2014).
20. Baker, M. J. et al. Stress-induced OMA1 activation and autocatalytic turnover regulate OPA1-dependent mitochondrial dynamics. *EMBO J.* **33**, 578–593 (2014).
21. de la Fuente, S., Fonteriz, R. I., de la Cruz, P. J., Montero, M. & Alvarez, J. Mitochondrial free [Ca(2+)] dynamics measured with a novel low-Ca(2+) affinity aequorin probe. *Biochem. J.* **445**, 371–376 (2012).
22. Hoth, M., Fanger, C. M. & Lewis, R. S. Mitochondrial regulation of store-operated calcium signaling in T lymphocytes. *J. Cell Biol.* **137**, 633–648 (1997).
23. de Andrade, P. B. et al. Diabetes-associated mitochondrial DNA mutation A3243G impairs cellular metabolic pathways necessary for beta cell function. *Diabetologia* **49**, 1816–1826 (2006).
24. Trenker, M., Malli, R., Fertschai, I., Levak-Frank, S. & Graier, W. F. Uncoupling proteins 2 and 3 are fundamental for mitochondrial Ca2+ uniport. *Nat. Cell Biol.* **9**, 445–452 (2007).
25. Fülöp, L., Szanda, G., Enyedi, B., Várnai, P. & Spät, A. The effect of OPA1 on mitochondrial Ca2+ signaling. *PLoS ONE* **6**, e25199 (2011).
26. MacVicar, T. & Langer, T. OPA1 processing in cell death and disease - the long and short of it. *J. Cell Sci.* **129**, 2297–2306 (2016).
27. Zick, M., Rabl, R. & Reichert, A. S. Cristae formation-linking ultrastructure and function of mitochondria. *Biochim. Biophys. Acta* **1793**, 5–19 (2009).
28. Scorrano, L. et al. A distinct pathway remodels mitochondrial cristae and mobilizes cytochrome c during apoptosis. *Dev. Cell* **2**, 55–67 (2002).
29. Anand, R. et al. The i-AAA protease YME1L and OMA1 cleave OPA1 to balance mitochondrial fusion and fission. *J. Cell Biol.* **204**, 919–929 (2014).
30. Head, B., Griparic, L., Amiri, M., Gandre-Babbe, S. & van der Bliek, A. M. Inducible proteolytic inactivation of OPA1 mediated by the OMA1 protease in mammalian cells. *J. Cell Biol.* **187**, 959–966 (2009).
31. Ishihara, N., Fujita, Y., Oka, T. & Mihara, K. Regulation of mitochondrial morphology through proteolytic cleavage of OPA1. *EMBO J.* **25**, 2966–2977 (2006).

32. Duvezin-Caubet, S. et al. Proteolytic processing of OPA1 links mitochondrial dysfunction to alterations in mitochondrial morphology. *J. Biol. Chem.* **281**, 37972–37979 (2006).
33. Wakabayashi, J. et al. The dynamin-related GTPase Drp1 is required for embryonic and brain development in mice. *J. Cell Biol.* **186**, 805–816 (2009).
34. Ishihara, N. et al. Mitochondrial fission factor Drp1 is essential for embryonic development and synapse formation in mice. *Nat. Cell Biol.* **11**, 958–966 (2009).
35. Suen, D. F., Norris, K. L. & Youle, R. J. Mitochondrial dynamics and apoptosis. *Genes Dev.* **22**, 1577–1590 (2008).
36. Labrousse, A. M., Zappaterra, M. D., Rube, D. A. & van der Bliek, A. M. *C. elegans* dynamin-related protein DRP-1 controls severing of the mitochondrial outer membrane. *Mol. Cell* **4**, 815–826 (1999).
37. Barrera, M., Koob, S., Dikov, D., Vogel, F. & Reichert, A. S. OPA1 functionally interacts with MIC60 but is dispensable for crista junction formation. *FEBS Lett.* **590**, 3309–3322 (2016).
38. van Meer, G. & de Kroon, A. I. Lipid map of the mammalian cell. *J. Cell Sci.* **124**, 5–8 (2011). (Pt 1).
39. Ardail, D. et al. Mitochondrial contact sites. Lipid composition and dynamics. *J. Biol. Chem.* **265**, 18797–18802 (1990).
40. Weber, T. A. et al. APOOL is a cardiolipin-binding constituent of the Mitofilin/MINOS protein complex determining cristae morphology in mammalian mitochondria. *PLoS ONE* **8**, e63683 (2013).
41. Planas-Iglesias, J. et al. Cardiolipin interactions with proteins. *Biophys. J.* **109**, 1282–1294 (2015).
42. Acehan, D. et al. Cardiolipin affects the supramolecular organization of ATP synthase in mitochondria. *Biophys. J.* **100**, 2184–2192 (2011).
43. Pfeiffer, K. et al. Cardiolipin stabilizes respiratory chain supercomplexes. *J. Biol. Chem.* **278**, 52873–52880 (2003).
44. Zhang, M., Mileykovskaya, E. & Dowhan, W. Gluing the respiratory chain together. Cardiolipin is required for supercomplex formation in the inner mitochondrial membrane. *J. Biol. Chem.* **277**, 43553–43556 (2002).
45. Bampton, E. T. W., Goemans, C. G., Niranjan, D., Mizushima, N. & Tolkovsky, A. M. The dynamics of autophagy visualised in live cells: from autophagosome formation to fusion with endo/lysosomes. *Autophagy* **1**, 23–36 (2014).
46. Ran, F. A. et al. Genome engineering using the CRISPR-Cas9 system. *Nat. Protoc.* **8**, 2281–2308 (2013).
47. Tait, S. W. et al. Resistance to caspase-independent cell death requires persistence of intact mitochondria. *Dev. Cell* **18**, 802–813 (2010).
48. Qin, T., Iwata, T., Ransom, T. T., Beutler, J. A. & Porco, J. A. Jr. Syntheses of dimeric tetrahydroxanthones with varied linkages: Investigation of "Shape-shifting" properties. *J. Am. Chem. Soc.* **137**, 15225–15233 (2015).
49. Hastie, C. J., McLauchlan, H. J. & Cohen, P. Assay of protein kinases using radiolabeled ATP: a protocol. *Nat. Protoc.* **1**, 968–971 (2006).
50. Bain, J. et al. The selectivity of protein kinase inhibitors: a further update. *Biochem. J.* **408**, 297–315 (2007).
51. Vervloessem, T., Ivanova, H., Luyten, T., Parys, J. B., Bultynck, G. The selective Bcl-2 inhibitor venetoclax, a BH3 mimetic, does not dysregulate intracellular Ca2+ signaling. *Biochim. Biophys. Acta* **1864**, 968–976 (2017).
52. Bittremieux, M. et al. DPB162-AE, an inhibitor of store-operated Ca2+ entry, can deplete the endoplasmic reticulum Ca2+ store. *Cell Calcium* **62**, 60–70 (2017).
53. Suzuki, J. et al. Imaging intraorganellar Ca2+ at subcellular resolution using CEPIA. *Nat. Commun.* **5**, 4153 (2014).
54. Nagai, T., Sawano, A., Park, E. S. & Miyawaki, A. Circularly permuted green fluorescent proteins engineered to sense Ca2+. *Proc. Natl Acad. Sci. USA* **98**, 3197–3202 (2001).
55. Filippin, L. et al. Improved strategies for the delivery of GFP-based Ca2+ sensors into the mitochondrial matrix. *Cell Calcium* **37**, 129–136 (2005).
56. Petronilli, V., Penzo, D., Scorrano, L., Bernardi, P. & Di Lisa, F. The mitochondrial permeability transition, release of cytochrome c and cell death. Correlation with the duration of pore openings in situ. *J. Biol. Chem.* **276**, 12030–12034 (2001).
57. Kuznetsov, A. V. et al. Analysis of mitochondrial function in situ in permeabilized muscle fibers, tissues and cells. *Nat. Protoc.* **3**, 965–976 (2008).
58. Warburg, O. On the origin of cancer cells. *Science* **123**, 309–314 (1956).
59. Marroquin, L. D., Hynes, J., Dykens, J. A., Jamieson, J. D. & Will, Y. Circumventing the Crabtree effect: replacing media glucose with galactose increases susceptibility of HepG2 cells to mitochondrial toxicants. *Toxicol. Sci.* **97**, 539–547 (2007).
60. Czugala, M. et al. Efficient and safe gene delivery to human corneal endothelium using magnetic nanoparticles. *Nanomedicine (Lond.)* **11**, 1787–1800 (2016).
61. Schindelin, J. et al. Fiji: an open-source platform for biological-image analysis. *Nat. Methods* **9**, 676–682 (2012).

Manuscript "Phomoxanthone A − from mangrove forests to anticancer therapy"

Frank M, Niemann H, Böhler P, Stork B, Wesselborg S, Lin W, Proksch P. *Current Medicinal Chemistry* (2015) **22**:3523, doi: 10.2174/0929867322666150716115300

Send Orders for Reprints to reprints@benthamscience.ae

Current Medicinal Chemistry, **2015**, *22,* **3523-3532**

Phomoxanthone A - From Mangrove Forests to Anticancer Therapy

Marian Frank[1], Hendrik Niemann[1], Philip Böhler[2], Björn Stork[2], Sebastian Wesselborg[2], Wenhan Lin[3] and Peter Proksch[1,*]

[1]*Institute of Pharmaceutical Biology and Biotechnology, Heinrich-Heine University, 40225 Duesseldorf, Germany;* [2]*Institute of Molecular Medicine, University Hospital, 40225 Duesseldorf, Germany;* [3]*National Research Laboratories of Natural and Biomimetic Drugs, Peking University, Health Science Center, 100083 Beijing, People's Republic of China*

Abstract: Mangrove associated endophytes are treasure chests for bioprospecting especially in light of the need for new anticancer leads that are necessary to overcome drug resistance of cancer cells. This review highlights the potent anti-tumour compound phomoxanthone A (PXA), which represents a tetrahydroxanthone atropisomer derived from the mangrove-associated fungus *Phomopsis longicolla*. PXA displayed strong anti-tumour activity when tested against a panel of solid (including cisplatin resistant) tumour cell lines or of blood cancer cell lines with IC_{50} values in the submicromolar range whereas it was up to 100 folds less active against peripheral blood mononuclear cells (PBMC) from healthy donors. The anti-tumour activity of PXA was demonstrated to be due to an induction of caspase 3 dependent apoptosis. At the same time PXA was shown to activate immune cells such as murine T-lymphocytes, NK cells and macrophages which might help in fighting resistance during cancer chemotherapy. Structure activity studies that involved several naturally occurring as well as semisynthetic derivatives of PXA indicated the position of the biaryl linkage and the acetyl substituents as structural features that are important for the activity of this natural product.

Keywords: Anticancer therapy, apoptosis, atropisomerism, endophytic fungi, immunostimulation, mangroves, polyketide, tetrahydroxanthone.

1. INTRODUCTION

1.1. Mangrove Forests - A Unique Stress Prone Habitat

Mangroves are swamps of the intertidal zone in (sub)tropical coastal regions that are predominantly colonized by trees [1]. By definition five characteristics determine a *true mangrove tree*: (i) exclusive occurrence in the intertidal zone; (ii) taxonomic isolation from terrestrial relatives (at least to the generic level); (iii) populations composed of individuals with insular stands; (iv) morphological adaptation, e.g. aerial roots or vivipary; and (v) physiological adaptation mechanisms such as salt exclusion, secretion and accumulation [2]. Salt exclusion is established by salt-excreting glands in the leaves, which are indispensable for the plant as the typical seawater salinity of mangrove habitats ranges from 17.0 - 36.4% [3]. The latter properties affiliate mangrove trees to the group of halophytes. Temperature forms another extreme of the mangrove habitat. Commonly, the average air temperature of the coldest month is found higher than 20 °C with an amplitude of maximum 10 °C [4, 5] whereas temperatures of the warm season may exceed 40 °C. Limitations in oxygen and nutrient supply, a high tidal range alternated with periods of drought and excessively high light exposure are further stress factors that typically confront mangrove trees [6]. In these harsh habitats mangroves play a crucial role in coastal stabilization and nutrient fixation. Additionally, they provide nurseries for juvenile fish [7]. In their warm and moist habitat mangrove plants are confronted with a plethora of invasive microbial plant pathogens. In order to guarantee survival Mangrove plants have evolved highly effective antimicrobial chemical defense mechanisms [3]. It is remarkable that opportunistic plant endophytes such as fungi, which inhabit these plants in often complex

*Address correspondence to this author at the Department of Pharmaceutical Biology and Biotechnology, Faculty of Pharmacy, Heinrich-Heine University, 40225 Duesseldorf, Germany;
Tel: +49-221-81-14173; Fax: +49-221-81-11923;
E-mail: proksch@uni-duesseldorf.de

1875-533X/15 $58.00+.00

communities [8], withstand this effective chemical barrier. Structurally diverse defense metabolites apparently have yielded a selection of unique endophytes that have evolved effective escape mechanisms against the plants' chemical defense. On the other hand it may be assumed that endophytes contribute to the ecological success of Mangrove plants as frequently shown for other plant-endophyte associations [9-11]. The highly active and diverse microbial communities living in association with the host plant [8] which have been shaped by co-evolution strongly contribute to the evolutionary success of mangrove trees, which is essential for their survival in this extreme habitat. Both, Mangrove plants and their associated endophytes represent treasure chests for bioprospecting due to the occurrence of structurally unusual bioactive metabolites [12-14].

1.2. Chemistry of the Mangrove Microbiome

Mangrove associated endophytes are highly diverse and include actinomycetes, bacteria, fungi, cyanobacteria, microalgae and protozoa [8]. Among these different phylogenetic groups bacteria and fungi are by far the most abundant phyla contributing approximately 91% of the total microbial biomass known from mangrove trees [15]. Nevertheless recent estimations state that more than 95% of the endophyte community of Mangroves remains unknown [15] leaving a broad spectrum of metabolites and producing endophytes undiscovered for future investigations. Among the above mentioned groups of Mangrove endophytes, fungi are not only the most abundant ones with regard to biomass production, but also with regard to their secondary metabolites that have so far shown the highest hit rate during bioprospecting [16].

Geographical hotspots of Mangrove habitats are found along the coastlines of the Indian, Pacific and Atlantic Oceans [17]. The South China Sea e.g. and in particular the mangrove forests at the coastline of the Chinese Island Hainan represent an exceptional fruitful source for bioprospecting as indicated by the rise of publications devoted to this topic that have appeared in the recent years [18-22]. Investigations of Mangrove derived endophytic fungi from this region have so far yielded numerous active natural products such as cytotoxic terpenoids [20, 23] and peptides [18], antibacterial fatty acid glycosides [19], protein kinase inhibiting decalactones [21] and polyphenols with anti-HCV activities isolated from a mangrove plant [22]. In addition, cytotoxic furanocumarins [24] and naphtopyrones [25] have been found in Mangrove endophytes from this most southern Chinese province. Interestingly, also flavonoids, which are rarely described as fungal secondary metabolites, have been reported from an endophytic *Fusarium* strain [26]. In spite of the various groups of compounds encountered in these endophytes polyketides are by far the most dominant class of natural products. Out of 464 new metabolites reported between January 2011-December 2013 from Mangrove endophytes 258 compounds represent polyketides [8]. A major group of bioactive polyketides from these fungal endopyhtes are xanthones [27]. Various fungal xanthones have been reported to possess pronounced biological activities including anti-tumour [28-30] activity. Among these compounds phomoxanthone A (PXA) can be pointed out as a putative lead structure for future anticancer therapy due to its potent, rapid and selective activity against tumour cells [31].

2. STRUCTURAL CHARACTERISTICS OF PHOMOXANTHONE A AND RELATED TETRAHYDROXANTHONE DIMERS

PXA is the dominating metabolite of *Phomopsis longicolla* being a fungal endophyte derived from the mangrove plant *Sonneratia caesolaris* (Lythraceae), which typically occurs in the intertidal zones of South China including the island of Hainan [31]. *P. longicolla* was first described in 1985, when Hobbs *et al*. isolated this fungus from soybeans where it is the causative agent of the so-called Phomopsis seed decay that is a major cause for poor-quality soybeen seed [32]. Fungi of the genus *Phomopsis* occur also in other Mangrove plants such as in *Excoecaria agallocha* (Euphorbiaceae), which is likewise typical for the South China Sea coast [33]. Several further reports on the occurrence of PXA in *Phomopsis* sp. from non Mangrove sources include the Costa Rican rain forest plant *Costus* sp. (Costaceae) [34], the teak plant *Tectona grandis* (Lamiaceae) [35] and the tropical plant *Garcinia dulcis* (Clusiaceae) [36]. The taxonomically closely related fungus *Phoma* sp., an endophyte inhabiting the African plant *Aizoon canariense* [37] (Aizoaceae) was likewise reported to accumulate this natural product. Structurally, PXA is a symmetrical atropisomer consisting of two tetrahydroxanthone monomers that are linked via an unsual 4,4'-biaryl linkage, which distinguishes this compound from other closely related natural products such as the dicerandrols, which show a 2,2'-biaryl linkage [8] or the eumitrins, the latter being xanthone dimers from lichens such as *Usnea baileyi*, which feature the biaryl linkage in positions 4,2' [34]. In addition to PXA talaroxanthone, a metabolite isolated from *Talaromyces* sp., an endophyte present in the Amazonian rainforest medicinal plant *Duguetia stelechantha* (An-

nonaceae) also exhibits the unusual 4,4'-biaryl linkage [38] (Fig. **1**). A further structural difference of PXA compared to other tetrahydroxanthone dimers lies in the substitution pattern at positions 10a and 10a' which either carry acetoxymethyl acids (PXA) or methoxycarbonyl groups (eumitrins and talaroxanthone) [35]. In PXA and other related xanthone dimers featured in this report all non-chelated hydroxyl groups are present in the acetylated form [34].

Both structural features, the unusual 4,4'-biaryl linkage as well as the bulky acetyl substituents contribute to a hindered rotation along the biaryl axis, leading to axial chirality of PXA [31, 34]. Interestingly, the methoxycarbonyls in 4,4'-linked talaroxanthone apparently do not lead to atropisomerism as Koolen *et al.* did not report atropisomerism for this PXA relative [38].

Several efforts have been undertaken to elucidate the absolute configuration of PXA. In an initial report on the structure of this intriguing metabolite Isaka *et al.* [35] determined the relative configuration of the six stereogenic centers based on NMR experiments and stated that the absolute configuration of the compound should be either 5*R*, 6*R*, 10a*R*, 5'*R*, 6'*R*, 10a'*R* or 5*S*, 6*S*, 10a*S*, 5'*S*, 6'*S*, 10a'*S*. Later, Elsässer *et al.* [34] reported the absolute configuration of PXA utilizing single-crystal X-ray analysis and comparison of quantum-mechanically calculated and experimentally measured CD spectra. The CD spectrum of PXA is dominated by the axial chirality of the compound, which enabled the authors to determine it as (*aS*). With the knowledge of the configuration of the biaryl axis, the absolute configurations of the stereogenic centers were determined by X-ray as 5*R*, 6*R*, 10a*R*, 5'*R*, 6'*R*, 10a'*R*. Recently, the absolute configuration of PXA was revised by X-ray analysis as being *aR*, 5*S*, 6*S*, 10a*S*, 5'*S*, 6'*S*, 10a'*S* [31] which is the enantiomer of the original structure proposed by Elsässer *et al.*

Taking into consideration several further structurally closely related polyketide derivatives that are likewise accumulated by *P. longicolla* such as the dicerandrols and a benzophenone intermediate (monodictyphenone) Rönsberg *et al.* proposed a plausible biosynthetic pathway leading to PXA (Scheme **1**). The initial step transforms eight acetate units into an octaketide (C-16 polyketide), a pathway which was discovered for polyphenols through ^{14}C-labelled acetate feeding experiments by Birch *et al.* already back in the 1950s [39]. The enzyme complex which is responsible for this decarboxylating Claisen condensation present in fungal metabolism is well understood today and belongs to the class of polyketide synthases (PKS) [40]. Subsequently this open-chain polyketide undergoes cyclization reactions affording the monomeric anthranoide congener emodin. *Via* oxidative ring-scission

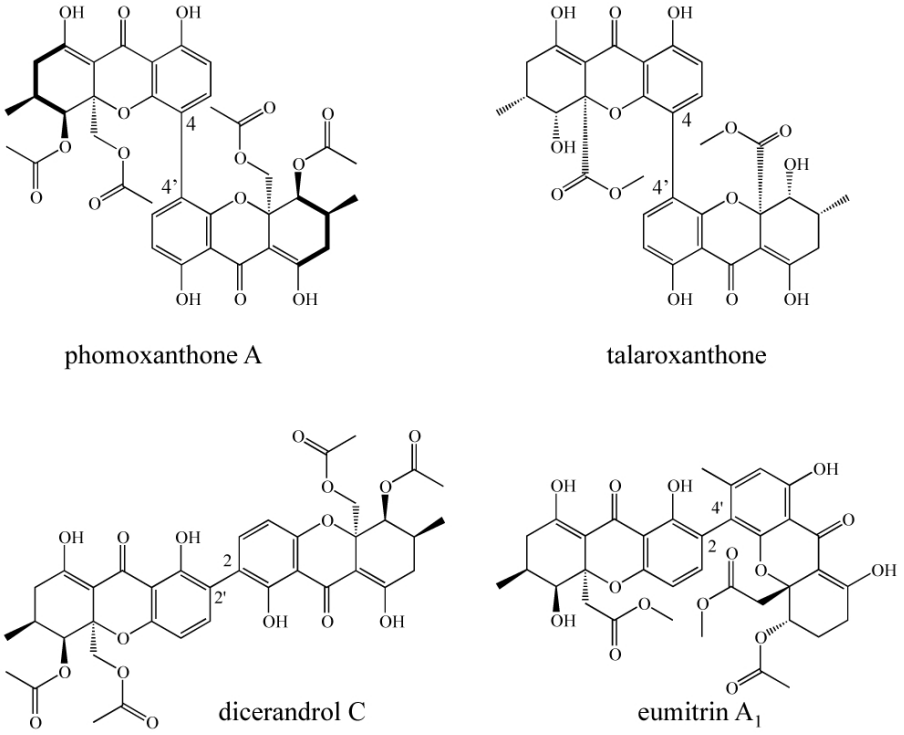

Fig. (1). Phomoxanthone A and further structurally related tetrahydroxanthone dimers.

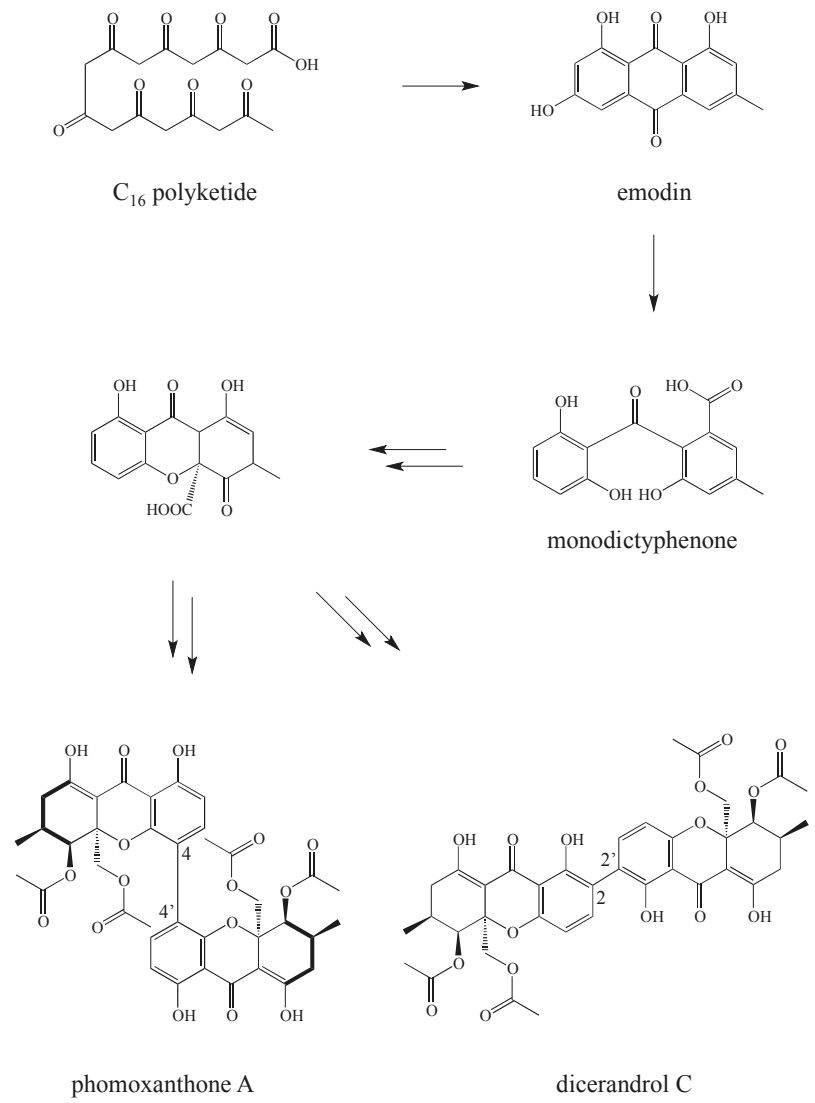

Scheme 1. Putative biosynthetic pathway of polyketides leading to 4,4'-linked phomoxanthone A and 2,2'-linked dicerandrols. Modified from Rönsberg *et al.* [31].

emodin is converted into monodictyphenone, which through subsequent decarboxylative cyclisation leads to the first xanthone indermediate [27]. The exact mechanism of dimerisation of xanthone monomers is so far not fully understood [27]. In this class of compounds linkages are found either as biaryl ether C-O-C linkages or as rotatable or atropisomeric biaryl C-C-bonds [27], the latter being present in PXA. In these dimeric xanthone C-C-bonds between monomers typically occur in positions 2 or 4 of ring A. A putative oxidative dimerisation mechanism proposed by Wezeman *et al.* (2015) postulated the occurrence of a xanthonyl radical that can be formed in either of these two positions by single-electron-transfer. Resonance contributors of the delocalised aryl radical can then couple to a second xanthone moiety that acts as an electron-donor [27]. The fact that identical xanthone monomers, as in the case of PXA and dicerandrol C, condense at different positions strongly suggests an enzymatic dimerisation mechanism, as was recently shown for dimeric fungal coumarins such as the *Aspergillus niger* derived kotanin [41]. In the respective study Girol *et al.* identified the cytochrome P450 monooxygenase KtnC as being responsible for the regio- and stereoselective C-C coupling of coumarin moieties.

3. ANTI-TUMOUR ACTIVITY OF PXA

A recent report indicated the pronounced anti-tumour activity of phomoxanthone A against a panel of

human and other cancer cell lines. PXA showed for example a remarkable activity against human epidermoid carcinoma KB cells (IC_{50} 1.32 μM), the human breast cancer cell line BC-1 (IC_{50} 0.68 μM), African monkey kidney fibroblast Vero cells (IC_{50} 1.87 μM) [36], and the L5178Y mouse lymphoma cell line (IC_{50} 0.3 μM) [31]. In addition PXA demonstrated strong growth inhibition against several cisplatin-sensitive (sens) and -resistant (CisR) solid tumour cells, e.g. human ovarian carcinoma cells A2780 (IC_{50} sens 0.7 μM; CisR 0.9 μM), human tongue carcinoma cells Cal27 (IC_{50} sens 5.2 μM; CisR 5.6 μM), and human esophagus cells Kyse510 (IC_{50} sens 0.8 μM; CisR 0.8 μM) [31]. Considering the clinical importance of cisplatin as a cytostatic drug in chemotherapy of cancer the fact that cancer cells which have become resistant and do no longer respond to this anti-cancer drug still succumb to PXA is a remarkable finding. Since selectivity of an anti-tumour drug compared to its effect against healthy cells is of utmost importance for potential future use in chemotherapy the selectivity of PXA was investigated against two human cancer cell lines including Jurkat J16 cells (T cell lymphoma) and DG75 cells (Burkitt's lymphoma) as well as against healthy human peripheral blood mononuclear cells (PBMCs). The selectivity index of PXA against the investigated cancer cells *vs*. PBMCs amounted to more than two orders of magnitude, suggesting a highly selective mode of action against cancer cells, which highlights PXA as an interesting candidate for further investigations.

When reporting on PXA for the first time Isaka *et al.* generated a semisynthetic derivative of this natural product through acidic hydrolysis thus generating tetradeacetylphomoxanthone A [35]. The latter proved to be inactive in all biological assays conducted such as cytotoxic [31], antibiotic [34, 35], antimalarial [35] and antifungal [34] assays. The naturally occurring 12-deacetylphomoxanthone A (12-dPXA) that was isolated from *P. longicolla* in addition to PXA was found to be about ten times less active than PXA with regard to growth inhibition of the mouse lymphoma cell line L5178 (PXA: IC_{50} 0.3 μM *vs*. 12-dPXA: IC_{50} 2.8 μM) [31]. This observance led to the hypothesis, that the acetate substituents modulate the anti-tumour activity of PXA. To further investigate the structure activity relationships of PXA and derivatives seven semisynthetic congeners of PXA (**2**-**8**) were prepared of which five (**3**-**7**) are new compounds and are described in this review for the first time (Scheme **2**, unpublished data). Acetylated compounds **3**-**6** were obtained by partial or complete acetylation of PXA, while compound **7** was generated through partial acidic hydrolysis of the parent compound. The anti-tumour activity of the various derivatives was evaluated against Jurkat 16 T lymphocytes and Ramos B lymphocytes. Hydrolysis of all acetate functions lead to a total loss of activity as previously reported for tetradeacetylphomoxanthone A (**2**). When comparing the IC_{50} values of all seven compounds (**2**-**8**) *vs*. the parent compound PXA (**1**) the latter turned out to be the most active congener. Acetylation of the phenolic and enolic hydroxyl-groups of the PXA core structure was found to decrease the anti-tumour activity even though the resulting derivatives still retained a certain level of activity. There was no clear trend with regard to the activity of the different congeners in relation to the positions of acetate substituents or to the number of free hydroxyl-groups. When comparing the deacetylation products 12-dPXA and 12,12'-dPXA (Jurkat T IC_{50} 1.25-1.44 μM; Ramos B IC_{50} 0.70-0.89 μM) to PXA the loss of activity was stronger than that caused by acetylation (**3**-**6**) (Jurkat T IC_{50} 0.48-0.56 μM; Ramos B IC_{50} 0.30-0.49 μM). The difference in activity between 12-dPXA (Jurkat T IC_{50} 1.44 μM; Ramos B IC_{50} 0.70 μM) and 12,12'-dPXA was negligible (Jurkat T IC_{50} 1.25 μM; Ramos B IC_{50} 0.89 μM), which lead to the conclusion that the acetyl-moiety at C-12 is not crucial for the anti-tumour activity of PXA. In conclusion, all structural alterations of the hydroxyl or acetyl ester moieties of PXA that were obtained by acetylation or by acidic hydrolysis of the parent compound lead to a decreased anti-tumour activity when compared to PXA. Hydrolysis of the ester moieties at C-12 resulted in a stronger decrease of activity compared to acetylation of free hydroxyl moieties.

The position of the biaryl axis linking the two tetrahydroxanthone monomers seems to be likewise important for the anti-tumour activity. Considering the structural similarity of PXA and dicerandrol C that differ with regard to the position of their biaryl axis the more than three fold higher activity of PXA *vs*. dicerandrol C against murine L5178Y lymphoma cells (PXA: IC_{50} 0.3 μM; dicerandrol C: IC_{50} 1.1 μM) can be clearly linked to the different positions of their biaryl axis (Scheme **3**). Since both compounds induce apoptosis in tumour cells as shown by Rönsberg *et al.* (2013) it is safe to assume that PXA and dicerandrol share a similar mode of action [31]. Hydrolysis of one ester moiety at C-12 of dicerandrol C leads to dicerandrol B, which exhibits a nearly ten-fold weaker cytotoxicity when compared with dicerandrol C against the mouse lymphoma cell line L5178Y (dicerandrol B: IC_{50} 10 μM; dicerandol C: IC_{50} 1.1 μM) [31]. In contrast, a stronger effect of dicerandrol B in comparison to dicerandrol C

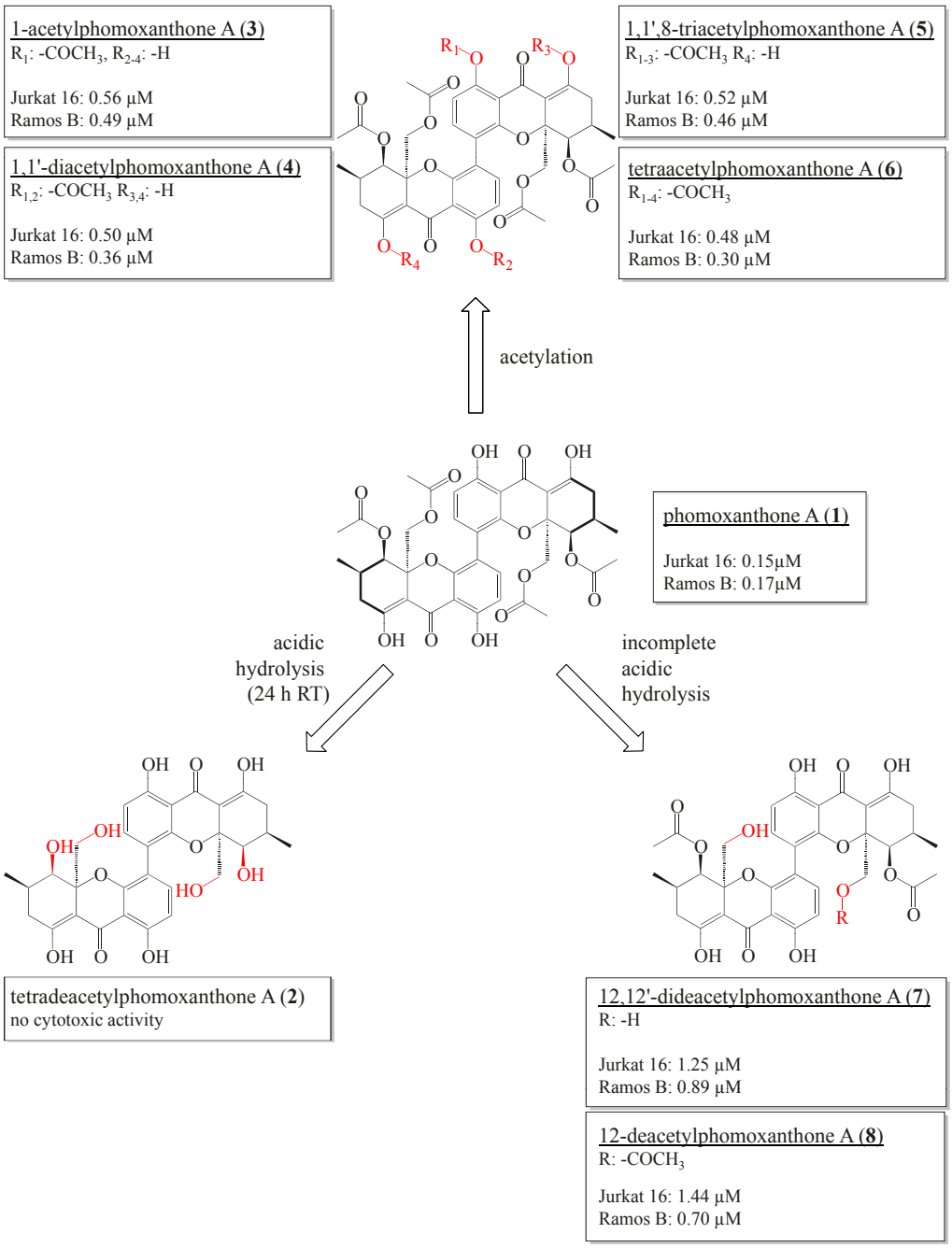

Scheme 2. SAR study on the influence of acetyl substituents on the anti-tumour activity of PXA against Jurkat 16 and Ramos B cells as evident from IC_{50} values after 72 h exposure (unpublished data).

was observed when tested against Dox40, H929, KMS34, L363, MM1S, OCIMY5, OPM2, RPMI8226 myeloma cell lines (IC_{50} 2.2-16.7 µM) [42], making a coherent statement on the influence of acetylation with regard to the cytotoxic potential of dicerandrols difficult. Interestingly, penexanthone B, which is the monomeric building block of PXA and of dicerandrol C alike showed only moderate to negligible activity in cytotoxicity assays against above mentioned myeloma cells (IC_{50} 11.6-464.2 µM) when compared to considerably active dicerandrol C (IC_{50} 4.8-14.7 µM) [42].

All structure-activity studies on PXA and congeners strongly suggest that the linkage of two xanthone monomers is important for the anti-tumour activity with a 4-4'-biaryl linkage as in PXA being favourable to a 2-2'-biaryl linkage as in the dicerandrols.

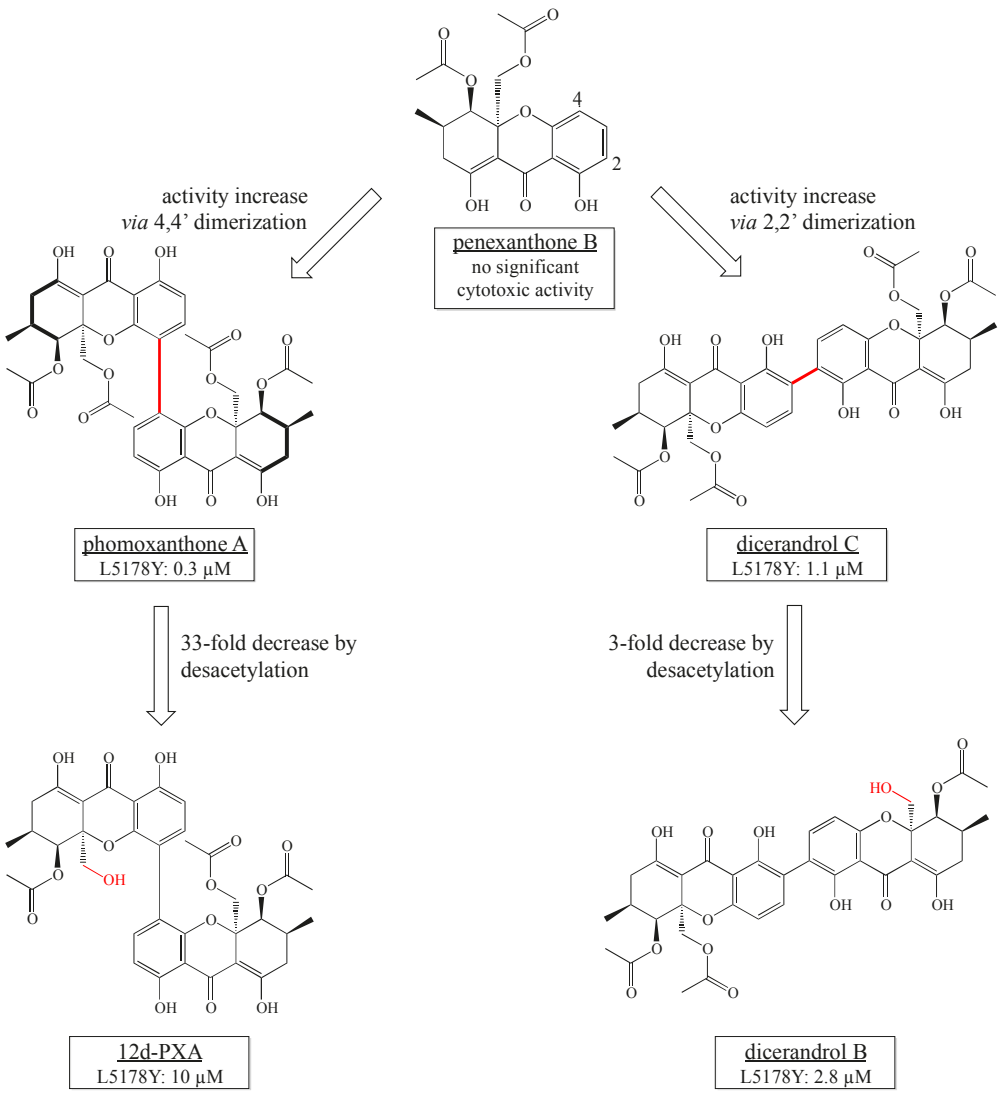

Scheme 3. Comparative SAR on the anti-tumour activity of monomeric penexanthone B against myeloma cells [42] and 4,4'-linked PXA and 2,2'-linked dicerandrols against murine L5178Y lymphoma cells [31] based on the respective IC_{50} values.

However, since only one atropisomer (the *aR* enantiomer) of PXA was isolated so far the influence of atropisomerism on the biological activity of PXA remains unknown. For other atropisomers such as for tetrahydroanthraquinones it was shown earlier that the nature of the biaryl axis has a profound influence on the biological activity as the (*aR*) acetylalterporriol E showed a remarkable activity against the L5178Y lymphoma cell line (IC_{50} 10.4 µM) while (*aS*) acetylalterporriol D exhibited no cytotoxicity [43].

4. INDUCTION OF APOPTOSIS AS A PLAUSIBLE MODE OF ACTION OF PXA

Even though detailed mechanistic studies on the exact molecular target and mode of action of PXA are still underway experimental evidence supports the induction of apoptosis in tumour cells by this natural product. The fragmentation of DNA through activation of caspases after treatment of tumour cells with PXA was used as an indicator for induction of apoptosis, since this effect could be blocked almost completely by addition of a caspase inhibitor (Q-VD-OPh). In addition to PXA, 12-dPXA and dicerandrol C significantly increased the number of apoptotic Jurkat T lymphocytes and DG75 B lymphocytes when the latter were treated with a concentration of 1 µM of either compound for 24 hours. This effect was strongest for PXA followed by 12-dPXA and dicerandrol C. Additionally, the cleavage of the caspase substrate poly(ADP-ribose)-polymerase (PARP) was investigated through

immunoblotting after treatment of Jurkat and DG75 cells with 1 μM and 10 μM PXA which in both cases showed cleavage of PARP which could be inhibited by addition of caspase inhibitors [31]. Further experiments compared the apoptosis inducing properties of PXA to its semisynthetic derivate 1,1'-diacetylphomoxanthone A (PXA-DA). The induction of apoptosis was investigated using Jurkat T lymphocytes and Ramos B lymphocytes which were treated with increasing concentrations of either PXA or PXA-DA for 24 and 48 hours. The percentage of apoptotic sub-G1 nuclei as a marker for apoptosis was assessed using propidium iodide staining and flow cytometry. The activities observed for the different compounds as indicated by the percentages of sub-G1-nuclei detected after 24 hours in Jurkat T lymphocytes were in accordance with their anti-tumour activities detected in the cellular assays, where PXA-DA showed slightly lower activity than PXA (PXA: EC_{50} 5.17 μM; PXA-DA: 8.26 μM). The results of these assays strongly suggest, that the acetyl-derivatives of PXA retain their apoptosis inducing properties even though their overall anti-tumour activity is reduced compared to the parent compound (unpublished results).

To further investigate the caspase dependent induction of apoptosis by PXA, the compound was compared to mitomycin C (a DNA-damaging anticancer drug) and with the broad range kinase inhibitor staurosporine in a time dependent caspase-3 activity assay. The activity of caspase-3 was measured using fluorescence detection methods utilising DEVD-AMC as a caspase-3 substrate fluorescence indicator (Fig. **2**). When comparing the time course of caspase induction it became apparent that PXA acts slower than staurosporine (STS) but in considerably faster kinetics than mitomycin C (MITO) which makes it unlikely for PXA to possess a mode of action involving direct DNA-damage. These findings suggest that the apoptotic sub-G1 nuclei observed after treament of cells with PXA [31] are in fact a result of the activation of caspases and not the effect of a direct DNA-damage.

5. PXA ACTIVATES IMMUNE CELLS

As tumour stem cells are known to persist and may cause recrudescence even after an effective chemotherapy, an activation of immune cells such as natural killer (NK) cells that specifically recognize cancer stem cells and trigger apoptosis is highly favourable for the overall success of an anticancer therapy. Therefore Roensberg *et al.* investigated the cell-type specific activation markers in murine immune cell subpopulations following treatment with PXA, 12d-PXA or dicerandrols B and C [31]. The population of $CD69^+$ T cells was most prominently enhanced by the treatment of the two 4-4'-

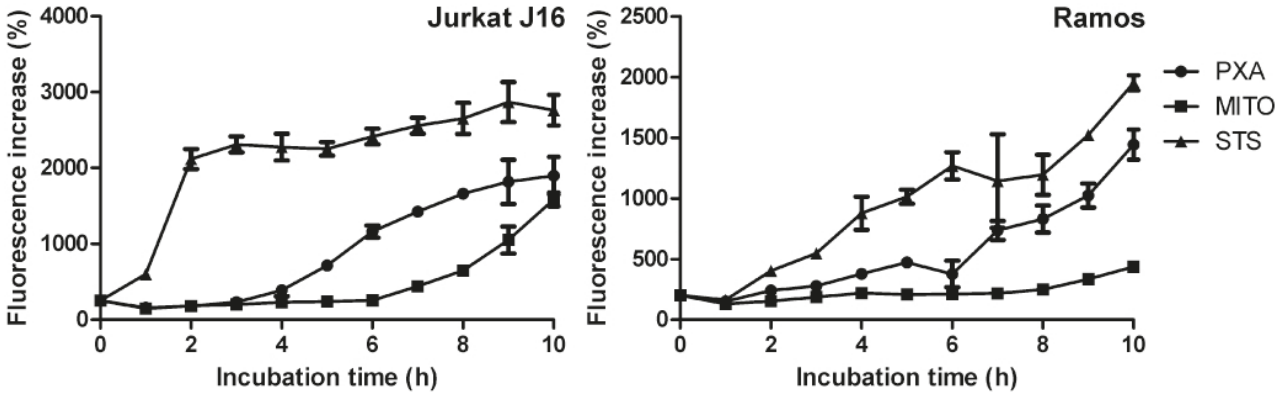

Fig. (2). Comparison of Caspase-3 induction by phomoxanthone A, mitomycin C, and staurosporine. Jurkat J16 cells (T lymphocytes; from DSMZ #ACC-282) or Ramos cells (Burkitt's lymphoma B lymphocytes; from Michael Engelke, University of Göttingen) were seeded at a density of 10^6 cells / mL and incubated with either 10 μM phomoxanthone A (PXA), 25 μg / mL mitomycin C (MITO), or 2.5 μM staurosporine (STS) for up to 10 h. Cells treated with DMSO (0.1% v/v) for 10 h were used as negative control. An amount of 100,000 cells per sample was harvested by centrifugation at 600 rcf and 4 °C for 5 min. The supernatant was removed and the cells were quick-frozen in liquid nitrogen. The cells were then thawed on ice, incubated with 150 μL of ice-cold lysis buffer (20 mM HEPES, 84 mM KCl, 10 mM MgCl2, 200 μM EDTA, 200 μM EGTA, 0.5% NP-40, 1 μg / mL leupeptin, 1 μg / mL pepstatin, 5 μg / mL aprotinin) for 10 min, and transferred to a clear flat-bottom 96-well plate. To each well, 150 μL of ice-cold reaction buffer (50 mM HEPES, 100 mM NaCl, 10% Sucrose, 0.1% CHAPS, 2 mM $CaCl_2$, 13.35 mM DTT, 70 μM DEVD-AMC) were added and the fluorescence (Ex 360 nm, Em 450 nm) was measured at 37 °C over a time course of 150 min using a multiplate reader (Synergy Mx, BioTek). The ratio of the highest to the lowest value of the linear range of the fluorescence curve was calculated. Data points shown are the mean of triplicates, error bars = SD.

linked dimeric xanthones with a 1.8-fold (PXA) and 1.4-fold (12d-PXA) increase when treated with 1 μM of either of the respective compounds. In accordance to the cytotoxicity data the activation of $CD69^+$ T cells was antagonised by hydrolysis of the acetyl groups as tetradeacetylphomoxanthone showed no effect even at the highest concentration investigated. The authors hypothesised that the reduction in the T cell recruiting potential might correlate with reduced cellular uptake as total desacetylation of PXA leads to a significant loss in lipophilicity. Therefore an intracellular target rather than a cell-surface interaction was proposed as a potential target structure for PXA. For dicerandrol C an activation of the same T cell population was likewise observed albeit only at a higher concentration of 10 μM while dicerandrol B completely lacked activity. Similarly, an activation was observed in primary murine NK cells and macrophages as indicated by an upregulation of CD69 and MHC class II, respectively. Nevertheless murine B lymphocytes were not activated by the tested dimeric xanthones as there was no significant induction of CD86. This immune and in particular T and NK cell stimulatory effect of PXA in combination with the strong pro-apoptotic properties of the compound represents a synergistic mechanism towards tumour elimination that could be valuable for tumour chemotherapy.

CONCLUSION

Mangrove plants that thrive in stress prone habitats harbour unique endophytes that accumulate structurally unusual and highly active natural products such as phomoxanthone A (PXA) that is highlighted in this review. PXA shows powerful anti-tumour activities against different human cancer cells that even include cells that have become resistant against the cytostatic drug cisplatin. The mode of action of PXA was shown to be due to an induction of caspase 3 dependent apoptosis. Remarkably, PXA is up to 100 folds less active against PBMC that were used as a control for healthy blood cells. The immune stimulatory activity of PXA that was demonstrated for murine T-lymphocytes, NK cells and for macrophages could be important during cancer chemotherapy in order to eradicate any surviving cancer cells. Further studies on the target and on the mechanism of this interesting anti-tumour drug are highly warranted.

CONFLICT OF INTEREST

The authors confirm that this article content has no conflict of interest.

ACKNOWLEDGEMENTS

Financial support by grants from BMBF to P.P. and MOST to W.L. are gratefully acknowledged.

REFERENCES

[1] Twilley, R.R.; Day, J.W. Mangrove Wetlands. In: *Estuarine Ecology,* 2nd ed.; Wiley-Blackwell: New York, **2012**.

[2] Tomlinson, P.B. *The Botany of Mangroves;* Cambridge University Press: New York, **1994**.

[3] Wu, J.; Xiao, Q.; Xu, J.; Li, M.Y.; Pan, J.Y.; Yang, M.H. Natural products from true mangrove flora: source, chemistry and bioactivities. *Nat. Prod. Rep.*, **2008**, *25*(5), 955-981.

[4] Walsh, G.E. Mangroves: A Review. In: *Ecology of Halophytes*; Academic Press, Inc.: New York, **1974**.

[5] Chapman, V.J. *Mangrove Vegetation;* J. Cramer: Vaduz, **1976**, p. 581.

[6] Feller, I.; Lovelock, C.; Berger, U.; McKee, K.; Joye, S.; Ball, M. Biocomplexity in mangrove ecosystems. *Ann. Rev. Mar. Sci.*, **2010**, *2*, 395-417.

[7] Valiela, I.; Bowen, J.L.; York, J.K. Mangrove forests: one of the world's threatened major tropical environments. *Bioscience*, **2001**, *51*(10), 807-815.

[8] Xu, J. Bioactive natural products derived from mangrove-associated microbes. *R. Soc. Chem. Adv.*, **2015**, *5*(2), 841-892.

[9] Arnold, A.E.; Mejía, L.C.; Kyllo, D.; Rojas, E.I.; Maynard, Z.; Robbins, N.; Herre, E.A. Fungal endophytes limit pathogen damage in a tropical tree. *Proc. Natl. Acad. Sci. USA*, **2003**, *100*(26), 15649-15654.

[10] Reinhold-Hurek, B.; Hurek, T. Living inside plants: bacterial endophytes. *Curr. Opin. Plant Biol.*, **2011**, *14*(4), 435-443.

[11] Aly, A.H.; Debbab, A.; Proksch, P. Fungal endophytes: unique plant inhabitants with great promises. *Appl. Microbiol. Biotechnol.*, **2011**, *90*(6), 1829-1845.

[12] Aly, A.H.; Debbab, A.; Kjer, J.; Proksch, P. Fungal endophytes from higher plants: a prolific source of phytochemicals and other bioactive natural products. *Fungal Divers.,* **2010**, *41*(1), 1-16.

[13] Strobel, G.; Daisy, B. Bioprospecting for microbial endophytes and their natural products. *Microbiol. Mol. Biol. Rev.*, **2003,** *67*(4), 491-502.

[14] Strobel, G.A. Endophytes as sources of bioactive products. *Microbes Infect*., **2003**, *5*(6), 535-544.

[15] Thatoi, H.; Behera, B.C.; Mishra, R.R.; Dutta, S.K. Biodiversity and biotechnological potential of microorganisms from mangrove ecosystems: a review. *Ann. Microbiol.*, **2013**, *63*(1), 1-19.

[16] Xu, J. Biomolecules produced by mangrove-associated microbes. *Curr. Med. Chem.*, **2011**, *18*(34), 5224-5266.

[17] Salini, G. Pharmacological profile of mangrove endophytes - a review. *Int. J. Pharm. Pharm. Sci.*, **2014**, *7*(1), 6-15.

[18] Ebrahim, W.; Kjer, J.; El Amrani, M.; Wray, V.; Lin, W.; Ebel, R.; Lai, D.; Proksch, P. Pullularins E and F, two new peptides from the endophytic fungus *Bionectria ochroleuca* isolated from the mangrove plant *Sonneratia caseolaris*. *Mar. Drugs*, **2012**, *10*(5), 1081-1091.

[19] Zeng, Y.B.; Wang, H.; Zuo, W.J.; Zheng, B.; Yang, T.; Dai, H.F.; Mei, W.L. A fatty acid glycoside from a marine-derived fungus isolated from mangrove plant *Scyphiphora hydrophyllacea*. *Mar. Drugs*, **2012**, *10*(3), 598-603.

[20] Mei, W.L.; Zheng, B.; Zhao, Y.X.; Zhong, H.M.; Chen, X.L. W.; Zeng, Y.B.; Dong, W.H.; Huang, J.L.; Proksch, P.; Dai, H.F. Meroterpenes from endophytic fungus A1 of mangrove plant *Scyphiphora hydrophyllacea*. *Mar.* Drugs, **2012**, *10*(9), 1993-2001.

[21] Ebrahim, W.; Aly, A.H.; Mándi, A.; Totzke, F.; Kubbutat, M. H.; Wray, V.; Lin, W. H.; Dai, H.; Proksch, P.; Kurtán, T.; Debbab, A. Decalactone derivatives from *Corynespora cassiicola*, an endophytic fungus of the mangrove plant *Laguncularia racemosa*. *Eur. J. Org. Chem.*, **2012**, *18*, 3476- 3484.

[22] Li, Y.; Yu, S.; Liu, D.; Proksch, P.; Lin, W. Inhibitory effects of polyphenols toward HCV from the mangrove plant *Excoecaria agallocha* L. *Bioorg. Med. Chem. Lett.*, **2012**, *22*(2), 1099-1102.

[23] Zeng, Y.B.; Gu, H.G.; Zuo, W.J.; Zhang, L.L.; Bai, H.J.; Guo, Z.K.; Proksch, P.; Mei, W.L.; Dai, H.F. Two new sesquiterpenoids from endophytic fungus J3 isolated from mangrove plant *Ceriops tagal*. *Arch. Pharm. Res.*, **2015**, *38*(5), 673-676.

[24] Huang, Z.; Yang, J.; Cai, X.; She, Z.; Lin, Y. A new furanocoumarin from the mangrove endophytic fungus *Penicillium* sp.(ZH16). *Nat. Prod. Res.*, **2012**, *26*(14), 1291-1295.

[25] Huang, Z.; Yang, R.; Guo, Z.; She, Z.; Lin, Y. A new naphtho-*γ*- pyrone from mangrove endophytic fungus ZSU-H26. *Chem. Nat. Compd.,* **2010**, *1*(46), 15-18.

[26] Huang, Z.; Yang, J.; She, Z.; Lin, Y. A new isoflavone from the mangrove endophytic fungus Fusarium sp.(ZZF60). *Nat. Prod. Res.*, **2012,** *26*(1), 11-15.

[27] Wezeman, T.; Brase, S.; Masters, K.S. Xanthone dimers: a compound family which is both common and privileged. *Nat. Prod. Rep.*, **2015**, *32*(1), 6-28.

[28] Na, Y. Recent cancer drug development with xanthone structures. *J. Pharm. Pharmacol.*, **2009**, *61* (6), 707-712.

[29] Pinto, M.; Sousa, M.; Nascimento, M. Xanthone derivatives: new insights in biological activities. *Curr. Med. Chem.*, **2005,** *12*(21), 2517-2538.

[30] Pouli, N.; Marakos, P. Fused xanthone derivatives as antiproliferative agents. *Anticancer Agents Med. Chem.,* **2009**, *9*(1), 77-98.

[31] Rönsberg, D.; Debbab, A.; Mándi, A.; Vasylyeva, V.; Böhler, P.; Stork, B.R.; Engelke, L.; Hamacher, A.; Sawadogo, R.; Diederich, M.; Wray, V.; Lin, W., Kassack, M.U.; Janiak, C.; Scheu, S.; Wesselborg, S.; Kurtán, T.; Aly, A.H.; Proksch, P. Pro-apoptotic and immunostimulatory tetrahydroxanthone dimers from the endophytic fungus *Phomopsis longicolla*. *J. Org. Chem.*, **2013**, *78*(24), 12409-12425.

[32] Li, S.; Hartman, G.L.; Boykin, D.L., Aggressiveness of *Phomopsis longicolla* and other *Phomopsis* spp. on soybean. *Plant Dis.*, **2010**, *94*(8), 1035-1040.

[33] Yang, J.; Xu, F.; Huang, C.; Li, J.; She, Z.; Pei, Z.; Lin, Y. Metabolites from the mangrove endophytic fungus *Phomopsis* sp. (# zsu-H76). *Eur. J. Org. Chem.,* **2010**, *19*, 3692-3695.

[34] Elsässer, B.; Krohn, K.; Flörke, U.; Root, N.; Aust, H.J.; Draeger, S.; Schulz, B.; Antus, S.; Kurtán, T. X-ray structure determination, absolute configuration and biological activity of phomoxanthone A. *Eur. J. Org. Chem.*, **2005**, *21*, 4563-4570.

[35] Isaka, M.; Jaturapat, A.; Rukseree, K.; Danwisetkanjana, K.; Tanticharoen, M.; Thebtaranonth, Y. Phomoxanthones A and B, novel xanthone dimers from the endophytic fungus *Phomopsis* species. *J. Nat. Prod.*, **2001**, *64*(8), 1015-1018.

[36] Rukachaisirikul, V.; Sommart, U.; Phongpaichit, S.; Sakayaroj, J.; Kirtikara, K. Metabolites from the endophytic fungus *Phomopsis* sp. PSU-D15. *Phytochemistry*, **2008**, *69*(3), 783-787.

[37] Dai, J.; Hussain, H.; Draeger, S.; Schulz, B.; Kurtán, T.; Pescitelli, G.; Floerke, U.; Krohn, K. Metabolites from the fungus *Phoma* sp. 7210, associated with *Aizoon canariense*. *Nat. Prod. Commun.*, **2010**, *5*(8), 1175-1180.

[38] Koolen, H.H.; Menezes, L.S.; Souza, M.P.; Silva, F.; Almeida, F.G.; de Souza, A.Q.; Nepel, A.; Barison, A.; Silva, F.H.D.; Evangelista, D. E. Talaroxanthone, a novel xanthone dimer from the endophytic fungus *Talaromyces* sp. associated with *Duguetia stelechantha* (Diels) RE Fries. *J. Braz. Chem. Soc.*, **2013**, *24*(5), 880-883.

[39] Birch, A.; Massy-Westropp, R.; Moye, C. Studies in relation to biosynthesis. VII. 2-Hydroxy-6-methylbenzoic acid in *Penicillium griseofulvum* Dierckx. *Aust. J. Chem.*, **1955,** *8*(4), 539-544.

[40] Simpson, T. J. Genetic and biosynthetic studies of the fungal prenylated xanthone shamixanthone and related metabolites in *Aspergillus* spp. revisited. *Chembiochem*, **2012,** *13*(11), 1680-1688.

[41] Gil Girol, C.; Fisch, K.M.; Heinekamp, T.; Günther, S.; Hüttel, W.; Piel, J.; Brakhage, A.A.; Müller, M. Regio- and stereoselective oxidative phenol coupling in *Aspergillus niger*. *Angew. Chem.*, **2012**, *124*(39), 9926-9929.

[42] Cao, S.; McMillin, D.W.; Tamayo, G.; Delmore, J.; Mitsiades, C.S.; Clardy, J. Inhibition of tumor cells interacting with stromal cells by xanthones isolated from a Costa Rican *Penicillium* sp. *J. Nat. Prod.*, **2012,** *75*(4), 793-797.

[43] Liu, Y.; Marmann, A.; Abdel-Aziz, M.S.; Wang, C.Y.; Müller, W.E.; Lin, W.H.; Mándi, A.; Kurtán, T.; Daletos, G.; Proksch, P. Tetrahydroanthraquinone derivatives from the endophytic fungus stemphylium globuliferum. *Eur. J. Org. Chem.*, **2015**, *12*, 2646-2653.

Received: May 11, 2015 **Revised: June 18, 2015** **Accepted: June 19, 2015**

Manuscript "Pro-apoptotic and immunostimulatory tetrahydroxanthone dimers from the endophytic fungus *Phomopsis longicolla*"

Rönsberg D, Debbab A, Mándi A, Vasylyeva V, Böhler P, Stork B, Engelke L, Hamacher A, Sawadogo R, Diederich M, Wray V, Lin W, Kassack MU, Janiak C, Scheu S, Wesselborg S, Kurtán T, Aly AH, Proksch P. *The Journal of Organic Chemistry* (2013) **78**:12409, doi: 10.1021/jo402066b

JOC The Journal of Organic Chemistry

Article

pubs.acs.org/joc

Pro-Apoptotic and Immunostimulatory Tetrahydroxanthone Dimers from the Endophytic Fungus *Phomopsis longicolla*

David Rönsberg,[†] Abdessamad Debbab,[†] Attila Mándi,[‡] Vera Vasylyeva,[§] Philip Böhler,[∥] Björn Stork,[∥] Laura Engelke,[⊥] Alexandra Hamacher,[⊥] Richard Sawadogo,[#] Marc Diederich,[#] Victor Wray,[▽] WenHan Lin,[○] Matthias U. Kassack,[⊥] Christoph Janiak,[§] Stefanie Scheu,[◆] Sebastian Wesselborg,[∥] Tibor Kurtán,[‡] Amal H. Aly,*[,†] and Peter Proksch*[,†]

[†]Institut für Pharmazeutische Biologie und Biotechnologie, Heinrich-Heine-Universität, Universitätsstrasse 1, 40225 Düsseldorf, Germany

[‡]Department of Organic Chemistry, University of Debrecen, POB 20, 4010 Debrecen, Hungary

[§]Institut für Anorganische Chemie und Strukturchemie, Heinrich-Heine-Universität, Universitätsstrasse 1, 40225 Düsseldorf, Germany

[∥]Institut für Molekulare Medizin, Universitätsklinikum Düsseldorf, Heinrich-Heine-Universität, Universitätsstrasse 1, 40225 Düsseldorf, Germany

[⊥]Institut für Pharmazeutische und Medizinische Chemie, Heinrich-Heine-Universität, Universitätsstrasse 1, 40225 Düsseldorf, Germany

[#]Laboratory of Molecular and Cellular Biology of Cancer (LBMCC), Hôpital Kirchberg, 9 rue Edward Steichen, 2540 Luxembourg, Luxembourg

[▽]Helmholtz Centre for Infection Research, Inhoffenstraße 7, 38124 Braunschweig, Germany

[○]National Research Laboratories of Natural and Biomimetic Drugs, Peking University, Health Science Center, 100083 Beijing, China

[◆]Institut für Medizinische Mikrobiologie und Krankenhaushygiene, Heinrich-Heine-Universität, Universitätsstrasse 1, 40225 Düsseldorf, Germany

Supporting Information

ABSTRACT: Four tetrahydroxanthone dimers (**1**–**4**) and four biogenetically related monomers (**5**–**8**), including the new derivatives **4**–**6**, were isolated from the endophyte *Phomopsis longicolla*. The absolute configurations of **2**–**4** were established for the first time by TDDFT electronic circular dichroism calculations, and that of phomoxanthone A (**1**) was revised by X-ray crystallography. Phomoxanthone A (**1**) showed the strongest pro-apoptotic activity when tested against a panel of human cancer cell lines, including cisplatin-resistant cells, whereas it was up to 100-fold less active against healthy blood cells. It was also the most potent activator of murine T lymphocytes, NK cells, and macrophages, suggesting an activation of the immune system in parallel to its pro-apoptotic activity. This dual effect in combating cancer cells could help in fighting resistance during chemotherapy. Preliminary structure–activity studies of isolated compounds and derivatives obtained by semisynthesis (**9a**–**11**) hinted at the location of the biaryl axis and the presence of acetyl groups as important structural elements for the biological activity of the studied tetrahydroxanthones.

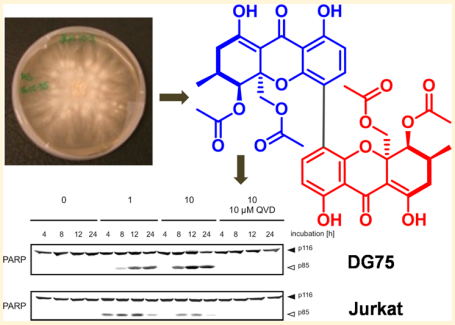

INTRODUCTION

Cancer still poses one of the most serious health problems and ranks as the second leading cause of death in the Western World after heart/circulatory problems.[1] Problems in treating cancer are closely linked to chemoresistance against currently available cytostatic drugs.[2] During the onset of a chemotherapeutic cycle, cancer cells usually react favorably to the drugs administered, and a vast majority of the cancer cells are killed. A few surviving cells might display a highly chemoresistant phenotype due to successive mutations of oncogenes and suppressor genes that deregulate the cell cycle.[3] This type of chemoresistance is known as secondary or acquired resistance.[4] Chemoresistance may also pre-exist in a few cells, which are then selected by chemotherapy.[3] This model supports the idea of a heterogeneous population of cancer cells (intrinsic resistance).[4] Resistant cancer cells are difficult to treat by currently available chemotherapy or by radiotherapy.

Received: September 17, 2013
Published: December 2, 2013

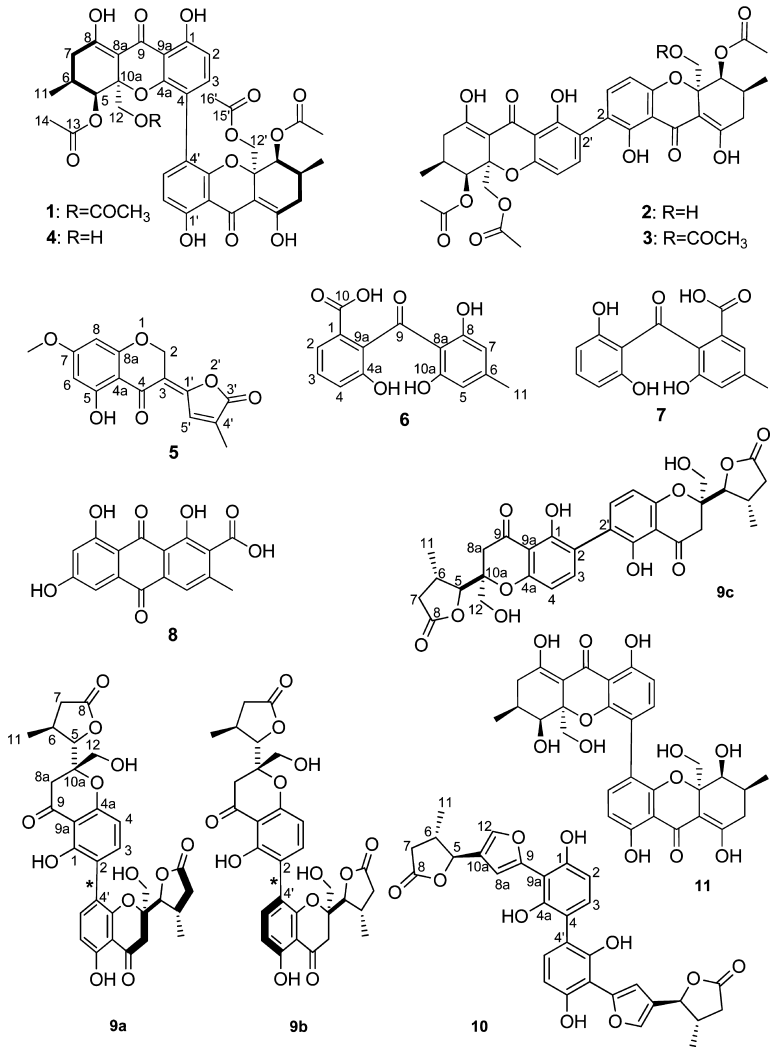

Figure 1. Chemical structures of compounds **1**–**11**. The axial chiralities (*) of the atropodiastereomers (**9a** and **9b**) have not been assigned.

They rapidly spread and develop metastases that attack vital organs of the body, with ultimate patient death. In this context, the identification of tumor-specific antigens and their recognition by T cells[5] indicates the paradoxical fact that in spite of the natural capability of the immune system to recognize cancer cells, it often fails to control malignant growth. This may be explained by generalized immunodeficiency associated with tumor growth or by immunomodulatory properties of cancer within its microenvironment.[6] The latter could be reversed by immunotherapy through activation of immune effector functions to promote tumor destruction.[7] However, the impact of tumor immunology on the clinical management of cancer is still a matter of intensive investigation. Increasing evidence suggests that anticancer immune responses may contribute to the control of cancer after conventional therapy, helping to eliminate residual cancer cells or prevent micrometastases.[8] Thus, the involvement of antitumor immune responses in the therapeutic management of cancer or the development of chemotherapeutic agents inducing specific immune responses, in addition to their direct cytotoxic effects on tumor cells, would attribute promising dual functions to a single molecule, offering a great improvement of cancer treatment that is less hampered by or even able to prevent the development of chemical resistance.[9]

Natural products and natural product analogues have a long and impressive success story with regard to the treatment of cancer. More than two-thirds of the currently available anticancer drugs are derived from or inspired by nature.[10] Prominent examples include plant-derived compounds such as paclitaxel; dimeric alkaloids from *Catharanthus roseus* (and their semisynthetic products); the camptothecin-derived drugs irinotecan and topotecan; and etoposide, a derivative of the naturally occurring lignan podophyllotoxin. However, recent research endeavors have shown that other less investigated organisms such as marine invertebrates and endophytic fungi harbor a wealth of structurally unprecedented and pharmacologically highly active compounds that can likewise provide important drug leads for the future.

Endophytic fungi spend the whole or part of their life cycle colonizing healthy tissues of their host plants, typically causing no apparent symptoms of disease.[11] This colonization is believed to contribute to host plant adaptation to biotic and abiotic stress factors,[12−15] which in many cases has been correlated with fungal natural products. For instance, a vast array of antiproliferative secondary metabolites from endo-

dx.doi.org/10.1021/jo402066b | J. Org. Chem. 2013, 78, 12409−12425

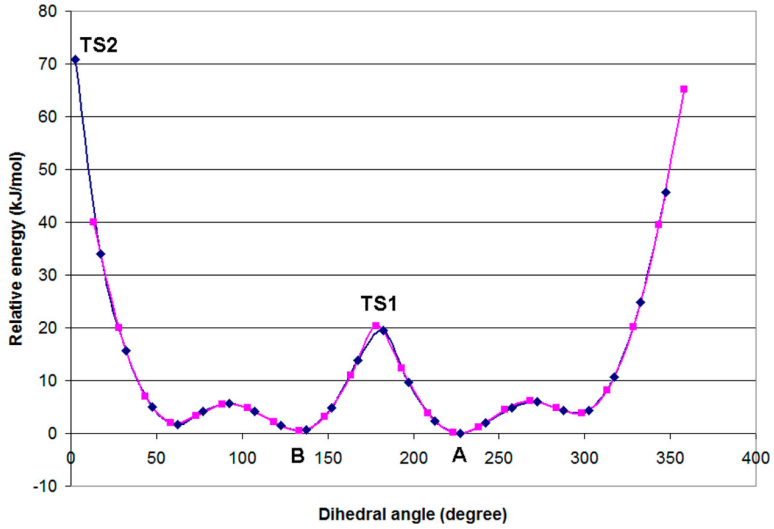

Figure 2. Preliminary torsional angle scans for determining the rotational energy barrier around the C2−C2′ bond ($\omega_{C1'-C2'-C2-C1}$ torsional angle) of (5*R*,6*R*,10a*R*,5′*R*,6′*R*,10a′*R*)-**2**. The scans were started from the lowest-energy in vacuo conformers of *M* and *P* helicity (A and B, respectively). Relative energy (kJ mol^{-1}) is plotted as a function of the $\omega_{C1'-C2'-C2-C1}$ torsional angle. TS1 and TS2 denote the two transition states for inversion of the helicity.

phytic fungi have hitherto been reported.[16] Examples include the farnesyl protein transferase-inhibiting chaetomellic acids A and B isolated from endophytic *Chaetomella acutisea*,[17] pro-apoptotic and c-Myc down-regulating secalonic acid D from the mangrove endophytic fungus ZSU44,[18] heat shock protein (HSP90)-inhibiting radicicol from *Chaetomium chiversii*,[19] and DNA polymerase inhibiting kasanosins A and B from *Talaromyces* sp.[20]

It has been hypothesized that endophytes that survive under harsh environmental conditions should be prioritized for bioprospecting,[10,21,22] as stress factors are known to induce biosynthetic pathways leading to bioactive metabolites. Mangrove swamps, with their high salinity and periodic changes in tidal submergence, represent one of the most stressful habitats for host plants and endophytes alike. Hence, endophytes from mangrove plants have recently attracted considerable attention from natural products chemists looking for new inspirations from nature.[23−27] The present study focuses on the endophytic fungus *Phomopsis longicolla*, which was isolated from leaves of the mangrove plant *Sonneratia caseolaris* growing in South China. The genus *Phomopsis* contains more than 900 species that occur in a wide range of habitats, and some of them are known as endophytes.[28] Endophytic species of *Phomopsis* are known to produce an impressive variety of bioactive natural products,[29−41] including the tremorgenic mycotoxins paspalitrems A and C; the actin-binding cytochalasins,[42] which are potent inhibitors of microtubule assembly; and xanthone derivatives such as phomoxanthone A (**1**) (Figure 1).[17,26−29] Our interest in *P. longicolla* was aroused by the strong inhibitory activity of a crude EtOAc extract (dose: 10 μg/mL) of the endophyte in an MTT assay using the mouse lymphoma cell line L5178Y (data not shown). Subsequent chromatographic separation of the extract yielded eight natural products, including the new 12-deacetylphomoxanthone A (**4**), phomo-2,3-dihydrochromone (**5**), and isomonodictyphenone (**6**) (Figure 1) in addition to **1**, whereas dicerandrols B (**2**) and C (**3**), monodictyphenone (**7**), and endocrocin (**8**) have been described previously. In addition, five semisynthetic derivatives (**9a**−**11**; Figure 1) were obtained following acidic or alkaline hydrolysis of **1**. All of the compounds were unequivocally identified on the basis of a combination of multidimensional NMR and MS data and comparison with the literature. The absolute configuration of **1** was revised by X-ray crystallography compared with the originally reported configuration,[43] and those of **2**−**4** were established for the first time by CD calculations and comparison with **1**. The dimeric tetrahydroxanthone derivatives **1**−**4** showed strong inhibition of proliferation of the lymphoma cell line L5178Y, with phomoxanthone A (**1**) as the most active compound. Interestingly, the activity of phomoxanthone A extended also to several other human cancer cell lines, including cancer cells that are resistant to the well-known chemotherapeutic drug cisplatin, making this compound an interesting candidate for further studies. The cytotoxicity of **1** displayed selectivity toward cancer cells, as it was found to be over 100-fold less toxic to healthy blood cells than to lymphoma cell lines. We could also show for the first time that the cytostatic activity of **1** is due to its pro-apoptotic potential. Phomoxanthone A (**1**) followed by the less active dicerandrols B (**2**) and C (**3**) furthermore showed clear upregulation of murine CD69$^+$ T and NK cells as well as of macrophages, indicating that **1** exhibits a dual efficacy in combating cancer cells through induction of apoptosis and activation of the immune system, which could help in fighting tumor resistance during chemotherapy.

RESULTS AND DISCUSSION

The EtOAc extract of *Phomopsis longicolla*, following cultivation on rice solid medium, was subjected to column chromatography using silica gel, Diaion HP20, and Sephadex LH-20 as alternating stationary phases followed by semipreparative HPLC for final purification. The tetrahydroxanthone dimer phomoxanthone A (**1**) (Figure 1) was obtained as the major constituent upon fractionation of the crude extract. Compound **1** had been reported previously to have the (a*S*,5*R*,6*R*,10a*R*,5′*R*,6′*R*,10a′*R*) configuration,[43,44] which was revised in this study. In addition, the known tetrahydroxanthone dimers dicerandrols B (**2**)[45] and C (**3**)[45] (Figure 1) were readily

dx.doi.org/10.1021/jo402066b | *J. Org. Chem.* 2013, 78, 12409−12425

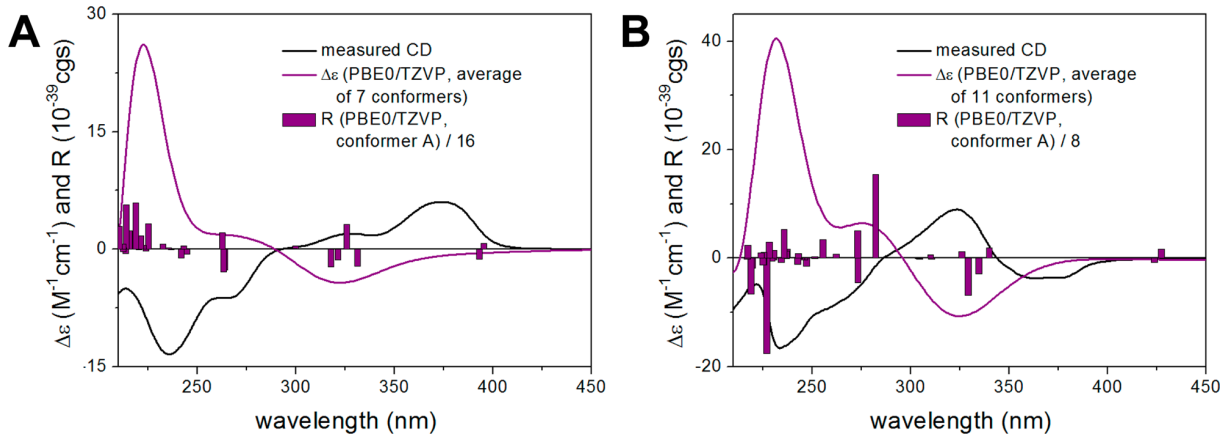

Figure 3. Experimental and PBE0/TZVP-calculated ECD spectra of the B3LYP/TZVP- and B3LYP/6-31G(d)-reoptimized low-energy geometries of (A) (5*R*,6*R*,10a*R*,5′*R*,6′*R*,10a′*R*)-**2** and (B) (5*R*,6*R*,10a*R*,5′*R*,6′*R*,10a′*R*)-**3**, respectively, in acetonitrile. Bars represent the calculated rotational strengths of the lowest-energy conformers.

identified by detailed analyses of their mass spectra and 1D and 2D NMR spectra as well as by comparison with published data.

For **2** and **3**, only the relative configuration had been published previously. Their absolute configurations were determined in the present work by TDDFT electronic circular dichroism (ECD) calculations. Dicerandrol B (**2**) features a 2,2′-linkage of two slightly different homochiral monomeric units, which in analogy to secalonic acid F[46] is expected to allow interconversion of the *P* and *M* helicity forms at room temperature, since the 1- and 1′-OH groups at the *ortho* positions do not impose sufficient steric hindrance to interrupt free rotation about the biaryl axis. In order to exclude the possibility of axially chiral atropisomers and to estimate the rotational barrier around the C2−C2′ bond, torsional scans were performed on the $\omega_{C1'-C2'-C2-C1}$ angle from the lowest-energy conformers of *P* and *M* helicity in vacuo (Figure 2). The scans started from the two low-energy conformers (A and B in Figure 2) and gave approximately the same results, showing two energy barriers with different energies. Next, transition-state calculations were run at the two maxima, which identified the energy barrier of the lower transition state (TS1) as 20.5 kJ/mol and that of the higher one (TS2) as 70.9 kJ/mol (Figure S1 in the Supporting Information). The 20.5 kJ/mol energy barrier indicated that the *P* and *M* helicity forms can freely equilibrate at room temperature, and they appear as conformers with different populations. The *P* and *M* helicity conformers are expected to produce different ECD curves, and hence, their populations determine the experimental solution ECD spectrum. The populations of the *P* and *M* helicity conformers are governed by the central chirality elements, and their accurate estimation by conformational analysis is crucial for the agreement of the computed and experimental ECD spectra.

Dicerandrol B (**2**) showed a broad positive Cotton effect (CE) at 373 nm with shoulders at 344 and 328 nm, and three negative CEs at 268, 233, and 198 nm. The solution TDDFT ECD approach was pursued to determine the absolute configuration of **2**. The initial MMFF conformational search of the arbitrarily chosen (5*R*,6*R*,10a*R*,5′*R*,6′*R*,10a′*R*)-**2** resulted in 84 conformers in a 21 kJ/mol energy window, DFT reoptimization of which yielded 11, 7, and 11 conformers at the B3LYP/6-31G(d) level in vacuo, the B3LYP/TZVP level with the PCM model for acetonitrile, and the M06/TZVP level[47] with the PCM model for MeCN, respectively. The three methods of conformational analysis applied for the optimizations yielded similar sets of conformers with a predominant population of the *M* helicity conformers (negative $\omega_{C1'-C2'-C2-C1}$ torsional angle). For instance, the B3LYP/TZVP reoptimization with the PCM model for acetonitrile resulted in seven conformers above 2% population (Figure S2 in the Supporting Information). The lowest-energy conformer had *M* helicity with $\omega_{C1'-C2'-C2-C1}$ = −122.3° and 30.8% population, and conformers C−F also had *M* helicity with slightly different orientations of the acetoxy groups. Conformer B had *P* helicity with $\omega_{C1'-C2'-C2-C1}$ = +124.75° and 21.8% population, and conformer G (2.0%) had also *P* helicity. The overall population of the *M* helicity conformers was 56.6%, while that of the *P* helicity conformers was 23.8%. The C5 and C10a (C5′ and C10a′) substituents are trans-diaxial in all conformers, and the C6 (C6′) methyl group adopts an equatorial orientation. The Boltzmann-averaged ECD spectra were calculated with the TZVP basis set and three functionals (B3LYP, BHandHLYP, and PBE0) for the three sets of solution conformers of (5*R*,6*R*,10a*R*,5′*R*,6′*R*,10a′*R*)-**2**. The *M* and *P* helicity conformers had opposite CEs for the two high-energy transitions, but all of the conformers had a negative CE around 330 nm. The Boltzmann-averaged ECD spectra were near mirror images of the experimental spectrum (Figure 3A), which allowed the determination of the absolute configuration as (5*S*,6*S*,10a*S*,5′*S*,6′*S*,10a′*S*).

Dicerandrol C (**3**) is a homodimer and the acetoxy derivative of dicenrandrol B (**2**), but interestingly, it has negative CEs at 373 and 365 nm, opposite to those of **2**. In order to identify the origin of their different ECDs, TDDFT calculations were performed. The MMFF conformational search of (5*R*,6*R*,10a*R*,5′*R*,6′*R*,10a′*R*)-**3** resulted in 71 conformers in a 21 kJ/mol energy window, DFT reoptimization of which yielded 11 and 17 conformers at the B3LYP/6-31G(d) level in vacuo and the M06/TZVP level with the PCM model for MeCN, respectively (Figure S3 in the Supporting Information). Both the gas-phase and PCM-model ECD calculations showed nearly mirror-image spectra compared with the experimental one, but the lowest-energy negative transition could not be predicted well in the averaged spectra. However, the ECD spectra of the lowest-energy conformers obtained at both levels showed positive computed CEs above 340 nm, giving further

dx.doi.org/10.1021/jo402066b | J. Org. Chem. 2013, 78, 12409−12425

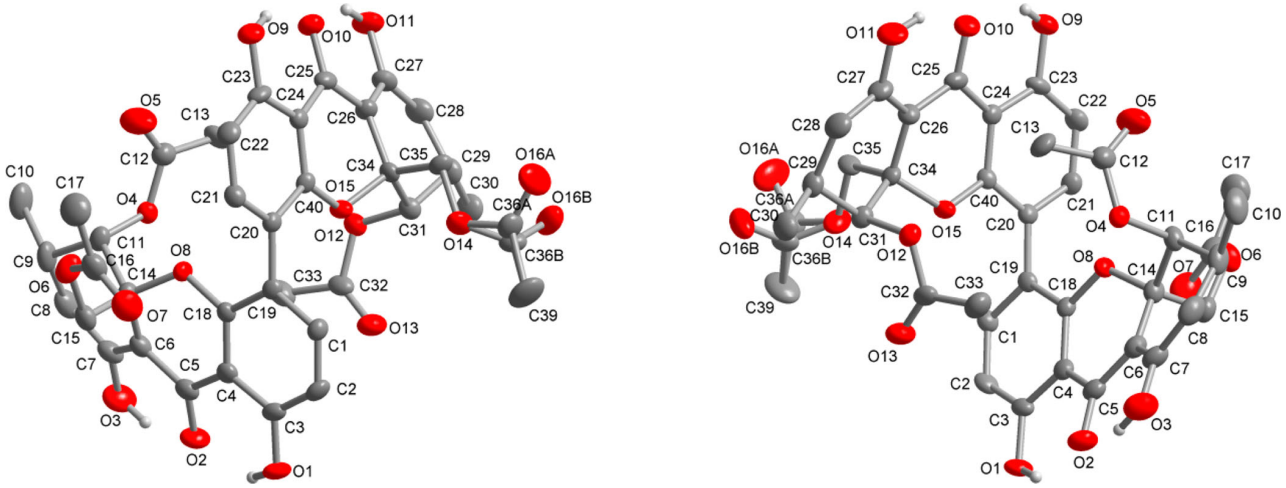

Figure 4. Two views of the molecular structure of phomoxanthone A (**1**) (50% thermal ellipsoids) with the determined absolute configuration. For clarity, H atoms on carbons are not shown. The torsional disorder of one acetyl group should be noted.

support to the mirror-image relationship of the calculated and measured ECD spectra. This finding also suggests that the population of the lowest-energy conformers may have been underestimated at both levels of theory. The lowest-energy conformer of the M06/TZVP reoptimization with the PCM model had *P* helicity with $\omega_{C1'-C2'-C2-C1}$ = +61.3°, and in the B3LYP/6-31G(d) in vacuo optimization, the lowest-energy conformer had *P* helicity with $\omega_{C1'-C2'-C2-C1}$ = +132.1°. The overall population of the *P* helicity conformers totaled 47.3%, while that of the *M* helicity ones was 29.9%. The additional acetoxy group changed the preferred sign and value of the biaryl dihedral angle, and this conformational change is responsible for the different ECD spectra of **2** and **3**. (5*R*,6*R*,10a*R*,5′*R*,6′*R*,10a′*R*)-**3** produced near mirror-image Boltzmann-averaged ECD spectra compared with the experimental one at the three levels of ECD calculations, which allowed the assignment of the absolute configuration as (5*S*,6*S*,10a*S*,5′*S*,6′*S*,10a′*S*) (Figure 3B).

The all-*S* absolute configurations of dicerandrols B and C prompted us to reinvestigate the absolute configuration of phomoxanthone A (**1**).[43] Since our phomoxanthone A sample was isolated together with dicerandrols B and C, it was expected also to contain monomers with the all-*S* absolute configuration on the basis of biogenetic considerations. Our phomoxanthone A sample showed the same specific rotation and ECD data as the previously reported one, for which the (a*S*,5*R*,6*R*,10a*R*,5′*R*,6′*R*,10a′*R*) absolute configuration had been assigned.[43] Theoretically, it was possible that the phomoxanthone A sample isolated in this study could have the (a*S*,5*S*,6*S*,10a*S*,5′*S*,6′*S*,10a′*S*) absolute configuration, since the chiroptical parameters are determined by the axial chirality. In order to clarify this issue, an X-ray analysis of our phomoxanthone A sample was initiated.

In the previous study[43] phomoxanthone A (**1**) crystals were obtained as yellowish needles from a dichloromethane/diethyl ether solution. It was reported that **1** crystallized in space group $P2_1$ with two independent but geometrically identical molecules per asymmetric unit as well as two solvent water molecules. X-ray analysis of these crystals revealed only the relative configuration of the stereogenic elements, whereas the absolute configuration of the compound was deduced on the basis of semiempirical ECD calculations on the solid-state conformers.[43] The authors noted that "in the absence of significant anomalous scattering effects, the Flack parameter is essentially meaningless. Accordingly, Friedel pairs were merged."

In the present study, **1** also crystallized in the noncentrosymmetric space group $P2_1$ from EtOAc solution but with only one phomoxanthone A molecule in the asymmetric unit (Figure 4 and Figure S4 in the Supporting Information) and one water and one EtOAc solvent molecule in the unit cell.

We could now determine the absolute structure from anomalous dispersion with Cu−Kα radiation using the Flack parameter (for details, see the Supporting Information).[48−51] Friedel pairs were not merged. The absolute configuration of phomoxanthone A (**1**) was determined as (a*R*,5*S*,6*S*,10a*S*,5′*S*,6′*S*,10a′*S*), which is enantiomeric to the previously reported absolute configuration (Figure 1 and Figure S5 in the Supporting Information). Accordingly, the previously reported absolute configuration of **1** has to be revised. In order to reveal the origin of the previous wrong configurational assignment on the basis of ECD calculations, TDDFT ECD calculations were performed on the previously reported and the recently determined X-ray structures of **1** at three levels of theory (B3LYP/TZVP, BHandHLYP/TZVP, and PBE0/TZVP). Since the previous assignment was made on the basis of a semiempirical ECD method, ECD spectra of the B3LYP/6-31G(d)-optimized and original X-ray structures of **1** were also calculated by the semiempirical ZINDO method for comparison. All of the DFT methods applied to the optimized and original X-ray geometries of (a*S*,5*R*,6*R*,10a*R*,5′*R*,6′*R*,10a′*R*)-**1** gave opposite effects relative to the negative CE at 341 nm and the positive CE at 316 nm in the solution ECD spectrum as well as to the intense negative CEs at 228 and 222 nm when they were red-shifted by 12 nm (Figure 5).

In contrast, the agreement with the solid-state ECD spectrum was poor, and the computed low-energy negative transition had no oppositely signed counterpart in the experimental solid-state ECD spectrum (Figure S6 in the Supporting Information). The negative CE at 342 nm in the solution ECD spectrum disappeared in the solid-state ECD spectrum, most likely as a result of intermolecular exciton-coupled interactions in the solid state. The computed ZINDO spectra showed poor agreement with the experimental spectrum compared with those from the DFT methods, and

dx.doi.org/10.1021/jo402066b | *J. Org. Chem.* 2013, 78, 12409−12425

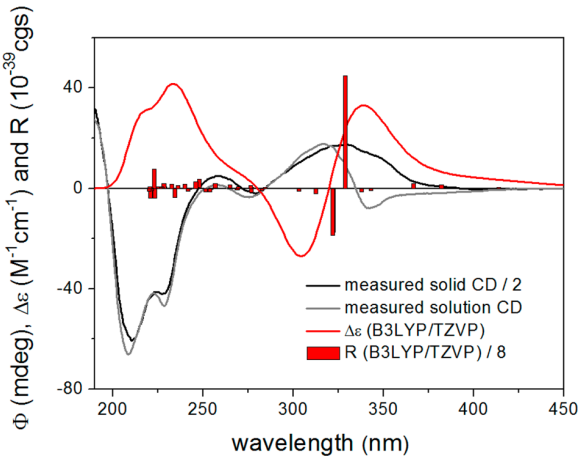

Figure 5. Experimental and B3LYP/TZVP-calculated ECD spectra of the X-ray conformers of (a*S*,5*R*,6*R*,10a*R*,5′*R*,6′*R*,10a′*R*)-**1** in vacuo (avarage of the two conformers). The computed spectrum is shifted 12 nm to the red.

the spectra had to be shifted by about 100 nm. The intermolecular interactions in the solid state and the missing negative band of the solid-state ECD spectrum could have led to the wrong configurational assignment of phomoxanthone A during the previously published configurational assignment by ECD calculations. It has to be noted as well that even a comparison of the DFT-computed ECD spectra of the X-ray geometry with the solid-state experimental spectrum would not allow an unambiguous conclusion.

The new compound **4** has the molecular formula $C_{36}H_{36}O_{15}$ as determined by HR-ESI-MS (*m*/*z* 709.2127 $[M + H]^+$), showing a mass difference of 42 amu relative to **1**, which corresponds to the absence of an acetyl moiety. In addition, the UV spectra of **4** were almost identical to those of **1**, indicating that the two compounds share very similar structural scaffolds. The ^{1}H NMR spectrum of **4** exhibited a set of signals similar to those observed for **1** but with only three acetyl methyl groups resonating at δ_H 1.75 (16′-CH_3), 2.10 (14-CH_3), and 2.11 (14′-CH_3) (Table 1). The ^{13}C NMR and DEPT spectra revealed the presence of 36 carbon atoms in total, including signals for only five carbonyl groups (Table 1). The structure was further confirmed by thorough analysis of 2D NMR spectra (Figure 6). The position of the acetyl functions was realized from ^3J correlations of H5/H5′ to C13/C13′ and of $(H12')_2$ to C15′, thus indicating the loss of the acetyl function present at 12-OH in **1**. Furthermore, ROESY correlations among H5/H5′, H6/H6′, and $(H12)_2$/$(H12')_2$ indicated their cofacial orientation. Analysis of coupling constants indicated that H6 ($J_{6,7\beta}$ = 10 Hz) and H5 ($J_{5,6}$ = 1.7 Hz) are in axial and equatorial positions, respectively. Compound **4** was thus identified as the new natural product 12-deacetylphomoxanthone A (Figure 1). The ECD spectrum of **4** was found to be quite different from that of phomoxanthone A (**1**) above 240 nm. A broad positive CE at 346 nm and weak negative plateau between 274 and 310 nm were observed for **4** instead of the negative CE at 341 nm and the positive CE at 316 nm for **1**. These differences are attributed to the lack of the acetoxy group, which changes the preferred biaryl dihedral angle as demonstrated by dicerandrols B and C.

HR-ESI-MS analysis of the new compound **5** showed the molecular ion peak at *m*/*z* 289.0707 $[M + H]^+$, indicating the molecular formula $C_{15}H_{12}O_6$. The ^{1}H NMR spectrum (Table 2) exhibited two aromatic *meta*-coupled protons at δ_H 6.88 (H6) and 6.73 (H8), one olefinic proton singlet at δ_H 6.27 (H5′), one aliphatic oxygenated methylene group at δ_H 5.15 $[(H2)_2]$, one methyl group at δ_H 2.38 (4′-CH_3), and one methoxy group at δ_H 3.91 (7-OCH_3). The ^{13}C NMR spectrum (Table 2) displayed 15 carbon atoms, including a keto group, an ester carbonyl group, 10 olefinic carbon signals (including four oxygenated carbons), one oxygenated methylene, one methoxy group, and one methyl group. The COSY spectrum revealed the *meta*-coupled protons H6 and H8 as well as a long-range coupling between 4′-CH_3 and H5′ (Figure 6). HMBC measurements (Figure 6) confirmed the presence of a chromone moiety from the observed correlations of H8 to C4a, C6, C7, and C8a; H6 to C4a, C5, C7, and C8; and $(H2)_2$ to C1′, C4, C4a, and C8a. The oxofuranylidene moiety was deduced from the correlations of H5′ to C2, C3, C4, C3′, and 4′-CH_3 and 4′-CH_3 to C3′ and C5′. The position of the methoxy group was confirmed by its correlation to C7. Furthermore, analysis of the ROESY spectrum allowed the assignment of the stereochemistry around the C3=C1′ double bond. The absence of a cross-peak between $(H2)_2$ and H5′ indicated spatial separation of these protons and thus an *E* configuration of the double bond in **5**, for which we suggest the name phomo-2,3-dihydrochromone (Figure 1).

Compounds **6** and **7** shared the same molecular formula of $C_{15}H_{12}O_6$, as indicated by their HR-ESI-MS data (*m*/*z* 289.07028 $[M + H]^+$). ^{1}H and ^{13}C NMR, COSY, and HMBC data (Table 3 and Figure 6) indicated that **7** was identical and **6** was closely related to the known compound monodictyphenone.[52] The HMBC correlations of 11-CH_3 to C5, C6, and C7 unambiguously showed that the methyl group is attached at C6 of the symmetric dihydroxyphenyl moiety in **6**, in contrast to **7**, where the methyl substituent is located at C3. This could be explained by cleavage of the presumed anthraquinone precursor emodin either between C4a and C10 or C10a and C10, resulting in **6** or **7**, respectively (Scheme 1). Accordingly, **6** was identified as a new natural product for which we suggest the name isomonodictyphenone (Figure 1).

In addition to the previously described natural products, the known compound endocrocin (**8**) was isolated and identified by comparison of its UV, NMR, and mass spectral data with published values.[53,54]

The biosynthetic relationship between the secondary metabolites of polyketide origin, including monomeric and dimeric xanthone derivatives, has been the subject of intensive investigations.[21,55−57] The polyketides isolated from *P. longicolla* in this study are assumed to be derived from a C_{16}-octaketide that undergoes condensation and cyclization to yield anthraquinone precursors such as endocrocin (**8**) or emodin, even though the latter was not isolated in this study. Emodin may be enzymatically transformed into monodictyphenone (**7**) by oxidative ring opening[58−62] between C4a and C10. Isomonodictyphenone (**6**) most likely originates in the same way by cleavage of the covalent C10−C10a bond of emodin. Benzophenones can be enzymatically converted into xanthones by oxidative phenolic coupling, which is followed by dimerization to yield phomoxanthones, dicerandrols, and similar compounds, as proposed for secalonic acids by Kurobane et al.[57] Breinholt et al.[63] showed that the triketide xanthofusin emerges from an aromatic precursor by oxidative ring opening, which may explain the formation of the oxofuranylidene substructure in phomo-2,3-dihydrochromone

dx.doi.org/10.1021/jo402066b | *J. Org. Chem.* 2013, 78, 12409−12425

Table 1. ^{1}H and ^{13}C NMR, COSY, and HMBC Data for 4 at 600 (^{1}H) or 75 (^{13}C) MHz (MeOH-d_4, δ in ppm, J in Hz)

atom	δ_H	δ_C	COSY	HMBC
1		162.5		
2	6.46, *d* (8.7)	110.3	3	1, 4, 4a, 9, 9a
3	7.41, *d* (8.7)	142.4	2	1, 4′, 4a, 9a
4		116.8		
4a		155.3		
5	5.59, *d* (1.7)	72.5	6	6, 7, 8a, 10a, 11, 12, 13
6	2.49, *m*	29.1	5, 7, 11	7, 11
7	2.49, *dd* (6.2, 18.0)	34.1	6, 7, 11	5, 6, 8, 8a
	2.33, *dd* (10.0, 18.0)			6, 8, 8a, 11
8		178.8		
8a		102.0		
9		189.1		
9a		107.5		
10a		83.8		
11	1.00, *d* (6.4)	17.7	6, 7	5, 6, 7
12	3.87, *d* (13.2)	65.5	12	5
	3.53, *d* (13.2)			5, 8a, 10a
13		171.9		
14	2.10, *s*	20.7		13
1′		162.5		
2′	6.43, *d* (8.7)	109.6	3′	1′, 4′, 4a′, 9′, 9a′
3′	7.33, *d* (8.7)	142.0	2′	1′, 4, 4a′, 9a′
4′		116.8		
4a′		155.8		
5′	5.49, br. *s*	71.7	6′	6′, 7′, 8a′, 10a′, 11′, 12′, 13′
6′	2.49, *m*	28.8	5′, 7′, 11′	7′, 11′
7′	2.54, *dd* (5.5, 17.5)	34.1	5′, 6′, 7′, 11′	5′, 6′, 8′, 8a′
	2.35, *dd* (10.0, 17.5)		5′, 6′, 7′, 11′	6′, 8′, 8a′, 11′
8′		179.4		
8a′		100.1		
9′		189.1		
9a′		107.6		
10a′		82.3		
11′	1.01, *d* (6.5)	17.7	6′, 7′	5′, 6′, 7′
12′	4.78, *d* (12.9)	65.5	12′	5′, 10a′, 15′
	4.01, *d* (12.9)			5′, 8a′, 10a′, 15′
13′		171.9		
14′	2.11, *s*	20.8		13′
15′		172.4		
16′	1.75, *s*	20.4		15′

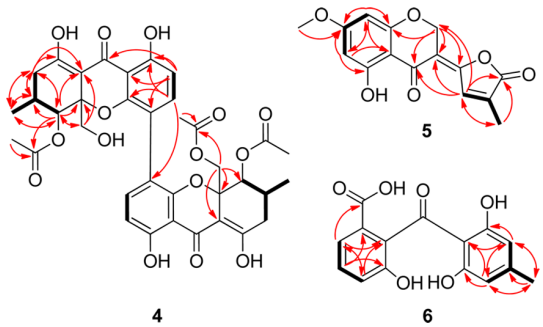

Figure 6. Key COSY (bold black bonds) and HMBC (red arrows) correlations in **4**–**6**.

(**5**). Accordingly, a plausible biosynthetic pathway for the polyketides isolated in this study could be depicted as shown in Scheme 1.

Table 2. ^{1}H and ^{13}C NMR, COSY, and HMBC Data for 5 at 300 (^{1}H) or 100 (^{13}C) MHz (MeOH-d_4, δ in ppm, J in Hz)

atom	δ_H	δ_C	COSY	HMBC
2	5.15, *s*	63.6		1′, 3, 4, 4a, 8a
3		113.3		
4		178.3		
4a		107.6		
5		172.0		
6	6.88, *d* (2.5)	111.2	8	4a, 5, 7, 8
7		165.2		
8	6.73, *d* (2.4)	104.3	6, 7-OCH_3	4a, 6, 7, 8a
8a		161.3		
1′		157.5		
3′		167.7		
4′		114.3		
5′	6.27, *s*	114.3	4′-CH_3	2, 3, 4, 3′, 4′-CH_3
7-OCH_3	3.91, *s*	56.5	8	7
4′-CH_3	2.38, *s*	19.2	5′	3′, 5′

dx.doi.org/10.1021/jo402066b | J. Org. Chem. 2013, 78, 12409−12425

Table 3. ^{1}H and ^{13}C NMR, COSY, and HMBC Data for 6 at 600 (^{1}H) or 100 (^{13}C) MHz (MeOH-d_4, δ in ppm, J in Hz)

atom	δ_H	δ_C	COSY	HMBC
1		130.0[a]		
2	7.53, *dd* (1.0, 7.9)	122.0	3, 4	4, 9a, 10
3	7.28, *t* (7.9)	129.5	2, 4	1, 4a
4	7.05, *dd* (1.0, 7.9)	120.8	2, 3	2, 9a
4a		154.6		
5	6.16,[b] *s*	108.7[c]	11	7, 8a, 10a, 11
6		149.0[a]		
7	6.16,[b] *s*	108.7[c]	11	5, 8, 8a, 11
8		163.4[d]		
8a		110.1[a]		
9		–[e]		
9a		135.0[a]		
10		169.2		
10a		163.4[d]		
11	2.24, *s*	21.5	5, 7	5, 6, 7

[a]No ^{13}C NMR signal was detected; the chemical shift was deduced from the HMBC correlation. [b,c,d]Superimposed signals due to chemical equivalence. [e]No ^{13}C NMR signal was detected.

Scheme 1. Putative Biosynthetic Pathway for the Polyketides 1–8

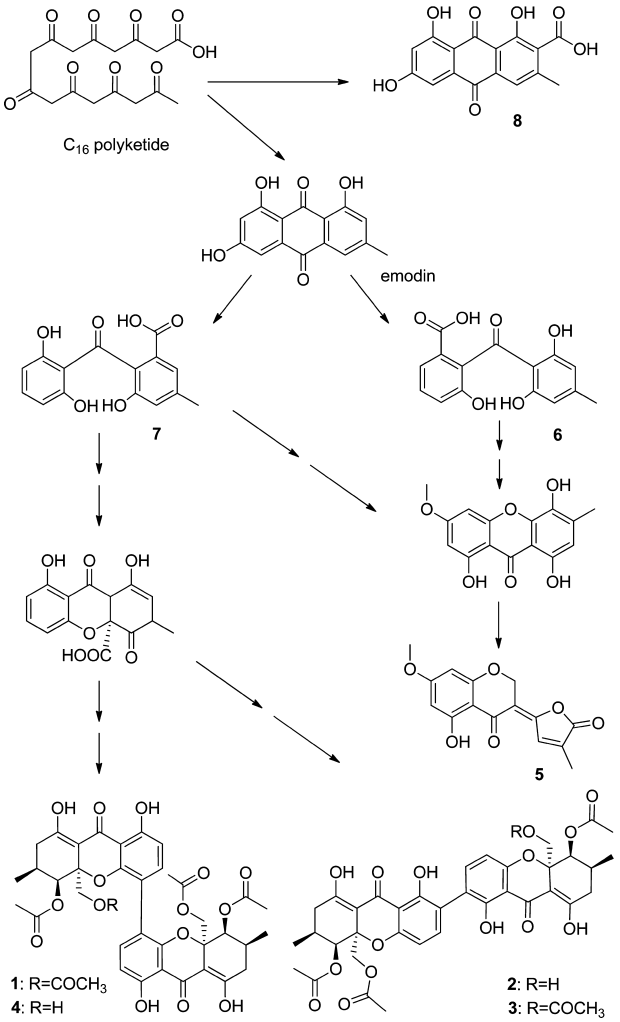

To increase the chemical diversity of congeners for a first evaluation of structure–activity relationships, the dominant natural product phomoxanthone A (**1**) was subjected to acidic and alkaline hydrolysis. Acidic hydrolysis according to the method described by Isaka et al.[44] resulted in the formation of **11**, a previously described deacetyl analogue of **1**. On the other hand, alkaline hydrolysis of **1** with alcoholic NaOH at room temperature yielded the new derivatives **9a–c**, whereas treatment of **1** with aqueous NaOH under reflux resulted in the formation of a single new derivative (**10**). By analogy with **11**, **9a–c** showed a difference of 168 amu relative to **1** upon mass spectral analysis, corresponding to the loss of four acetate functions. However, inspection of the NMR data indicated further structural rearrangements in the core structures of **9a–c**.

The molecular formula of **9a** was assigned as $C_{30}H_{30}O_{12}$ on the basis of HR-ESI-MS data showing the molecular ion peak at m/z 583.18110 $[M + H]^+$. The ^{1}H NMR spectrum (Table 4) revealed two almost identical sets of signals, indicating an asymmetrical dimeric structure composed of closely related monomers. It exhibited two aromatic and two aliphatic hydroxy groups resonating at δ_H 12.01 (1-OH), 11.74 (1′-OH), 5.45 (12′-OH), and 5.35 (12-OH). Signals of the aromatic protons appeared at δ_H 7.37 (H3′), 7.34 (H3), 6.50 (H2′), and 6.44 (H4), thus indicating two sets of *ortho*-coupled protons, as found in the biaryl units of other phomoxanthone derivatives.[44] In total, six methylene groups were detected at δ_H 3.75/3.66 [(H12′)$_2$], 3.66 [(H12)$_2$], 3.18/2.83 [(H8a)$_2$], 3.10/3.06 [(H8a′)$_2$], 2.78/2.20 [(H7′)$_2$], and 2.25/1.93 [(H7)$_2$]. The remaining signals were assigned to two oxymethine protons at δ_H 4.39 (H5′) and 4.21 (H5), two tertiary methine groups at δ_H 2.87 (H6′) and 2.72 (H6), and two methyl groups at δ_H 1.15 (11′-CH$_3$) and 1.02 (11-CH$_3$). Thorough analyses of HMBC spectral data (Table 4 and Figure 7) allowed the construction of two partially saturated γ-pyrone moieties annulated to the aromatic rings. The involved methylene groups (8a-CH$_2$/8a′-CH$_2$) showed correlations to the sp^2 carbons C9a/C9a′, the carbonyl carbons C9/C9′, and the sp^3 carbons C10a/C10a′. According to the molecular formula, the unsaturation index of **9a** is 16. The presence of four carbonyl groups [δ_C 197.7 (C9′), 197.5 (C9), 175.9 (C8), and 175.7 (C8′)] and the tetracyclic biaryl scaffold accounted for 14 elements of unsaturation, thus indicating that the remaining part of **9a** should include two aliphatic ring systems. The structures of the latter were established by exhaustive analyses of the 2D NMR spectral data (Figure 7). Correlations of the tertiary methine protons H6/H6′ to the oxymethines H5/H5′, the methylene groups 7-CH$_2$/7′-CH$_2$, and the methyl groups 11-CH$_3$/11′-CH$_3$ were observed in the COSY spectrum, thus establishing the fragments 5-CH–6-CH(11-CH$_3$)–7-CH$_2$ and 5′-CH–6′-CH(11′-CH$_3$)–7′-CH$_2$. Moreover, the HMBC spectrum provided a full set of all possible ^2J and ^3J correlations for H5/H5′, H6/H6′, and (H7)$_2$/(H7′)$_2$, confirming the fragment deduced from the COSY spectrum and allowing the construction of two 3-methyl-γ-butyrolactone moieties on the basis of the correlations observed from H5/H5′ and (H7)$_2$/(H7′)$_2$ to C8/C8′. The two 3-methyl-γ-butyrolactone rings were found to be linked to the tetracyclic biaryl skeleton at C10a and C10a′, as indicated by the ^3J correlations of the tertiary methine protons H5/H5′ to C10a/C10a′. The 2,4′-linkage in the biaryl system was proven by HMBC correlations of H3 to C4′; H3′ to C2; and 1-OH/1′-OH to C1/C1′, C2/C2′, and C9a/C9a′. The two oxymethine protons (H5/H5′)

dx.doi.org/10.1021/jo402066b | J. Org. Chem. 2013, 78, 12409–12425

Table 4. ^{1}H and ^{13}C NMR, COSY, and HMBC Data for 9a–c at 600 (^{1}H) or 100 (^{13}C) MHz (DMSO-d_6, δ in ppm, J in Hz)

	9a				9b				9c			
atom	δ_H	δ_C	COSY	HMBC	δ_H	δ_C	COSY	HMBC	δ_H	δ_C[a]	COSY	HMBC
1		157.7				157.5				159.2		
2		116.1				116.4				115.6		
3	7.34, *d* (8.5)	139.5	4	1, 4′, 4a	7.35, *d* (8.5)	139.8	4	1, 4′, 4a	7.33, *d* (8.5)	136.2	4	1, 2′, 4a
4	6.44, *d* (8.5)	106.8	3	2, 4a, 9, 9a	6.52, *d* (8.6)	106.7	3	2, 4a, 9, 9a	6.47, *d* (8.5)	105.6	3	2, 4a, 9a
4a		158.5				157.8				157.2		
5	4.21, *d* (3.6)	86.3	6	6, 8, 10a, 11	4.37, *d* (4.7)	87.1	6	6, 8, 8a, 10a, 11, 12	4.33, *d* (4.7)	86.7	6	6, 8, 10a, 11
6	2.72, *m*	28.7	5, 7, 11		2.86, *m*	28.7	5, 7, 11	8, 11	2.82, *m*	27	5, 7, 11	
7	2.25, *dd* (9.2, 17.9)	35.4	6, 7	5, 6, 8, 11	2.77, *dd* (9.4, 17.8)	35.9	6, 7	5, 6, 8, 11	2.74, *dd* (9.3, 17.7)	34.8	6, 7	5, 6, 8, 11
	1.93, *dd* (4.3, 17.9)				2.23, *dd* (5.5, 17.8)				2.19, *dd* (5.5, 17.7)			
8		175.9				175.7				175.6		
8a	3.18, *d* (17.2)	37.1	8a	5, 9, 9a, 10a, 12	3.16, *d* (17.5)	38.6	8a	5, 9, 9a, 10a, 12	3.15, *d* (17.4)	37.6	8a	5, 9, 10a, 12
	2.83, *d* (17.2)				3.05, *d* (17.3)				2.93, *d* (17.4)			
9		197.5				197.6				196.6		
9a		106.6				106.6				105.7		
10a		83.8				83.8				82.8		
11	1.02, *d* (7.0)	20.4	6	5, 6, 7	1.16, *d* (6.8)	20	6	5, 6, 7	1.12, *d* (6.8)	19.4	6	5, 6, 7
12	3.66, *d* (4.7)	61.3	12-OH	5, 8a, 10a	3.71, *dd* (5.1, 11.6)	62.5	12, 12-OH	5, 8a, 10a	3.65, *dd* (4.9, 11.7)	62.2	12, 12-OH	5, 8a, 10a
					3.65, *dd* (5.2, 11.8)				3.63, *dd* (4.9, 11.7)			
1-OH	12.01, *s*			1, 2, 9a	11.97, *s*			1, 2, 9a	11.95, *s*			1, 2, 9a
12-OH	5.35, *t* (5.0)		12	10a	5.49, *t* (5.2)		12	10a, 12	5.47, *t* (5.0)		12	10a
1′		160				158.8				159.2		
2′	6.50, *d* (8.5)	107.9	3′	1′, 4′, 9a′	6.50, *d* (8.8)	108.1	3′	1′, 4′, 9a′		115.6		
3′	7.37, *d* (8.5)	139.8	2′	1′, 2, 4a′	7.33, *d* (8.5)	139.8	2′	1′, 2, 4a′	7.33, *d* (8.5)	136.2	4′	1′, 2, 4a′
4′		115.1				115.3			6.47, *d* (8.5)	105.6	3′	2′, 4a′, 9a′
4a′		156.1				156.1				157.2		
5′	4.39, *d* (4.7)	87.4	6′	6′, 8′, 10a′, 11′	4.22, *d* (3.9)	86.3	6′	6′, 8′, 10a′, 11′	4.33, *d* (4.7)	86.7	6′	6′, 8′, 10a′, 11′
6′	2.87, *m*	28.6	5′, 7′, 11′		2.51, *m*	28.2	5′, 7′, 11′		2.82, *m*	27	5′, 7′, 11′	
7′	2.78, *dd* (9.4, 17.8)	35.9	6′, 7′	5′, 6′, 8′, 11′	2.13, *dd* (9.4, 17.9)	35.4	6′, 7′	5′, 6′, 8′, 11′	2.74, *dd* (9.3, 17.7)	34.8	6′, 7′	5′, 6′, 8′, 11′
	2.20, *dd* (5.4, 17.8)				1.96, *dd* (4.7, 17.9)				2.19, *dd* (5.5, 17.7)			
8′		175.7				175.9			–	175.6		
8a′	3.10, *d* (17.3)	38.8	8a′	5′, 9′, 10a′, 12′	3.21, *d* (17.3)	38.3	8a′	5′, 9′, 9a′, 10a′, 12′	3.15, *d* (17.4)	37.6	8a′	5′, 9′, 10a′, 12′
	3.06, *d* (17.3)				2.86, *d* (17.1)				2.93, *d* (17.4)			
9′		197.7				197.7				196.6		
9a′		107.1				106.9				105.7		
10a′		83.6				83.7				82.8		
11′	1.15, *d* (6.8)	20	6′	5′, 6′, 7′	1.01, *d* (7.0)	20.2	6′	5′, 6′, 7′	1.12, *d* (6.8)	19.4	6′	5′, 6′, 7′
12′	3.75, *dd* (5.0, 11.7)	62.1	12′, 12′-OH	5′, 8a′, 10a′	3.66, *dd* (5.0, 11.6)	61.6	12′, 12′-OH	5, 8a′, 10a′	3.65, *dd* (4.9, 11.7)	62.2	12′, 12′-OH	5′, 8a′, 10a′
	3.66, *dd* (5.0, 11.7)				3.58, *dd* (5.3, 11.6)				3.63, *dd* (4.9, 11.7)			
1′-OH	11.74, *s*			1′, 2′, 9a′	11.72, *s*			1′, 2′, 9a′	11.95, *s*			1′, 2′, 9a′
12′–OH	5.45, *t* (5.3)		12′	10a′	5.43, *t* (5.2)		12′	10a′, 12′	5.47, *t* (5.0)		12′	10a′

[a]Chemical shifts deduced from HMBC correlations.

dx.doi.org/10.1021/jo402066b | J. Org. Chem. 2013, 78, 12409–12425

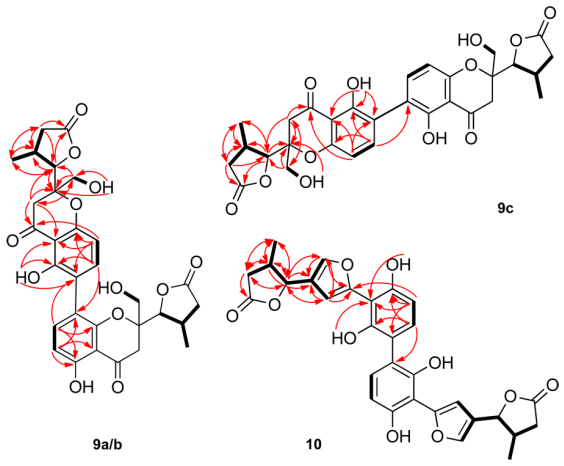

Figure 7. Key COSY (bold black bonds) and HMBC (red arrows) correlations in **9a–c** and **10**.

were coupled to the corresponding tertiary methine protons (H6/H6′) with coupling constants of $J_{5,6}$ = 3.6 Hz and $J_{5',6'}$ = 4.7 Hz, characteristic of *trans*-oriented protons in these ring systems.[64] This finding was supported by detailed analysis of the ROESY spectrum, which showed strong correlations between H5/H5′ and the methyl protons (11-CH_3/11′-CH_3), thus unambiguously confirming their *cis* orientation. In addition, the ROESY correlations between the methylene groups 12-CH_2/12′-CH_2 and H8aβ/H8a′β, H5/H5′, H6/H6′ and 11-CH_3/11′-CH_3 as well as the absence of strong correlations to 7-CH_2/7′-CH_2 indicated an α orientation of the 3-methyl-γ-butyrolactone rings, as reported for the structurally related compound blennolide E.[65]

Compound **9b** showed UV, HR-ESI-MS, and 1D and 2D NMR spectra (Figure 7) that were almost identical to those of **9a**. The presence of the same sets of signals in the ^{1}H and ^{13}C NMR spectra indicated the same dimeric structural scaffold. Furthermore, ROESY spectra of **9b** revealed the same relative stereochemistry as in **9a**. However, the distinct difference in the measured $[\alpha]_D$ values (+6° for **9a** and −28° for **9b**) indicated stereochemical differences between the two molecules. Their solution ECD spectra had opposite CEs below 330 nm and positive CEs at about 350 nm, which suggested that they are atropodiastereomers with the same absolute configuration in the chromanone ring. In contrast to **9a** and **9b**, compound **9c** showed only one set of ^{1}H and ^{13}C NMR signals (Table 4), indicating a symmetrical dimer. Analysis of the 2D NMR spectra (Figure 7) revealed the same monomeric building units as in **9a** and **9b**. However, a 2,2′-linkage within the biaryl system was established by the HMBC correlations observed from H4/H4′ to C2/C2′, C4a/C4a′, and C9a/C9a′; from H3/H3′ to C1/C1′, C2′/C2, and C4a/C4a′; and from 1/1′-OH to C1/C1′, C2/C2′, and C9a/C9a′. On the basis of the $[\alpha]_D$ value ($[\alpha]_D^{20}$ = −68°) and the ROESY spectrum, which showed the same correlations as observed for **9a** and **9b**, the relative configuration of **9c** was established as depicted in Figure 1.

The molecular formula of **10** was determined from HR-ESI-MS data as $C_{30}H_{26}O_{10}$ (*m*/*z* 547.1603 $[M + H]^+$), implying 18 degrees of unsaturation as well as molecular weight decreases of 204 and 36 amu relative to **1** and **9a–c**, respectively. Detailed analysis of the NMR spectra of **10** revealed that the compound is a symmetrical dimer (Table 5 and Figure 7). Furthermore, comparison of the 1D and 2D NMR spectral data of **10** to those of **9c** illustrated similar structural features of the two compounds. The symmetrical biaryl system, including four *ortho*-coupled protons at δ_H 6.94 (H3/H3′) and 6.51 (H2/H2′), as well as the 3-methyl-γ-butyrolactone moieties were retained in **10**. The corresponding signals of the tertiary methine, methylene, and oxymethine protons of the lactone moieties appeared at δ_H 2.65 (H6/H6′), 2.76/2.43 [$(H7)_2$/$(H7')_2$], and 5.05 (H5/H5′), respectively. A significant difference in the ^{1}H NMR spectrum of **10** compared with that of **9c** was the disappearance of the methylene groups 8a-CH_2/8a′-CH_2 and 12-CH_2/12′-CH_2 and the presence of two additional signals at δ_H 6.66 (H8a/H8a′) and 7.82 (H12/H12′) that were assigned to the olefinic protons. The ^{13}C NMR spectrum of **10** showed 15 signals, corresponding to two carbonyl carbons at δ_C 176.0 (C8/C8′); 20 olefinic carbons at

Table 5. ^{1}H and ^{13}C NMR, COSY, and HMBC Data for 10 at 600 (^{1}H) or 100 (^{13}C) MHz (DMSO-d_6, δ in ppm, *J* in Hz)

atom	δ_H	δ_C	COSY[a]	HMBC[a]
1/1′		155.4		
2/2′	6.51, *d* (8.3)	107.4	3	1, 4, 9, 9a
3/3′	6.94, *d* (8.4)	131.8	2	1, 4′, 4a
4/4′		118.5		
4a/4a′		152.1		
5/5′	5.05, *d* (8.7)	80.3	6, 12	6, 7, 8a, 10a, 11, 12
6/6′	2.65, *m*	36.9	5, 7, 11	5, 7, 10a, 11
7/7′	2.76, *dd* (7.9, 17.0)	36.6	6, 7	5, 6, 8, 11
	2.43, *dd* (10.3, 17.0)			
8/8′		176.0		
8a/8a′	6.66, *s*	109.3	12	5, 9, 10a, 12
9/9′		149.3		
9a/9a′		106.8		
10a/10a′		123.5		
11/11′	1.10, *d* (6.5)	15.9	6	5, 6, 7
12/12′	7.82, *s*	139.7	5, 8a	8a, 10a, 9
1/1′-OH	9.6, *s*			9a
4a/4a′-OH	9.48, *s*			9a

[a]Correlations are listed for only one monomeric building unit.

dx.doi.org/10.1021/jo402066b | J. Org. Chem. 2013, 78, 12409–12425

δ_C 155.4 (C1/C1′), 152.1 (C4a/C4a′), 149.3 (C9/C9′), 139.7 (C12/C12′), 131.8 (C3/C3′), 123.5 (C10a/C10a′), 118.5 (C4/C4′), 109.3 (C8a/C8a′), 107.4 (C2/C2′), and 106.8 ppm (C9a/9a′); two oximethines at δ_C 80.3 (C5/C5′); and six aliphatic carbons at δ_C 36.9 (C6/C6′), 36.6 (C7/C7′), and 15.9 (C11/C11′). The HMBC spectrum (Figure 7) disclosed correlations of H8a/H8a′ and H12/H12′ to C12/C12′ and C8a/C8a′, respectively, and to both C9/C9′ and C10a/C10a′. These data allowed the construction of two furan rings located between the already identified structural elements, as evidenced by ^3J correlations from H8a/H8a′ to C5/C5′ and H6/H6′ to C10a/C10a′ and by ^4J correlations from the aromatic protons H2/H2′ to C9/C9′. Furthermore, the 4,4′-linkage of the aromatic rings in **10** was deduced from the strong ^3J correlations of H3 and H3′ to C4′ and C4, respectively. In analogy to **9a−c**, strong ROESY correlations between the oxymethine protons (H5/H5′) and the methyl groups (11-CH_3/11′-CH_3) confirmed the *trans* orientation of H5/H5′ and H6/H6′ in the terminal lactone rings.

Initial experiments employing a crude EtOAc extract of *P. longicolla* following cultivation on rice resulted in complete inhibition of the growth of the murine lymphoma cell line L5178Y (at a dose of 10 μg/mL), as indicated by an MTT assay (data not shown). When compounds **1−11** were assayed for their activity in the same cell line (Table 6), the dimeric tetrahydroxanthone derivatives (**1−4**) were found to be active, with IC_{50} values in the range 0.3−10 μM (Table 6). These results were in accordance with the published cytotoxic activity of **1** toward mouth epidermal carcinoma (KB) and lymphoma (BC1) cells and of **2** and **3** against lung (A549) and colon (HCT116) carcinoma cells.[44,45] The remaining compounds showed no activity. The 4,4′-linked substances phomoxanthone A (**1**) and 12-deacetylphomoxanthone A (**4**) featured IC_{50} values of 0.3 and 2.8 μM, respectively, whereas values of 1.1 and 10.0 μM were detected for the corresponding 2,2′-linked derivatives dicerandrol C (**3**) and dicerandrol B (**2**), respectively. These results indicated that the cytotoxic potential of this class of compounds is enhanced by a 4,4′-linkage of the tetrahydroxanthone monomers (**1** vs **3**) and decreased upon loss of acetyl groups (**1** vs **4** and **11**; **2** vs **3**). Deacetylphomoxanthone A (**11**) showed no activity against L5178Y mouse lymphoma cells, which may at least partly be due to the lower lipophilicity and hence hindered transmembrane diffusion of the deacetylated compound compared with the acetylated phomoxanthone A (logP = 2.230 for **1** vs logP = 0.125 for **11**). Alternatively, phomoxanthone A (**1**) may have a favored pharmacophore, whereas the deacetylated congener **11** may have no or less affinity to the respective target. The structural modifications of phomoxanthone A (**1**) caused by alkaline hydrolysis to afford compounds **9a−c** and **10** resulted in complete loss of activity (Table 6), implying that the dimeric tetrahydroxanthenone core structure is mandatory for cytotoxic activity. Phomoxanthone A (**1**), which proved to be the most active compound isolated in this study, was subjected to further in vitro assays using different human cancer cell lines, including both cisplatin-sensitive and -resistant cells (Table 6). The chosen cell lines included the human ovarian carcinoma A2780, human tongue Cal27, and human esophagus Kyse510 cell lines. Remarkably, **1** showed almost the same potency against both anticancer-drug-sensitive and -resistant cell lines (Table 6). In order to probe the selectivity of **1** against cancer cells versus normal cells, we tested its effect on the human Burkitt's lymphoma cell line DG75 and the human T cell lymphoma cell line Jurkat versus healthy human peripheral blood mononuclear cells (PBMCs). The results showed that **1** is highly selective against cancer cells, as it is over 100-fold less toxic to PBMCs (IC_{50} = 61.2 μM) compared with DG75 (IC_{50} = 0.1 μM) and Jurkat (IC_{50} = 0.5 μM) (Table 6).

In order to characterize the cytotoxic effect of the dimeric tetrahydroxanthone derivatives in more detail with regard to their mode of action, we analyzed the apoptosis-inducing potential of the lead compound phomoxanthone A (**1**) for the first time. Apoptosis is the programmed form of cell death, and it is central to many developmental and immunological processes. It is accompanied by specific molecular events, including the activation of aspartate-directed cysteine proteases (caspases) or fragmentation of chromosomal DNA. First we assessed the amount of apoptotic hypodiploid nuclei upon phomoxanthone A treatment of human DG75 B lymphocytes or Jurkat T lymphocytes. Hypodiploid nuclei are indicative of DNA fragmentation caused by the activation of caspases. Phomoxanthone A (**1**) significantly increased the amount of hypodiploid nuclei in both cell lines at a concentration of 1 μM (Figure 8A). This effect could be entirely blocked by the addition of the caspase inhibitor *N*-(2-quinolyl)valyl-aspartyl-(2,6-difluorophenoxy)methyl ketone (Q-VD-OPh) (Figure 8A). Next, we analyzed the activation of caspases by detection of the proteolytic processing of the caspase substrate poly(ADP-ribose) polymerase (PARP) by immunoblotting. Cleavage of PARP could be detected in both DG75 B cells and Jurkat T cells upon phomoxanthone A treatment, and again this effect could be entirely blocked by the addition of Q-VD-OPh (Figure 8B). Finally, we assessed the apoptosis-inducing capacities of compounds **1−11** by flow cytometric analyses of hypodiploid nuclei in Jurkat T cells. The dimeric tetrahydroxanthone derivatives were the most potent substances, thus

Table 6. Cytotoxic Activities of the Isolated Compounds

compound	L5178Y growth (%) (conc = 10 μg/mL)	IC_{50} (μM)[a]
1	1.2	0.3
2	6.6	10
3	0.5	1.1
4	0.5	2.8
5	85.6	
6	92.6	
7	100	
8	100	
9a	90.7	
9b	97.4	
9c	89.2	
10	100	
11	100	

	IC_{50} (μM) in Various Cell Lines[a,b]					
	Cal27		Kyse510		A2780	
compound	sens	CisR	sens	CisR	sens	CisR
1	5.2	5.6	0.8	0.8	0.7	0.9
Cisplatin	7.8	41.4	2.5	8.4	1.2	10.2

Selectivity of **1**			
cell line	DG75	Jurkat	PBMC
IC_{50} (μM)[c]	0.1	0.5	61.2

[a]Incubation for 72 h. [b]Abbreviations: sens, sensitive to cisplatin; CisR, cisplatin-resistant. [c]Incubation for 48 h.

dx.doi.org/10.1021/jo402066b | J. Org. Chem. 2013, 78, 12409−12425

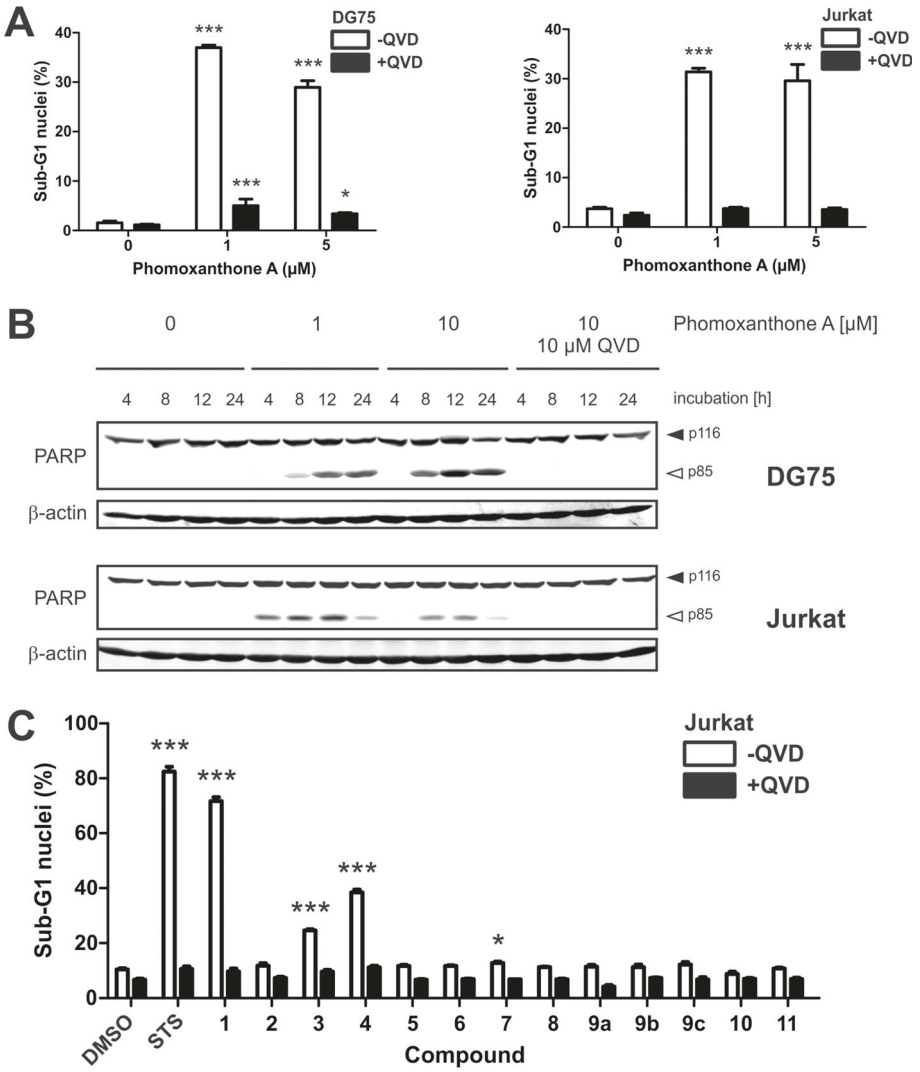

Figure 8. Apoptosis induction by dimeric tetrahydroxanthenone derivatives. (A) DG75 B cells (left panel) and Jurkat T cells (right panel) were treated with the indicated concentrations of phomoxanthone A (**1**) in the absence or presence of the caspase inhibitor Q-VD-OPh (10 μM) for 24 h. Subsequently, apoptosis was assessed by propidium iodide staining of hypodiploid apoptotic nuclei and flow cytometry. (B) DG75 B cells (upper panels) and Jurkat T cells (lower panels) were treated with the indicated concentrations of phomoxanthone A (**1**) in the absence or presence of 10 μM Q-VD-OPh for the indicated times. Cleared cellular lysates were analyzed for PARP and β-actin by immunoblotting. Solid arrowheads indicate the uncleaved form of PARP, and open arrowheads indicate the cleaved form. (C) Jurkat T cells were incubated with 0.1% DMSO (negative control), 2.5 μM staurosporine (STS; positive control), or 10 μM **1**−**11** in the absence or presence of 10 μM Q-VD-OPh for 24 h. Apoptosis was then assessed by propidium iodide staining of hypodiploid apoptotic nuclei and flow cytometry. The analyses in (A) and (C) were performed in triplicate; error bars = SD; p values were calculated by two-way ANOVA with the Bonferroni post-test; * = $p < 0.05$, ** = $p < 0.01$, *** = $p < 0.001$.

confirming the data obtained from the cytotoxicity assay with the L5178Y cell line (Table 6). The 4,4′-linked derivatives phomoxanthone A (**1**) and 12-deacetylphomoxanthone A (**4**) showed the highest activities (Figure 8C). Again, modifications of the tetrahydroxanthone core structure as in **9a**−**c** and **10** abrogated the pro-apoptotic effect. Collectively, these results indicate that the dimeric tetrahydroxanthone core structure is essential for the induction of apoptosis and hence the cytotoxic effect against cancer cells.

Since **1** displayed a cytotoxic potential in tumor cells but not in primary immune cells (PBMCs) (Table 6), we further examined whether the dimeric tetrahydroxanthone derivatives might in contrast affect the activation of immune cells such as primary B and T lymphocytes, NK cells, and macrophages. Therefore, we tested the compounds for their ability to activate immune effector functions as measured by upregulation of cell-type-specific activation markers on the respective murine immune cell subpopulations (Figure 9A). In analogy to the findings of the cytotoxicity assays, titrated concentrations of the two 4,4′-linked dimeric tetrahydroxanthone derivatives phomoxanthone A (**1**) and 12-deacetylphomoxanthone A (**4**) induced the most prominent upregulation of the early-activation antigen CD69 on primary murine T lymphocytes. Specifically, 1.8-fold and 1.4-fold increases in the percentage of $CD69^+$ T cells, respectively, were observed after incubation for 12 h with these substances at a concentration of 1 μM. The 2,2′-linkage of the tetrahydroxanthone monomers completely abolished the T cell activatory function or induced CD69 upregulation only at the highest concentration of 10 μM, as for **2** and **3**, respectively. Furthermore, the complete absence of

dx.doi.org/10.1021/jo402066b | J. Org. Chem. 2013, 78, 12409−12425

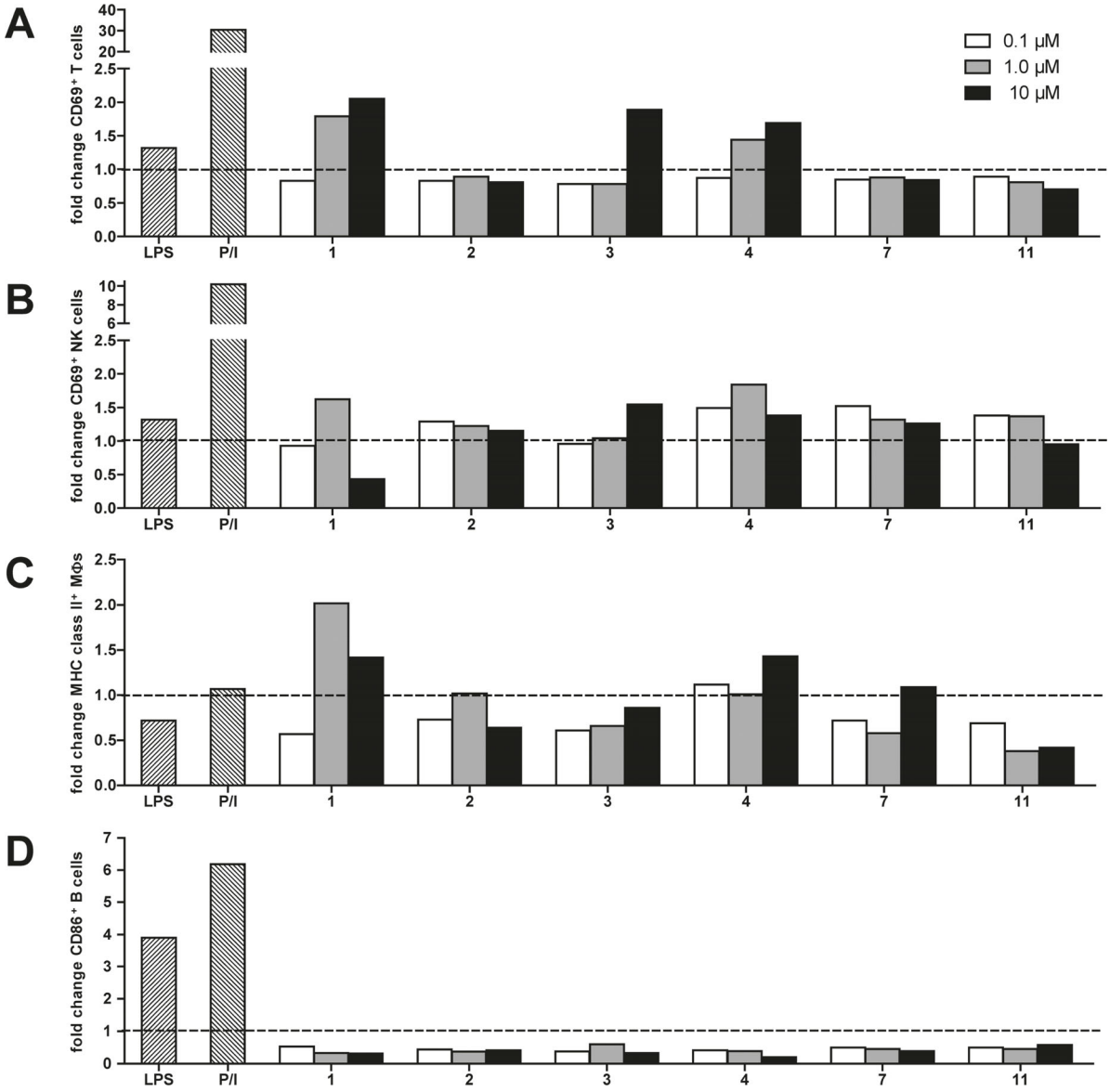

Figure 9. Immunostimulatory capacities of selected tetrahydroxanthenone derivatives. Single cell suspensions from whole spleens of C57BL/6 mice were incubated for 12 h with the indicated concentration of **1**–**4**, **7**, or **11**, 0.1% DMSO (negative control), LPS (positive control), or PMA and ionomycin (P/I; positive control). Cell activation was measured by flow cytometry as the expression of the surface markers CD69 on T cells (A) and NK cells (B), MHC class II on MΦs (C), and CD86 on B cells (D), and the results are given as fold increase relative to the DMSO negative control. Shown are one representative of two independent experiments for **2**–**4**, **7**, and **11** and of three independent experiments for **1**.

acetyl groups (**11**) blunted the activation ability of the 4,4′-linked dimers. The positive correlation of lipophilicity with the T cell activation capacity of the substances (**1** vs **11**) indicates the necessity of passing cellular membrane compartments rather than an interaction with cell-surface molecules as the underlying mechanism of activation. Similar relative activation potentials for the studied substances could be found for primary murine NK cells and macrophages (MΦ), as measured by upregulation of CD69 and MHC class II, respectively, while none of the compounds tested were able to induce upregulation of the costimulatory molecule CD86 on primary murine B lymphocytes (Figure 9B–D). Accordingly, in addition to their direct cytotoxic and pro-apoptotic activities on tumor cells, as shown above, the 4,4′-linked dimeric tetrahydroxanthones **1** and **4** exhibit an intrinsic immunostimulatory capacity on primary nontransformed T cells, NK cells, and MΦ by yet unknown signal transduction pathways. This dual activity offers interesting synergistic mechanisms to increase the efficiency of cancer treatment and to counteract the establishment of resistance pathways in cancer cells, making phomoxanthone A (**1**) an interesting candidate for further studies.

■ CONCLUSION

This study has revised the structure of the previously reported compound phomoxanthone A (**1**) as being (a*R*,5*S*,6-*S*,10a*S*,5′*S*,6′*S*,10a′*S*). In addition, the absolute configurations of dicerandrol B (**2**), dicerandrol C (**3**), and 12-deacetylphomoxanthone (**4**) were established for the first time. The marked cytotoxicity of **1** against a set of cancer cell lines, including

dx.doi.org/10.1021/jo402066b | J. Org. Chem. 2013, 78, 12409–12425

some cisplatin-resistant ones, was shown to be due to induction of apoptosis. The significant difference of activity of **1** against cancer cells versus healthy blood cells makes this compound an interesting candidate for further studies. Furthermore, **1** was shown to be a potent activator of murine T cells, NK cells, and macrophages, suggesting activation of the immune system, which would help to eradicate any tumor cells surviving chemotherapeutic treatment. The location of the biaryl axis in the investigated tetrahydroxanthone dimers (**1**−**4**) and the presence of acetyl groups were identified as being important structural elements that influence the biological activities of the studied compounds.

EXPERIMENTAL SECTION

General Experimental Procedures. Fractions and pure compounds were analyzed on an HPLC system coupled to a photodiode array detector, and routine detection was performed at 235, 254, 280, and 340 nm. Separation was carried out over a C18 reversed-phase column (5 μm; 125 mm × 4 mm length × i.d.), and the following linear gradient was used: 0.02% H_3PO_4 in H_2O and MeOH; flow rate 1.0 mL/min. Final purification was performed on a semipreparative HPLC system with a C18 reversed-phase column (5 μm; 300 mm × 8 mm, length × i.d.), flow rate 5.0 mL/min. 1D and 2D NMR spectra were recorded on 600 or 500 MHz NMR spectrometers. HRMS analysis was recorded on a Q-TOF mass spectrometer in ESI mode. Solvents were distilled prior to use, and spectral-grade solvents were used for spectroscopic measurements.

Fungal Material and Cultivation. The fungal strain *P. longicolla* was isolated from fresh healthy leaves of the mangrove tree *S. caseolaris* that were collected in October 2005 in Dong Zhai Gang-Mangrove Garden on Hainan Island, P. R. China, using a protocol previously described.[66] *P. longicolla* was taxonomically identified according to a previously described method.[67,68] The sequence data has been submitted to GenBank with accession number AY857868.1. The fungus was cultivated on solid rice medium (to 100 g of commercially available rice was added 100 mL of distilled water and kept overnight prior to autoclaving) at room temperature under static conditions.[67,68]

Extraction and Isolation. The solid rice culture of *P. longicolla* was overlaid and extracted with EtOAc, and then the solvent was removed under reduced pressure. The crude extract (24.9 g) was washed with distilled water and then fractionated between MeOH 90% and *n*-hexane. The MeOH fraction (16.4 g) was then subjected to Diaion HP-20 and eluted using a stepwise gradient system from 100% H_2O to 100% MeOH and from 1:1 MeOH/acetone to 100% acetone. Promising fractions were subjected to further chromatographic separation using Diaion HP-20 with H_2O, MeOH, and acetone as eluting solvents; silica (VLC) with a stepwise gradient system from 100% *n*-hexane to 100% EtOAc and from 100% DCM to 100% MeOH; or Sephadex LH-20 (100% MeOH or 1:1 DCM/MeOH). If necessary, final purification was performed by semipreparative HPLC to yield **1** (3.4 g), **2** (5.3 mg), **3** (3.2 mg), **4** (6.1 mg), **5** (3.9 mg), **6** (3.1 mg), **7** (2.1 mg), and **8** (5.4 mg).

*Phomoxanthone A (**1**).* Yellowish amorphous granules. $[\alpha]_D^{20}$ = +83 (*c* 0.3, $CHCl_3$). UV λ_{max} (PDA): 218, 258, 333 nm. ECD (MeCN, *c* = 1.10 × 10^{-4}) λ_{max}/nm ($\Delta\varepsilon$): 341 (−7.79) with a flat negative plateau up to 420 nm, 316 (17.65), 275 (−3.49), 257 (1.33), 228 (−46.79), 208 (−66.22), positive below 197 nm. ECD (86 μg of **1** in 250 mg of KCl) λ_{max}/nm ($\Delta\varepsilon$): 350 (19.16), 324 (32.71), 278 (−2.77), 258 (11.57), 227 (−87.44), 209 (−122.92), positive below 197 nm.

*Dicerandrol B (**2**).* Yellow amorphous powder. $[\alpha]_D^{20}$ = −25 (*c* 0.4, $CHCl_3$). UV λ_{max} (PDA): 215, 258, 338 nm. ECD (MeCN, *c* = 1.30 × 10^{-4}) λ_{max}/nm ($\Delta\varepsilon$): 373 br (6.08), 344 sh (2.09), 328 sh (2.11), 268 sh (−6.42), 233 (−13.74), 198 (−13.2).

*Dicernadrol C (**3**).* Yellow amorphous powder. $[\alpha]_D^{20}$ = −17 (*c* 0.1, $CHCl_3$). UV λ_{max} (PDA): 212, 260, 340 nm. ECD (MeCN, *c* = 0.99 × 10^{-4}) λ_{max}/nm ($\Delta\varepsilon$): 375 sh (−3.61), 365 (−3.70), 324 (9.01), 297 sh (2.55), 258 sh (−9.25), 233 (−16.57), 202 (−14.13).

*12-Deacetylphomoxanthone (**4**).* Yellow amorphous powder. $[\alpha]_D^{20}$ = +35 (*c* 0.2, MeOH). UV λ_{max} (PDA): 221, 259, 337 nm. ECD (MeCN, *c* = 1.26 × 10^{-4}) λ_{max}/nm ($\Delta\varepsilon$): 346 br (19.19), 300 (−0.71), 277 (−0.62), 252 (7.07), 226 sh (−56.48), 211 (−62.70). ^{1}H and ^{13}C NMR: Table 1. HR-ESI-MS: *m*/*z* 709.2127 $[M + H]^+$ (calcd for $C_{36}H_{37}O_{15}$, 709.2127).

*Phomo-2,3-dihydrochromone (**5**).* Brown amorphous mass. UV λ_{max} (PDA): 215, 250, 345 nm. ^{1}H and ^{13}C NMR: Table 2. HR-ESI-MS: *m*/*z* 289.0707 $[M + H]^+$ (calcd for $C_{15}H_{13}O_6$, 289.0707).

*Isomonodictyphenone (**6**).* Yellowish powder. UV λ_{max} (PDA): 209, 286 nm. ^{1}H and ^{13}C NMR: Table 3. HR-ESI-MS: *m*/*z* 289.0703 $[M + H]^+$ (calcd for $C_{15}H_{13}O_6$, 289.0707).

Structural Derivatization of Phomoxanthone A. *Alcoholic Alkaline Hydrolysis.* A solution of phomoxanthone A (**1**) (30 mg) in ethanolic NaOH (5 mL, 0.5 N) was stirred for 4 h at 23 °C, followed by dropwise treatment with hydrochloric acid (37 wt %). When the pH reached 4, the solution was neutralized with sodium bicarbonate (q.s.). Water (100 mL) was added, and the aqueous dilution was extracted three times with EtOAc (30 mL). The combined solvent extracts were evaporated to dryness. The obtained mixture was purified by semipreparative HPLC to yield **9a** (5.6 mg), **9b** (4.0 mg), and **9c** (9.4 mg).

*Hydrolysis Product I (**9a**).* Brownish amorphous powder. $[\alpha]_D^{20}$ = +6 (*c* 1.1, DMSO). UV λ_{max} (PDA): 251, 360 nm. ECD (MeCN, *c* = 2.86 × 10^{-4}) λ_{max}/nm ($\Delta\varepsilon$): 357 sh (0.39), 306 sh (2.08), 285 (3.78), 258 (−0.15), 237 (3.57), 208 (−8.05). ^{1}H and ^{13}C NMR: Table 4. HR-ESI-MS: *m*/*z* 583.1810 $[M + H]^+$ (calcd for $C_{30}H_{31}O_{12}$, 583.1810).

*Hydrolysis Product II (**9b**).* Brownish amorphous powder. $[\alpha]_D^{20}$ = −28 (*c* 0.8, DMSO). UV λ_{max} (PDA): 250, 359 nm. ECD (MeCN, *c* = 2.86 × 10^{-4}) λ_{max}/nm ($\Delta\varepsilon$): 351 (1.23), 306 sh (−1.76), 283 (−2.77), 237 (−3.06), 206 (4.01). ^{1}H and ^{13}C NMR: Table 4. HR-ESI-MS: *m*/*z* 583.1810 $[M + H]^+$ (calcd for $C_{30}H_{31}O_{12}$, 583.1810).

*Hydrolysis Product III (**9c**).* Brownish amorphous powder. $[\alpha]_D^{20}$ = −68 (*c* 0.9, DMSO). UV λ_{max} (PDA): 252, 363 nm. ECD (MeCN, *c* = 2.86 × 10^{-4}) λ_{max}/nm ($\Delta\varepsilon$): 356 (1.01), 285 (0.34), 266 (−0.37), 236 (2.43), 208 (−5.67). ^{1}H and ^{13}C NMR: Table 4. HR-ESI-MS: *m*/*z* 583.1810 $[M + H]^+$ (calcd for $C_{30}H_{31}O_{12}$, 583.1810).

Aqueous Alkaline Hydrolysis. A solution of phomoxanthone A (**1**) (50 mg) in aqueous NaOH solution (100 mL, 0.5 N) was heated under reflux for 1 h. After the mixture was cooled, the pH was adjusted to 5 with hydrochloric acid (37 wt %), and the mixture was extracted three times by shaking with 30 mL of EtOAc. The combined solvent extracts were evaporated to dryness. The obtained mixture was purified by semipreparative HPLC to yield **10** (4.8 mg).

*Hydrolysis Product IV (**10**).* Brownish amorphous powder. $[\alpha]_D^{20}$ = −127 (*c* 0.5, DMSO). UV λ_{max} (PDA): 215, 260 nm. ^{1}H and ^{13}C NMR: Table 5. HR-ESI-MS: *m*/*z* 547.1603 $[M + H]^+$ (calcd for $C_{30}H_{27}O_{10}$, 547.1599).

Cell Proliferation Assay. Cytotoxicity was tested against the L5178Y mouse lymphoma cell line using the MTT assay [MTT = 3-(4,5-dimethylthiazol-2-yl)-2,5-diphenyl-2*H*-tetrazolium bromide].[69,70] Furthermore, the cytotoxicity was evaluated against the human ovarian carcinoma cell line A2780, the human tongue cell line Cal27, the human esophagus cell line Kyse510, the human T cell lymphoma cell line Jurkat, and the human Burkitt's lymphoma cell line DG75 by an MTT assay as previously described, except that for Jurkat and DG75, incubation with DMSO at RT for 20 min was used to extract the formazan product from the cells.[71] The A2780 cell line was obtained from the European Collection of Cell Cultures (ECACC, Salisbury, UK). The Cal27 and Kyse510 cell lines as well as Jurkat (no. ACC-282) and DG75 (no. ACC-83) were obtained from the German Collection of Microorganisms and Cell Cultures (DSMZ, Germany). The cisplatin-resistant (CisR) cell lines were generated by exposing the parental cell lines to weekly cycles of cisplatin in an IC_{50} concentration over a period of 24−30 weeks, as described by Gosepath et al.[72] and Eckstein et al.[73] All of the cancer cell lines were grown at 37 °C under humidified air supplemented with 5% CO_2 in RPMI 1640 (A2780, Kyse510, Jurkat, DG75) or DMEM (Cal27) containing 10% fetal calf serum, 120 IU/mL penicillin, and 120 μg/mL streptomycin. The medium for Jurkat and DG75 was additionally

supplemented with 1% HEPES. The cells were grown to 80% confluency before they were used for the cell proliferation assay.

The selectivity of phomoxanthone A (**1**) cytotoxicity was assessed on PBMCs by trypan blue exclusion assay. Different concentrations of **1** were used to treat cells while the negative control was treated with the same volume of DMSO. At each time course (24 and 48 h), 20 μL of the cell suspension was mixed with 20 μL of trypan blue, and 20 μL of this mixture was applied to a hemocytometer and observed by a binocular microscope. The unstained cells (viable) in the negative control and treated samples were counted, and the percentage of viability was calculated from three independent tests.

Apoptosis Assay. DG75 cells (Burkitt's lymphoma-derived human B cell line; DSMZ no. ACC-83) or Jurkat cells (leukemia-derived human T cell line; DSMZ no. ACC-282) were cultivated in medium containing the indicated concentrations of compounds for 24 h, and apoptosis was measured. Nuclei were prepared by lysing cells in hypotonic lysis buffer (1% sodium citrate, 0.1% Triton X-100, 50 μg/mL propidium iodide) and subsequently analyzed by flow cytometry using FACSDiva software. Nuclei to the left of the 2 N peak were considered as apoptotic.

Cell Extracts and Immunoblotting. DG75 B cells or Jurkat T cells were treated with the different compounds at the indicated concentrations for the indicated times. Cells were lysed in lysis buffer [20 mM Tris-HCl, pH 7.5, 150 mM NaCl, 0.5 mM EDTA, 1% Triton X-100, 10 mM NaF, 2.5 mM NaPP, 10 μM Na_2MoO_4, 1 mM Na_3VO_4, protease inhibitors (P2714)], and the lysates were clarified by centrifugation at 16000*g* for 10 min. Equal total protein amounts, as determined by Bradford, were separated on 10% SDS-polyacrylamide gels and transferred to a PVDF membrane. Immunoblot analysis was performed using primary mouse antibodies to PARP (no. BML-SA250) or β-actin (no. A5316) and IRDye800- or IRDye680-conjugated secondary antibodies. Signals were detected with an infrared imaging system.

FACS Analysis of Immune Cell Activation Markers. Spleens of female C57BL/6 mice were digested with collagenase VIII and DNase I and homogenized using a cell strainer. Cell suspensions were incubated with the indicated compounds for 12 h in DMSO as 1:100 dilutions in medium at the indicated final concentrations. As positive controls, cells were stimulated for 12 h with 10 ng/mL PMA and 500 ng/mL ionomycin or 100 ng/mL LPS (*Salmonella Minnesota*, List Laboratories). For FACS analysis cells, were labeled with the following antibodies: CD11b (M1/70), B220 (Ra3-6B2), CD11c (HL3), CD3ε (145-2C11), CD19 (1D3), CD86 (GL1), CD69 (H1.2F3), MHC class II (AF6-120.1), and CD49 (DX5). DAPI was added for dead cell discrimination. Samples were acquired on a flow cytometer and analyzed with FlowJo software. T lymphocytes were defined as $CD3\varepsilon^+CD49^-$, B lymphocytes as $B220^+CD11c^-$, NK cells as $CD49^+CD3\varepsilon^-$, and MΦs as $CD11b^+CD11c^-$.

X-ray Crystallography. Single crystals of phomoxanthone A (**1**) suitable for X-ray diffraction were crystallized from EtOAc at room temperature. A single crystal was mounted on a loop under a polarizing microscope. Data for compound **1** were collected as follows: diffractometer (with microfocus tube), Cu Kα radiation (λ = 1.54178 Å), 123 ± 2 K, multilayer mirror, ω and ϕ scan, data collection with Apex2,[74] cell refinement and data reduction with SAINT,[74] and experimental absorption correction with SADABS.[75]

The structure of **1** was solved by direct methods using SHELXS-97; refinement was done by full-matrix least-squares on F^2 using the SHELXL-97 program suite.[76] All non-hydrogen positions were refined with anisotropic displacement parameters. Hydrogen atoms of two hydroxyl groups, aromatic CH groups, and aliphatic CH, CH_2, and CH_3 groups were positioned geometrically (O−H = 0.84 Å for OH; C−H = 0.95 Å for aromatic CH; C−H = 1.00 Å for aliphatic and olefinic CH; C−H = 0.99 Å for CH_2; C−H = 0.98 Å for CH_3) and refined using riding models with $U_{iso}(H) = 1.2U_{eq}$(CH, CH_2) and $U_{iso}(H) = 1.5U_{eq}$(O, CH_3). Hydrogen atoms of the other two hydroxyl groups (C−OH) were found and refined with $U_{iso}(H) = 1.5U_{eq}(O)$.

The absolute structure assignment was based on anomalous dispersion using the Flack parameter.[48−51] Friedel opposites were not merged. The correct assignment in the absence of any heavy atoms was checked by inverting the structure (MOVE 1 1 1 −1), which then led to a Flack parameter close to 1.

The crystal solvent molecules EtOAc and water in the channels of **1** were found to be highly disordered and could not be properly defined. Hence, the SQUEEZE option in PLATON for Windows[77−80] was used to refine the framework structure without the disordered electron density in the voids. One EtOAc and one water molecule per unit cell were squeezed. With two phomoxanthone molecules in the unit cell, **1** should be named as phomoxanthone A hemi(ethyl acetate) hemihydrate. The SQUEEZE routine suggested a 277 $Å^3$ (13.8%) cavity in the unit cell with a population of 87 electrons [roughly in agreement with 48 electrons for $CH_3C(O)OC_2H_5$ and 10 electrons for H_2O] for the solvated form. A PLATON[77−80] void calculation for the solvent-free form with a probe radius of 1.2 Å gave a total potential solvent volume of 291 $Å^3$ (14.5%).

The crystal structure is disordered at the O16 and C36 positions (the C═O moiety) as part of a torsional disorder of the acetyl group. The respective A atoms and B atoms were refined with about equal occupations, and A and B components were separated by a PART instruction. This torsional disorder is due to the presence of only very weak C−H···O interactions in the packing diagram, allowing this moiety to assume two different orientations (Figure S7 in the Supporting Information). The displacement of the acetyl group does not affect and is independent of the absolute structure assignment.

Crystal data and details of the structure refinement are given in Table S1 in the Supporting Information. Graphics were drawn with DIAMOND,[81] and analyses of the O−H···O hydrogen bonds were performed with PLATON for Windows.[77−80] The structural data have been deposited with the Cambridge Crystallographic Data Center (CCDC no. 937755).

COMPUTATIONAL SECTION

Mixed torsional/low-frequency mode conformational searches were carried out by means of the Macromodel 9.9.223 software using the Merck Molecular Force Field (MMFF) with an implicit solvent model for chloroform.[82] Geometry reoptimizations were carried out at the B3LYP/6-31G(d) level in vacuo, the B3LYP/TZVP level with a PCM solvent model for acetonitrile, and the M06/TZVP level[47] with the PCM model for acetonitrile. TDDFT ECD calculations were run with various functionals (B3LYP, BHandHLYP, PBE0) and the TZVP basis set as implemented in the Gaussian 09 package.[83] Scans and TS calculations were carried out at the B3LYP/6-31G(d) level in vacuo. ECD spectra were generated as sums of Gaussians with 2400 and 3000 cm^{-1} widths at half-height (corresponding to ca. 13 and 16 at 230 nm), using dipole-velocity-computed rotational strengths.[84] Boltzmann distributions were estimated from the ZPVE-corrected B3LYP/6-31G(d) energies in the gas phase calculations and from the B3LYP/TZVP and M06/TZVP energies in the solvated ones. For computation of the rotational barriers, the ZPVE-corrected B3LYP/6-31G(d) energies were applied. The MOLEKEL software package was used for visualization of the results.[85]

ASSOCIATED CONTENT

Supporting Information

Supplementary figures showing structures of the low- and high-energy transition states for the inversion of the C2−C2′ bond of (5*R*,6*R*,10a*R*,5′*R*,6′*R*,10a′*R*)-**2**, solution conformers and populations (≥2%) of (5*R*,6*R*,10a*R*,5′*R*,6′*R*,10a′*R*)-**2** and (5*R*,6*R*,10a*R*,5′*R*,6′*R*,10a′*R*)-**3**, molecular structure of phomoxanthone A (**1**) with determined absolute configuration (different views), previous and redetermined absolute structures of phomoxanthone A (**1**), experimental and calculated ECD spectra of the nonoptimized "old" (a*S*,5*R*,6*R*,10a*R*,5′*R*,6′*R*,10a′*R*) X-ray structures of **1** in vacuo, and section of the packing diagram of phomoxanthone A (**1**); supplementary tables showing crystal data and structure refinement for **1**, inter- and intramolecular interactions with lengths (Å) and angles

dx.doi.org/10.1021/jo402066b | J. Org. Chem. 2013, 78, 12409−12425

(deg) in **1**, and selected bond lengths (Å) and angles (deg) in **1**; references; description of the Flack parameter; thermal ellipsoid plots for **1**; ^{1}H and ^{13}C NMR spectra of the new compounds (**4**−**6** and **9a**−**10**); and Cartesian coordinates of the low-energy reoptimized conformers of **2** and **3**, the low- and high-energy transition states for the inversion of the C2−C2′ bond of **2**, and the optimized X-ray structures of **1**. This material is available free of charge via the Internet at http://pubs.acs.org.

AUTHOR INFORMATION

Corresponding Authors

*P.P.: Phone: 0049-211-8114163. Fax: 0049-211-8111923. E-mail: proksch@uni-duesseldorf.de.
*A.H.A.: Phone: 0049-211-8114173. E-mail: amal.hassan@uni-duesseldorf.de.

Notes

The authors declare no competing financial interest.

ACKNOWLEDGMENTS

Financial support by grants from BMBF to P.P. is gratefully acknowledged. T.K. and A.M. thank the Hungarian National Research Foundation (OTKA K105871) and the TÁMOP 4.2.4. A/2-11-1-2012-0001 National Excellence Program for financial support and the National Information Infrastructure Development Institute (NIIFI 10038) for CPU time. S.S. was supported by the Deutsche Forschungsgemeinschaft (SCHE692/3-1, SCHE692/4-1). R.S. was supported by an AFR Fellowship from the Fonds National de la Recherche in Luxembourg. Research at LBMCC was financially supported by the Fondation de Recherche Cancer et Sang, the Recherches Scientifiques Luxembourg Association, the Een Haerz fir kriibskrank Kanner Association, the Action Lions Vaincre le Cancer Association, the European Union (ITN "RedCat" 215009, Interreg Iva Project "Corena"), and the Télévie Luxembourg. M.D. was supported by the National Research Foundation (NRF) of the MEST of Korea through a Tumor Microenvironment Global Core Research Center (GCRC) grant (2012-0001184), by a Seoul National University research grant, and by the Research Settlement Fund for New Faculty of SNU. We thank Prof. W. E. G. Müller (University of Mainz, Germany) for MTT analysis using the L5178Y cell line.

REFERENCES

(1) Halpin, H. A.; Morales-Suárez-Varela, M. M.; Martin-Moreno, J. M. *Public Health Rev.* **2010**, *32*, 120−154.
(2) Pritchard, J. R.; Lauffenburger, D. A.; Hemann, M. T. *Drug Resist. Updates* **2012**, *15*, 249−257.
(3) Loeb, K. R.; Loeb, L. A. *Carcinogenesis* **2000**, *21*, 379−385.
(4) Lippert, T. H.; Ruoff, H.-J.; Volm, M. *Arzneimittelforschung* **2008**, *58*, 261−264.
(5) Brichard, V. G.; Lejeune, D. *Expert Opin. Biol. Ther.* **2008**, *8*, 951−968.
(6) Mantovani, A.; Romero, P.; Palucka, A. K.; Marincola, F. M. *Lancet* **2008**, *371*, 771−783.
(7) Marincola, F. M.; Wang, E.; Herlyn, M.; Seliger, B.; Ferrone, S. *Trends Immunol.* **2003**, *24*, 334−341.
(8) Zitvogel, L.; Apetoh, L.; Ghiringhelli, F.; Andre, F.; Tesniere, A.; Kroemer, G. *J. Clin. Invest.* **2008**, *118*, 1991−2001.
(9) Kiladjian, J.-J.; Mesa, R. A.; Hoffman, R. *Blood* **2011**, *117*, 4706−4715.
(10) Newman, D. J.; Cragg, G. M. *J. Nat. Prod.* **2012**, *75*, 311−335.
(11) Bacon, C. W.; White, J. F. Coevolution of Fungal Endophytes with Grasses: The Significance of Secondary Metabolites. In *Microbial Endophytes*; Bacon, C. W., White, J. F., Eds.; Marcel Dekker: New York, 2000; pp 341−388.
(12) Redman, R. S.; Sheehan, K. B.; Stout, R. G.; Rodriguez, R. J.; Henson, J. M. *Science* **2002**, *298*, 1581.
(13) Giordano, L.; Gonthier, P.; Varese, G. C.; Miserere, L.; Nicolotti, G. *Fungal Diversity* **2009**, *38*, 69−83.
(14) Bae, H.; Sicher, R. C.; Kim, M. S.; Kim, S.-H.; Strem, M. D.; Melnick, R. L.; Bailey, B. A. *J. Exp. Bot.* **2009**, *60*, 3279−3295.
(15) Singh, L. P.; Gill, S. S.; Tuteja, N. *Plant Signaling Behav.* **2011**, *6*, 175−191.
(16) Kharwar, R. N.; Mishra, A.; Gond, S. K.; Stierle, A.; Stierle, D. *Nat. Prod. Rep.* **2011**, *28*, 1208−1228.
(17) Lingham, R. B.; Silverman, K. C.; Bills, G. F.; Cascales, C.; Sanchez, M.; Jenkins, R. G.; Gartner, S. E.; Martin, I.; Diez, M. T.; Peláez, F.; Mochales, S.; Kong, Y.-L.; Burg, R. W.; Meinz, M. S.; Huang, L.; Nallin-Omstead, M.; Mosser, S. D.; Schaber, M. D.; Omer, C. A.; Pompliano, D. L.; Gibbs, J. B.; Singh, S. B. *Appl. Microbiol. Biotechnol.* **1993**, *40*, 370−374.
(18) Zhang, J.-Y.; Tao, L.-Y.; Liang, Y.-J.; Yan, Y.-Y.; Dai, C.-L.; Xia, X.-K.; She, Z.-G.; Lin, Y.-C.; Fu, L.-W. *Cell Cycle* **2009**, *8*, 2444−2450.
(19) Turbyville, T. J.; Wijeratne, E. M. K.; Liu, M. X.; Burns, A. M.; Seliga, C. J.; Luevano, L. A.; David, C. L.; Faeth, S. H.; Whitesell, L.; Gunatilaka, A. A. L. *J. Nat. Prod.* **2006**, *69*, 178−184.
(20) Kimura, T.; Nishida, M.; Kuramochi, K.; Sugawara, F.; Yoshida, H.; Mizushina, Y. *Bioorg. Med. Chem.* **2008**, *16*, 4594−4599.
(21) Kusari, S.; Hertweck, C.; Spiteller, M. *Chem. Biol.* **2012**, *19*, 792−798.
(22) Strobel, G.; Daisy, B. *Microbiol. Mol. Biol. Rev.* **2003**, *67*, 491−502.
(23) Klaiklay, S.; Rukachaisirikul, V.; Tadpetch, K.; Sukpondma, Y.; Phongpaichit, S.; Buatong, J.; Sakayaroj, J. *Tetrahedron* **2012**, *68*, 2299−2305.
(24) Liu, D.; Li, X.-M.; Meng, L.; Li, C.-S.; Gao, S.-S.; Shang, Z.; Proksch, P.; Huang, C.-G.; Wang, B.-G. *J. Nat. Prod.* **2011**, *74*, 1787−1791.
(25) Xu, J.; Aly, A. H.; Wray, V.; Proksch, P. *Tetrahedron Lett.* **2011**, *52*, 21−25.
(26) Li, H.; Huang, H.; Shao, C.; Huang, H.; Jiang, J.; Zhu, X.; Liu, Y.; Liu, L.; Lu, Y.; Li, M.; Lin, Y.; She, Z. *J. Nat. Prod.* **2011**, *74*, 1230−1235.
(27) Debbab, A.; Aly, A. H.; Proksch, P. *Fungal Diversity* **2013**, *61*, 1−27.
(28) Udayanga, D.; Liu, X.; McKenzie, E. C.; Chukeatirote, E.; Bahkali, A. A.; Hyde, K. *Fungal Diversity* **2011**, *50*, 189−225.
(29) Dai, J.; Krohn, K.; Gehle, D.; Kock, I.; Flörke, U.; Aust, H.-J.; Draeger, S.; Schulz, B.; Rheinheimer, J. *Eur. J. Org. Chem.* **2005**, 4009−4016.
(30) Hussain, H.; Akhtar, N.; Draeger, S.; Schulz, B.; Pescitelli, G.; Salvadori, P.; Antus, S.; Kurtán, T.; Krohn, K. *Eur. J. Org. Chem.* **2009**, 749−756.
(31) Claydon, N.; Grove, J. F.; Pople, M. *Phytochemistry* **1985**, *24*, 937−943.
(32) Hussain, H.; Ahmed, I.; Schulz, B.; Draeger, S.; Krohn, K. *Fitoterapia* **2012**, *83*, 523−526.
(33) Krohn, K.; Hussain, H.; Egold, H.; Schulz, B.; Green, I. *ARKIVOC* **2012**, *2012* (vi), 71−89.
(34) Krohn, K.; Michel, A.; Römer, E.; Flörke, U.; Aust, H.-J.; Draeger, S.; Schulz, B.; Wray, V. *Nat. Prod. Lett.* **1995**, *6*, 309−314.
(35) Li, Y.-Y.; Wang, M.-Z.; Huang, Y.-J.; Shen, Y.-M. *Mycology* **2010**, *1*, 254−261.
(36) Lim, C.; Kim, J.; Choi, J. N.; Ponnusamy, K.; Jeon, Y.; Kim, S. U.; Kim, J. G.; Lee, C. *J. Microbiol. Biotechnol.* **2010**, *20*, 494−500.
(37) Lin, T.; Lin, X.; Lu, C.; Hu, Z.; Huang, W.; Huang, Y.; Shen, Y. *Eur. J. Org. Chem.* **2009**, 2975−2982.
(38) Nithya, K.; Muthumary, J. *Recent Res. Sci. Technol.* **2010**, *2*, 99−103.
(39) Rukachaisirikul, V.; Sommart, U.; Phongpaichit, S.; Sakayaroj, J.; Kirtikara, K. *Phytochemistry* **2008**, *69*, 783−787.

(40) Talontsi, F. M.; Islam, M. T.; Facey, P.; Douanla-Meli, C.; von Tiedemann, A.; Laatsch, H. *Phytochem. Lett.* **2012**, *5*, 657−664.
(41) Toyomasu, T.; Kaneko, A.; Tokiwano, T.; Kanno, Y.; Kanno, Y.; Niida, R.; Miura, S.; Nishioka, T.; Ikeda, C.; Mitsuhashi, W.; Dairi, T.; Kawano, T.; Oikawa, H.; Kato, N.; Sassa, T. *J. Org. Chem.* **2009**, *74*, 1541−1548.
(42) Izawa, Y.; Hirose, T.; Shimizu, T.; Koyama, K.; Natori, S. *Tetrahedron* **1989**, *45*, 2323−2335.
(43) Elsässer, B.; Krohn, K.; Flörke, U.; Root, N.; Aust, H.-J.; Draeger, S.; Schulz, B.; Antus, S.; Kurtán, T. *Eur. J. Org. Chem.* **2005**, 4563−4570.
(44) Isaka, M.; Jaturapat, A.; Rukseree, K.; Danwisetkanjana, K.; Tanticharoen, M.; Thebtaranonth, Y. *J. Nat. Prod.* **2001**, *64*, 1015−1018.
(45) Wagenaar, M. M.; Clardy, J. *J. Nat. Prod.* **2001**, *64*, 1006−1009.
(46) Andersen, R.; Buechi, G.; Kobbe, B.; Demain, A. L. *J. Org. Chem.* **1977**, *42*, 352−353.
(47) Zhao, Y.; Truhlar, D. *Theor. Chem. Acc.* **2008**, *120*, 215−241.
(48) Flack, H. *Acta Crystallogr., Sect. A* **1983**, *39*, 876−881.
(49) Flack, H. D.; Bernardinelli, G. *Acta Crystallogr., Sect. A* **1999**, *55*, 908−915.
(50) Flack, H. D.; Bernardinelli, G. *Chirality* **2008**, *20*, 681−690.
(51) Flack, H. D.; Sadki, M.; Thompson, A. L.; Watkin, D. J. *Acta Crystallogr., Sect. A* **2011**, *67*, 21−34.
(52) Krick, A.; Kehraus, S.; Gerhauser, C.; Klimo, K.; Nieger, M.; Maier, A.; Fiebig, H. H.; Atodiresei, I.; Raabe, G.; Fleischhauer, J.; Konig, G. M. *J. Nat. Prod.* **2007**, *70*, 353−360.
(53) Asahina, Y.; Fujikawa, F. *Ber. Dtsch. Chem. Ges.* **1935**, *68*, 1558−1565.
(54) Waser, M.; Lackner, B.; Zuschrader, J.; Müller, N.; Falk, H. *Tetrahedron Lett.* **2005**, *46*, 2377−2380.
(55) Lim, F. Y.; Hou, Y.; Chen, Y.; Oh, J.-H.; Lee, I.; Bugni, T. S.; Keller, N. P. *Appl. Environ. Microbiol.* **2012**, *78*, 4117−4125.
(56) Kikuchi, H.; Isobe, M.; Kurata, S.; Katou, Y.; Oshima, Y. *Tetrahedron* **2012**, *68*, 6218−6223.
(57) Kurobane, I.; Vining, L. C.; McInnes, A. G. *J. Antibiot.* **1979**, *32*, 1256−1266.
(58) Bok, J. W.; Chiang, Y.-M.; Szewczyk, E.; Reyes-Dominguez, Y.; Davidson, A. D.; Sanchez, J. F.; Lo, H.-C.; Watanabe, K.; Strauss, J.; Oakley, B. R.; Wang, C. C. C.; Keller, N. P. *Nat. Chem. Biol.* **2009**, *5*, 462−464.
(59) Chiang, Y. M.; Szewczyk, E.; Davidson, A. D.; Entwistle, R.; Keller, N. P.; Wang, C. C.; Oakley, B. R. *Appl. Environ. Microbiol.* **2010**, *76*, 2067−2074.
(60) Lu, P.; Zhang, A.; Dennis, L. M.; Dahl-Roshak, A. M.; Xia, Y. Q.; Arison, B.; An, Z.; Tkacz, J. S. *Mol. Genet. Genomics* **2005**, *273*, 207−216.
(61) Lin, J.; Liu, S.; Sun, B.; Niu, S.; Li, E.; Liu, X.; Che, Y. *J. Nat. Prod.* **2010**, *73*, 905−910.
(62) Sanchez, J. F.; Entwistle, R.; Hung, J.-H.; Yaegashi, J.; Jain, S.; Chiang, Y.-M.; Wang, C. C. C.; Oakley, B. R. *J. Am. Chem. Soc.* **2011**, *133*, 4010−4017.
(63) Breinholt, J.; Demuth, H.; Lange, L.; Kjaer, A.; Pedersen, C. *J. Antibiot.* **1993**, *46*, 1013−1015.
(64) Napolitano, J. G.; Gavin, J. A.; Garcia, C.; Norte, M.; Fernandez, J. J.; Daranas, A. H. *Chem.—Eur. J.* **2011**, *17*, 6338−6347.
(65) Zhang, W.; Krohn, K.; Zia, U.; Flörke, U.; Pescitelli, G.; Di Bari, L.; Antus, S.; Kurtán, T.; Rheinheimer, J.; Draeger, S.; Schulz, B. *Chem.—Eur. J.* **2008**, *14*, 4913−4923.
(66) Rönsberg, D.; Debbab, A.; Mándi, A.; Wray, V.; Dai, H.; Kurtán, T.; Proksch, P.; Aly, A. H. *Tetrahedron Lett.* **2013**, *54*, 3256−3259.
(67) Aly, A. H.; Edrada-Ebel, R.; Indriani, I. D.; Wray, V.; Müller, W. E.; Totzke, F.; Zirrgiebel, U.; Schächtele, C.; Kubbutat, M. H.; Lin, W. H.; Proksch, P.; Ebel, R. *J. Nat. Prod.* **2008**, *71*, 972−980.
(68) Kjer, J.; Debbab, A.; Aly, A. H.; Proksch, P. *Nat. Protoc.* **2010**, *5*, 479−490.
(69) Carmichael, J.; DeGraff, W. G.; Gazdar, A. F.; Minna, J. D.; Mitchell, J. B. *Cancer Res.* **1987**, *47*, 936−942.
(70) Ashour, M.; Edrada, R. A.; Ebel, R.; Wray, V.; Wätjen, W.; Padmakumar, K.; Müller, W. E. G.; Lin, W. H.; Proksch, P. *J. Nat. Prod.* **2006**, *69*, 1547−1553.
(71) Mueller, H.; Kassack, M. U.; Wiese, M. *J. Biomol. Screening* **2004**, *9*, 506−515.
(72) Gosepath, E. M.; Eckstein, N.; Hamacher, A.; Servan, K.; von Jonquieres, G.; Lage, H.; Györffy, B.; Royer, H. D.; Kassack, M. U. *Int. J. Cancer* **2008**, *123*, 2013−2019.
(73) Eckstein, N.; Servan, K.; Girard, L.; Cai, D.; von Jonquieres, G.; Jaehde, U.; Kassack, M. U.; Gazdar, A. F.; Minna, J. D.; Royer, H.-D. *J. Biol. Chem.* **2008**, *283*, 739−750.
(74) *Apex2: Data Collection Program for the CCD Area-Detector System*; Bruker Analytical X-ray Systems: Madison, WI, 1997−2011. *SAINT: Data Reduction and Frame Integration Program for the CCD Area-Detector System*; Bruker Analytical X-ray Systems: Madison, WI, 1997−2011.
(75) Sheldrick, G. *SADABS: Program for Area-Detector Absorption Correction*; University of Göttingen: Göttingen, Germany, 1996.
(76) Sheldrick, G. *Acta Crystallogr., Sect. A* **2008**, *64*, 112−122.
(77) Spek, A. L. *PLATON: A Multipurpose Crystallographic Tool*; Utrecht University: Utrecht, The Netherlands, 2008.
(78) Farrugia, L. J. *PLATON for Windows*, version 40608; University of Glasgow; Glasgow, U.K., 2008.
(79) Spek, A. *J. Appl. Crystallogr.* **2003**, *36*, 7−13.
(80) Spek, A. *Acta Crystallogr., Sect. D* **2009**, *65*, 148−155.
(81) Brandenburg, K. *Diamond: Crystal and Molecular Structure Visualization Software*, version 3.2; Crystal Impact: Bonn, Germany, 2009.
(82) *MacroModel*; Schrödinger LLC: New York, 2012; http://www.schrodinger.com/productpage/14/11/
(83) Frisch, M. J.; Trucks, G. W.; Schlegel, H. B.; Scuseria, G. E.; Robb, M. A.; Cheeseman, J. R.; Scalmani, G.; Barone, V.; Mennucci, B.; Petersson, G. A.; Nakatsuji, H.; Caricato, M.; Li, X.; Hratchian, H. P.; Izmaylov, A. F.; Bloino, J.; Zheng, G.; Sonnenberg, J. L.; Hada, M.; Ehara, M.; Toyota, K.; Fukuda, R.; Hasegawa, J.; Ishida, M.; Nakajima, T.; Honda, Y.; Kitao, O.; Nakai, H.; Vreven, T.; Montgomery, J. A., Jr.; Peralta, J. E.; Ogliaro, F.; Bearpark, M.; Heyd, J. J.; Brothers, E.; Kudin, K. N.; Staroverov, V. N.; Kobayashi, R.; Normand, J.; Raghavachari, K.; Rendell, A.; Burant, J. C.; Iyengar, S. S.; Tomasi, J.; Cossi, M.; Rega, N.; Millam, J. M.; Klene, M.; Knox, J. E.; Cross, J. B.; Bakken, V.; Adamo, C.; Jaramillo, J.; Gomperts, R.; Stratmann, R. E.; Yazyev, O.; Austin, A. J.; Cammi, R.; Pomelli, C.; Ochterski, J. W.; Martin, R. L.; Morokuma, K.; Zakrzewski, V. G.; Voth, G. A.; Salvador, P.; Dannenberg, J. J.; Dapprich, S.; Daniels, A. D.; Farkas, Ö.; Foresman, J. B.; Ortiz, J. V.; Cioslowski, J.; Fox, D. J. *Gaussian 09*, revision B.01; Gaussian, Inc.: Wallingford, CT, 2010.
(84) Stephens, P. J.; Harada, N. *Chirality* **2010**, *22*, 229−233.
(85) Varetto, U. *MOLEKEL*, version 5.4; Swiss National Supercomputing Centre: Manno, Switzerland, 2009.

Manuscript "PDK1 controls upstream PI3K expression and PIP3 generation"

Dieterle AM*, Böhler P*, Keppeler H, Alers S, Berleth N, Drießen S, Hieke N, Pietkiewicz S, Löffler AS, Peter C, Gray A, Leslie NR, Shinohara H, Kurosaki T, Engelke M, Wienands J, Bonin M, Wesselborg S, Stork B. *Oncogene* (2014) **33**:3043, doi: 10.1038/onc.2013.266

* These authors contributed equally to the manuscript.

Oncogene (2014) **33,** 3043–3053

www.nature.com/onc

ORIGINAL ARTICLE

PDK1 controls upstream PI3K expression and PIP_3 generation

AM Dieterle[1,9], P Böhler[2,9], H Keppeler[1], S Alers[1], N Berleth[2], S Drießen[2], N Hieke[2], S Pietkiewicz[2,7], AS Löffler[2], C Peter[2], A Gray[3], NR Leslie[3,8], H Shinohara[4], T Kurosaki[4], M Engelke[5], J Wienands[5], M Bonin[6], S Wesselborg[2] and B Stork[2]

The PI3K/PDK1/Akt signaling axis is centrally involved in cellular homeostasis and controls cell growth and proliferation. Due to its key function as regulator of cell survival and metabolism, the dysregulation of this pathway is manifested in several human pathologies including cancers and immunological diseases. Thus, current therapeutic strategies target the components of this signaling cascade. In recent years, numerous feedback loops have been identified that attenuate PI3K/PDK1/Akt-dependent signaling. Here, we report the identification of an additional level of feedback regulation that depends on the negative transcriptional control of phosphatidylinositol 3-kinase (PI3K) class IA subunits. Genetic deletion of 3-phosphoinositide-dependent protein kinase 1 (PDK1) or the pharmacological inhibition of its downstream effectors, that is, Akt and mammalian target of rapamycin (mTOR), relieves this suppression and leads to the upregulation of PI3K subunits, resulting in enhanced generation of phosphatidylinositol-3,4,5-trisphosphate (PIP_3). Apparently, this transcriptional induction is mediated by the concerted action of different transcription factor families, including the transcription factors cAMP-responsive element-binding protein and forkhead box O. Collectively, we propose that PDK1 functions as a cellular sensor that balances basal PIP_3 generation at levels sufficient for survival but below a threshold being harmful to the cell. Our study suggests that the efficiency of therapies targeting the aberrantly activated PI3K/PDK1/Akt pathway might be increased by the parallel blockade of feedback circuits.

Oncogene (2014) **33,** 3043–3053; doi:10.1038/onc.2013.266; published online 29 July 2013

Keywords: Akt; PDK1; PI3K; survival; B lymphocytes

INTRODUCTION

The PI3K/PDK1/Akt pathway regulates various cellular processes, including cell growth, survival and proliferation. Accordingly, the dysregulation of this pathway has been implicated in several human cancers and immunological diseases, and the components of this pathway are attractive targets of current therapeutic strategies (reviewed in references[1–8]).

Phosphatidylinositol 3-kinases (PI3Ks) are intracellular lipid kinases, which are grouped into three classes (I–III). Class I PI3Ks generate phosphatidylinositol-3,4,5-trisphosphate (PIP_3) by phosphorylating phosphatidylinositol-4,5-bisphosphate (PIP_2) at the D3 position of the inositol ring.[9] Class I PI3Ks are heterodimers consisting of a p110 catalytic subunit (p110α, p110β, p110δ and p110γ) and a regulatory subunit. The class IA isoforms p110α, p110β and p110δ pair with the p85 subfamily of regulatory subunits (p85α, p85β, p55α, p50α and p55γ). The class IB p110γ isoform associates with p101 or p84/p87 subunits.[9,10] In turn, PIP_3 levels are negatively regulated by the action of lipid phosphatases, which remove the different phosphate groups from the inositol ring.[11]

Most of the cellular responses to PI3K activation and PIP_3 generation are mediated by the activation of AGC kinases such as Akt (also termed protein kinase B), p70S6K and serum- and glucocorticoid-induced protein kinase (SGK) (reviewed by Mora *et al.*[12] and Pearce *et al.*[13]). For full activation, these kinases have to be phosphorylated both in an activation segment (T-loop) and within a hydrophobic motif.[13] The common upstream activator of these kinases is the AGC kinase 3-phosphoinositide-dependent protein kinase 1 (PDK1), which catalyzes the T-loop phosphorylation.[13–23] PDK1 possesses an N-terminal serine/threonine kinase domain and a C-terminal pleckstrin homology (PH) domain, which binds to PIP_3 and its degradation product phosphatidylinositol-3,4-bisphosphate.[14,15,24,25] The constitutively active PDK1 itself is not stimulated by PI3K.[14] However, the mechanism by which PDK1 activates its substrates is controlled by PIP_3. In case of Akt, PIP_3 induces a conformational change of Akt by binding its N-terminal PH domain, which leads to PDK1-mediated phosphorylation of T308 in the activation segment of Akt.[25] Full Akt activation is achieved by phosphorylation of S473 within the hydrophobic motif via the mammalian target of rapamycin complex 2 (mTORC2).[26,27] In contrast to Akt, the kinases p70S6K and SGK lack a PH domain. They get phosphorylated in the hydrophobic motif by mTORC1 or mTORC2 following PI3K activation.[13,28,29] The hydrophobic motif phosphorylation does not directly activate p70S6K and SGK but regulates their interaction with PDK1.[30,31] PDK1 binds to the phosphorylated hydrophobic motif via its PDK1-interacting fragment pocket and consequently phosphorylates the activation segment and thereby activates these kinases.[13] Upon activation of PI3Ks by insulin, growth factors or antigens, AGC kinases get activated and

[1]Department of Internal Medicine I, University Hospital Tübingen, Tübingen, Germany; [2]Institute of Molecular Medicine, University Hospital Düsseldorf, Düsseldorf, Germany; [3]Division of Cell Signaling and Immunology, College of Life Sciences, University of Dundee, Dundee, UK; [4]Laboratory for Lymphocyte Differentiation, RIKEN Research Center for Allergy and Immunology, Yokohama, Japan; [5]Institute of Cellular and Molecular Immunology, University Hospital Göttingen, Göttingen, Germany and [6]Department of Medical Genetics, MFT Services, University Hospital Tübingen, Tübingen, Germany. Correspondence: Dr B Stork, Institute of Molecular Medicine, University Hospital Düsseldorf, Building 23.12, Universitätsstr. 1, 40225 Düsseldorf, Germany.
E-mail: bjoern.stork@uni-duesseldorf.de
[7]Current address: Department of Translational Inflammation Research, Institute of Experimental Internal Medicine, Otto von Guericke University, Magdeburg, Germany.
[8]Current address: Institute of Biological Chemistry, Biophysics and Bioengineering, EPS, Nasmyth Building, Heriot Watt University, Edinburgh, UK.
[9]These authors contributed equally to this work.
Received 17 September 2012; revised 30 April 2013; accepted 20 May 2013; published online 29 July 2013

in turn phosphorylate various downstream targets, for example, glycogen synthase kinase 3β (GSK3β), tuberous sclerosis complex 2 (TSC2) or forkhead box O (FOXO) transcription factors.[6,13] Additionally, in recent years, it became evident that PI3K is tightly controlled by its downstream targets, thus providing feedback regulation in response to extracellular signals.[32]

To further characterize the involvement of PDK1 in pro-survival signaling pathways and its contribution to feedback regulation of PI3K, we analyzed the transcriptome in an inducible *PDK1*-knockout system. We show that upon *PDK1*-knockout induction in DT40 B lymphocytes the PI3K class IA subunits p85α, p110β and p110δ are upregulated on both mRNA and protein level. Furthermore, we demonstrate that PDK1 depletion increases the amount of the PI3K product PIP_3 in the plasma membrane. It appears that this PDK1-dependent transcriptional repression of PI3K class IA subunits is mainly mediated via the Akt/mTORC1 signaling axis and members of different transcription factor families, including cAMP-responsive element-binding protein (CREB) and FOXOs. Collectively, we propose a transcriptional level of feedback regulation targeting the PI3K/PDK1/Akt/mTOR signaling pathway. This novel feedback mechanism might further emphasize the need for dual inhibitors of PI3K and mTOR in cancer therapy.

RESULTS

Tonic PDK1 signaling is essential for survival of DT40 B lymphocytes

To gain further insight into the function of PDK1 in survival signaling, we made use of the conditional *PDK1*-knockout chicken DT40 B cell line (*PDK1* − /cond).[33] In these cells, 4-hydroxytamoxifen (OH-TAM)-activated Cre recombinase induces the deletion of the floxed *PDK1* gene. We treated DT40 *PDK1* − /cond cells with OH-TAM and verified the absence of PDK1 expression by immunoblotting. In DT40 wild-type (wt) cells, OH-TAM alone had no effect on PDK1 expression (Figure 1a).

PDK1 plays an important role in survival signaling, and embryos of *Pdk1* − / − mice die at day 9.5.[34] Thus, we analyzed apoptosis in OH-TAM-treated DT40 *PDK1* − /cond and wt cells by measuring hypodiploid nuclei. OH-TAM-treated *PDK1* − /cond cells underwent apoptosis from day 6 of treatment, but not the wt or ethanol (EtOH)-treated cells (Figure 1b). As DT40 cells are immature B lymphocytes and therefore respond with apoptosis induction upon crosslinking of the B-cell antigen receptor (BCR),[35] we investigated if the loss of PDK1 has any effect on BCR-induced apoptosis. We stimulated DT40 *PDK1* − /cond cells on day 4 of OH-TAM treatment, on which the cells were PDK1 negative but still viable (Figures 1a and b), with anti-chicken-IgM antibodies and analyzed apoptosis by measuring hypodiploid nuclei. As control, we used EtOH-treated *PDK1* − /cond and wt cells. Although loss of PDK1 strongly increased BCR-induced apoptosis, wt cells did not display any differences in BCR-induced apoptosis following OH-TAM treatment (Figure 1c).

Taken together, PDK1 is mandatory for the constitutive survival signaling in DT40 cells, and its loss sensitizes these cells to BCR-induced apoptosis.

Microarray analysis of *PDK1* − /cond cells

Next, we addressed the question whether PDK1 also regulates long-term transcription dynamics. To investigate this, we performed microarray analyses using the Affymetrix GeneChip Chicken Genome Array. We treated DT40 *PDK1* − /cond cells with OH-TAM or EtOH to identify PDK1-dependent target genes. Additionally, we treated DT40 wt cells with OH-TAM or EtOH to exclude OH-TAM-dependent effects. Successful depletion of PDK1 in *PDK1* − /cond cells used for microarray analyses was confirmed by immunoblotting and real-time reverse transcription (RT)–PCR

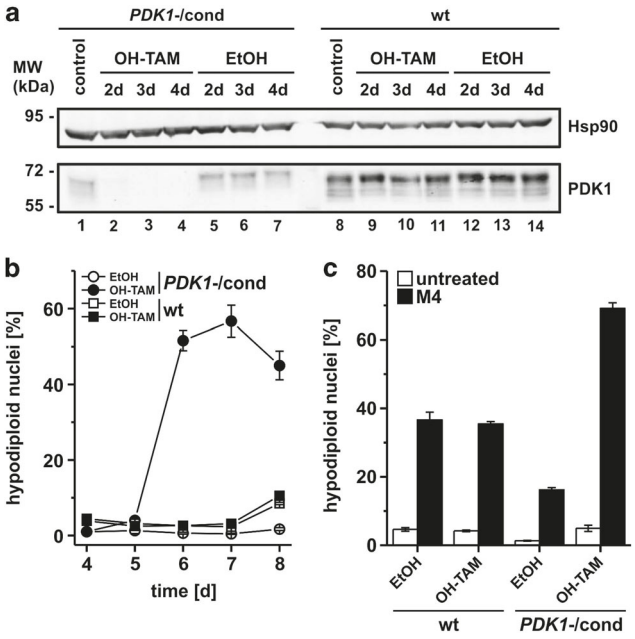

Figure 1. PDK1 is essential for survival of DT40 cells. (**a**) Conditional *PDK1* − /cond chicken DT40 B cells (*PDK1* − /cond) and DT40 wt cells were treated with 0.5 μM OH-TAM or 0.05% EtOH for 48 h or left untreated (control). Then, cells were transferred to normal DT40 medium. On days 2–4 after beginning of OH-TAM/EtOH treatment, cleared cellular lysates were prepared and analyzed for PDK1 and Hsp90 by immunoblotting. Data shown are representative of three independent experiments. (**b**) DT40 *PDK1* − /cond and wt cells were treated with 0.5 μM OH-TAM or 0.05% EtOH for 48 h. Then, cells were transferred to normal DT40 medium. On days 4–8 after beginning of OH-TAM/EtOH treatment, apoptosis was assessed by propidium iodide staining of hypodiploid apoptotic nuclei and flow cytometry. Data shown are mean of triplicates ± s.d. and are representative of three independent experiments. (**c**) DT40 *PDK1* − /cond and wt cells were treated with 0.5 μM OH-TAM or 0.05% EtOH for 48 h. Then, cells were transferred to normal DT40 medium. On day 4 after beginning of OH-TAM/EtOH treatment, cells were stimulated with 10 μg/ml anti-chicken IgM antibody (M4) for 24 h. Apoptosis was assessed by propidium iodide staining of hypodiploid apoptotic nuclei and flow cytometry. Data shown are mean of triplicates ± s.d. and are representative of three independent experiments.

(Supplementary Figures 1A and B). Only transcripts that were regulated with ⩾2-fold changes were considered as relevant. When comparing the transcripts of *PDK1* − /cond and wt cells both treated with OH-TAM, we identified 1696 relevant transcripts. In turn, the comparison of *PDK1* − /cond cells treated with OH-TAM or EtOH revealed 764 relevant transcripts. Altogether 503 transcripts were regulated in both entity lists (Supplementary Figure 1C). Next, we performed global function and pathway analyses of the gene products of the 503 transcripts using Ingenuity Pathway Analysis Software (Supplementary Figure 1D). We observed that the 503 gene products play key roles in cellular homeostasis and immune responses. Due to the fact that PDK1 deletion is lethal, we were mostly interested in regulated genes of survival signaling pathways. It has been previously reported that transcription factors of the FOXO family are regulated via the PI3K/PDK1/Akt signaling pathway.[36,37] In our microarray analysis, several apoptosis-relevant FOXO target genes such as *TNFSF10 (TRAIL)*, *CDKN1B* and *BCL6* were PDK1-dependently regulated (Figure 2a). Strikingly, our microarray results revealed PDK1-dependent regulation of gene products that regulate the signaling pathway upstream of PDK1. Among these gene products were the

a

gene symbol (protein name)	regulation
known targets of PDK1	
TNFSF10 **(Tumor necrosis factor ligand superfamily member 10; synonym: TRAIL)**	↑
CDKN1B **(cyclin-dependent kinase inhibitor 1B; synonyms: p27, Kip1)**	↑
BCL6 **(B-cell lymphoma 6 protein)**	↑
CCNG2 **(cyclin G2)**	↑
CCND1 **(cyclin D1)**	↓
new targets of PDK1	
PIK3CB **(phosphatidylinositol 4,5-bisphosphate 3-kinase, catalytic subunit beta; PI3K p110β)**	↑
PIK3CD **(phosphatidylinositol 4,5-bisphosphate 3-kinase, catalytic subunit delta; PI3K p110δ)**	↑
PIK3R1 **(phosphoinositide-3-kinase, regulatory subunit 1 (alpha); PI3K p85α)**	↑
INPP5B **(inositol polyphosphate-5-phosphatase)**	↓
PIP5K1B **(phosphatidylinositol-4-phosphate 5-kinase, type I, beta)**	↑
PIK3IP1 **(phosphoinositide-3-kinase interacting protein 1)**	↑
LYN **(v-yes-1 Yamaguchi sarcoma viral related oncogene homolog; synonym: Lyn)**	↑

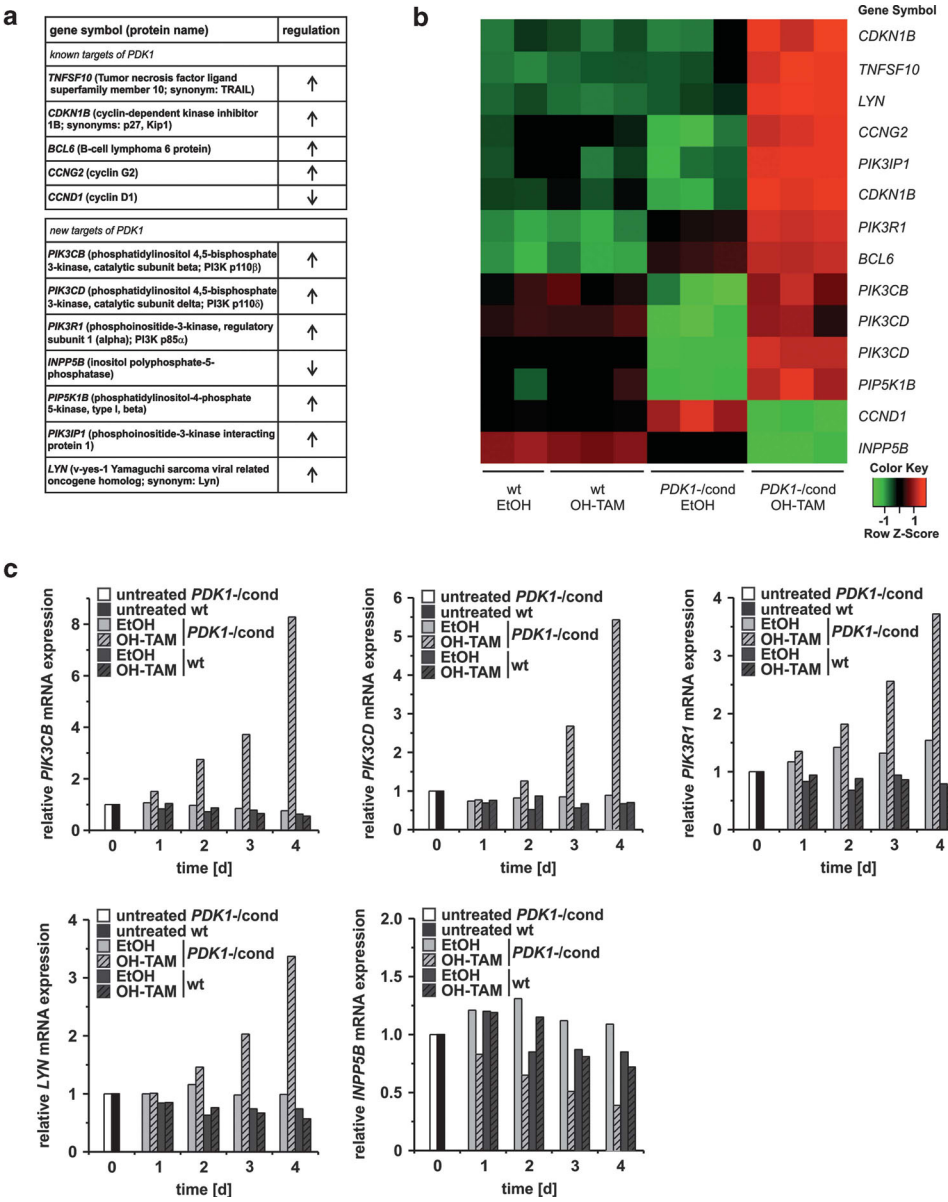

Figure 2. PDK1 negatively regulates transcription of PI3K subunits. (**a**) The table lists known and newly identified target genes of PDK1 and their regulation in *PDK1* − /cond cells compared with that in control cells. (**b**) Cluster analysis for selected probe sets was performed using the statistics software R 2.15.1. Signal intensities were scaled and centered, and the distance between two expression profiles was calculated using Manhattan distance measure. Hierarchical cluster analysis was performed with average linkage. Heatmaps were generated with Bioconductor package geneplotter. (**c**) DT40 *PDK1* − /cond and wt cells were treated with 0.5 μM OH-TAM or 0.05% EtOH for 48 h. Then, cells were transferred to normal DT40 medium. At the indicated time points, the relative mRNA expression of *PIK3CB* (PI3K p110β), *PIK3CD* (PI3K p110δ), *PIK3R1* (PI3K p85α), *LYN* (Lyn) and *INPP5B* was analyzed by quantitative real-time RT–PCR.

PI3K class IA subunits p110β and p110δ (catalytic subunits), p85α (regulatory subunit), additional phosphoinositide-modifying enzymes (INPP5B, PIP5K1-β), the PI3K-interacting protein 1 and the B-cell-specific Src family tyrosine kinase Lyn (Figures 2a and b). Lyn links the BCR to the activation of PI3K/PDK1/Akt signaling in B lymphocytes, as it directly phosphorylates CD19 and contributes to the activation of the tyrosine kinases Syk and Btk, which both phosphorylate the B-cell adapter for PI3K.[38] Tyrosine-phosphorylated CD19 and/or B-cell adapter for PI3K then recruit the regulatory PI3K subunit p85α.[38]

Next, we performed quantitative real-time RT–PCRs of the *PIK3CB* (PI3K p110β subunit), *PIK3CD* (PI3K p110δ subunit), *PIK3R1* (PI3K p85α subunit), *LYN* (Lyn) and *INPP5B* (phosphoinositide 5-phosphatase) genes to confirm the microarray results. We treated DT40 *PDK1* − /cond and wt cells with OH-TAM or EtOH and determined the mRNA level at the indicated time points (Figure 2c). In accordance with the microarray results, *PIK3CB*, *PIK3CD, PIK3R1* and *LYN* were upregulated, and *INPP5B* was downregulated.

Taken together, we showed that knockout of PDK1 indirectly alters the PI3K/PDK1 signaling axis by regulating gene transcription of Lyn, PI3K subunits and phosphoinositide-modifying enzymes.

PDK1 negatively regulates expression of PI3K subunits

To confirm the results obtained by microarray analysis and RT–PCR on the protein level, we used immunoblotting to analyze the

expression of the PI3K subunits p110β, p110δ and p85α, Lyn and INPP5B in DT40 *PDK1* − /cond cells treated with OH-TAM or EtOH. We observed an increase of protein expression of all three PI3K subunits (Figure 3a). Similarly, protein levels of the Src family kinase Lyn were elevated upon PDK1 depletion (Figure 3a). In contrast and confirming the microarray and RT–PCR results, deletion of PDK1 resulted in a downregulation of INPP5B (Figure 3b).

To analyze whether known downstream signaling pathways are affected by the loss of PDK1, we analyzed the phosphorylation status of different PDK1 effector proteins following OH-TAM treatment, such as Akt (T308), GSK3β (S9), FOXO1 (S256) and TSC2 (S939). With loss of PDK1, T308 phosphorylation of Akt is strongly reduced in PDK1-deleted cells (Figure 3c). Additionally, phosphorylation of the Akt substrates GSK3β, FOXO1 and TSC2 was significantly decreased, whereas total expression levels of these proteins remained largely unaffected (Figure 3c). All results obtained by the OH-TAM-induced PDK1 deletion were compared with the effect of the PDK1 inhibitor BX-795.[39] BX-795 essentially phenocopied the effect of the induced PDK1 deletion, that is, reduced phosphorylation of Akt and its substrates, upregulation of the PI3K subunits p110β and p110δ and downregulation of INPP5B (Figure 3c).

To prove the PDK1-mediated regulation of PI3K subunit expression in alternative cell models, we treated human DG75 and Ramos B cells with the PDK1 inhibitor BX-795 and analyzed p110β, p110δ and p85α expression. A significant upregulation of the PI3K subunits was detectable in both cell lines (Supplementary Figures 2A and B). Furthermore, we were interested whether the observed transcriptional control is valid for cells derived from solid tumors. Accordingly, we treated prostate carcinoma PC-3 cells with BX-795 for 2 days. The efficacy of BX-795 in this cell line was confirmed by analyzing the phosphorylation of Akt, GSK3β, TSC2 and FOXO1, respectively. Similar to the B cell lines described above, the expression of the PI3K subunits p110β and p110δ increased upon BX-795 treatment (Supplementary Figure 2C). Collectively, these findings indicate that the PDK1-dependent control of PI3K subunit expression also exists in mammals and non-lymphoid cells.

To ultimately confirm that the above-described effects can be attributed to the loss of PDK1, we reconstituted DT40 *PDK1* − /cond cells with chicken *PDK1* complementary DNA (cDNA). Expression of chicken PDK1 in knockout cells was able to restore the wt phenotype and prevented the decrease of GSK3β phosphorylation and the upregulation of the PI3K subunits following OH-TAM treatment (Supplementary Figure 3A). Furthermore, exogenous PDK1 expression completely inhibited apoptosis induced by PDK1 knockout (Supplementary Figure 3B).

In summary, the conditional knockout of PDK1 leads to upregulation of the upstream PI3K subunits p110β, p110δ and p85α in different cellular model systems. This effect can be prevented by the exogenous expression of PDK1.

Promoter analysis of *PDK1* − /cond cells

As FOXOs are known downstream targets of the PI3K/PDK1/Akt signaling pathway and we observed reduced FOXO1 phosphorylation upon induced PDK1 depletion or BX-795 treatment, we were next interested in the common transcriptional regulation of these genes. Thus, we analyzed the promoter regions of the genes encoding the PI3K subunits p110β, p110δ and p85α; the phosphoinositide-modifying enzymes (INPP5B, PIP5K1-β); the PI3K-interacting protein and Lyn by performing transcription factor mapping using Genomatix Software. Within the promoter regions of these regulated genes, we mainly identified binding sites for

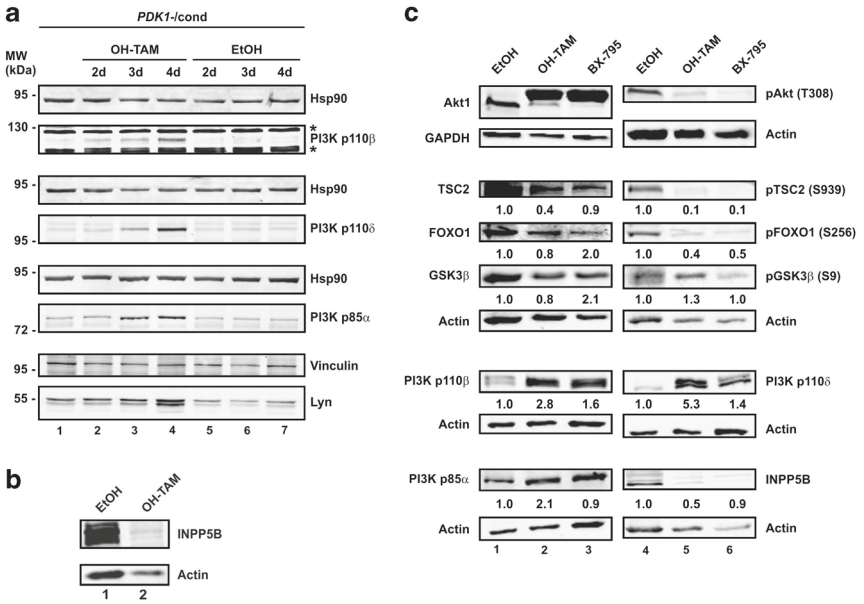

Figure 3. PDK1 negatively regulates expression of PI3K subunits. (**a**) DT40 *PDK1* − /cond and DT40 wt cells were treated with 0.5 μM OH-TAM or 0.05% EtOH for 48 h or left untreated. Then, cells were transferred to normal DT40 medium. On days 2–4 after beginning of OH-TAM/EtOH treatment, cleared cellular lysates were prepared and analyzed for PI3K p110β, PI3K p110δ, PI3K p85α, Lyn, Hsp90 and vinculin by immunoblotting. Data shown are representative of three independent experiments. * Indicates unspecific background bands. (**b**) DT40 *PDK1* − /cond cells were treated with 0.05% EtOH or 0.5 μM OH-TAM for 48 h. Then, cells were transferred to normal DT40 medium and incubated for additional 48 h. Cleared cellular lysates were prepared and analyzed for INPP5B and actin by immunoblotting. Data shown are representative of three independent experiments. (**c**) DT40 *PDK1* − /cond cells were treated with 0.05% EtOH or 0.5 μM OH-TAM for 48 h. Then, cells were transferred to normal DT40 medium and incubated for additional 48 h. Alternatively, DT40 *PDK1* − /cond cells were treated with 10 μM of the PDK1 inhibitor BX-795 for 48 h. Cleared cellular lysates were prepared and analyzed for Akt1, phospho-Akt (T308), TSC2, phospho-TSC2 (S939), FOXO1, phospho-FOXO1 (S256), GSK3β, phospho-GSK3β (S9), PI3K p110β, PI3K p110δ, PI3K p85α, INPP5B, GAPDH and actin by immunoblotting. Protein/loading control ratios were calculated and normalized to EtOH-treated controls. Data shown are representative of three independent experiments.

E-twenty six factors (ETSF), sex/testis-determining and related HMG box factors (SORY), forkhead domain factors (FKHD), heat-shock factors (HEAT) and cAMP response element-binding proteins (CREB) (Figure 4a). Next to FOXOs, which belong to the forkhead domain family, and CREB, the transcription factor families nuclear factor-κB and p53 have previously been shown to be regulated by the PDK1/Akt axis.[6,40,41] However, binding sites for both transcription factor families were not significantly enriched in the promoter regions of the analyzed transcripts (Figure 4a), and functional p53 is absent in DT40 cells.[42] Accordingly, we concentrated on the known Akt-regulated transcription factors FOXO and CREB. First, we employed the FOXO1 inhibitor AS1842856 (ref. 43) and analyzed its effect on the transcriptional upregulation of PI3K subunits upon OH-TAM-induced PDK1 depletion or BX-795-mediated PDK1 inhibition, respectively. Notably, the upregulation of the PI3K subunits p110β, p110δ and p85α was strongly blocked by the simultaneous inhibition of FOXO1, albeit not completely (Figure 4b). In turn, induction of CREB with forskolin (FSK) or CREB inhibition with the CBP–CREB interaction inhibitor resulted in the up- or downregulation of Lyn in DT40 cells (Figure 4c). Additionally, BX-795 treatment led to the induction of CREB-dependent transcription in Jurkat T lymphocytes as detected by a reporter gene assay (Figure 4d). Collectively, these experiments indicate that the CREB transcription factor (family) might also contribute to the transcriptional regulation of the PI3K/PDK1/Akt signaling axis. To further validate these results, we performed an upstream regulator analysis using Ingenuity Pathway Analysis Software with the two complete entity lists obtained by the microarray analysis. Indeed, both transcription factor families were identified as significant upstream regulators (Supplementary Figure 4).

It appears that the transcriptional regulation of Lyn, PI3K subunits and phosphoinositide-modifying enzymes in response to lack of active PDK1 is mainly mediated by transcription factors of the FOXO and CREB family, although the contribution of additional transcription factor families such as ETS has to be investigated in future studies.

PDK1 deficiency leads to increased PIP_3 levels in the plasma membrane

As PI3K class I enzymes produce PIP_3 and INPP5B can degrade PIP_3, we asked if the abundance of this lipid is affected upon upregulation of the PI3K subunits and downregulation of INPP5B following induction of PDK1 knockout. To address this question, we treated DT40 *PDK1* − /cond and wt cells with OH-TAM or EtOH and analyzed the amount of PIP_3 in these cells by a time-resolved

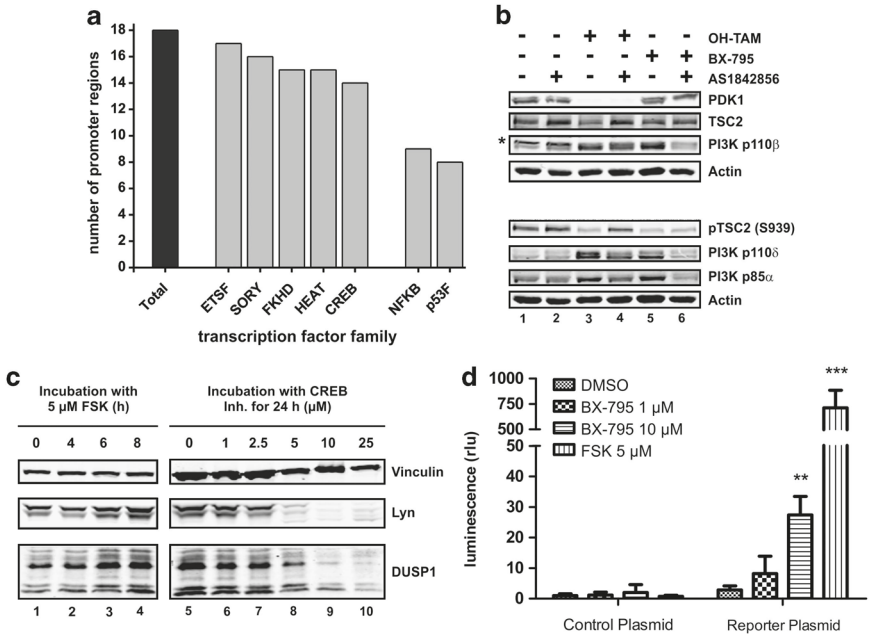

Figure 4. Promoter analysis of PDK1-regulated genes. (**a**) The promoter regions of the genes encoding the PI3K subunits p110β, p110δ and p85α; the phosphoinositide-modifying enzymes (INPP5B, PIP5K1-β); the PI3K-interacting protein and Lyn were analyzed by performing transcription factor mapping using Genomatix Software. The total number of identified promoter regions for these genes is 18 (black bar). The number of promoter regions containing binding sites for the following transcription factors are depicted (gray bars): E-twenty six factors (ETSF), sex/testis-determining and related HMG box factors (SORY), forkhead domain factors (FKHD), heat-shock factors (HEAT), cAMP response element-binding proteins (CREB), nuclear factor-κB (NFKB) and p53 family (p53F). (**b**) DT40 *PDK1* − /cond cells were treated with 0.05% EtOH or 0.5 μM OH-TAM for 48 h. Then, cells were transferred to normal DT40 medium and incubated for 24 h. Either the PDK1 inhibitor BX-795 or the FOXO1 inhibitor AS1842856 or both were added to a final concentration of 10 μM, and 0.1% v/v dimethylsulfoxide (DMSO) was used as control. After another 24 h, cleared cellular lysates were prepared and analyzed for PDK1, TSC2, phospho-TSC2 (S939), PI3K p110β, PI3K p110δ, PI3K p85α and actin by immunoblotting. Data shown are representative of three independent experiments. (**c**) DT40 *PDK1* − /cond cells were incubated with 5 μM forskolin (FSK) for the indicated times or the CREB–CBP interaction inhibitor for 24 h with the indicated concentrations. Cleared cellular lysates were prepared and analyzed for Lyn, the known CREB-regulated protein DUSP1 and vinculin by immunoblotting. Data shown are representative of three independent experiments. (**d**) Jurkat T lymphocytes were transfected with a CREB reporter plasmid or a control plasmid (CRE/CREB Reporter Assay Kit, BPS Bioscience) as described in the Materials and methods section. A plasmid containing a constitutively expressed Renilla luciferase gene served as a control of transfection efficiency. The PDK1 inhibitor BX-795 was added to a final concentration of 1 or 10 μM, and 0.1% DMSO was used as a negative control. The cells were incubated for 24 h. Cells treated with 5 μM of the CREB-inducer FSK for 6 h were used as positive control. Firefly luciferase activity was measured using a Dual-Luciferase Reporter Assay System (Promega) according to the manufacturer's instructions. The firefly luminescence value of each well was divided by the respective Renilla luminescence value. Each column was individually compared with the negative control by unpaired two-tailed Student's *t*-test. Data shown are mean of three independent experiments ± s.d. $^{**}P < 0.01$, $^{***}P < 0.001$.

fluorescence resonance energy transfer assay.[44] As controls, we treated DT40 *PDK1* − /cond cells with H_2O_2, which activates PI3K, or with the broad-band PI3K inhibitor LY294002. Strikingly, the amount of PIP_3 was significantly increased in the *PDK1* − /cond cells, but not in the control cells (Figure 5a). Furthermore, it appears that incubation with LY294002 for 30 min is not potent enough to completely block the increase of PIP_3 upon PI3K subunit upregulation, whereas it is sufficient for control cells.

Subsequently, we asked if increased PIP_3 levels at the plasma membrane can be detected *in vivo* by exogenous expression of the PDK1 PH domain fused to enhanced green fluorescent protein (EGFP). For that, we generated DT40 *PDK1* − /cond cells stably expressing fluorescently labeled chicken PDK1 PH domain (EGFP-PH_{chPDK1}) or a mutant version (EGFP-$PH_{chPDK1\text{-}K468E}$), which cannot bind to PIP_3.[45] We induced the deletion of PDK1 in these cells and analyzed the recruitment of the EGFP-tagged PH domain by confocal microscopy. Indeed, the PDK1 knockout led to increased binding of EGFP-PH_{chPDK1} to the plasma membrane compared with that in EtOH-treated cells (Figure 5b). Next, we wanted to investigate whether the recruitment could be inhibited by the addition of different PI3K inhibitors. As we observed that incubation with LY294002 for 30 min could not completely block PIP_3 generation (Figure 5a), we made use of a more selective PI3K class I inhibitor (GDC-0941) and treated the cells for 12 h. The translocation of EGFP-PH_{chPDK1} to the plasma membrane was entirely blocked by the simultaneous treatment with this pan-specific PI3K class I inhibitor. In contrast, application of the p110β- and p110δ-specific inhibitors TGX-221 and IC87114 (for 24 h) only resulted in a partially blocked recruitment, suggesting that the two catalytic PI3K subunits fulfill partially redundant functions. In cells expressing the mutant PH domain, no recruitment was detectable, confirming that PH domain translocation depends on PIP_3 in the plasma membrane (Figure 5b).

Collectively, these results indicate that PDK1 negatively regulates the amount of PIP_3 in the plasma membrane via the negative transcriptional regulation of PI3K subunits. This feedback suppression is apparently relieved upon depletion of PDK1.

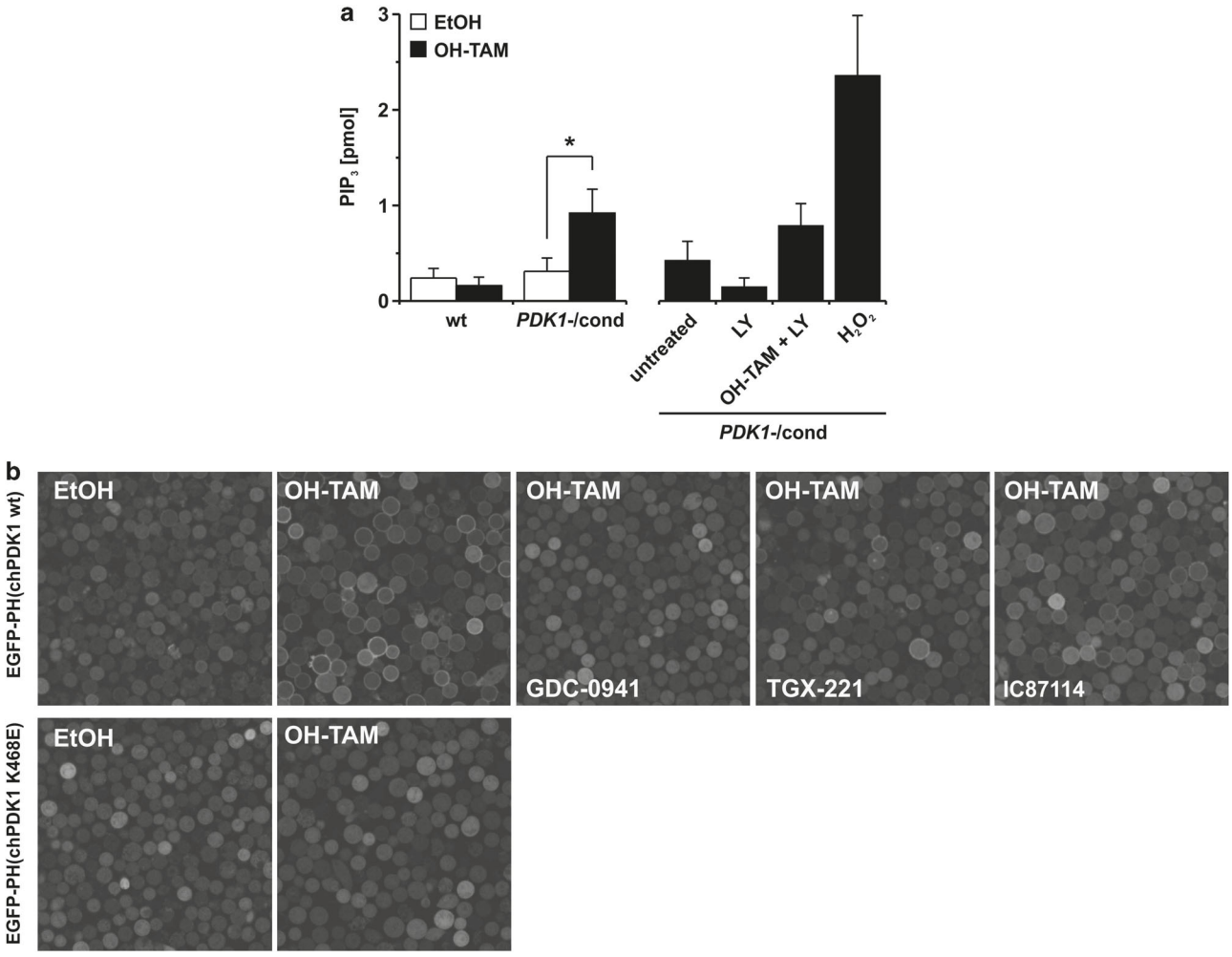

Figure 5. PDK1 deficiency increases PIP_3 levels in the plasma membrane. (**a**) DT40 *PDK1* − /cond and wt cells were treated with 0.5 μM OH-TAM or 0.05% EtOH for 48 h or left untreated. Then, cells were transferred to normal DT40 medium. On day 4 after beginning of OH-TAM treatment, control cells were treated with 10 μM LY294002 (LY) for 30 min (cells treated with OH-TAM or left untreated), 5 mM H_2O_2 for 2 min or left untreated. PIP_3 levels were measured using a time-resolved fluorescent resonance energy transfer displacement assay as described in detail in the Materials and methods section. Data shown are mean of triplicates ± s.d. and are representative of three independent experiments. *$P < 0.014$ (two-tailed paired *t*-test). (**b**) DT40 *PDK1* − /cond cells, retrovirally transfected with EGFP-PH(chPDK1 wt) or EGFP-PH(chPDK1 K468E) cDNAs, were treated with 0.5 μM OH-TAM or 0.05% EtOH for 48 h. Then, cells were transferred to normal DT40 medium and incubated for additional 48 h. Alternatively, OH-TAM-treated DT40 *PDK1* − /cond cells expressing EGFP-PH(chPDK1 wt) were incubated with 5 μM GDC-0941 (for 12 h prior to analysis), 10 μM TGX-221 (for 24 h prior to analysis) or 10 μM IC87114 (for 24 h prior to analysis). Cells were analyzed by confocal laser scanning microscopy. Data shown are representative of three independent experiments.

Akt and mTOR are important for the regulation of PI3K expression

PDK1 is an upstream activator of at least 23 different AGC family protein kinases including Akt, SGK, p70S6K, ribosomal S6 kinase, protein kinase C and protein kinase N.[12,13] The recruitment and activation of Akt can be blocked by mutating K465 in the PH domain of human PDK1 to glutamate.[45] In contrast, mutation of L155 to glutamate in the PDK1-interacting fragment pocket of human PDK1 reduces phosphorylation of SGK and p70S6K.[30,31] To address the relative contribution of the two different branches of PDK1 signaling to the negative transcriptional regulation of PI3K subunits, we mutated the corresponding amino acids in chicken PDK1 (L158 and K468) to glutamate, expressed these mutants in DT40 *PDK1* − /cond cells and analyzed the ability of both mutations to retain the knockout phenotype. Upon deletion of endogenous PDK1, PI3K subunit expression was increased in both cell lines expressing the single-mutated PDK1 variants, but not to the extent as in completely PDK1-depleted cells (Figure 6a). In contrast, cells expressing the double-mutated PDK1 version retained the knockout phenotype, indicating that both branches of PDK1 signaling are involved in the regulation of PI3K expression (Figure 6a). Next, we directly inhibited Akt using the inhibitor Akti-1/2/3 (MK-2206).[46,47] This led to a strong increase of the expression of the PI3K subunits p110δ and p85α and to a lesser extent p110β (Figure 6b). Similarly, treatment of human Jurkat T lymphocytes, DG75 B lymphocytes or Nalm-6 B lymphocytes with Akti-1/2/3 resulted in increased p110δ levels (Supplementary Figure 5A).

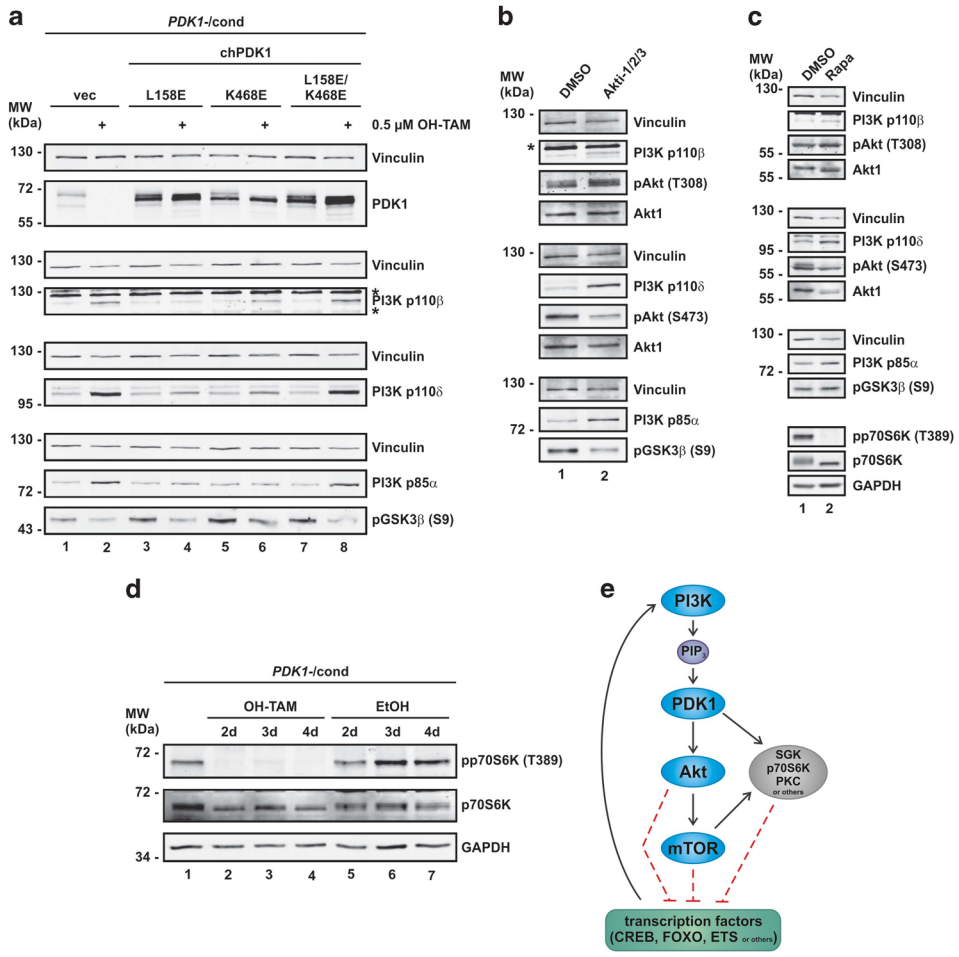

Figure 6. The PDK1 effector proteins Akt and mTOR are involved in the suppression of PI3K subunits. (**a**) DT40 *PDK1* − /cond cells, retrovirally transfected with chicken PDK1-L158E cDNA (L158E), chicken PDK1-K468E cDNA (K468E), chicken PDK1-L158E/K468E cDNA (L158E/K468E) or an empty vector (vec) were treated with 0.5 μM OH-TAM or 0.05% EtOH for 48 h. Then, cells were transferred to normal DT40 medium. On day 4 after beginning of OH-TAM/EtOH treatment, cleared cellular lysates were prepared and analyzed for PDK1, PI3K p110β, PI3K p110δ, PI3K p85α, phospho-GSK3β (S9) and vinculin by immunoblotting. Data shown are representative of three independent experiments. * Indicates unspecific background bands. (**b**) DT40 *PDK1* − /cond cells were treated with 1 μM Akti-1/2/3 for 48 h. Cleared cellular lysates were prepared and analyzed for PI3K p110β, PI3K p110δ, PI3K p85α, phospho-Akt (T308 and S473), Akt1, phospho-GSK3β (S9) and vinculin by immunoblotting. Data shown are representative of three independent experiments. * Indicates unspecific background band. (**c**) DT40 *PDK1* − /cond cells were treated with 100 nM rapamycin (Rapa) for 48 h. Cleared cellular lysates were prepared and analyzed for PI3K p110β, PI3K p110δ, PI3K p85α, phospho-Akt (T308 and S473), Akt1, phospho-GSK3β (S9), p70S6K, phospho-p70S6K (T389), vinculin and GAPDH by immunoblotting. Data shown are representative of three independent experiments. (**d**) DT40 *PDK1* − /cond cells were treated with 0.5 μM OH-TAM or 0.05% EtOH for 48 h or left untreated. Then, cells were transferred to normal DT40 medium. On day 4 after beginning of OH-TAM/EtOH treatment, cleared cellular lysates were prepared and analyzed for p70S6K, phospho-p70S6K (T389) and GAPDH by immunoblotting. Data shown are representative of three independent experiments. (**e**) Schematic diagram of the negative feedback regulation of the PI3K/PDK1/Akt signaling pathway. PDK1 activates Akt and other AGC kinases such as SGK, p70S6K or PKC. These kinases together with their downstream effectors (e.g., mTOR) in turn inhibit the transcription of PI3K subunits via the regulation of transcription factors of the CREB, FOXO, ETS and/or other families. By this means, cellular PIP_3 amounts are fine-tuned to levels that are sufficient for cell survival.

Several feedback signaling loops targeting the PI3K/PDK1/Akt pathway are controlled by mTOR. Thus, we analyzed the contribution of mTOR to the negative transcriptional regulation of the PI3K subunits. Inhibition of mTORC1 with rapamycin resulted in a similar effect as observed for Akt inhibition, that is, distinctly increased expression of p85α and p110δ and slightly increased expression of p110β (Figure 6c). Additionally, we observed that PDK1 depletion results in a complete inhibition of mTORC1 activity, as detected by phospho-p70S6K immunoblotting (Figure 6d). The rapamycin-mediated increase of PI3K subunit expression could also be demonstrated in Jurkat T lymphocytes (Supplementary Figure 5B). Collectively, we conclude that the Akt/mTORC1 axis is mainly responsible for the negative regulation of PI3K subunit expression downstream of PDK1. Additionally, the above-described feedback suppression appears to exist in different species and cell types.

DISCUSSION

The PI3K/PDK1/Akt signaling pathway plays a central role in cellular homeostasis by producing specific 'zip codes' at the inner leaflet of the plasma membrane. The PI3K product PIP_3 serves as an anchor for the recruitment of downstream effectors, including PDK1 and Akt. It has been confirmed that PIP_3 is the essential component of PI3K-mediated oncogenesis,[48] and accordingly increased levels of PIP_3 caused by either activation of PI3K or inactivation of phosphatase and tensin homolog (PTEN) are frequently found in tumor cells.[1–7] Concomitantly, aberrantly activated downstream effectors are frequently detectable in these cells. Generally, PI3K and PTEN activity is tightly controlled by a complex network of feedback regulations to maintain basal PIP_3 levels below a threshold for signaling activation. In this study, we identified an additional level of feedback control, that is, the PDK1-dependent transcriptional regulation of PI3K subunits and additional phosphoinositide-modifying enzymes. We showed that depletion of PDK1 or inactivation of its downstream effectors Akt or mTOR leads to the transcriptional upregulation of enzymes able to elevate PIP_3 levels in the plasma membrane and the concomitant downregulation of a PIP_3-degrading phosphatase. This transcriptional control is at least in part mediated by transcription factors of the FOXO and/or CREB family, although we cannot exclude the contribution of additional transcription factors (families) at this stage. Our observations strongly support a model of PDK1-dependent negative feedback regulation and indicate that the PIP_3-binding kinase PDK1 is a central negative regulator of PI3K expression. In this scenario, PDK1 functions as a sensor for PIP_3 levels and orchestrates pro-survival signals via the direct regulation of the activation threshold and signaling strength of Akt and mTOR.

It appears that the sole upregulation of PI3K subunits is sufficient to increase PIP_3 levels in DT40 B cells and that no additional activating stimulus is necessary. Along these lines, it has been previously reported that the overexpression of wt subunits p110β and p110δ is sufficient to induce an oncogenic phenotype in cultured chicken embryonic fibroblasts[49] and that p110β and p110δ subunits can lead to basal PI3K activity in PTEN-deficient human prostate cancer cells independently of receptor tyrosine kinase activation.[50]

Multiple branches of PI3K-dependent signal transduction converge on the level of PDK1.[12,13] The model of PDK1 as a gatekeeper of PI3K expression levels is attractive, as (1) PDK1 itself is constitutively active and (2) it regulates the activation of several downstream kinases that depend on the PI3K product PIP_3. This PIP_3 dependency might be either direct, for example, by PH domain-mediated recruitment in the case of Akt, or indirect, for example, by PIP_3-induced signaling cascades leading to the phosphorylation of the hydrophobic motif in the case of p70S6K or SGK.[13] According to our mutational analyses, both branches of PDK1 signaling participate in the negative regulation of PI3K subunit expression. It is tempting to speculate that the different branches of PDK1 signaling differently affect the expression of PI3K subunits. Indeed, the usage of Akti-1/2/3 and rapamycin leads to an upregulation of p110δ and p85α, whereas the p110β increase is rather moderate. This would suggest that the indirect PIP_3 signaling axis regulates p110β expression. Interestingly, the PH domain mutant in turn does not preferentially regulate the levels of p110δ and p85α, which might be explained by the fact that this mutation does not completely abolish Akt T308 phosphorylation.[45] Furthermore, it has recently been published that Akt might also be activated by a PDK1-interacting fragment pocket-dependent mechanism.[51] Accordingly, our data obtained with the pharmacological inhibition of Akt or mTORC1 in different cell lines indicate that this axis is centrally involved in the transcriptional regulation of PI3K expression.

Next to the PI3K catalytic subunits, PIP_3 levels are regulated by additional enzymatic activities. Interestingly, our microarray results revealed that non-PI3K PIP_3-regulating proteins are also regulated on a transcriptional level. These targets include the lipid phosphatase INPP5B, the phosphatidylinositol kinase PIP5K1-β and the PI3K-interacting protein 1. Of note, the transcriptional regulation of INPP5B and PIP5K1-β follows the ultimate goal to increase cellular PIP_3 levels: INPP5B, which accepts PIP_3 as substrate and has been implicated in the systemic dephosphorylation of PIP_3 to PI-3-P,[52] is downregulated upon PDK1 depletion, whereas PIP5K1-β, which participates in the synthesis of the PI3K substrate phosphatidylinositol-4,5-bisphosphate,[53] is upregulated.

At first glance, it seems paradoxical that Akt should contribute to the negative regulation of PIP_3 levels, as PIP_3 itself is mandatory for Akt activation and many tumorigenic effects of increased PIP_3 concentrations are mediated by Akt. However, it appears comprehensive that PIP_3 levels are tightly kept at a certain level sufficient for Akt-dependent pro-survival signaling. In this regard, one might speculate that 'basally active' PDK1/Akt adjust PIP_3 levels to a value that is sufficient for their own activation and the generation of survival signals but does not exceed a harmful threshold leading to the demise of the cell. Indeed, it has been reported that chronic Akt activation leads to apoptosis and that Akt sensitizes cells to reactive oxygen species-induced apoptosis.[40,41,54] Given the existence of this 'dark side' of Akt together with the observation that Akt is the only critical target activated by increased PIP_3 concentrations due to loss of PTEN (at least in *Drosophila*),[55] it readily makes sense that PI3K expression levels are adjusted to a certain level. As soon as one interferes with these PI3K/PIP_3 levels necessary for the mere pro-survival machinery, for example, by PDK1 depletion or Akt inhibition, this repression is relieved and PIP_3 generation is increased.

Major classes of transcription factors are controlled by Akt, such as the FOXO family of transcription factors, CREB, nuclear factor-κB or p53.[6,56,57] Akt-mediated phosphorylation of CREB enables the binding of accessory proteins that are necessary for the transcription of pro-survival genes such as *BCL2* and *MCL1*.[6,58,59] According to our data, it appears that either the deletion of PDK1 or the inhibition of Akt might positively affect CREB-dependent transcription. The second major component that participates in the transcriptional control of PI3K subunits and PIP_3-modifying enzymes are members of the FOXO famiy of transcription factors. Akt-catalyzed phosphorylation of FOXO1, FOXO3a and FOXO4 transcription factors leads to their binding to 14-3-3 proteins and their retention in the cytoplasm. This in turn prevents the transcription of pro-apoptotic target genes such as the BH3-only family proteins and the Fas ligand.[6,36] Accordingly, so far CREB and FOXOs have been essentially placed downstream of the PI3K/PDK1/Akt signaling cascade. Although our data suggest that the CREB and FOXO transcription factors mediate the observed

upregulation of Lyn, PI3K subunits and phosphoinositide subunits, we cannot exclude the involvement of additional transcription factor families. Our *in silico* analysis revealed that binding sites for family members of the ETS transcription factor exist in most promoter regions of the relevant genes, and different reports describe the Akt-mediated control of ETS family members or even the cooperativity between CREB and c-Ets1.[60–62] Additionally, a highly conserved transcription factor-binding cluster containing an ETS-binding sequence has been identified for the murine and human *PIK3CD* gene encoding p110δ.[63] Nevertheless, further experiments are required to elucidate the exact mechanistic details. This is also underlined by the observation that the Akt effector protein mTOR participates in the described regulation. The kinase mTOR has been shown to be involved in the regulation of gene transcription.[64] Gene expression-profiling experiments have shown that ~5% of the transcriptome are differentially expressed in response to rapamycin-mediated mTOR inhibition.[65] Accordingly, we cannot exclude that mTOR also directly regulates the expression of PI3K subunits and PIP_3-modifying enzymes. The antidromic regulation of PIP_3-generating kinases and the PIP_3-degrading phosphatase INPP5B already indicates that additional factors are necessary for this transcriptional regulation. It is tempting to speculate that different Akt effectors (CREB, FOXOs and mTOR) control the overall signaling strength of the upstream tyrosine kinase/PI3K/PDK1/Akt signaling pathway, for example, CREB-mediated control of Lyn or FOXO-mediated control of PI3K subunits.

In summary, we identified a novel negative feedback regulation of the PI3K/PDK1/Akt pathway. This feedback depends on the PDK1-mediated suppression of regulatory and catalytic PI3K subunits. Upon PDK1 deletion or Akt inhibition, this suppression is relieved and the corresponding mRNAs are transcribed under the control of CREB/FOXO transcription factors (Figure 6e). This transcriptional feedback regulation adds to the existing 'catalog' of feedback mechanisms that attenuate PI3K/PDK1/Akt signaling. These feedback loops include the mTORC1-dependent transcriptional downregulation or post-translational inhibition of insulin receptor substrate-1/2, insulin-like growth factor-1 or insulin-like growth factor-1R or the recently reported Akt-dependent suppression of receptor tyrosine kinase expression and activity.[32,66] Collectively, all these regulatory feedback loops underscore the necessity of novel therapeutic strategies based upon combinatorial approaches. In recent years, mTOR inhibitors have been developed as potential therapeutics. However, one might hypothesize that the efficiency of therapies that are mainly aiming at mTOR inhibition could be further improved by the parallel inhibition of PI3K, PIP_3, PDK1 or Akt, depending on the malignancy-dependent existence or emergence of feedback signaling cascades.

MATERIALS AND METHODS

Cell culture

Chicken DT40 wt B cells, human DG75 B cells, human Nalm-6 B cells, human Ramos B cells, human Jurkat T cells and human prostate carcinoma PC-3 cells were obtained from DSMZ (Braunschweig, Germany). Chicken DT40 conditional *PDK1* −/cond cells (DT40 *PDK1* −/cond) have been previously described[33] and were kindly provided by Tomohiro Kurosaki (RIKEN Research Center for Allergy and Immunology, Yokohama, Japan). All cell lines were maintained in 5% CO_2 at 37 °C. All chicken DT40 cell lines were cultivated in RPMI 1640 (Lonza, Cologne, Germany) supplemented with 10% fetal calf serum, 1% chicken serum, 3 mM L-glutamine, 50 μM β-mercaptoethanol, 50 U/ml penicillin and 50 μg/ml streptomycin. Human DG75 and Nalm-6 B cells and human PC-3 prostate carcinoma cells were grown in RPMI 1640 supplemented with 10% fetal calf serum, 50 U/ml penicillin and 50 μg/ml streptomycin. Human Jurkat T cells and human Ramos B cells were cultivated in RPMI 1640 supplemented with 10% fetal calf serum, 10 mM HEPES (4-(2-hydroxyethyl)-1-piperazineethanesulfonic acid), 50 U/ml penicillin and 50 μg/ml streptomycin.

Antibodies and reagents

Anti-Akt, anti-phospho-Akt (T308 and S473), anti-FOXO1, anti-phospho-FOXO1 (S256), anti-phospho-GSK3β (S9) and anti-GSK3β antibodies were purchased from Cell Signaling Technology (New England Biolabs, Frankfurt, Germany), anti-Akt1, anti-PI3K p110δ, anti-Lyn and anti-GAPDH (glyceraldehyde 3-phosphate dehydrogenase) antibodies from Abcam (Cambridge, UK), anti-PDK1 and anti-PI3K p85α antibodies from Epitomics (Abcam), anti-PI3K p110β from Santa Cruz Biotechnology (Heidelberg, Germany), anti-Hsp90 from BD Biosciences (Heidelberg, Germany), anti-INPP5B from GeneTex (Irvine, CA, USA), anti-DUSP1 from Novus Biologicals (Acris Antibodies, Herford, Germany) and anti-actin and anti-vinculin from Sigma-Aldrich (Schnelldorf, Germany). OH-TAM was purchased from Sigma-Aldrich and the broad-band PI3K inhibitor LY294002 from Cell Signaling Technology. The pan-PI3K inhibitor GDC-0941, the PI3K p110β inhibitor TGX-221 and the PI3K p110δ inhibitor IC-87114 were purchased from Selleckchem (ICS International Clinical Service GmbH, Munich, Germany). FSK, the CBP–CREB interaction inhibitor, and the FOXO1 inhibitor AS1842856 were purchased from Calbiochem (Merck KGaA, Darmstadt, Germany). Anti-chicken-IgM (M4) was obtained from Southern Biotech (Biozol, Eching, Germany). Puromycin was purchased from InvivoGen (Toulouse, France). BX-795 was purchased from Axon Medchem (Groningen, The Netherlands). Akti-1/2/3 (MK-2206) was kindly provided by Dario R Alessi.

Expression constructs and retroviral infection

Wild-type chicken *PDK1* cDNA was cloned into pMSCVpuro (Clontech, Takara, Saint-Germain-en-Laye, France). cDNA encoding the chicken PDK1 PH domain (codons 409–557) was cloned into pEGFP-C1 (Clontech). pMSCVpuro-EGFP-PH_{chPDK1} was generated by cloning of *EGFP-PH*$_{chPDK1}$ cDNA into pMSCVpuro. Substitutions of leucine 158 and lysine 468 to glutamate were generated by site-directed mutagenesis to create a PDK1-interacting fragment-binding pocket mutant, PH domain mutant or double-mutant chicken PDK1. For retroviral gene transfer, Plat-E cells were transfected with pMSCV-based vectors using FuGENE 6 transfection reagent (Roche, Mannheim, Germany). The MMLV was pseudotyped with VSV-G. DT40 *PDK1* −/cond cells were incubated with retroviral supernatant containing 3 μg/ml Polybrene (Sigma-Aldrich) and selected in a medium containing 0.5 μg/ml puromycin.

Reporter gene assay

A number of 4×10^6 Jurkat cells was harvested by centrifugation at $600 \times g$ for 5 min at 4 °C, washed with phosphate-buffered saline and transfected with 300 ng of either CREB reporter plasmid or control plasmid (CRE/CREB Reporter Assay Kit, BPS Bioscience, San Diego, CA, USA) using an Amaxa Nucleofector I device with program K-25 and Solution T (Lonza) according to the manufacturer's instructions. After transfection, the cells were incubated at room temperature for 10 min and then transferred to a prewarmed medium and incubated overnight. BX-795 was added to a final concentration of 1 or 10 μM, and 0.1% dimethylsulfoxide was used as a negative control. After 24 h of incubation, FSK was added to previously untreated cells to a final concentration of 5 μM. The cells were transferred to a white opaque 96-well plate and incubated for another 6 h. The plate was then centrifuged at $600 \times g$ for 5 min at 4 °C. The cells were washed with phosphate-buffered saline, and firefly luciferase activity was measured using a Dual-Luciferase Reporter Assay System (Promega, Mannheim, Germany) according to the manufacturer's instructions, using a Synergy MX multiwell reader with dispenser (BioTek, Bad Friedrichshall, Germany).

Measurement of apoptosis

DT40 cells were cultivated in a medium containing 0.5 μM OH-TAM or 0.05% EtOH as control. After 48 h, OH-TAM-treated cells were transferred to a normal medium. Either the leakage of fragmented DNA was measured 4–8 days after beginning of OH-TAM treatment or on day 4 cells were stimulated with 10 μg/ml anti-chicken-IgM (M4) for 24 h and apoptosis was measured. Nuclei were prepared by lysing cells in hypotonic lysis buffer (1% sodium citrate, 0.1% Triton X-100 and 50 μg/ml propidium iodide) and subsequently analyzed by flow cytometry. Nuclei to the left of the 2N peak were considered as apoptotic. Flow cytometric analyses were performed on FACSCalibur (BD Biosciences) using CellQuest software or on LSRFortessa (BD Biosciences) using FACSDiva software.

Cell extracts and immunoblotting

DT40 cells were incubated in a medium containing 0.5 μM OH-TAM or 0.05% EtOH as control. After 48 h, OH-TAM-treated cells were transferred to a normal medium and harvested at the indicated time points. Following treatment of DT40, DG75, Nalm-6 or Jurkat cells with the different compounds at the indicated concentrations for the indicated times, cells were lysed in lysis buffer (20 mM Tris–HCl, pH 7.5, 150 mM NaCl, 0.5 mM EDTA, 1% Triton X-100, 10 mM NaF, 2.5 mM NaPP, 10 μM Na_2MoO_4, 1 mM Na_3VO_4 and protease inhibitors (P2714, Sigma-Aldrich)), and lysates were clarified by centrifugation at 16 000 × *g* for 10 min. Equal total protein amounts, as determined by the Bradford method, were separated on 8% or 10% SDS–polyacrylamide gels and transferred to PVDF membrane (Merck, Millipore, Darmstadt, Germany). Immunoblot analysis was performed using the indicated primary antibodies and appropriate IRDye 800- or IRDye 680-conjugated secondary antibodies (LI-COR Biosciences, Bad Homburg, Germany). Signals were detected with an Odyssey Infrared Imaging system (LI-COR Biosciences).

Analysis of PIP_3 levels

DT40 cells were incubated in a medium containing 0.5 μM OH-TAM or 0.05% EtOH as control. After 48 h, OH-TAM-treated cells were transferred to a normal medium. On day 4, control cells were treated with 10 μM LY294002 (LY) for 30 min (cells treated with OH-TAM or left untreated), 5 mM H_2O_2 for 2 min or left untreated. Subsequently, cells were harvested and the mass of PIP_3 was determined. Cells were precipitated by the addition of 0.5 ml ice-cold 0.5 M trichloroacetic acid and kept on ice for 5 min. The precipitated cells were collected by centrifugation, trichloroacetic acid was aspirated and the pellet was immediately frozen on dry ice until lipids were extracted. The mass of PIP_3 was estimated using a time-resolved fluorescence resonance energy transfer displacement assay as described previously.[44]

Quantitative real-time RT–PCR

Quantitative real-time RT–PCR analysis was performed using the ABI Prism 7000 Sequence Detection System (Applied Biosystems, Darmstadt, Germany) and Maxima qPCR Master Mix (Fermentas, Thermo Scientific, St Leon-Rot, Germany). Total RNA from 1×10^6 cells was isolated using the NucleoSpin RNA II-Kit (Macherey–Nagel, Düren, Germany). cDNA was generated from 1 μg of total RNA with 200 U RevertAid H Minus reverse transcriptase, 50 μM random hexamers, 400 μM dNTPs and 1.6 U/μl RiboLock RNase inhibitor (all from Fermentas), according to the manufacturer's recommendations. A portion of 50 ng of the resulting cDNA was applied to quantitative RT–PCR analyses (20 μl final volume) and amplified in the presence of 200 nM primers and 100 nM probe or 300 nM primers in the case of SYBR Green detection with the standard temperature profile (2 min 50 °C, 10 min 95 °C, 40 cycles 15 s 95 °C and 1 min 60 °C). Relative quantification was performed employing the standard curve method. The results were normalized on the reference gene *18S ribosomal RNA*. The cell populations on day 0 of OH-TAM treatment were used as calibrator.

Confocal laser scanning microscopy

Cells were resuspended in Krebs–Ringer solution (10 mM HEPES, pH 7.0, 140 mM NaCl, 4 mM KCl, 1 mM $MgCl_2$, 1 mM $CaCl_2$ and 10 mM glucose) and seeded onto chambered cover glasses (Nunc, Thermo Scientific, Langenselbold, Germany). After 20 min, cells were analyzed on a Leica TCS SP II confocal laser scanning microscope (Leica, Wetzlar, Germany). EGFP was excited at 488 nm.

CONFLICT OF INTEREST

The authors declare no conflict of interest.

ACKNOWLEDGEMENTS

We thank Dario Alessi for providing Akti-1/2/3 (MK-2206) and for helpful discussions. This study was supported by grants from the Deutsche Forschungsgemeinschaft SFB 773 and GRK 1302 (to SW and BS) and from the Interdisciplinary Center of Clinical Research, Faculty of Medicine, Tübingen (Nachwuchsgruppe 1866-0-0, to BS).

REFERENCES

1 Bunney TD, Katan M. Phosphoinositide signalling in cancer: beyond PI3K and PTEN. *Nat Rev Cancer* 2010; **10**: 342–352.
2 Carnero A. The PKB/AKT pathway in cancer. *Curr Pharm Des* 2010; **16**: 34–44.
3 Chalhoub N, Baker SJ. PTEN and the PI3-kinase pathway in cancer. *Annu Rev Pathol* 2009; **4**: 127–150.
4 Cully M, You H, Levine AJ, Mak TW. Beyond PTEN mutations: the PI3K pathway as an integrator of multiple inputs during tumorigenesis. *Nat Rev Cancer* 2006; **6**: 184–192.
5 Engelman JA. Targeting PI3K signalling in cancer: opportunities, challenges and limitations. *Nat Rev Cancer* 2009; **9**: 550–562.
6 Hers I, Vincent EE, Tavare JM. Akt signalling in health and disease. *Cell Signal* 2011; **23**: 1515–1527.
7 Vivanco I, Sawyers CL. The phosphatidylinositol 3-kinase AKT pathway in human cancer. *Nat Rev Cancer* 2002; **2**: 489–501.
8 So L, Fruman DA. PI3K signalling in B- and T-lymphocytes: new developments and therapeutic advances. *Biochem J* 2012; **442**: 465–481.
9 Engelman JA, Luo J, Cantley LC. The evolution of phosphatidylinositol 3-kinases as regulators of growth and metabolism. *Nat Rev Genet* 2006; **7**: 606–619.
10 Vanhaesebroeck B, Guillermet-Guibert J, Graupera M, Bilanges B. The emerging mechanisms of isoform-specific PI3K signalling. *Nat Rev Mol Cell Biol* 2010; **11**: 329–341.
11 Liu Y, Bankaitis VA. Phosphoinositide phosphatases in cell biology and disease. *Prog Lipid Res* 2010; **49**: 201–217.
12 Mora A, Komander D, van Aalten DM, Alessi DR. PDK1, the master regulator of AGC kinase signal transduction. *Semin Cell Dev Biol* 2004; **15**: 161–170.
13 Pearce LR, Komander D, Alessi DR. The nuts and bolts of AGC protein kinases. *Nat Rev Mol Cell Biol* 2010; **11**: 9–22.
14 Alessi DR, Deak M, Casamayor A, Caudwell FB, Morrice N, Norman DG *et al.* 3-Phosphoinositide-dependent protein kinase-1 (PDK1): structural and functional homology with the Drosophila DSTPK61 kinase. *Curr Biol* 1997; **7**: 776–789.
15 Alessi DR, James SR, Downes CP, Holmes AB, Gaffney PR, Reese CB *et al.* Characterization of a 3-phosphoinositide-dependent protein kinase which phosphorylates and activates protein kinase Balpha. *Curr Biol* 1997; **7**: 261–269.
16 Alessi DR, Kozlowski MT, Weng QP, Morrice N, Avruch J. 3-Phosphoinositide-dependent protein kinase 1 (PDK1) phosphorylates and activates the p70 S6 kinase *in vivo* and *in vitro*. *Curr Biol* 1998; **8**: 69–81.
17 Kobayashi T, Cohen P. Activation of serum- and glucocorticoid-regulated protein kinase by agonists that activate phosphatidylinositide 3-kinase is mediated by 3-phosphoinositide-dependent protein kinase-1 (PDK1) and PDK2. *Biochem J* 1999; **339**: 319–328.
18 Kobayashi T, Deak M, Morrice N, Cohen P. Characterization of the structure and regulation of two novel isoforms of serum- and glucocorticoid-induced protein kinase. *Biochem J* 1999; **344**: 189–197.
19 Dong LQ, Zhang RB, Langlais P, He H, Clark M, Zhu L *et al.* Primary structure, tissue distribution, and expression of mouse phosphoinositide-dependent protein kinase-1, a protein kinase that phosphorylates and activates protein kinase Czeta. *J Biol Chem* 1999; **274**: 8117–8122.
20 Jensen CJ, Buch MB, Krag TO, Hemmings BA, Gammeltoft S, Frodin M. 90-kDa ribosomal S6 kinase is phosphorylated and activated by 3-phosphoinositide-dependent protein kinase-1. *J Biol Chem* 1999; **274**: 27168–27176.
21 Le Good JA, Ziegler WH, Parekh DB, Alessi DR, Cohen P, Parker PJ. Protein kinase C isotypes controlled by phosphoinositide 3-kinase through the protein kinase PDK1. *Science* 1998; **281**: 2042–2045.
22 Park J, Leong ML, Buse P, Maiyar AC, Firestone GL, Hemmings BA. Serum and glucocorticoid-inducible kinase (SGK) is a target of the PI 3-kinase-stimulated signaling pathway. *EMBO J* 1999; **18**: 3024–3033.
23 Pullen N, Dennis PB, Andjelkovic M, Dufner A, Kozma SC, Hemmings BA *et al.* Phosphorylation and activation of p70s6k by PDK1. *Science* 1998; **279**: 707–710.
24 Bayascas JR. PDK1: the major transducer of PI 3-kinase actions. *Curr Top Microbiol Immunol* 2010; **346**: 9–29.
25 Currie RA, Walker KS, Gray A, Deak M, Casamayor A, Downes CP *et al.* Role of phosphatidylinositol 3,4,5-trisphosphate in regulating the activity and localization of 3-phosphoinositide-dependent protein kinase-1. *Biochem J* 1999; **337**: 575–583.
26 Fayard E, Xue G, Parcellier A, Bozulic L, Hemmings BA. Protein kinase B (PKB/Akt), a key mediator of the PI3K signaling pathway. *Curr Top Microbiol Immunol* 2010; **346**: 31–56.
27 Sarbassov DD, Guertin DA, Ali SM, Sabatini DM. Phosphorylation and regulation of Akt/PKB by the rictor–mTOR complex. *Science* 2005; **307**: 1098–1101.
28 Burnett PE, Barrow RK, Cohen NA, Snyder SH, Sabatini DM. RAFT1 phosphorylation of the translational regulators p70 S6 kinase and 4E-BP1. *Proc Natl Acad Sci USA* 1998; **95**: 1432–1437.
29 Garcia-Martinez JM, Alessi DR. mTOR complex 2 (mTORC2) controls hydrophobic motif phosphorylation and activation of serum- and glucocorticoid-induced protein kinase 1 (SGK1). *Biochem J* 2008; **416**: 375–385.

30 Balendran A, Biondi RM, Cheung PC, Casamayor A, Deak M, Alessi DR. A 3-phosphoinositide-dependent protein kinase-1 (PDK1) docking site is required for the phosphorylation of protein kinase Czeta (PKCzeta) and PKC-related kinase 2 by PDK1. *J Biol Chem* 2000; **275**: 20806–20813.
31 Biondi RM, Kieloch A, Currie RA, Deak M, Alessi DR. The PIF-binding pocket in PDK1 is essential for activation of S6K and SGK, but not PKB. *EMBO J* 2001; **20**: 4380–4390.
32 Carracedo A, Pandolfi PP. The PTEN-PI3K pathway: of feedbacks and cross-talks. *Oncogene* 2008; **27**: 5527–5541.
33 Shinohara H, Maeda S, Watarai H, Kurosaki T. IkappaB kinase beta-induced phosphorylation of CARMA1 contributes to CARMA1 Bcl10 MALT1 complex formation in B cells. *J Exp Med* 2007; **204**: 3285–3293.
34 Lawlor MA, Mora A, Ashby PR, Williams MR, Murray-Tait V, Malone L *et al.* Essential role of PDK1 in regulating cell size and development in mice. *EMBO J* 2002; **21**: 3728–3738.
35 Takata M, Homma Y, Kurosaki T. Requirement of phospholipase C-gamma 2 activation in surface immunoglobulin M-induced B cell apoptosis. *J Exp Med* 1995; **182**: 907–914.
36 Brunet A, Bonni A, Zigmond MJ, Lin MZ, Juo P, Hu LS *et al.* Akt promotes cell survival by phosphorylating and inhibiting a forkhead transcription factor. *Cell* 1999; **96**: 857–868.
37 Kops GJ, Medema RH, Glassford J, Essers MA, Dijkers PF, Coffer PJ *et al.* Control of cell cycle exit and entry by protein kinase B-regulated forkhead transcription factors. *Mol Cell Biol* 2002; **22**: 2025–2036.
38 Kurosaki T. Regulation of BCR signaling. *Mol Immunol* 2011; **48**: 1287–1291.
39 Feldman RI, Wu JM, Polokoff MA, Kochanny MJ, Dinter H, Zhu D *et al.* Novel small molecule inhibitors of 3-phosphoinositide-dependent kinase-1. *J Biol Chem* 2005; **280**: 19867–19874.
40 Los M, Maddika S, Erb B, Schulze-Osthoff K. Switching Akt: from survival signaling to deadly response. *Bioessays* 2009; **31**: 492–495.
41 Nogueira V, Park Y, Chen CC, Xu PZ, Chen ML, Tonic I *et al.* Akt determines replicative senescence and oxidative or oncogenic premature senescence and sensitizes cells to oxidative apoptosis. *Cancer Cell* 2008; **14**: 458–470.
42 Yamazoe M, Sonoda E, Hochegger H, Takeda S. Reverse genetic studies of the DNA damage response in the chicken B lymphocyte line DT40. *DNA Repair (Amst)* 2004; **3**: 1175–1185.
43 Nagashima T, Shigematsu N, Maruki R, Urano Y, Tanaka H, Shimaya A *et al.* Discovery of novel forkhead box O1 inhibitors for treating type 2 diabetes: improvement of fasting glycemia in diabetic db/db mice. *Mol Pharmacol* 2010; **78**: 961–970.
44 Gray A, Olsson H, Batty IH, Priganica L, Peter Downes C. Nonradioactive methods for the assay of phosphoinositide 3-kinases and phosphoinositide phosphatases and selective detection of signaling lipids in cell and tissue extracts. *Anal Biochem* 2003; **313**: 234–245.
45 Bayascas JR, Wullschleger S, Sakamoto K, Garcia-Martinez JM, Clacher C, Komander D *et al.* Mutation of the PDK1 PH domain inhibits protein kinase B/Akt, leading to small size and insulin resistance. *Mol Cell Biol* 2008; **28**: 3258–3272.
46 Hirai H, Sootome H, Nakatsuru Y, Miyama K, Taguchi S, Tsujioka K *et al.* MK-2206, an allosteric Akt inhibitor, enhances antitumor efficacy by standard chemotherapeutic agents or molecular targeted drugs *in vitro* and *in vivo*. *Mol Cancer Ther* 2010; **9**: 1956–1967.
47 Lindsley CW. The Akt/PKB family of protein kinases: a review of small molecule inhibitors and progress towards target validation: a 2009 update. *Curr Top Med Chem* 2010; **10**: 458–477.
48 Denley A, Gymnopoulos M, Kang S, Mitchell C, Vogt PK. Requirement of phosphatidylinositol(3,4,5)trisphosphate in phosphatidylinositol 3-kinase-induced oncogenic transformation. *Mol Cancer Res* 2009; **7**: 1132–1138.
49 Kang S, Denley A, Vanhaesebroeck B, Vogt PK. Oncogenic transformation induced by the p110beta, -gamma, and -delta isoforms of class I phosphoinositide 3-kinase. *Proc Natl Acad Sci USA* 2006; **103**: 1289–1294.
50 Jiang X, Chen S, Asara JM, Balk SP. Phosphoinositide 3-kinase pathway activation in phosphate and tensin homolog (PTEN)-deficient prostate cancer cells is independent of receptor tyrosine kinases and mediated by the p110beta and p110delta catalytic subunits. *J Biol Chem* 2010; **285**: 14980–14989.
51 Najafov A, Shpiro N, Alessi DR. Akt is efficiently activated by PIF-pocket- and PtdIns(3,4,5)P3-dependent mechanisms leading to resistance to PDK1 inhibitors. *Biochem J* 2012; **448**: 285–295.
52 Shin HW, Hayashi M, Christoforidis S, Lacas-Gervais S, Hoepfner S, Wenk MR *et al.* An enzymatic cascade of Rab5 effectors regulates phosphoinositide turnover in the endocytic pathway. *J Cell Biol* 2005; **170**: 607–618.
53 van den Bout I, Divecha N. PIP5K-driven PtdIns(4,5)P2 synthesis: regulation and cellular functions. *J Cell Sci* 2009; **122**: 3837–3850.
54 van Gorp AG, Pomeranz KM, Birkenkamp KU, Hui RC, Lam EW, Coffer PJ. Chronic protein kinase B (PKB/c-akt) activation leads to apoptosis induced by oxidative stress-mediated Foxo3a transcriptional up-regulation. *Cancer Res* 2006; **66**: 10760–10769.
55 Stocker H, Andjelkovic M, Oldham S, Laffargue M, Wymann MP, Hemmings BA *et al.* Living with lethal PIP3 levels: viability of flies lacking PTEN restored by a PH domain mutation in Akt/PKB. *Science* 2002; **295**: 2088–2091.
56 Brunet A, Datta SR, Greenberg ME. Transcription-dependent and -independent control of neuronal survival by the PI3K–Akt signaling pathway. *Curr Opin Neurobiol* 2001; **11**: 297–305.
57 Parcellier A, Tintignac LA, Zhuravleva E, Hemmings BA. PKB and the mitochondria: AKTing on apoptosis. *Cell Signal* 2008; **20**: 21–30.
58 Nicholson KM, Anderson NG. The protein kinase B/Akt signalling pathway in human malignancy. *Cell Signal* 2002; **14**: 381–395.
59 Wang JM, Chao JR, Chen W, Kuo ML, Yen JJ, Yang-Yen HF. The antiapoptotic gene mcl-1 is up-regulated by the phosphatidylinositol 3-kinase/Akt signaling pathway through a transcription factor complex containing CREB. *Mol Cell Biol* 1999; **19**: 6195–6206.
60 Bujor AM, Nakerakanti S, Morris E, Hant FN, Trojanowska M. Akt inhibition up-regulates MMP1 through a CCN2-dependent pathway in human dermal fibroblasts. *Exp Dermatol* 2010; **19**: 347–354.
61 Figueroa C, Vojtek AB. Akt negatively regulates translation of the ternary complex factor Elk-1. *Oncogene* 2003; **22**: 5554–5561.
62 Song KS, Lee TJ, Kim K, Chung KC, Yoon JH. cAMP-responding element-binding protein and c-Ets1 interact in the regulation of ATP-dependent MUC5AC gene expression. *J Biol Chem* 2008; **283**: 26869–26878.
63 Kok K, Nock GE, Verrall EA, Mitchell MP, Hommes DW, Peppelenbosch MP *et al.* Regulation of p110delta PI 3-kinase gene expression. *PLoS One* 2009; **4**: e5145.
64 Caron E, Ghosh S, Matsuoka Y, Ashton-Beaucage D, Therrien M, Lemieux S *et al.* A comprehensive map of the mTOR signaling network. *Mol Syst Biol* 2010; **6**: 453.
65 Guertin DA, Guntur KV, Bell GW, Thoreen CC, Sabatini DM. Functional genomics identifies TOR-regulated genes that control growth and division. *Curr Biol* 2006; **16**: 958–970.
66 Chandarlapaty S, Sawai A, Scaltriti M, Rodrik-Outmezguine V, Grbovic-Huezo O, Serra V *et al.* AKT inhibition relieves feedback suppression of receptor tyrosine kinase expression and activity. *Cancer Cell* 2011; **19**: 58–71.

Supplementary Information accompanies this paper on the Oncogene website (http://www.nature.com/onc)

Manuscript "Efficient and safe gene delivery to human corneal endothelium using magnetic nanoparticles"

Czugala M, Mykhaylyk O, Böhler P, Onderka J, Stork B, Wesselborg S, Kruse FE, Plank C, Singer BB, Fuchsluger TA. *Nanomedicine* (2016) **11**:1787, doi: 10.2217/nnm-2016-0144

Research Article

For reprint orders, please contact: reprints@futuremedicine.com

Nanomedicine

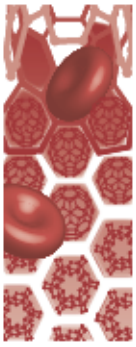

Efficient and safe gene delivery to human corneal endothelium using magnetic nanoparticles

Aim: To develop a safe and efficient method for targeted, anti-apoptotic gene therapy of corneal endothelial cells (CECs). **Materials & methods:** Magnetofection (MF), a combination of lipofection with magnetic nanoparticles (MNPs; PEI-Mag2, SO-Mag5, PalD1-Mag1), was tested in human CECs and in explanted human corneas. Effects on cell viability and function were investigated. Immunocompatibility was assessed in human peripheral blood mononuclear cells. **Results:** Silica iron-oxide MNPs (SO-Mag5) combined with X-tremeGENE-HP achieved high transfection efficiency in human CECs and explanted human corneas, without altering cell viability or function. Magnetofection caused no immunomodulatory effects in human peripheral blood mononuclear cells. Magnetofection with anti-apoptotic *P35* gene effectively blocked apoptosis in CECs. **Conclusion:** Magnetofection is a promising tool for gene therapy of corneal endothelial cells with potential for targeted on-site delivery.

First draft submitted: 5 April 2016; Accepted for publication: 1 June 2016; Published online: 7 July 2016

Keywords: apoptosis • corneal endothelium • gene therapy • magnetic nanoparticles • magnetofection

Marta Czugala[1,3], Olga Mykhaylyk[2], Philip Böhler[4], Jasmine Onderka[1], Björn Stork[4], Sebastian Wesselborg[4], Friedrich E Kruse[1], Christian Plank[2], Bernhard B Singer[3] & Thomas A Fuchsluger*[,1]

[1]Department of Ophthalmology, Friedrich-Alexander-Universität Erlangen-Nürnberg, Erlangen, Germany
[2]Institute of Immunology & Experimental Oncology, Klinikum rechts der Isar, Technische Universität München, Munich, Germany
[3]Institute of Anatomy, University Duisburg-Essen, Essen, Germany
[4]Institute of Molecular Medicine I, Heinrich Heine University Düsseldorf, Düsseldorf, Germany
*Author for correspondence:
Tel.: +49 0 9131 85 44519
Fax: +49 0 9131 85 34631
thomas.fuchsluger@uk-erlangen.de

Background

The corneal endothelium plays a crucial role in maintaining corneal clarity and quality of vision due to the function of its pump/leak mechanism. Human corneal endothelial cells (CECs) possess low proliferative capacity [1,2], therefore any significant loss of cells results in permanent loss of endothelial function [3]. Several corneal endothelial dystrophies, for example, Fuchs endothelial corneal dystrophy (FECD; MIM136800), result from primary endothelial dysfunction. To date, the sole available treatment involves corneal transplantation. Accordingly, the main focus of recent research has been to prevent corneal graft failure after transplantation and to increase the availability and quality of donor corneas. However, as epidemiological studies show, corneal endothelial failure due to trauma during cataract surgery and endothelial pathologies are responsible for the major portion of corneal failures that lead to corneal transplantation, and this tendency is growing [4,5]. Thus an optimized method preventing endothelial cell loss, not only in storage but especially to protect patients' own cornea, is urgently needed.

One postulated treatment for FECD involves the Rho-associated kinase inhibitor Y-27632. A pilot clinical study on eye drops containing Y-27632 has shown to support corneal endothelial regeneration and to restore corneal clarity in FECD patients [6–8]. However, there is still no *in vivo* approach available to specifically target a patient's own corneal endothelium without uncontrolled administration of therapeutic agents into the entire anterior compartment of the eye.

Diverse, polymer-based nanoparticles have been reported for ocular gene therapy, for example, hyaluronic acid-chitosan nanoparticles [9], cationized gelatin nanoparticles [10], chitosan

Future Medicine part of fsg

Table 1. Characteristics of core-shell type iron oxide magnetic nanoparticles.

Characteristics	Core-shell type MNPs		
	PEI-Mag2	SO-Mag5	PalD1-Mag1
Average crystallite size of the core, <*d*> (nm)	9	6.8	8.5
Saturation magnetization of the core, M_s (A m^2/kg of Fe)	62	94	55
Effective magnetic moment of the particle, m_{eff} (A m^2)[†]	8.2×10^{-20}	5.4×10^{-20}	6.2×10^{-20}
Iron content of the particle (g of Fe/g dry weight)	0.56	0.50	0.526
Shell composition	Fluorosurfactant ZONYL FSA and PEI-25$_{Br}$	TEOS[‡], THPMP[§]	Palmitoyl dextran
Mean hydrodynamic diameter of the particles in ddH_2O, D_h (nm)	28 ± 2	40 ± 14	55 ± 10
Zeta potential of the particles in ddH_2O, ξ (mV)	+55.0 ± 0.7	-38.0 ± 2.0	-15.6 ± 1.6

[†]Calculations account for magnetite structure and crystallite size of the core of the particles, and magnetization in a magnetic field of 0.213T.
[‡]Tetraethyl orthosilicate.
[§]3-(trihydroxysilyl) propylmethylphosphonate.

oligomers [11] and polyethylenimine-conjugated gold nanoparticles [12]. None of these particles provide specific on-site delivery. Magnetic nanoparticles (MNPs) offer this feature when applied under gradient magnetic fields. Recent studies report the use of MNPs for targeted gene and drug delivery in cancer therapy [13,14], including delivery of therapeutic plasmid for treatment of melanoma [15] and adenocarcinoma [16]. In eye research, MNPs have been successfully tested for both drug delivery and cell therapy to the retina [17] and to corneal endothelium [18,19]. In numerous studies, including long-term studies [18,20–22], diverse MNPs have been reported to show little or no toxicity to ocular cells. As magnets can be shaped concavely to meet the requirements of corneal therapy [23], this type of carriers represents a promising tool to deliver therapeutic nucleic acids to corneal endothelium *in vivo*.

The purpose of this study was to develop an optimized magnetic delivery vector formulated of different MNPs combined with liposomal enhancers for gene delivery to human CECs. This method, further referred to as magnetofection, was tested for its efficiency, bio- and immunocompatibility and effects on corneal endothelial cell function. The long-term goal of the project is to develop a safe and efficient delivery system for targeted gene therapy of corneal endothelium *in vivo* to reduce the need for transplantation, for example, by protecting the endothelium of the patients' own cornea against apoptosis.

Materials & methods

Synthesis & characterization of iron oxide nanoparticles

Three types of MNPs were tested in this study: PEI-Mag2 [24], SO-Mag5 [25] and PalD1-Mag1 [26]. All aqueous MNP suspensions were sterilized using ^{60}Co gamma-irradiation at a dose of 25 kGy. The MNP concentration was determined in terms of the iron content in aqueous suspension as described previously [27].

The different MNPs have an average magnetite core size from of 6.5 to 9 nm and high saturation magnetization of the core material. Positive (PEI-Mag2) or negative (PalD1-Mag1 and SO-Mag5) surface charge (Table 1) enables assembling with pDNA and liposomal transfection reagents into magnetic lipoplexes. These were assembled at Fe-to-pDNA w/w ratios ranging from 1:4 (0.25) to 1:1 and possessed intensity weighted hydrodynamic diameters from about 800 to 1000 nm (Table 3).

Preparation of magnetic lipoplexes

To prepare the magnetic lipoplexes for single transfection in 48-well cell culture plates, 16.4 µl of MNP suspension (19.7 µg Fe/ml in water) were mixed with 5.2 µl of transfection reagent (DreamFectGold, OZBiosciences, Marseille, France or X-tremeGENE HP™, Roche, Basel, Switzerland) and 108 µl of pDNA solution (12 µg/ml in serum- and supplement-free DMEM) resulting in 129.6 µl of complex with a final pDNA concentration of 10 µg/ml for complex assembly. The transfection reagent-to-pDNA v/w ratio was 4:1, and the MNP-to-pDNA w/w ratio in terms of iron-to-pDNA w/w ratio was 0.25. The mixture was incubated for 20 min at RT to allow the complexes to assemble, as described before [27]. After that, 158.4 µl of DMEM was added for a total volume of 288 µl, and 1:1 dilutions were performed, resulting in doses of 6, 3, 1.5 and 0.75 pg/cell given in 120 µl of complexes. Lipoplexes were used as reference and prepared following the same protocol with water instead of MNPs. For the complexes with MNP-to-pDNA w/w ratios of 0.5 and 1, the nanoparticle concentration was adjusted accordingly. The pDNAs used in this study were pcDNA3.1-EGFP for HCEC-12 in all experiments, pcDNA3.1

Table 2. qPCR primers (human).

Gene	Accession	Forward primer	Reverse primer	Product size
ATP1A1	NM_000701.7	TCTCTGATTCTCCAGCGACA	GGCTCATACTTATCACGTCCAA	87 bp
SLC4A4	NM_001098484.2	CCTCAAGCATGTGTGTGATGA	ACTCTTCGGCACATGGACTC	76 bp
COL4A2	NM_001846.2	TCCCTATAGACCACTGGGTTTG	GCAAGGCTGACAATGATGTCTA	74 bp
COL8A2	NM_005202.2	GGGCAAAGGCCAGTACCT	GGGCTCTCCCTTCAGGTC	64 bp
CDH2	NM_001792.3	GGTGGAGGAGAAGAAGACCAG	GGCATCAGGCTCCACAGT	72 bp
GAPDH	NM_002046.3	AGCCACATCGCTCAGACAC	GCCCAATACGACCAAATCC	66 bp

for peripheral blood mononuclear cells (PBMCs) and either pCB-MCS-IZsGreen or pCB-P35-IZsGreen for corneas. For 96- or 6-well plate transfections, amounts of components were adjusted proportionally.

Characterization of magnetic lipoplexes

To confirm proper complexing and stability of magnetic lipoplexes, a gel retardation assay and heparin displacement assay were performed (Supplementary Figure 1).

The mean hydrodynamic diameter (D_h) and electrokinetic or ζ-potential of the MNPs and magnetic lipoplexes were determined by photon correlation spectroscopy (PCS) using a Zetasizer Nano Series 3000 HS (Malvern Instruments, Malvern, UK).

To evaluate the rate of the magnetic vector migration in inhomogenous magnetic fields (magnetophoretic velocity), the clarification kinetics were registered for the suspensions of the vectors by measuring space- and time-resolved extinction profiles using a customized LUMiReader® device (LUM GmbH, Berlin, Germany) equipped with a set of Neodymium-Iron-Boron magnets positioned underneath the cuvette (Figure 1A) as recently described [28]. The integral extinction (E) was calculated by averaging over a selected region of extinction profiles between meniscus and bottom of the cuvette, and the relative extinction E/E_0 was determined and plotted versus time. Here, E_0 is the initial extinction of the sample. In the linear range of the Lambert-Beer law, the relative extinction E_{rel} can be considered as a relative concentration and represents the rate of the complexes remaining in suspension. The relative concentration E/E_0 plotted against the magnetophoretic velocity Y represents a cumulative distribution function Φ(Y), which describes the particle ratio having a magnetophoretic velocity Y_i less or equal to the Y_i value. The efficient magnetophoretic velocity of particles was calculated as Y=<L>/t. Here, <L> is a mean path of the particles upon magnetophoresis. With a sample height of 5 mm (250 µl probe), <L>=2.5 mm. The median values of magnetic moment M of the complex and number of magnetic nanoparticles $N=M/m_{eff}$ per complex/complex assembly were calculated as previously described [29]. Here, m_{eff} is an effective magnetic moment of the core of the nanoparticles accounting for the average diameter and saturation magnetization of the magnetite core.

Cell & organ culture

Human corneal endothelial cells (HCEC-12) were obtained from DSMZ (Braunschweig, Germany)

Table 3. Characteristics of the magnetic lipoplexes assembled at a pDNA concentration of 10 µg/ml and different Fe-to-pDNA w/w ratios: electrokinetic (ζ) potential, intensity weighted hydrodynamic diameter D_h; time for magnetic separation of 50% of the complexes $t_{0.5}$, median values of the magnetophoretic mobility $\upsilon_{0.5}$, effective magnetic moment M of the complex, and number of magnetic nanoparticles N per complex/complex assembly measured at an applied magnetic flux density and field gradient of 0.16 T and 33.5 T/m, respectively; m_{eff} is the effective magnetic moment of the core of the nanoparticles as given in Table 1.

Complex	Fe:pDNA w/w ratio	ζ (mV)	D_h (nm)	$t_{0.5}$ (s)	$\upsilon_{0.5}$ (µm/s)	M (10^{-15} Am²)	n = M/m_{eff}
SO-Mag5/X-tremeGENE HP/pDNA-EGFP	0.25	-0.1 ± 0.8	834	428	5.8	1.2	$2.3 \times 10^{+04}$
	0.5	1.2 ± 1.0	862	180	13.9	3.0	$5.5 \times 10^{+04}$
	1	2.8 ± 1.3	1098	98	25.6	7.0	$1.3 \times 10^{+05}$
PalD1-Mag1/X-tremeGENE HP/pDNA-EGFP	0.25	4.9 ± 0.7	1052	222	11.3	3.0	$4.8 \times 10^{+04}$
PEI-Mag2/X-tremeGENE HP/pDNA-EGFP	0.25	-1.3 ± 0.6	930	1379	1.8	0.4	$5.1 \times 10^{+03}$

and were cultured in MEM supplemented with 5% fetal calf serum (FCS) and 50 µg/ml gentamycin at 37°C/5% CO_2.

Explanted human donor corneas were kindly provided by the Cornea Bank of the Düsseldorf University Hospital. Informed consent for research use was given for all corneas beforehand, and this study was approved by the university ethics committee. Corneas were stored in Culture Medium I (Biochrome AG, Berlin, Germany) at 37°C and 5% CO_2.

Magnetofection studies on HCEC-12 and explanted human corneas

HCEC-12 were seeded at 9×10^4 cells/cm^2 in 48-well cell culture plates. After addition of regular or magnetic lipoplexes 24 h later, the cells were incubated for 20 min on a magnetic plate creating a magnetic field of 70-250 mT and a field gradient of 50-130 T/m, respectively, at the cell layer location (Super Magnetic Plate, OZBiosciences, Marseille, France). Magnetofection time was set based on magnetophoretic mobility experiments (Figure 1). At 24 h after transfection, HCEC-12 were harvested by trypsinization and resuspended in DMEM supplemented with 5 µg/ml propidium iodide (PI). EGFP expression and PI uptake were measured by flow cytometry (LSRFortessa, FACSDiva Software, BD Biosciences, NJ, USA).

Human corneas with intact endothelium were used. Each cornea was cut into four pieces. Transfection complexes were prepared estimating 7×10^4 endothelial cells per piece. Estimation was based on endothelial cell density of 2000 cells/mm^2 as determined by eye bank and posterior corneal surface area of 137 mm^2 as calculated by Kwok LS [30]. Estimated dose of 1.6 and 3.2 pg pDNA/cell were tested, both for regular lipoplexes and magnetic lipoplexes formulated at an MNP-to-pDNA ratio of 0.25. At 72 h after magnetofection, corneal pieces were fixed in 4% formaldehyde, stained with DAPI (1 µg/ml in PBS, 10 min, RT), and mounted with VectaShield mounting medium (Vector Laboratories, CA, USA). EGFP expression was examined by confocal microscopy (Zeiss LSM 780, Carl Zeiss GmbH, Jena, Germany).

Immunocytochemistry

HCEC-12 were seeded in 4-well chamber slides (BD Biosciences) and transfected as described above. At 24 h after magnetofection, cells were fixed using 4% formaldehyde, washed with PBS and incubated in PBS-based buffer containing 1% BSA and 0.1% Triton X-100 for 30 min. Cells were incubated overnight at 4°C with rabbit anti-ZO-1 antibody (1 µg/ml; Life Technologies, CA, USA) or Phalloidin CF™647-conjugate (according to manufacturer's protocol; Biotium, Inc., CA, USA). After washing with PBS, cells were incubated for 1 h at RT with Alexa® Fluor 647-labelled anti-rabbit-IgG (3 µg/ml; Jackson ImmunoResearch Laboratories Inc., PA, USA). Nuclei were counterstained with DAPI (1 µg/ml). Specimens were mounted using Dako Fluorescence Mounting Medium (Dako, Glostrup, Denmark) and observed with an inverted microscope (Axio Observer; Carl Zeiss GmbH, Jena, Germany).

qPCR

Total RNA from cells was extracted using the RNeasy Mini Kit (Qiagen, Venlo, The Netherlands). Synthesis of cDNA was performed using SuperScript® II Reverse Transcriptase (Life Technologies, CA, USA). Quantitative real-time PCR (qPCR) was conducted on a CFX Connect™ Real-Time PCR Detection System using the Roche LC480 Probes Master (Roche, Basel, Switzerland). Each reaction was carried out in technical duplicates, using cDNA obtained from 25 ng of total RNA as template. Primer pairs for each gene were used at 300 nM. Results were analyzed using GAPDH as reference gene. The qPCR primers for all targets were designed using the Roche Universal ProbeLibrary Assay Design Center and employed with corresponding UPL probes (Table 2). The data were analyzed using the $2^{-\Delta\Delta Ct}$ method utilizing Biorad CFX Manager Software (Bio-Rad Laboratories Inc.).

Western Blot

At 24 h after magnetofection, HCEC-12 cells were lysed in Laemmli Buffer (63 mM Tris pH 6.8, 8.6% v/v glycerol, 2% w/v SDS, 0.1% v/v β-mercaptoethanol). The lysates were centrifuged at 11,000 × *g* for 15 min, and the total protein concentration was measured using Pierce 660nm Protein Assay Reagent (Thermo Fisher Scientific Inc., MA, USA). For each sample, bromophenol blue was added and 25 µg of total protein was loaded. The proteins were then separated by SDS-PAGE and transferred to a PVDF membrane by western blotting. Antibodies used for detection were mouse anti-Na^+/K^+-ATPase (Santa Cruz, TX, USA) and mouse anti-β-Actin (Sigma Aldrich, MO, USA). A LI-COR Odyssey fluorescence scanner system using Image Studio v4.0 software (LI-COR Biosciences, NE, USA) was used for visualization and quantification of the western blots.

Isolation of human PBMCs

Heparinized venous blood was obtained from healthy volunteers. PBMCs of the leukocyte-rich plasma were separated by gradient centrifugation via Ficoll-Paque (Amersham, UK). The PBMC fraction was collected and washed twice with PBS. The residual erythrocytes were lysed with ice-cold dH_2O for 10 s. The purity of

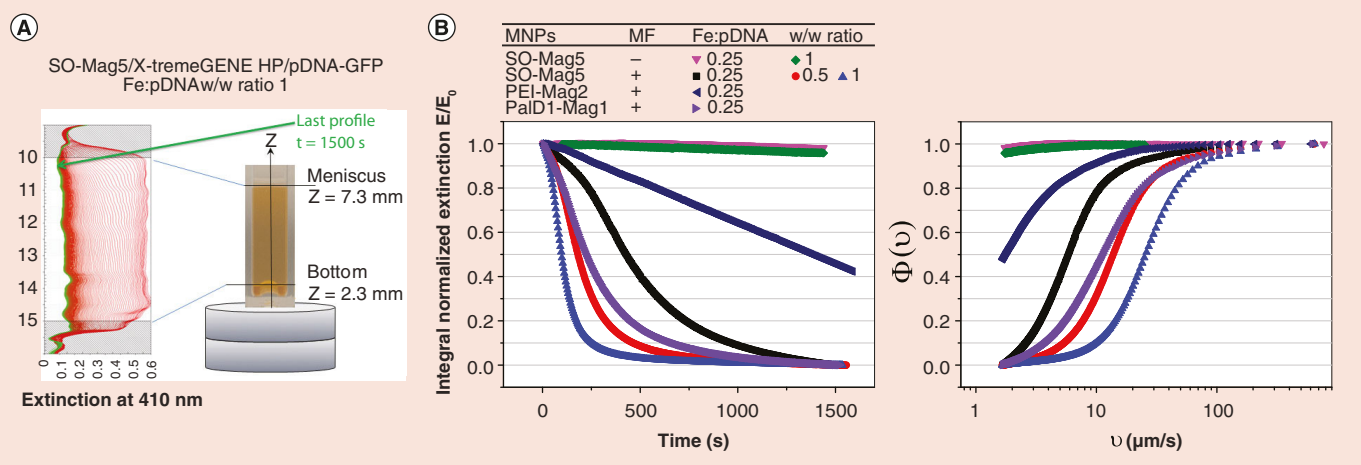

Figure 1. Magnetophoretic velocity of the magnetic vectors characterized by kinetics of clearance of the suspensions in applied gradient magnetic fields. **(A)** Extinction profiles at 410 nm for the suspension of the magnetic SO-Mag5 magnetic lipoplexes, registered along the vertical axis of the cuvette with a customized LUMiReader® device with two disk Neodymium-iron-boron-magnets positioned underneath optical cuvette; resulting magnetic flux density and gradient averaged over vertical sample height were of 0.16 T and 33.5T/m, respectively. **(B)** Integral normalized extinction at 410 nm, E/E_0, averaged through the selected probe height, versus time upon exposure to magnetic field or with no field applied and derived data on cumulative distribution functions of the effective magnetophoretic mobility $\Phi(v)$. E_0 is an initial extinction of the cell suspension.

the isolated PBMCs was 92–96% as determined by flow cytometry (FACS Calibur with CellQuest software; BD Biosciences). PBMCs were then cultured in RPMI supplemented with 10% (v/v) heat inactivated FCS, 2 mM L-glutamine, 100 IU/ml penicillin and 100 mg/ml streptomycin.

Magnetofection in human PBMCs

Freshly isolated PBMCs from healthy individuals were sedimented in culture plates by centrifugation (10^5 cells/well in 96-well plate). For each tested component, naive PMBCs as well as PBMCs stimulated with anti-CD3 antibody (125 ng/ml, clone OKT3; Biolegend, CA, USA) were analyzed. Either magnetic lipoplexes formulated at an MNP-to-pDNA w/w ratio of 0.25 at an applied dose of 90 ng pDNA/well (resulting in 0.9 pg pDNA/cell and 0.225 pg Fe/cell) or an equivalent dose of single components were added to the cells. Cells were incubated for 20 min on a magnetic plate.

Analysis of the cell survival, CD69 and CD25 expression and proliferation of PBMC

Cell viability was tested at 24 and 72 h after magnetofection by Annexin-FITC/ PI staining according to the manufacturer's protocol (Immunotools, Friesoythe, Germany). Activation of T cells was measured at 30 h after magnetofection. PBMCs were collected and labeled with FITC-coupled anti-CD69 and anti-CD25 antibody (5 µg/ml; Immunotools). For proliferation studies, PBMCs were labeled with CFSE using the CellTrace™ CFSE Cell Proliferation Kit according to manufacturer's protocol (Life Technologies, CA, USA) and magnetofected. CFSE fluorescence was measured at day 4. All measurements and analysis were performed using FACSCalibur flow cytometer with the CellQuest software (BD Biosciences).

Anti-apoptotic gene transfer

Cells were seeded and magnetofected with either the plasmid pCB-P35-IZsGreen (tandem construct for expression of both the anti-apoptotic Early 35 kDa protein (P35) and ZsGreen) or pCB-MCS-IZsGreen (empty vector control). At 24 h after magnetofection, cells were treated either with 2.5 µM staurosporine (Adipogen Int., CA, USA) for 5 h, or with 85 µM etoposide (Sigma Aldrich) for 7 h to induce apoptosis.

Caspase-3 activity assay

Cells were harvested and lysed with 50 µl of ice-cold Lysis Buffer (20 mM HEPES, 84 mM KCl, 10 mM $MgCl_2$, 200 µM EDTA, 200 µM EGTA, 0.5% NP-40, 1 µg/ml leupeptin, 1 µg/ml pepstatin, 5 µg/ml aprotinin) on ice for 10 min. Cell lysates were transferred to a black flat-bottom multiwell plate and mixed with 150 µl of ice-cold Reaction Buffer (50 mM HEPES, 100 mM NaCl, 10% sucrose, 0.1% CHAPS, 2 mM $CaCl_2$, 13.35 mM DTT, 70 µM Ac-DEVD-AMC). The kinetics of the AMC release were monitored by measuring fluorescence intensity (Ex 360 nm, Em 450 nm) at 37°C in intervals of 2 min over a time course of 150 min using a Synergy Mx multiwell plate reader (BioTek, VT, USA). The slope of the linear range of the fluorescence curves (Δrfu min^{-1}) was considered as corresponding to caspase-3 activity.

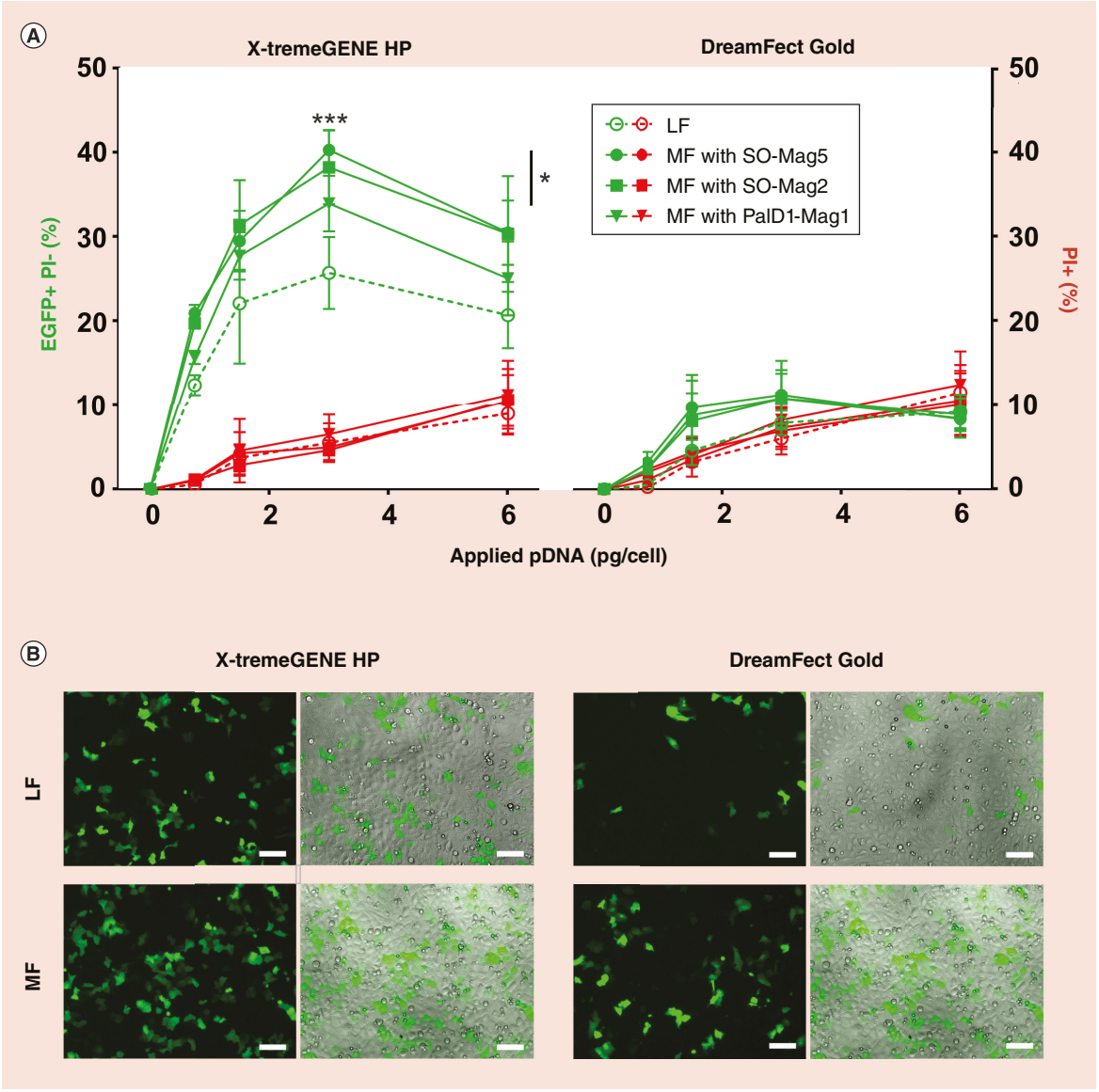

Figure 2. Magnetofection versus lipofection efficacy in HCEC-12 cells. (A) Percentage of EGFP and propidium iodide (PI) positive cells at 24 h after pDNA-GFP transfection using lipoplexes or magnetic lipoplexes formed with PEI-Mag2, SO-Mag5 and PalD1-Mag1 magnetic nanoparticles at an MNP-to-pDNA w/w ratio of 0.25 and DreamFect-Gold or X-tremeGENE HP. For X-tremeGENE, MF efficiency was significantly higher comparing to LF (One-way ANOVA/Uncorrected Fisher's LSD ***$p < 0.0005$). SO-Mag5 magnetic lipoplexes provided significantly higher transfection efficiency than PalD1 Mag1magnetic lipolexes (*$p = 0.0305$). **(B)** Microscopy images (FL and FL/BF overlay) for LF and magnetofection MF using X-tremeGENE HP and DreamFect Gold, with SO-Mag5 nanoparticles at optimal pDNA dose of 3 pg/cell and iron to pDNA ratio of 0.25. Scale bars indicate 50 μm. Representative data for three independent experiments are shown.
LF: Lipofection; MF: Magnetofection.

Statistical analysis

All data are reported as mean with standard deviation (SD). qPCR data are reported as mean with SEM. Statistical significance was determined by comparison to untreated controls or to day 1 values (for normalized data), using GraphPad Prism v6.0 for Windows (GraphPad Software, CA, USA).

Results

Characterization of magnetic nanoparticles & magnetic lipoplexes

The characteristics of the MNPs used to formulate magnetic lipoplexes are listed in Table 1. A gel retardation assay confirmed that all magnetic lipoplexes assembled properly and that pDNA was fully bound within the

complex. Additionally, a heparin displacement assay showed the release of intact pDNA from complexes after their disassembling (Supplementary Figure 1). STEP-Mag measurements were performed as described in Figure 1A to evaluate the magnetic responsiveness of the complexes, which is important for the efficient local transfection of the cornea. Without magnetic field application, no complex sedimentation was observed in the time window sufficient for magnetic separation of the complexes upon magnetic field application (Figure 1B, left). The data on clarification of the complex suspension, when subjected to a defined gradient field, were plotted against the magnetophoretic velocity Y to give a cumulative velocity distribution function $\Phi(Y)$, which describes the particle ratio having a magnetophoretic velocity Y_i less or equal to the Y_i value (Figure 1B, right). The derived median magnetophoretic values $Y_{0.5}$ for the three complexes and the correspondent median values

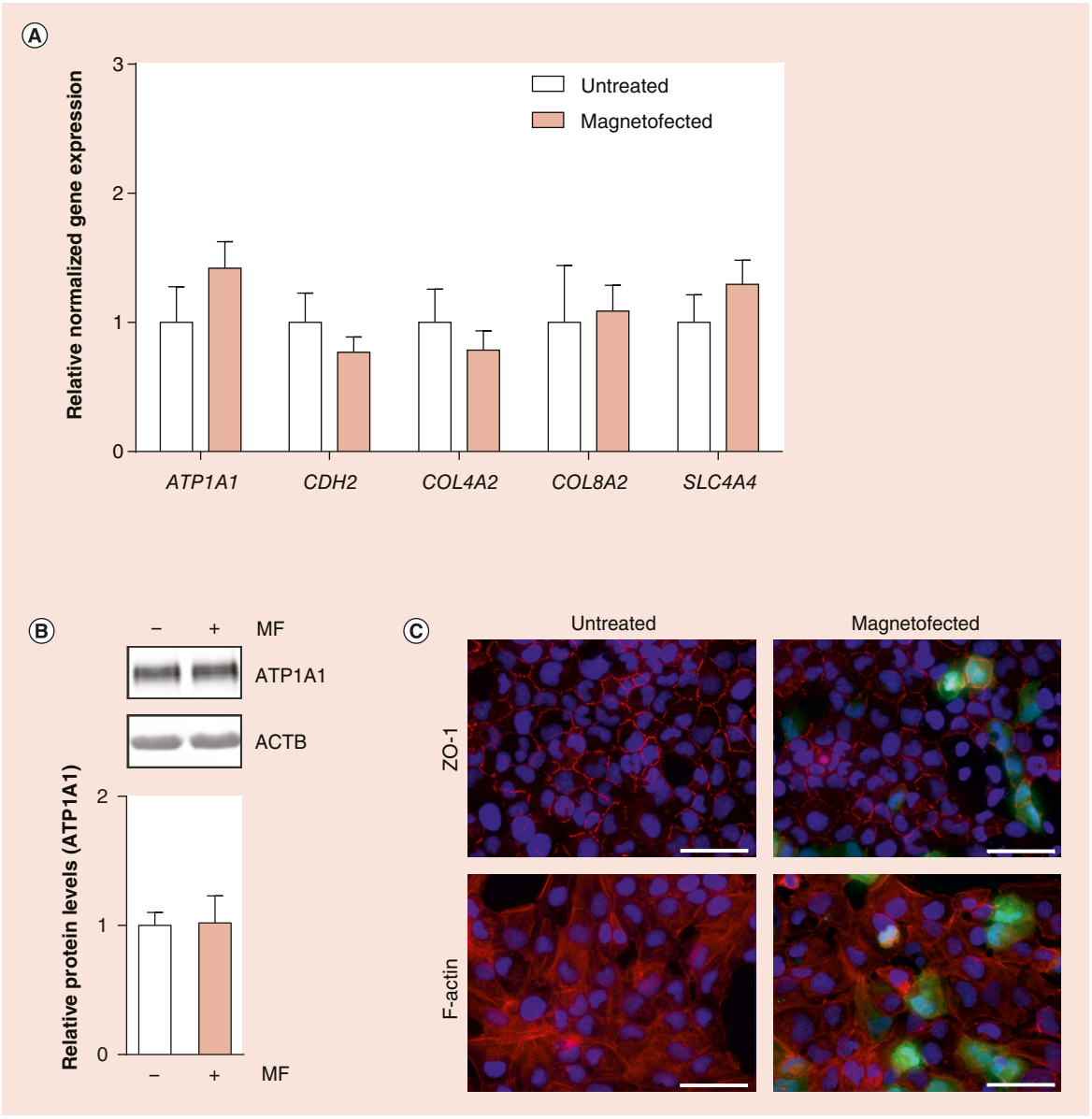

Figure 3. Functional markers of corneal endothelium before and after magnetofection with SO-Mag5/X-tremeGENE/pcDNA3-EGFP at optimal pDNA dose of 3 pg/cell. (A) Gene expression levels for *ATP1A1*, *CDH2*, *COL4A2*, *COL8A2* and *SLC4A4*. **(B)** ATP1A1 protein levels as investigated by western blot. **(C)** Distribution of endothelial markers ZO-1 and F-actin filaments (red) examined by immunofluorescence. GFP-expressing cells are shown in green, cell nuclei are shown in blue. Scale bars indicate 50 μm. No significant differences were measured in both untreated cells and after magnetofection. Representative data for three independent experiments are shown.

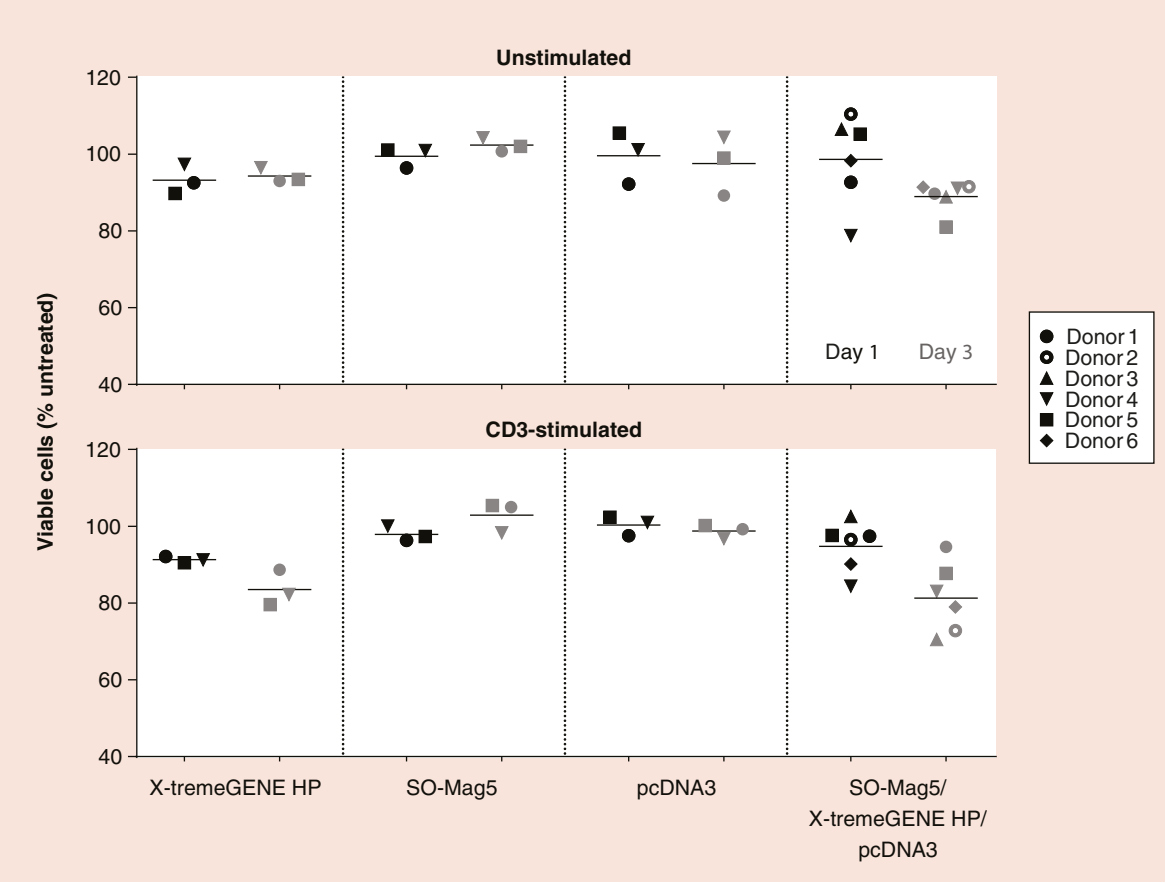

Figure 4. Viability of peripheral blood mononuclear cells after magnetofection. Naive (upper panel) and CD3-stimulated (lower panel) PBMCs from six healthy donors were exposed to SOMag5/X-tremeGENE HP/pcDNA magnetic lipoplexes (Fe:pDNA w/w ratio of 0.25, 0.9 pg pDNA/cell) or equivalent dose of single components. At day 1 (black symbols) and day 3 (gray symbols), cell viability/cell death were assessed. AnnexinV-/PI- cells were considered viable. Individual values for each donor normalized to untreated cells are shown, black line indicates mean. Tested treatments did not cause statistically significant differences in cell viability.

of magnetic moment M of the complex and number of magnetic nanoparticles *N* per complex/complex assembly are given in Table 3. The results suggest that each individual complex contains multiple nanoparticles. Increasing the MNP-to-pDNA ratio in SO-Mag5/X-tremeGene HP/pDNA complexes resulted in a considerable increase in the number of the particles associated with the complex and in an increase in magnetophoretic velocity of the complexes in applied magnetic fields up to about 25 µm/s at an MNP-to-pDNA w/w ratio of 1.

Optimization of gene transfer into HCEC-12 by magnetofection

To test the ability of MNPs to enhance the transfection efficiency in HCEC-12 cells, the two liposomal enhancers X-tremeGENE HP and DreamFectGold were applied either alone or in combination with different types of MNPs. Association with MNPs generally increased transfection efficiency compared with the lipoplexes (Figure 2A). The lipoplexes formulated with X-tremeGENE HP achieved considerably higher transfection efficiency than DreamFect Gold lipoplexes (25.8 vs 8.0% maximum). This difference is also visible microscopically (Figure 2B). While MNPs increased the transfection efficiency of both reagents, the increase was much more pronounced with the already more efficient X-tremeGENE HP, reaching 40.4% comparing to 11.2% for DreamFect Gold in case of SO-Mag5 nanoparticles at an applied pDNA dose of 3 pg/cell (Figure 2A & B).

Out of the three types of magnetic particles tested here, both SO-Mag5 as well as PEI-Mag2 particles enhanced transfection efficiency best when combined with X-tremeGENE HP, with up to 40.4% for SO-Mag5 and 38.3% for PEI-Mag2, comparing to about 34% for PalD1-Mag1 particles. When combined with the DreamFectGold transfection reagent, the overall transfection efficiency was minimal, so that no significant difference between three magnetic nanoparticle types could be noticed (Figure 2A, green panel).

Next, we assessed cell viability after transfection. All three MNPs examined (PEI-Mag2, SO-Mag5 and PalD1-Mag1), both in combination with X-tremeGENE HP as well as with DreamFectGold, resulted in cell viability values comparable to the lipofection reagents alone, indicating that MNPs do not negatively affect cell viability of HCEC-12 (Figure 2A, red panel). However, a correlation between an increase in pDNA and MNP dose per cell with an increase in the percentage of nonviable cells was seen, from about 1.1% at 0.75 pg/cell to 11.3% nonviable cells at 6 pg/cell. MNPs and magnetic field treatment alone or combined showed no significant effect (data not shown).

Summarizing, the combination of X-tremeGENE HP with SO-Mag5 MNPs at an applied pDNA dose of 3 pg/cell appeared to be most efficient and was used for following experiments. The data refer to complexes formulated at MNP-to-pDNA ratio of 0.25. Other ratios were also tested in optimization phase but proved inferior in regard to transfection efficiency and cell viability and therefore were omitted.

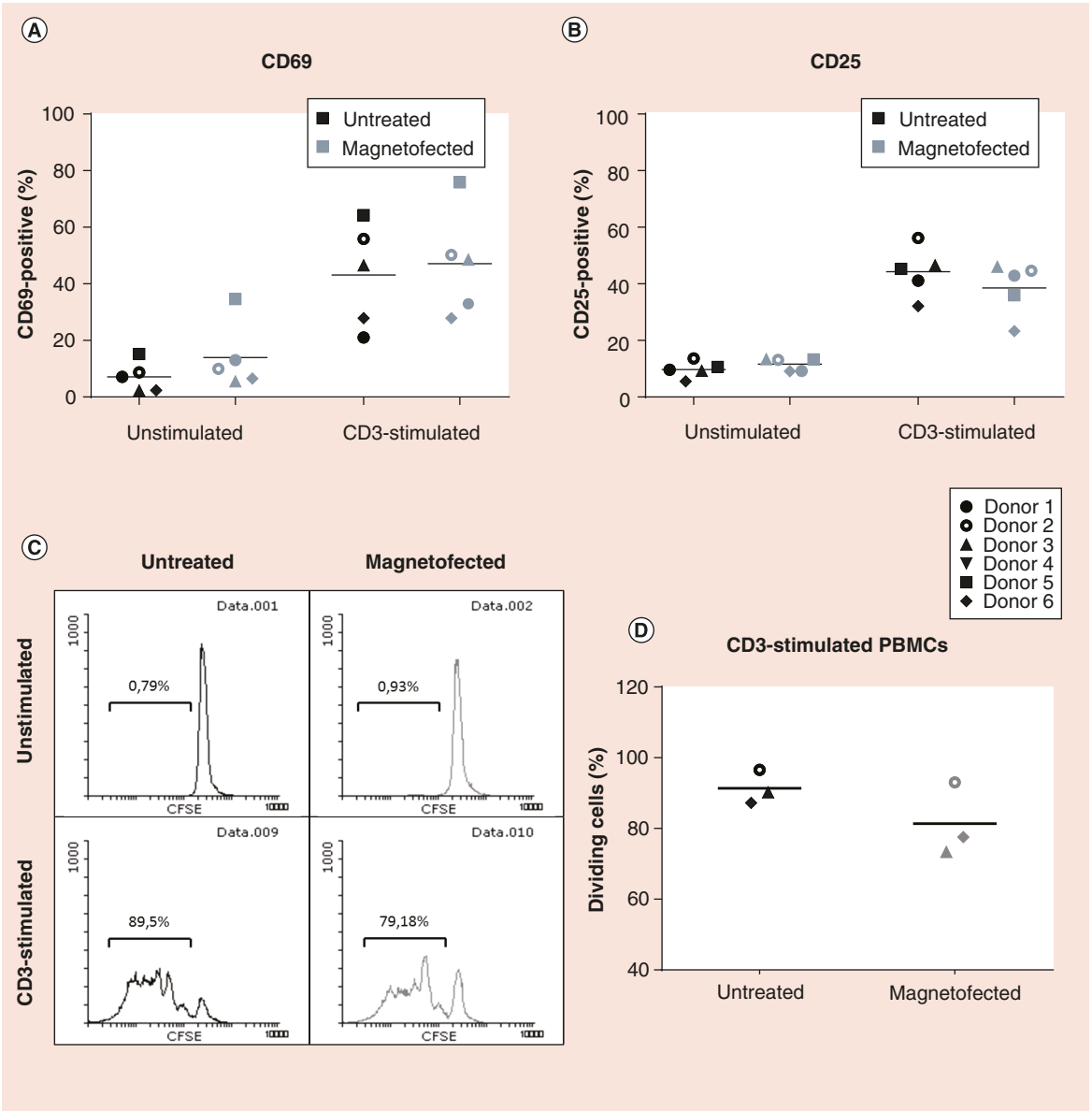

Figure 5. Expression of T-cell activation markers CD69 (A) and CD25 (B) in naive and in CD3 stimulated PBMCs at 30 h after magnetofection. Treatment with magnetic lipoplexes (SOMag5/X-tremeGENE HP/pcDNA, Fe:pDNA w/w ratio of 0.25, 0.9 pg pDNA/cell) did not cause statistically significant differences in the expression levels. **(C)** Influence of magnetofection on proliferation of naive and CD3-stimulated PBMCs as assessed by CFSE fluorescence at 4 days post-transfection. Exemplary flow cytometry dataset of one individual is presented. No significant difference was observed in the proliferation profile after magnetofection **(C & D)**.

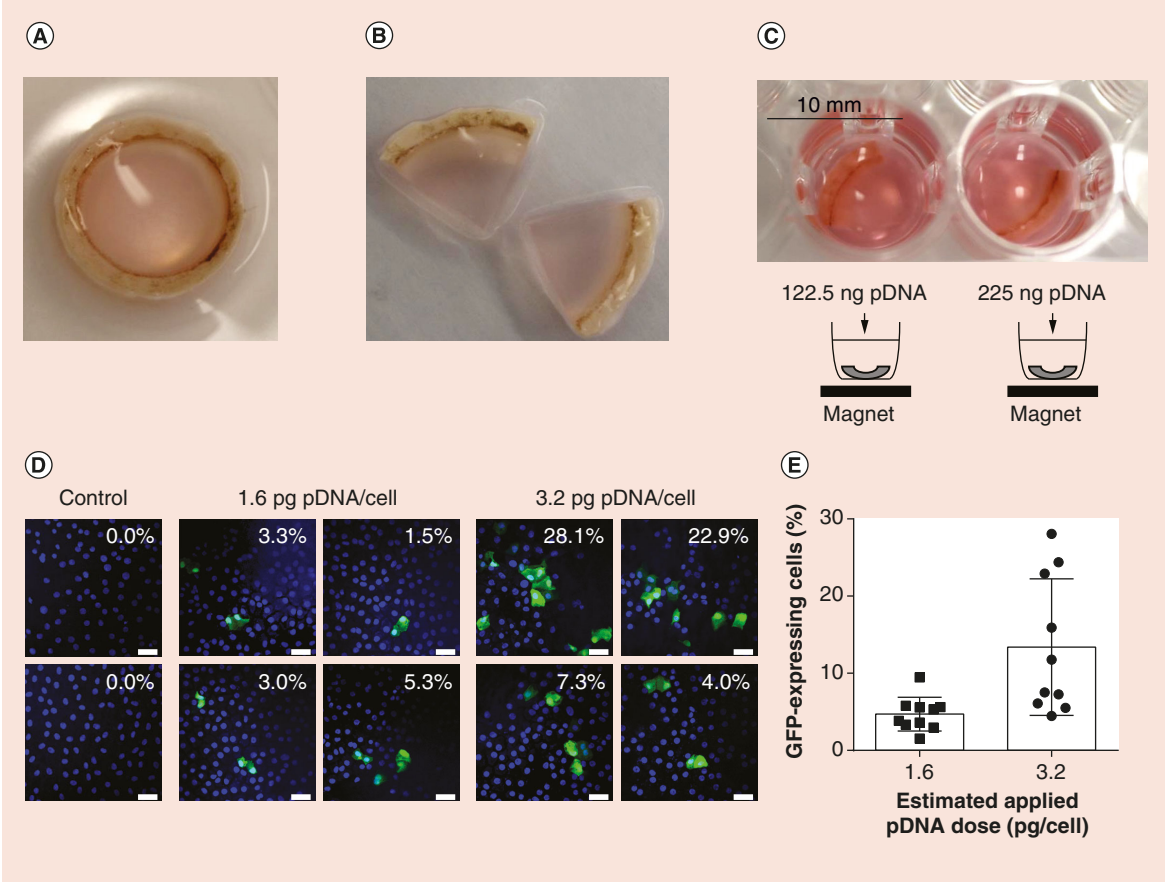

Figure 6. Cornea magnetofection *ex vivo*. Explanted cornea **(A)** was quartered **(B)**, and the pieces were positioned at the bottom of the well of 48-well plate placed on a magnetic plate. The SO-Mag5/X-tremeGENE HP/pcDNA-EGFP magnetic lipoplexes formulated at MNP:pDNA w/w ratio of 0.25 were added to the wells at a dose of 122.5 and 225 ng pDNA, resulting in 1.6 and 3.2 pg/cell **(C)**. Efficacy of transfection was evaluated at 72 h after magnetofection by confocal microscopy. **(D)** shows exemplary visual fields of corneal endothelium with overlaid GFP fluorescence (green) and cell nuclei staining (DAPI, blue) for negative controls and magnetofected samples; scale bars indicate 50 μm. **(E)** Percentage of the EGFP-positive cells from a total of ten visual fields per corneal piece (1.6 pg/cell: n_{total}=995, n_{GFP+}=43; 3.2 pg/cell: n_{total}=648, n_{GFP+}=72; negative control n_{total}=855, n_{GFP+}=0).

Magnetofection does not negatively affect endothelial function

Next we analyzed whether the process of magnetofection affects the endothelial function. We used qPCR to analyze the expression of endothelial functional markers Na^+/K^+-ATPase (*ATP1A1*), sodium bicarbonate cotransporter 1 (*SLC4A4*), N-cadherin (*CDH2*), collagen type IV alpha-2 chain (*COL4A2*) and collagen type VIII alpha-2 chain (*COL8A2*). No significant effect of magnetofection on any of the markers was found (Figure 2A). In addition, we analyzed the expression of the crucial functional marker Na^+/K^+-ATPase (*ATP1A1*) by western blot. Again, there was no significant effect caused by magnetofection (Figure 3B).

Furthermore, morphology and organization of the cytoskeleton in transfected cells were investigated by immunofluorescence staining of the tight junction protein 1 (ZO-1) and F-actin filaments, respectively (Figure 3C). No differences caused by magnetofection appeared, also in GFP expressing cells.

Effect of magnetofection on immune cell survival, differentiation and proliferation

To evaluate the immunocompatibility of our optimized magnetofection protocol, we investigated immunomodulatory effects of applied reagents in combination with magnetic field on naive and activated human immune cells of the peripheral blood (PBMCs). Stimulation with anti-CD3 antibody was used in order to mimic conditions of inflammation.

To exclude immunosuppressive effects, the influence of the magnetofection reagents on PBMC survival was monitored over the course of 3 days (Figure 4). Both the individual reagents and the magnetic lipoplexes did not significantly decrease cell viability or cell survival in naive as well as in stimulated PBMCs (Figure 4).

To explore immunostimulatory effects of magnetofection, the expression of the early and late T-cell activation markers CD69 and CD25, respectively, was measured by flow cytometry (Figure 5A & B). While stimulation with anti-CD3 expectedly caused an increased expression of both activation markers within 30 h, magnetofection alone had no effect. Additionally, magnetofection did not alter the percentage of CD69- or CD25-positive cells, neither with nor without anti-CD3 stimulation.

Finally, the mitogenic effect of magnetofection on PBMC was examined by CFSE assay. Under unstimulated conditions, no proliferation of PBMCs was induced both with and without magnetofection. In CD3-stimulated PBMCs, a slight but nonsignificant proliferation-inhibiting effect was seen (Figure 5C & D). This indicates that under tested conditions the magnetofection procedure triggered no significant immunomodulatory effects.

Magnetofection is suitable for gene delivery to explanted human corneas

Having optimized magnetofection in HCEC-12, we applied this approach to the primary endothelium of explanted human donor corneas. The overall workflow of this procedure as well as the outcome are presented in Figure 6. The corneas were cultivated, quartered and prepared for magnetofection (Figure 6A–C). We used a pDNA dose of 122.5 ng/well (1.6 pg/cell) and 225 ng/well (3.2 pg/cell) (Figure 6C). Transfection efficiency proved to be dose-dependent and varied between different sections of the same specimen with an average of 4.7 ± 2.2% and 13.4 ± 8.9% of transfected endothelial cells for applied DNA doses of 125 ng and 225 ng pDNA per cornea piece, respectively (Figure 6D & E). Lipofection alone did not achieve observable levels of GFP expression in explanted corneas (data not shown).

Magnetofection with the *P35* gene reduces apoptosis in human corneal endothelial cells

To prove suitability of our optimized magnetofection method for anti-apoptotic gene therapy into corneal endothelium, we transfected HCEC-12 cells with a plasmid coding for the pan-caspase inhibitor P35 (baculoviral Early 35 kDa protein). Subsequently, we analyzed whether this treatment leads to the protection of CECs from apoptosis induced by two well-known stimuli, staurosporine and etoposide. Caspase-3 activity was measured as a metric for apoptosis. As shown in Figure 7A & B, magnetofection with *P35* could strongly attenuate apoptosis caused by both, staurosporine and etoposide, resulting in a fourfold and in a sixfold decrease in apoptosis, respectively, as compared with an empty control vector.

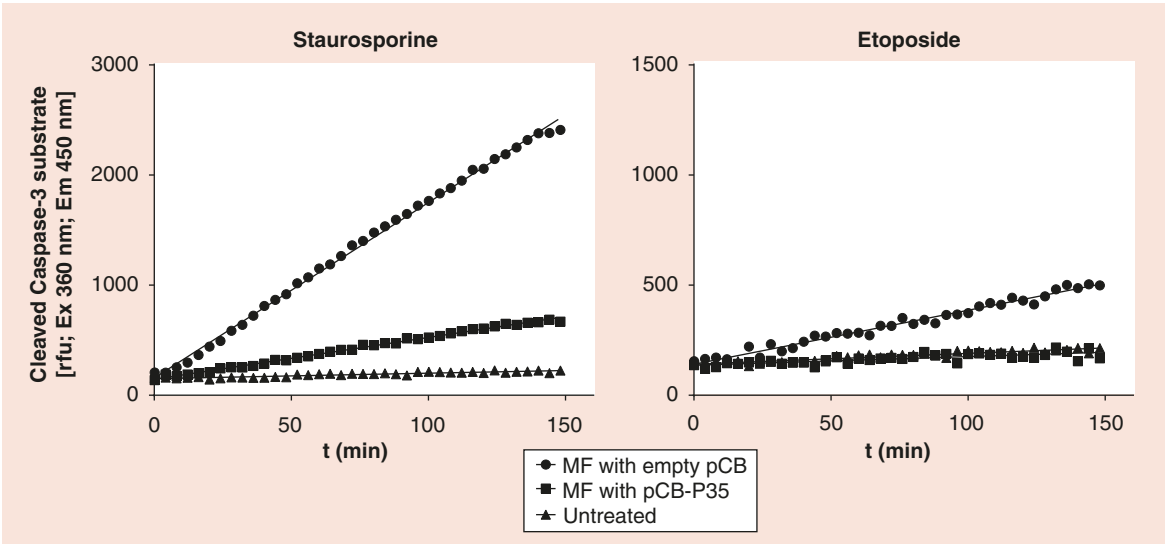

Figure 7. Anti-apoptotic effect of magnetofection with P35-coding pDNA in HCEC-12. Cells were magnetofected either with empty pCB-MCS-IZsGreen (empty pCB) or pCB-P35-IZsGreen carrying the baculoviral antiapoptotic *p35* gene (pCB-P35) using SOMag5/X-tremeGeneHP/pDNA complexes (MNP:pDNA w/w ratio of 0.25, 3 pg pDNA/cell). At 24 h after magnetofection, transfection efficiency was 35.4 and 31% ZsGreen-expressing cells for empty plasmid and pCB-P35, respectively. Apoptosis was induced by addition of either staurosporine (2.5 μM, 5 h) or etoposide (85 μM, 7 h). Negative control represents untreated cells. Sixfold and fourfold decreases in Caspase-3 activity after apoptosis induction with etoposide and staurosporin, respectively, were revealed in the cells magnetofected with *P35* compared with the empty vector (slope values: staurosporine: empty pCB 15.9, pCB-P35 3.8; etoposide: empty pCB 2.5, pCB-P35 0.42).

Discussion

In this study, we have developed an efficient magnetofection protocol for *in situ* gene delivery to corneal endothelium combining selected lipofection reagents with suitable magnetic nanoparticles. We have proven that pDNA is fully bound within the magnetic lipoplexes, thus excluding any false-positive effects on transfection efficiency due to release of pDNA in the culture medium. We optimized the conditions for use of the selected magnetic lipoplexes and extensively tested their biocompatibility and impact on viability and function of corneal endothelium and – more globally – on the immune system. The results presented in this work demonstrate a high suitability of MNPs, especially silica-coated SO-Mag5 particles, for the transfer of nucleic acids to human CECs. Selected magnetic lipoplexes have proven to enhance the efficiency of pDNA delivery to CECs and to explanted human corneas, while not altering endothelial cell viability or cell function. Moreover, the results obtained in PBMCs from healthy donors indicate that under tested conditions magnetofection can be considered both a bio- and immunocompatible delivery system.

Using our optimized magnetofection in CECs, we achieved a transfection efficiency of more than 40% transgene positive cells at a low pDNA dose of only 3 pg/cell. This result is a considerable improvement over lipofection and many existing nanoparticle-based nonviral transfection methods. For example, hyaluronic acid-chitosan nanoparticles merely achieved a transfection efficiency of 15% in the same cell line using similar pDNA dose per cell [9]. It is also important to emphasize that the dose of pDNA used in this experiment was very low. In our previous study utilizing calcium phosphate nanoparticles (CaP/pDNA/CaP/PEI0.5), we achieved a similar efficiency of 39% but applied a more than five-times higher dose of pDNA [31].

In endothelium of explanted human corneas, magnetofection achieved a transfection efficiency of up to 28% in some parts of the specimen. In comparison to other available transfection methods for primary HCECs summarized in a recent study, with efficiencies ranging from 5 to 30% [32], this is a relatively high value. The concave shape of the cornea in combination with a one-directional magnetic field leads to an uneven distribution of magnetic force and thus limits the efficiency. This issue will be addressed in future studies employing a concavely shaped magnet to achieve homogenous complex distribution through the targeted area of corneal endothelium.

Regarding the use of MNPs in living tissue, a possible concern is their potential toxicity to cells through oxidative stress due to their high iron content [22]. However, previous studies applying MNPs to CECs already reported very low or no toxicity [21,33], and our results are congruent with these findings. Still, it seems reasonable to reduce the amount of iron introduced to the eye to necessary minimum. It is thus worth noting that the amount of iron introduced into the cells with SO-Mag5 MNPs is much lower than with any other nanoparticles reported in similar studies. In this study we used MNPs at a final dose of only 0.75 pg Fe/cell, while dose commonly used to label the cells for magnetic resonance imaging (MRI) is usually around 10–30 pg Fe/cell [34].

In addition to its low toxicity, we also found no detrimental effects of the applied magnetofection protocol on the expression of genes important for the endothelial pump function, collagen secretion or apical junction [2,35]. Changes in Na^+/K^+-ATPase expression were additionally investigated on the protein level, and again, no significant differences were encountered. This all indicates that magnetofection does not alter endothelial functionality.

To minimize the risk of any immunological rejection reactions, it is crucial to use transfection reagents that are possibly bio-inert. Our results show that SO-Mag5 MNPs at the applied dose and formulation do not have any significant effects on the immune system, neither inducing nor suppressive. This is consistent with and extends beyond the scope of previous studies on the effect of MNPs on the immune system, which merely examined their potential toxicity to naive PBMCs [36,37]. We investigated not only viability, but also the presence of activation markers and proliferation of both naive as well as activated PBMCs. Although the values among all tested subjects showed individual variations, the results show clearly that no immune response was elicited, and an already ongoing response was not significantly suppressed.

Concerning the promising outcome of this study, we intended to combine our previous experience on anti-apoptotic gene therapy in corneal tissue [38,39] with the advantages of magnetofection. Our first data on magnetofection with the anti-apoptotic *P35* gene have shown that this method can be used to inhibit apoptosis in CECs even after treatment with the known strong apoptosis inducers, staurosporine and etoposide. Further studies on magnetofection of corneal cells with *P35* and other anti-apoptotic genes are currently ongoing.

Taken together, we present an efficient magnetofection procedure for gene delivery to human corneal endothelial cells and primary endothelial cells of explanted human corneas. The presented method is highly bio- and immunocompatible and has no negative influence on functionality of the cells. Successful protection of CECs against apoptosis by magnetofection with the anti-apoptotic *P35* gene suggests that this system presents a promising tool for on-site

anti-apoptotic gene therapy in the treatment of corneal endothelial dystrophies. Advantages of magnetofection using the silica stabilized MNPs will next be further investigated *in vivo* in a mouse model.

Supplementary data

To view the supplementary data that accompany this paper please visit the journal website at: www.futuremedicine.com/doi/full/10.2217/nnm-2016-0144

Financial & competing interests disclosure

This research was funded in part by the German Research Foundation (Unit FOR917, Project PL 281/3–1, O Mykhaylyk; DFG grant INST 410/45–1 FUGG, Zeiss LSM 780) and German Academic Exchange Service (DAAD) (PhD Fellowship, M Czugala). The authors have no other relevant affiliations or financial involvement with any organization or entity with a financial interest in or financial conflict with the subject matter or materials discussed in the manuscript apart from those disclosed.

No writing assistance was utilized in the production of this manuscript.

Ethical conduct of research

The authors state that they have obtained appropriate institutional review board approval or have followed the principles outlined in the Declaration of Helsinki for all human or animal experimental investigations. In addition, for investigations involving human subjects, informed consent has been obtained from the participants involved.

Executive summary

Background

- The development of a safe and efficient method for targeted gene therapy of the corneal endothelium remains an ongoing challenge in ocular research. Magnetic nanoparticles (MNPs) are a promising tool to address this issue, since a magnetic field can be used to guide them to the endothelium *in situ*.

Aims

- To test the ability of magnetofection, an approach combining MNPs with lipofection, to transfect corneal endothelial cells (CECs).
- To test the bio- and immunocompatibility of magnetofection.
- To use magnetofection for anti-apoptotic gene therapy of CECs.

Results

- Out of the MNPs and lipofection reagents tested, the combination of SO-Mag5 MNPs with the reagent X-tremeGENE yielded the highest transfection efficiency (40.4%) with low cytotoxicity (<5%) in corneal endothelial cell line.
- Magnetofection does not negatively affect corneal endothelial function, cell morphology or endothelial structure.
- Magnetofection does not have any immunosuppressive or immunostimulatory effects in human PBMCs.
- Magnetofection in *ex vivo* corneal tissue allowed transfection of corneal endothelium with average efficiency of 13.4 ± 8.9%.
- Magnetofection with the anti-apoptotic *p35* gene was efficient in preventing staurosporine- and etoposide-induced apoptosis in corneal endothelial cells.

Conclusion

- The developed magnetofection protocol employing SO-Mag5 MNPs achieves high efficiency and protects CECs from apoptosis, while resulting in low toxicity and no detrimental effects on cell function or on the immune system. The transfection efficiency is higher than that of comparable nanoparticle-based methods, while additionally enabling targeted gene delivery.

References

1 Joyce NC. Proliferative capacity of the corneal endothelium. *Prog. Retin. Eye Res.* 22(3), 359–389 (2003).

2 Bourne WM. Biology of the corneal endothelium in health and disease. *Eye (Lond.)* 17(8), 912–918 (2003).

3 Murphy C, Alvarado J, Juster R, Maglio M. Prenatal and postnatal cellularity of the human corneal endothelium. A quantitative histologic study. *Invest. Ophthalmol. Vis. Sci.* 25(3), 312–322 (1984).

4 Ghosheh FR, Cremona FA, Rapuano CJ *et al.* Trends in penetrating keratoplasty in the United States 1980–2005. *Int. Ophthalmol.* 28(3), 147–153 (2008).

5 Keenan TD, Jones MN, Rushton S *et al.* Trends in the indications for corneal graft surgery in the United Kingdom: 1999 through 2009. *Arch. Ophthalmol.* 130(5), 621–628 (2012).

6 Koizumi N, Okumura N, Ueno M, Kinoshita S. New therapeutic modality for corneal endothelial disease using Rho-associated kinase inhibitor eye drops. *Cornea* 33(Suppl. 11), S25–S31 (2014).

7 Koizumi N, Okumura N, Ueno M, Nakagawa H, Hamuro J, Kinoshita S. Rho-associated kinase inhibitor eye drop treatment as a possible medical treatment for Fuchs corneal dystrophy. *Cornea* 32(8), 1167–1170 (2013).

8 Okumura N, Koizumi N, Kay EP *et al.* The ROCK inhibitor eye drop accelerates corneal endothelium wound healing. *Invest. Ophthalmol. Vis. Sci.* 54(4), 2493–2502 (2013).

9 De La Fuente M, Seijo B, Alonso MJ. Novel hyaluronic acid-chitosan nanoparticles for ocular gene therapy. *Invest. Ophthalmol. Vis. Sci.* 49(5), 2016–2024 (2008).

10 Konat Zorzi G, Contreras-Ruiz L, Parraga JE *et al.* Expression of MUC5AC in ocular surface epithelial cells using cationized gelatin nanoparticles. *Mol. Pharm.* 8(5), 1783–1788 (2011).

11 Klausner EA, Zhang Z, Chapman RL, Multack RF, Volin MV. Ultrapure chitosan oligomers as carriers for corneal gene transfer. *Biomaterials* 31(7), 1814–1820 (2010).

12 Sharma A, Tandon A, Tovey JC *et al.* Polyethylenimine-conjugated gold nanoparticles: gene transfer potential and low toxicity in the cornea. *Nanomedicine* 7(4), 505–513 (2011).

13 Mu Q, Jeon M, Hsiao MH *et al.* Stable and efficient Paclitaxel nanoparticles for targeted glioblastoma therapy. *Adv. Healthc. Mater.* 4(8), 1236–1245 (2015).

14 Almstatter I, Mykhaylyk O, Settles M *et al.* Characterization of magnetic viral complexes for targeted delivery in oncology. *Theranostics* 5(7), 667–685 (2015).

15 Prosen L, Hudoklin S, Cemazar M *et al.* Magnetic field contributes to the cellular uptake for effective therapy with magnetofection using plasmid DNA encoding against Mcam in B16F10 melanoma *in vivo*. *Nanomedicine (Lond.)* 11(6), 627–641 (2016).

16 Prijic S, Prosen L, Cemazar M *et al.* Surface modified magnetic nanoparticles for immuno-gene therapy of murine mammary adenocarcinoma. *Biomaterials* 33(17), 4379–4391 (2012).

17 Yanai A, Hafeli UO, Metcalfe AL *et al.* Focused magnetic stem cell targeting to the retina using superparamagnetic iron oxide nanoparticles. *Cell Transplant.* 21(6), 1137–1148 (2012).

18 Patel SV, Bachman LA, Hann CR, Bahler CK, Fautsch MP. Human corneal endothelial cell transplantation in a human *ex vivo* model. *Invest. Ophthalmol. Vis. Sci.* 50(5), 2123–2131 (2009).

19 Mimura T, Shimomura N, Usui T *et al.* Magnetic attraction of iron-endocytosed corneal endothelial cells to Descemet's membrane. *Exp. Eye Res.* 76(6), 745–751 (2003).

20 Mimura T, Yamagami S, Usui T *et al.* Long-term outcome of iron-endocytosing cultured corneal endothelial cell transplantation with magnetic attraction. *Exp. Eye Res.* 80(2), 149–157 (2005).

21 Raju HB, Hu Y, Vedula A, Dubovy SR, Goldberg JL. Evaluation of magnetic micro- and nanoparticle toxicity to ocular tissues. *PLoS ONE* 6(5), e17452 (2011).

22 Prow TW. Toxicity of nanomaterials to the eye. *Wiley Interdiscip. Rev. Nanomed. Nanobiotechnol.* 2(4), 317–333 (2010).

23 Shapiro B, Kulkarni S, Nacev A, Sarwar A, Preciado D, Depireux DA. Shaping magnetic fields to direct therapy to ears and eyes. *Annu. Rev. Biomed. Eng.* 16, 455–481 (2014).

24 Sanchez-Antequera Y, Mykhaylyk O, Thalhammer S, Plank C. Gene delivery to Jurkat T cells using non-viral vectors associated with magnetic nanoparticles. *Int. J. Biomed. Nanosci. Nanotechnol.* 1(2–4/2010), 202–229 (2010).

25 Mykhaylyk O, Sobisch T, Almstatter I *et al.* Silica-iron oxide magnetic nanoparticles modified for gene delivery: a search for optimum and quantitative criteria. *Pharm. Res.* 29(5), 1344–1365 (2012).

26 Mykhaylyk O, Sanchez-Antequera Y, Vlaskou D *et al.* Magnetic nanoparticle and magnetic field assisted siRNA delivery *in vitro*. *Methods Mol. Biol.* 1218, 53–106 (2015).

27 Mykhaylyk O, Antequera YS, Vlaskou D, Plank C. Generation of magnetic nonviral gene transfer agents and magnetofection *in vitro*. *Nat. Protoc.* 2(10), 2391–2411 (2007).

28 Mykhaylyk O, Lerche D, Vlaskou D *et al.* Magnetophoretic mobility: determination by space and time resolved extinction profiles. *IEEE Magnetic Letters* 6, 1–4 (2015).

29 Wilhelm C, Gazeau F, Bacri JC. Magnetophoresis and ferromagnetic resonance of magnetically labeled cells. *Eur. Biophys. J.* 31(2), 118–125 (2002).

30 Kwok LS. Calculation and application of the anterior surface area of a model human cornea. *J. Theor. Biol.* 108(2), 295–313 (1984).

31 Hu J, Kovtun A, Tomaszewski A *et al.* A new tool for the transfection of corneal endothelial cells: calcium phosphate nanoparticles. *Acta Biomater.* 8(3), 1156–1163 (2012).

32 Engler C, Kelliher C, Wahlin KJ, Speck CL, Jun AS. Comparison of non-viral methods to genetically modify and enrich populations of primary human corneal endothelial cells. *Mol. Vis.* 15, 629–637 (2009).

33 Moysidis SN, Alvarez-Delfin K, Peschansky VJ *et al.* Magnetic field-guided cell delivery with nanoparticle-loaded human corneal endothelial cells. *Nanomedicine* 11(3), 499–509 (2015).

34 Arbab AS, Yocum GT, Kalish H *et al.* Efficient magnetic cell labeling with protamine sulfate complexed to ferumoxides for cellular MRI. *Blood* 104(4), 1217–1223 (2004).

35 Vassilev VS, Mandai M, Yonemura S, Takeichi M. Loss of N-cadherin from the endothelium causes stromal edema and epithelial dysgenesis in the mouse cornea. *Invest. Ophthalmol. Vis. Sci.* 53(11), 7183–7193 (2012).

36 Bhattacharya K, Gogoi B, Buragohain AK, Deb P. Fe(2)O(3)/C nanocomposites having distinctive antioxidant activity and hemolysis prevention efficiency. *Mater. Sci. Eng. C Mater. Biol. Appl.* 42, 595–600 (2014).

37 Ding J, Tao K, Li J, Song S, Sun K. Cell-specific cytotoxicity of dextran-stabilized magnetite nanoparticles. *Colloids Surf. B. Biointerfaces* 79(1), 184–190 (2010).

38 Fuchsluger TA, Jurkunas U, Kazlauskas A, Dana R. Anti-apoptotic gene therapy prolongs survival of corneal endothelial cells during storage. *Gene Ther.* 18(8), 778–787 (2011).

39 Fuchsluger TA, Jurkunas U, Kazlauskas A, Dana R. Corneal endothelial cells are protected from apoptosis by gene therapy. *Hum. Gene Ther.* 22(5), 549–558 (2011).

Manuscript "CASP3 inactivates BMAL1 by cleaving off its transactivation domain at D585"

Böhler P, Peter C, Friesen O, Berleth N, Deitersen J, Schlütermann D, Stuhldreier F, Wu W, Dibner C, Schoder G, Reinke H, Stork B. *Manuscript prepared for publication.*

CASP3 inactivates BMAL1 by cleaving off its transactivation domain at D585

Philip Böhler[1], Christoph Peter[1], Olena Friesen[1], Niklas Berleth[1], Jana Deitersen[1], David Schlütermann[1], Fabian Stuhldreier[1], Wenxian Wu[1], Charna Dibner[2], Gabriele Schoder[3], Hans Reinke[3,4], Björn Stork[1]

[1] Institute of Molecular Medicine I, Medical Faculty, Heinrich Heine University Düsseldorf, 40225 Düsseldorf, Germany

[2] Laboratory of Circadian Endocrinology, Geneva University Hospitals, Geneva, Switzerland

[3] Institute of Clinical Chemistry and Laboratory Diagnostics, Medical Faculty, Heinrich Heine University Düsseldorf, 40225 Düsseldorf, Germany

[4] IUF – Leibniz Research Institute for Environmental Medicine, 40225 Düsseldorf, Germany

Correspondence / Lead Contact: Björn Stork, Universitätsstraße 1, Building 23.12, 40225 Düsseldorf, Germany. Tel: +49-(0)211-81-11954; Fax: +49-(0)211-81-11611954; E-mail: bjoern.stork@hhu.de

Running title: CASP3 inactivates BMAL1

Key words: ARNTL, BMAL1, CASP3, apoptosis, circadian clock, transactivation domain

Highlights:

- CASP3 cleaves BMAL1 at D585 both in vitro and in vivo
- Cleaved BMAL1 is transcriptionally inactive and cannot generate circadian rhythms
- This may play a role in shifting the DNA damage response from cell cycle arrest to apoptosis

eTOC Blurb: Böhler et al. demonstrate that apoptosis inactivates the circadian clock via CASP3-mediated cleavage of BMAL1. CASP3 cleaves off the transactivation domain of BMAL1, thus rendering it transcriptionally inactive and unable to maintain circadian rhythms.

Abbreviations: bHLH, basic helix–loop–helix; BMAL1, brain muscle aryl nuclear translocase like-1; CASP3, caspase-3; CASP9, caspase-9; CBP, CREB-binding protein; CLOCK, circadian locomotor

output cycles kaput; CRY, cryptochrome; GST, glutathione S-transferase; HAT, histone acetylase; KIX domain, kinase-inducible domain interacting domain; MLF, murine lung fibroblast; p21, Cyclin-dependent kinase inhibitor 1; P300, histone acetyltransferase p300; PAS domain, PER-ARNT-SIM domain; PER, period; QVD, Q-VD-OPh; STS, staurosporine; TAD, transactivation domain; TRAIL, TNF-related apoptosis-inducing ligand; TTFL, transcription / translation feedback loop; WEE1, Wee1-like protein kinase.

Summary

The transcription factor BMAL1 (ARNTL) is a key regulator of the mammalian circadian clock with functions extending to other cellular pathways such as cell cycle control and tumour suppression. Here, we show that BMAL1 is inactivated upon induction of apoptosis. The apoptotic effector caspase CASP3 cleaves BMAL1 at residue D585, both in vitro and in vivo, and thus removes its transactivation domain. Cleaved BMAL1 has no transcriptional activity and cannot generate circadian rhythms. We thus demonstrate that apoptosis causes a shutdown of the circadian clock and thus an interruption of the myriad of processes it regulates, and we discuss how this may contribute to a shift of the DNA damage response away from cell cycle arrest and towards cell death.

Introduction

The protein BMAL1 (ARNTL) is a core component of the mammalian circadian clock. This network of cellular pathways generates physiological day/night cycles that govern processes such as sleep, metabolism, and DNA damage repair (Takahashi, 2017).

Within the circadian clock, BMAL1 is an activating part of the main transcription / translation feedback loop (TTFL). BMAL1 dimerizes with another TTFL activator, CLOCK, both of which are members of the basic helix–loop–helix (bHLH)/ Per-ARNT-Sim (PAS) family of transcription factors. The BMAL1:CLOCK heterodimer binds to E-box regulatory elements located in the 5' region of its target genes to upregulate their expression. Among the target genes of BMAL1:CLOCK are its own repressors, CRY1/CRY2 and PER1/PER2/PER3, whose expression decreases the transcriptional

activity of BMAl1:CLOCK until the repressors are proteasomally degraded and the circadian cycle begins again. This delayed negative feedback loop results in a 24 h rhythm of alternating transcriptional activation and repression (Partch et al., 2014).

BMAL1 contains several structural elements related to its function as a transcription factor: a nuclear localisation signal (N-terminal) and two nuclear export signals (internal) (Kwon et al., 2006), as well as the bHLH domain (N-terminal) that enables DNA binding if BMAL1 is dimerized with CLOCK. In addition, BMAL1 contains two functional PAS domains (internal) that mediate its interaction with CLOCK (Huang et al., 2012).

The transactivation domain (TAD) of BMAL1, located at its very C-terminus, is essential to its transcriptional activity and to circadian rhythmicity in general (Kiyohara et al., 2006; Xu et al., 2015). Two types of proteins compete for binding to the TAD: The transcriptional activators CBP and P300 (via their KIX domains), and the transcriptional repressor CRY1 (via its C-terminal coiled-coil domain) (Czarna et al., 2011; Takahata et al., 2000; Xu et al., 2015). CBP and P300 facilitate transcription by recruiting the transcription preinitiation complex as well as by their histone acetylase (HAT) activity, which causes local chromatin decondensation and thus allows transcription to take place (Etchegaray et al., 2003; Hosoda et al., 2009). Conversely, CRY1 displaces CBP and P300 from the TAD and thus represses the transcription of BMAL1:CLOCK target genes.(Xu et al., 2015)

Among the BMAL1:CLOCK target genes are, aside from the repressors CRY and PER, a plethora of diverse other genes. A recent study estimated the percentage of genes undergoing circadian regulation at the mRNA level to be about 5–20% in any given tissue (Zhang et al., 2014). In genome-wide screenings, more than 5900 BMAL1 binding sites were found, corresponding to about 3000 unique genes that could be directly regulated by BMAL1:CLOCK (Koike et al., 2012; Rey et al., 2011). Many genes regulated by the circadian clock play a role in metabolic pathways, cell cycle control, and insulin signalling, all of which are linked to cell survival and proliferation (Hunt and Sassone-Corsi, 2007; Koike et al., 2012; Rey et al., 2011). However, so far, no direct crosstalk between the circadian clock and the pathways of apoptosis is known.

In the present study, we provide evidence for a direct interaction between BMAL1 and the apoptotic executioner protease CASP3. BMAL1 is proteolytically cleaved by CASP3 at residue D585, resulting in removal of the BMAL1 TAD. This cleavage inactivates BMAL1 and interrupts the circadian clock upon induction of apoptosis.

Results

Apoptosis induction results in CASP3-dependent cleavage of BMAL1

We observed that induction of apoptosis results in disappearance of the BMAL1 immunoblot band at the normally observed apparent size of 80 kDa (actual size 69 kDa). At the same time, a number of bands of apparent degradation products appear at about 76, 72, 68, and 65 kDa. Over time, all of these bands except the one at 65 kDa disappear, suggesting this is the final degradation product. This pattern of cleavage was observed in a number of different cells lines including Jurkat J16 (acute T cell leukaemia) and CASP3-positive MCF7 (breast cancer) (Figure 1a & 1c, right panel). Addition of the pan-caspase inhibitor QVD (Q-VD-OPh) before apoptosis induction completely prevented BMAL1 degradation independently of the type of apoptotic stimulus, suggesting the degradation is a direct consequence of apoptosis. We thus tried to determine whether BMAL1 is directly cleaved by a caspase, and if yes, by which one. For this purpose, we used Jurkat JMR cells, which are deficient for the initiator caspase CASP9 (Samraj et al., 2006), and MCF7 cells, which are naturally deficient for the executioner caspase CASP3 (Jänicke et al., 1998), as well as corresponding cells in which the respective caspases were reconstituted. In CASP9-deficient cells, treatment with staurosporine, an inducer of intrinsic apoptosis, resulted in neither apoptosis induction nor BMAL1 cleavage. However, treatment with TRAIL, an inducer of extrinsic apoptosis, still caused both apoptosis and BMAL1 cleavage, indicating that CASP9 is dispensable for this process (Figure 1b). In CASP3-deficient cells, however, no BMAL1 cleavage whatsoever was observed upon staurosporine treatment, yet reconstitution of CASP3 fully restored the phenotype with a cleavage pattern similar to that observed in other cell lines (Figure 1c). This indicates that CASP3 is required for BMAL1 cleavage in vivo. To determine whether CASP3 directly cleaves BMAL1, we performed an in vitro protease assay with purified recombinant CASP3 and N-terminally GST-tagged recombinant BMAL1 (Figure 1d). While

GST-BMAL1 itself produced a single band at about 110 kDa, addition of CASP3 resulted in a second band at about 105 kDa already after 1 min of incubation at 37°C. After longer incubation, the 110 kDa band disappeared while the 105 kDa band remained even after 4 h of incubation with CASP3, although it grew fainter over time. Both bands were observed at the same apparent size in immunoblots against both BMAL1 and GST. Since cleavage near the N-terminus would detach the GST tag, this indicates that CASP3 cleaves BMAL1 near its C-terminus.

CASP3 cleaves BMAL1 at D585 both in vitro and in vivo

We next tried to determine the location of the CASP3 cleavage site in BMAL1. For this purpose, we employed the heuristic cleavage site prediction tool *Cascleave* to predict high-probability cleavage sites *in silico* (Song et al., 2010). The five putative sites with the highest predictive score, in decreasing order, are the three C-terminal sites D610, D621 and D585, and the two N-terminal sites D45 and D56 (Table 1 & Figure 2a). Out of these five, only C-terminal cleavage at D585 would result in a size shift of the large cleavage fragment by roughly 5 kDa, as observed. We thus generated the N-terminally GST-tagged alanine mutant BMAL1-D585A and performed an in vitro protease assay. Indeed, mutation of D585 completely prevented cleavage of BMAL1 by CASP3 (Figure 2b). In addition, we also performed in vitro protease assays with BMAL1-D45A, BMAL1-D56A, BMAL1-D610A, and BMAL1-D621A, yet no difference in band size was observed in comparison to BMAL1-wt (data not shown). To test the effect of the D585A mutation on apoptotic BMAL1 cleavage in vivo, we used the BMAL1-deficient Burkitt lymphoma cell line BJAB (deficiency confirmed on both mRNA and protein level by qPCR and immunoblot, respectively – data not shown). We stably transfected BJAB cells with either BMAL1-wt or BMAL1-D585A and induced apoptosis via the extrinsic pathway using TRAIL. Again, BMAL1-wt was cleaved resulting in a fragment about 5 kDa smaller while BMAL1-D585A was not cleaved (Figure 2c). We additionally expressed a truncated form, BMAL1-M1-D585, which mimics the putative large cleavage fragment. Indeed, this truncated form has about the same size as the cleaved fragment (Figure 2c).

Cleaved BMAL1 has no transcriptional activity and cannot restore circadian function

Cleavage of BMAL1 cleavage at D585 results in removal of its transactivation domain (TAD), which is required for its transcriptional activity and for circadian rhythmicity in general. To confirm this effect, we expressed either full-length BMAL1 or the cleavage product BMAL1-M1-D585 in *Bmal1*-KO murine lung fibroblasts (MLFs) to test whether this could restore circadian function in these cells. For this purpose, we used qPCR to measure the circadian changes in mRNA levels of the BMAL1-regulated gene *Per2*. While both wild-type (*Bmal1*-wt) cells as well as *Bmal1*-KO cells reconstituted with full-length BMAL1 (BMAL1-RE) displayed 24 h rhythmicity in *Per2* mRNA levels, this could not be observed in non-reconstituted *Bmal1*-KO cells or in cells reconstituted with the cleavage product BMAL1-M1-D585. These results indicate that the cleaved form of BMAL1 is unable to restore circadian function (Figure 3a). Comparable results were obtained using a reporter gene assay employing a BMAL1-regulated luciferase gene: Again, reconstitution with full-length BMAL1 restored circadian function, while BMAL1-M1-D585 did not (Figure 3b). Taken together, these results show that cleavage of BMAL1 at D585 causes loss of its transcriptional activity and inactivates the circadian clock.

Discussion

That apoptosis inactivates BMAL1 came as a surprise, since BMAL1 is often considered a tumour suppressor that restricts proliferation and cell cycle progression, and that can sensitize cells to apoptosis (Fu and Lee, 2003; Jiang et al., 2016). Common antagonists of BMAL1 include positive regulators of proliferation, such as insulin signalling (Dang et al., 2016). However, BMAL1 has also been shown to promote tumour growth in certain types of cancer, where BMAL1 depletion results in cell cycle disruption and apoptosis (Elshazley et al., 2012).

One possible explanation for apoptotic BMAL1 inactivation is the known antagonism between BMAL1 and the oncogene MYC. Both of these compete for binding to some of the same E-box motifs in the DNA and act as mutual regulators: BMAL1 can negatively regulate the transcription of MYC (Fu et al., 2005; Hunt and Sassone-Corsi, 2007), whereas MYC in turn represses the expression of

BMAL1 through a variety of mechanisms (Altman et al., 2015; Shostak et al., 2016). This goes so far that many cell lines that overexpress MYC do not express BMAL1 at all due to epigenetic silencing (Shostak et al., 2016; Taniguchi et al., 2009). Overexpression of MYC can result in uncontrolled cell proliferation and has been observed in many cancers (Dang, 2012). However, MYC can also induce, or sensitize cells to, apoptosis. This apparently paradoxical function is believed to be a failsafe feature to prevent MYC-induced oncogenesis, and cancer cells that overexpress MYC consequently often also display defects in apoptosis induction (Hoffman and Liebermann, 2008). Apoptotic cleavage is thus another mechanism through which MYC can inactivate its regulator BMAL1.

A second possibility is that the cleavage of BMAL1 serves a similar purpose as the cleavage of the tumour suppressors WEE1 and $p21^{WAF1/CIP1}$ (CDKN1A), all three of which are cleaved by CASP3 upon apoptosis induction. WEE1 and p21 normally function as negative cell cycle regulators via inhibition of CDK1 and CDK2, respectively. In apoptotic cells, CASP3 cleaves both WEE1 and p21, most likely to further shift the DNA damage response from cell cycle arrest to apoptosis (Zhang et al., 1999; Zhou et al., 1998). Just like WEE1 and p21, BMAL1 is a negative cell cycle regulator (Cardone and Sassone-Corsi, 2003). In addition, BMAL1 regulates both p21 and WEE1 as well as another cell cycle regulator, cyclin B1 (CCNB1). For p21, both positive (Elshazley et al., 2012) and negative (Gréchez-Cassiau et al., 2008) regulation by BMAL1 have been reported, whereas for WEE1 and cyclin B1, only positive regulation has been reported (Elshazley et al., 2012; Farshadi et al., 2019; Matsuo et al., 2003). Active BMAL1 might thus keep a cell stuck in cell cycle arrest without progressing to cell death. Therefore, it is feasible that BMAL1 cleavage contributes to the shift away from DNA repair and towards apoptosis.

The null hypothesis, of course, has to be that apoptotic BMAL1 inactivation is merely the result of bystander cleavage and serves no specific function. This hypothesis is difficult to test since the effect of cleavage may be relevant only in certain cell types or under specific conditions (Crawford and Wells, 2011). Considering, however, that the CASP3 cleavage site in BMAL1 identified in this work is highly conserved between species, yet not conserved in the otherwise closely related BMAL1 paralog BMAL2 (ARNTL2), it appears likely to have an evolutionarily selected function.

In summary, we could show that BMAL1 is cleaved by CASP3 in apoptotic cells, resulting in loss of the BMAL1 transactivation domain and consequently loss of BMAL1 transcriptional activity. The inactivation of BMAL1 may serve a role in the DNA damage response and in particular in the shift from cell cycle arrest to apoptosis.

Acknowledgements

We thank Charlotte von Gall for providing BMAL1-KO murine lung fibroblasts and corresponding wild-type cells, Michael Engelke for providing Ramos B lymphocytes, Toshio Kitamura for providing Platinum-E (Plat-E) cells, Steven Brown for providing the pLV6-Bmal-luc reporter construct (Addgene plasmid #68833), and Hartmut Land and Jay Morgenstern and Bob Weinberg for providing the pBABEpuro vector (Addgene plasmid #1764).

This study was supported by the Deutsche Forschungsgemeinschaft STO 864/5-1 and GRK 2158 (to B.S.) and by the Düsseldorf School of Oncology (to B.S.; funded by the Comprehensive Cancer Center Düsseldorf/Deutsche Krebshilfe and the Medical Faculty of the Heinrich Heine University Düsseldorf).

Author contributions

Conceptualization, P.B. and B.S.; Methodology, P.B., C.P., C.D., H.S., and B.S.; Investigation, P.B., O.F., G.S., and C.D.; Resources, C.P., C.D., H.R., and B.S.; Writing – Original Draft, P.B.; Writing – Review & Editing, P.B., C.P., O.F., N.B., J.D., D.S., F.S., W.W., H.R., and B.S.; Visualization, P.B.; Supervision, B.S.; Project Administration, B.S.; Funding Acquisition, H.R. and B.S.

Declaration of interests

The authors declare no conflicts of interest.

202 # References

203 Altman, B.J., Hsieh, A.L., Sengupta, A., Krishnanaiah, S.Y., Stine, Z.E., Walton, Z.E., Gouw, A.M.,
204 Venkataraman, A., Li, B., Goraksha-Hicks, P.*, et al.* (2015). MYC Disrupts the Circadian Clock and
205 Metabolism in Cancer Cells. Cell Metab *22*, 1009–1019.

206 Cardone, L., and Sassone-Corsi, P. (2003). Timing the cell cycle. Nat Cell Biol *5*, 859–861.

207 Crawford, E.D., and Wells, J.A. (2011). Caspase substrates and cellular remodeling. Annu Rev
208 Biochem *80*, 1055–1087.

209 Czarna, A., Breitkreuz, H., Mahrenholz, C.C., Arens, J., Strauss, H.M., and Wolf, E. (2011).
210 Quantitative analyses of cryptochrome-mBMAL1 interactions: mechanistic insights into the
211 transcriptional regulation of the mammalian circadian clock. J Biol Chem *286*, 22414–22425.

212 Dang, C.V. (2012). MYC on the path to cancer. Cell *149*, 22–35.

213 Dang, F., Sun, X., Ma, X., Wu, R., Zhang, D., Chen, Y., Xu, Q., Wu, Y., and Liu, Y. (2016). Insulin
214 post-transcriptionally modulates Bmal1 protein to affect the hepatic circadian clock. Nat Commun *7*,
215 12696.

216 Elshazley, M., Sato, M., Hase, T., Yamashita, R., Yoshida, K., Toyokuni, S., Ishiguro, F., Osada, H.,
217 Sekido, Y., Yokoi, K.*, et al.* (2012). The circadian clock gene BMAL1 is a novel therapeutic target for
218 malignant pleural mesothelioma. International journal of cancer Journal international du cancer *131*,
219 2820–2831.

220 Etchegaray, J.P., Lee, C., Wade, P.A., and Reppert, S.M. (2003). Rhythmic histone acetylation
221 underlies transcription in the mammalian circadian clock. Nature *421*, 177–182.

222 Farshadi, E., Yan, J., Leclere, P., Goldbeter, A., Chaves, I., and van der Horst, G.T.J. (2019). The
223 positive circadian regulators CLOCK and BMAL1 control G2/M cell cycle transition through Cyclin
224 B1. Cell Cycle *18*, 16–33.

225 Fu, L., and Lee, C.C. (2003). The circadian clock: pacemaker and tumour suppressor. Nat Rev Cancer
226 *3*, 350–361.

227 Fu, L., Patel, M.S., Bradley, A., Wagner, E.F., and Karsenty, G. (2005). The molecular clock mediates
228 leptin-regulated bone formation. Cell *122*, 803–815.

229 Gréchez-Cassiau, A., Rayet, B., Guillaumond, F., Teboul, M., and Delaunay, F. (2008). The circadian
230 clock component BMAL1 is a critical regulator of p21WAF1/CIP1 expression and hepatocyte
231 proliferation. J Biol Chem *283*, 4535–4542.

232 Hoffman, B., and Liebermann, D.A. (2008). Apoptotic signaling by c-MYC. Oncogene *27*, 6462–
233 6472.

234 Hosoda, H., Kato, K., Asano, H., Ito, M., Kato, H., Iwamoto, T., Suzuki, A., Masushige, S., and Kida,
235 S. (2009). CBP/p300 is a cell type-specific modulator of CLOCK/BMAL1-mediated transcription.
236 Molecular brain *2*, 34.

237 Huang, N., Chelliah, Y., Shan, Y., Taylor, C.A., Yoo, S.H., Partch, C., Green, C.B., Zhang, H., and
238 Takahashi, J.S. (2012). Crystal structure of the heterodimeric CLOCK:BMAL1 transcriptional
239 activator complex. Science *337*, 189–194.

240 Hunt, T., and Sassone-Corsi, P. (2007). Riding tandem: circadian clocks and the cell cycle. Cell *129*,
241 461–464.

242 Jänicke, R.U., Sprengart, M.L., Wati, M.R., and Porter, A.G. (1998). Caspase-3 Is Required for DNA
243 Fragmentation and Morphological Changes Associated with Apoptosis. Journal of Biological
244 Chemistry *273*, 9357–9360.

245 Jiang, W., Zhao, S., Jiang, X., Zhang, E., Hu, G., Hu, B., Zheng, P., Xiao, J., Lu, Z., Lu, Y.*, et al.*
246 (2016). The circadian clock gene Bmal1 acts as a potential anti-oncogene in pancreatic cancer by
247 activating the p53 tumor suppressor pathway. Cancer Lett *371*, 314–325.

248 Kiyohara, Y.B., Tagao, S., Tamanini, F., Morita, A., Sugisawa, Y., Yasuda, M., Yamanaka, I., Ueda,
249 H.R., van der Horst, G.T., Kondo, T.*, et al.* (2006). The BMAL1 C terminus regulates the circadian
250 transcription feedback loop. Proc Natl Acad Sci U S A *103*, 10074–10079.

251 Koike, N., Yoo, S.H., Huang, H.C., Kumar, V., Lee, C., Kim, T.K., and Takahashi, J.S. (2012).
252 Transcriptional architecture and chromatin landscape of the core circadian clock in mammals. Science
253 *338*, 349–354.

254 Kwon, I., Lee, J., Chang, S.H., Jung, N.C., Lee, B.J., Son, G.H., Kim, K., and Lee, K.H. (2006).
255 BMAL1 shuttling controls transactivation and degradation of the CLOCK/BMAL1 heterodimer. Mol
256 Cell Biol *26*, 7318–7330.

257 Lauber, K., Appel, H.A., Schlosser, S.F., Gregor, M., Schulze-Osthoff, K., and Wesselborg, S. (2001).
258 The adapter protein apoptotic protease-activating factor-1 (Apaf-1) is proteolytically processed during
259 apoptosis. J Biol Chem *276*, 29772–29781.

260 Matsuo, T., Yamaguchi, S., Mitsui, S., Emi, A., Shimoda, F., and Okamura, H. (2003). Control
261 mechanism of the circadian clock for timing of cell division in vivo. Science *302*, 255–259.

262 Morgenstern, J.P., and Land, H. (1990). Advanced mammalian gene transfer: high titre retroviral
263 vectors with multiple drug selection markers and a complementary helper-free packaging cell line.
264 Nucleic acids research *18*, 3587–3596.

265 Partch, C.L., Green, C.B., and Takahashi, J.S. (2014). Molecular architecture of the mammalian
266 circadian clock. Trends Cell Biol *24*, 90–99.

267 Rey, G., Cesbron, F., Rougemont, J., Reinke, H., Brunner, M., and Naef, F. (2011). Genome-wide and
268 phase-specific DNA-binding rhythms of BMAL1 control circadian output functions in mouse liver.
269 PLoS Biol *9*, e1000595.

Samraj, A.K., Keil, E., Ueffing, N., Schulze-Osthoff, K., and Schmitz, I. (2006). Loss of caspase-9 provides genetic evidence for the type I/II concept of CD95-mediated apoptosis. J Biol Chem *281*, 29652–29659.

Shostak, A., Ruppert, B., Ha, N., Bruns, P., Toprak, U.H., Project, I.M.-S., Eils, R., Schlesner, M., Diernfellner, A., and Brunner, M. (2016). MYC/MIZ1-dependent gene repression inversely coordinates the circadian clock with cell cycle and proliferation. Nat Commun *7*, 11807.

Song, J., Tan, H., Shen, H., Mahmood, K., Boyd, S.E., Webb, G.I., Akutsu, T., and Whisstock, J.C. (2010). Cascleave: towards more accurate prediction of caspase substrate cleavage sites. Bioinformatics *26*, 752–760.

Takahashi, J.S. (2017). Transcriptional architecture of the mammalian circadian clock. Nat Rev Genet *18*, 164–179.

Takahata, S., Ozaki, T., Mimura, J., Kikuchi, Y., Sogawa, K., and Fujii-Kuriyama, Y. (2000). Transactivation mechanisms of mouse clock transcription factors, mClock and mArnt3. Genes to Cells *5*, 739–747.

Taniguchi, H., Fernandez, A.F., Setien, F., Ropero, S., Ballestar, E., Villanueva, A., Yamamoto, H., Imai, K., Shinomura, Y., and Esteller, M. (2009). Epigenetic inactivation of the circadian clock gene BMAL1 in hematologic malignancies. Cancer Res *69*, 8447–8454.

Xu, H., Gustafson, C.L., Sammons, P.J., Khan, S.K., Parsley, N.C., Ramanathan, C., Lee, H.W., Liu, A.C., and Partch, C.L. (2015). Cryptochrome 1 regulates the circadian clock through dynamic interactions with the BMAL1 C terminus. Nat Struct Mol Biol *22*, 476–484.

Zhang, R., Lahens, N.F., Ballance, H.I., Hughes, M.E., and Hogenesch, J.B. (2014). A circadian gene expression atlas in mammals: implications for biology and medicine. Proc Natl Acad Sci U S A *111*, 16219–16224.

Zhang, Y., Fujita, N., and Tsuruo, T. (1999). Caspase-mediated cleavage of p21Waf1/Cip1 converts cancer cells from growth arrest to undergoing apoptosis. Oncogene *18*, 1131–1138.

Zhou, B.B., Li, H., Yuan, J., and Kirschner, M.W. (1998). Caspase-dependent activation of cyclin-dependent kinases during Fas-induced apoptosis in Jurkat cells. Proc Natl Acad Sci U S A *95*, 6785–6790.

Figure legends

Figure 1: Apoptosis induction results in CASP3-dependent cleavage of BMAL1. (**a-c**) Apoptosis induction and cleavage of BMAL1 by CASP3 in different cell lines as detected by immunoblot. Either staurosporine (STS) or TRAIL were used to induce intrinsic or extrinsic apoptosis, respectively. The pan-caspase inhibitor QVD was used to test if the observed effects were the result of caspase activity. (**a**) Jurkat J16 T lymphocytes were treated with STS for up to 10 h. (**b**) Jurkat JMR T lymphocytes that were either deficient for CASP9 or reconstituted were treated with STS or TRAIL for 6 h. (**c**) MCF7 breast cancer cells that were either deficient for CASP3 or reconstituted were treated with STS for up to 10 h. (**d**) In vitro protease assay using recombinant GST-BMAL1 produced in wheat germ and recombinant CASP3-His produced in *E. coli*. Samples were subjected to SDS-PAGE and immunoblotting for BMAL1 and GST, respectively.

Figure 2: CASP3 cleaves BMAL1 at D585 both in vitro and in vivo. (**a**) Schematic of the BMAL1 protein showing the five putative CASP3 cleavage sites and recognition sequences at D45, D56, D585, D610, and D621; the antibody binding site at G552; and the transactivation domain (TAD, yellow). (**b**) In vitro protease assay using recombinant GST-BMAL1-wt or GST-BMAL1-D585A, both produced in wheat germ, and recombinant CASP3-His produced in *E. coli*. The pan-caspase inhibitor QVD was used to test if the observed effects were the result of caspase activity. Samples were subjected to SDS-PAGE and immunoblotting for BMAL1 and GST, respectively. (**c**) Effect of apoptosis induction on BMAL1-wt and BMAL1-D585A expressed in BJAB cells as detected by immunoblot. VC = vector control, M1-D585 = truncated BMAL1 mimicking the putative cleavage product.

Figure 3: Cleaved BMAL1 is transcriptionally inactive and cannot generate circadian rhythms. The effect of Bmal1 deficiency and reconstitution with either BMAL1 (BMAL1-RE) or BMAL1-M1-D585 on the circadian cycle was measured by (**a**) qPCR analysis of *Per2* mRNA levels or (**b**) reporter gene assay employing a BMAL1-regulated luciferase gene.

Tables

Table 1: Putative CASP3 cleavage sites in human BMAL1 and sizes of the respective cleavage fragments as predicted by *Cascleave*.

Position	Score	Site	N-term. fragment size	C-term. fragment size
45	0.815	SSTD*YQES	5 kDa	64 kDa
56	0.804	DKDD*PHGR	6 kDa	63 kDa
585	1.040	DMID*NDQG	65 kDa	4 kDa
610	1.131	LEAD*AGLG	67 kDa	2 kDa
621	1.076	DFSD*LPWP	68 kDa	1 kDa

Experimental procedures

Cell lines and cell culture

BJAB cells (#ACC-757) and Jurkat-wt cells (#ACC-282) were obtained from DSMZ. Jurkat JMR cells (CASP9-deficient and reconstituted) have been described previously (Samraj et al., 2006). MCF7 cells (CASP3-deficient and reconstituted) were kindly provided by Reiner U. Jänicke (Laboratory of Molecular Radiooncology, Heinrich Heine University Düsseldorf, Germany) and have been described previously (Jänicke et al., 1998). Primary murine lung fibroblasts (MLFs; *Bmal1*-KO and corresponding wild-type cells) were kindly provided by Charlotte von Gall (Institute of Anatomy II, Heinrich Heine University Düsseldorf, Germany) and were immortalised by the "plate-and-wait" method, i.e. spontaneous immortalisation. Ramos cells were kindly provided by Michael Engelke (Institute of Cellular and Molecular Immunology, University Hospital Göttingen, Göttingen, Germany). Cell lines stably expressing BMAL1-wt, BMAL1-D585A, or BMAL1-M1-D585 were generated by retroviral transfection using the Platinum-E (Plat-E) packaging cell line (kindly provided by Toshio Kitamura, Institute of Medical Science, University of Tokyo, Japan) and the retroviral vector pBABEpuro (Addgene plasmid #1764; kindly provided by Hartmut Land & Jay Morgenstern &

Bob Weinberg and described previously (Morgenstern and Land, 1990)). The following transfection vectors were generated and deposited at Addgene: pBABEpuro-BMAL1-wt (Addgene plasmid #107760), pBABEpuro-BMAL1-D585A (Addgene plasmid #107761), and pBABEpuro-BMAL1-M1-D585 (Addgene plasmid #107762). Cells lines stably expressing the Bmal1-luc reporter were generated by lentiviral transfection using the pLV6-Bmal-luc reporter construct (Addgene plasmid #68833; kindly provided by Steven Brown, Chronobiology and Sleep Research Group, Institute of Pharmacology and Toxicology, University of Zurich, Zurich, Switzerland). The medium used for the cultivation of BJAB and Jurkat cells was RPMI 1640 medium. All other cells were cultivated in high-glucose DMEM. All media were supplemented with 10% foetal calf serum (FCS), 100 U/mL penicillin, and 100 µg/ml streptomycin. All cell lines were maintained at 37°C and 5% CO_2 in a humidity-saturated atmosphere.

Reagents

Ac-DEVD-AMC was purchased from AAT Bioquest (Biomol GmbH, Hamburg, Germany), #ABD-13402; Q-VD-OPh (QVD) from Sigma (Munich, Germany), #SML0063; staurosporine (STS) from LC Laboratories (Woburn, MA, USA), #9300; and TRAIL from R&D Systems (Bio-Techne GmbH, Wiesbaden, Germany), #375-TL-010. All cell culture reagents were purchased from Life Technologies, and all other reagents where no manufacturer is explicitly mentioned were purchased from Carl Roth GmbH (Karlsruhe, Germany).

Replicates and statistical analysis

Experiments were replicated at least three times, and representative data are shown. Error bars indicate standard deviation. All statistical analysis was performed using *Prism v7.01* (GraphPad Software, La Jolla, CA, USA).

Immunoblotting

Cells were harvested by centrifugation at 11,000 rcf in 4°C for 10 s, quick-frozen in liquid nitrogen, thawed on ice, incubated in Lysis Buffer (20 mM Tris pH 7.5, 150 mM NaCl, 1% v/v Triton X–100, 0.5 mM EDTA, 1 mM Na_3VO_4, 10 mM NaF, 2.5 mM $Na_4P_2O_7$, protease inhibitor (Sigma, #P2714)) for 30 min and vortexed repeatedly. The cell lysates were then cleared from cell debris by

centrifugation at 20,000 rcf for 15 min. SDS-PAGE and immunoblot were performed according to standard protocol. Membranes were scanned by a *LI-COR Odyssey* fluorescence scanner using *Image Studio v4.0* software. The antibodies used for protein detection were mouse anti-ACTB (Sigma; clone AC-74, #A5316); rabbit anti-BMAL1 (Cell Signaling Technologies, clone D2L7G, #14020); goat anti-CASP3 (R&D Systems, Minneapolis, MN, USA; #AF-605-N); and goat anti-GST (GE Healthcare, #27-4577-01).

In vitro protease assay

N-terminally GST-tagged recombinant BMAL1 expressed in wheat germ was purchased from Abnova (BMAL1-wt: #H00000406-P01, lot no. FB101; fusion protein sequence identical to Addgene plasmid #107763. BMAL1-D585A: custom-made; fusion protein sequence identical to Addgene plasmid #107764). Expression and purification of recombinant CASP3 were performed as described previously (Lauber et al., 2001). For the in vitro protease assay, 0.5 µg of GST-BMAL1 per sample were mixed with 0.5 µg of active CASP3 in a final volume of 50 µL of Reaction Buffer (10 mM Tris pH 7.6, 150 mM NaCl, 10 mM DTT) and incubated at 37°C for up to 240 min. After incubation, 10 µL of 6× Laemmli Buffer (375 mM Tris pH 6.8, 51.6% v/v glycerol, 12.3% w/v SDS, 0.6% w/v bromophenol blue, 6% v/v β-mercaptoethanol) were added, and the samples were incubated at 95°C for 5 min. The proteins were then separated by SDS-PAGE with 4 µl of sample per lane and were detected by immunoblotting as described above.

Quantitative PCR

Cells were grown for 24 h to a density of ~60–90%. The circadian cycles of all cells were synchronised by 30 min incubation in serum-free medium supplemented with 100 nM dexamethasone (Sigma #D4902). The cells were then washed and covered with pre-warmed full growth medium. At the indicated time points, the cells were harvested using a cell scraper, pelletised by centrifugation at 11,000 rcf in 4°C for 10 s, quick-frozen in liquid nitrogen, and thawed on ice. Total RNA was isolated using the *NucleoSpin® RNA* kit (Macherey-Nagel, Düren, Germany) and transcribed into cDNA using the *High-Capacity cDNA Reverse Transcription Kit* (Thermo Fisher Scientific) according to the respective manufacturer‘s instructions. The relative mRNA levels of both the BMAL1-regulated gene

Per2 as well as of the housekeeping gene *Actb* were determined by qPCR using the TaqMan method (TaqMan Universal PCR Master Mix, #4324018; MicroAmp Optical 96-Well Reaction Plate, #N8010560; Optical Adhesive Covers, #4360954; *Per2* TaqMan probe, #Mm00478099; *Actb* TaqMan probe, #Mm01205647; all from Thermo Fisher Scientific). The qPCR reactions were run on a *7300 Real-Time PCR System* using *Sequence Detection Software v1.4.0.25* (Applied Biosystems). The relative mRNA levels are shown as $2^{-\Delta\Delta Ct}$ values calculated in reference to *Actb* mRNA levels.

Luciferase reporter assay

Cell lines stably expressing the Bmal1-luc reporter construct as described above were used in this experiment. Phenol red-free high-glucose (4.5 g/l) DMEM supplemented with 4 mM L-glutamine, 1 mM pyruvate, and 25 mM HEPES was used at every step in this experiment. A number of 5×10^5 cells was seeded in 3.5 mm dishes and grown for 24 h. The circadian cycles of the cells were synchronised by 30 min incubation in serum-free medium supplemented with 100 nM dexamethasone (Sigma #D4902). The cells were then washed and covered with pre-warmed medium supplemented with 10% FCS and 100 µM luciferin (Promega, Mannheim, Germany). The dishes were sealed with Parafilm®, and luminescence was continuously measured for up to five days using a *LumiCycle 32* luminometer with *LumiCycle Data Collection v5* software (Actimetrics, Evanston, IL, USA).

Graphical abstract

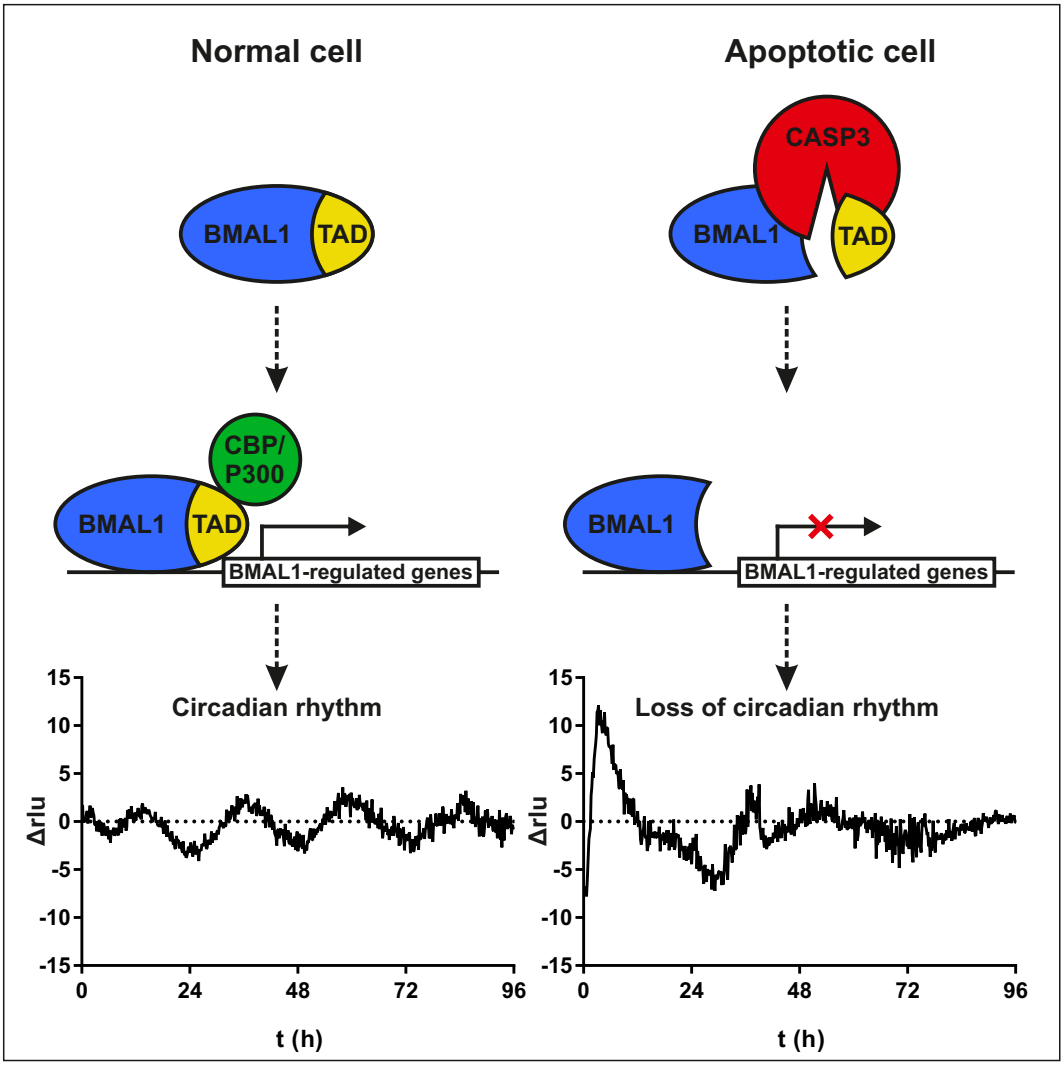

Figure 1

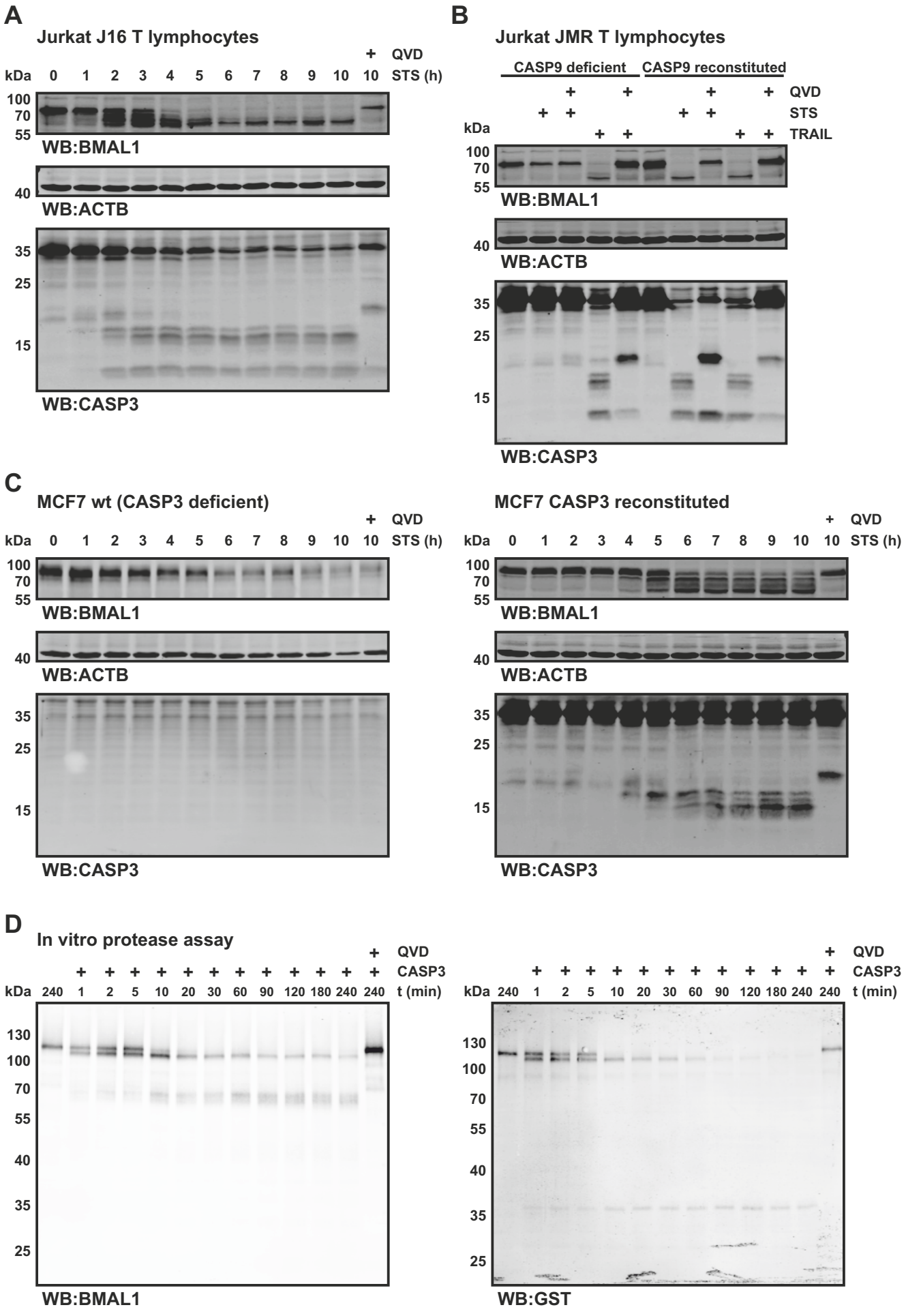
A
Jurkat J16 T lymphocytes
+ QVD
kDa 0 1 2 3 4 5 6 7 8 9 10 10 STS (h)
100
70
55
WB:BMAL1
40
WB:ACTB
35
25
15
WB:CASP3
B
Jurkat JMR T lymphocytes
CASP9 deficient
CASP9 reconstituted
QVD
STS
TRAIL
kDa
100
70
55
WB:BMAL1
40
WB:ACTB
35
25
15
WB:CASP3
C
MCF7 wt (CASP3 deficient)
+ QVD
kDa 0 1 2 3 4 5 6 7 8 9 10 10 STS (h)
100
70
55
WB:BMAL1
40
WB:ACTB
35
25
15
WB:CASP3
MCF7 CASP3 reconstituted
+ QVD
kDa 0 1 2 3 4 5 6 7 8 9 10 10 STS (h)
100
70
55
WB:BMAL1
40
WB:ACTB
35
25
15
WB:CASP3
D
In vitro protease assay
+ QVD
+ CASP3
kDa 240 1 2 5 10 20 30 60 90 120 180 240 240 t (min)
130
100
70
55
40
35
25
WB:BMAL1
+ QVD
+ CASP3
kDa 240 1 2 5 10 20 30 60 90 120 180 240 240 t (min)
130
100
70
55
40
35
25
WB:GST

Figure 2


A
SSTD, D45
DKDD, D56
G552
DMID, D585
LEAD, D610
DFSD, D621
TAD,
I583–L625

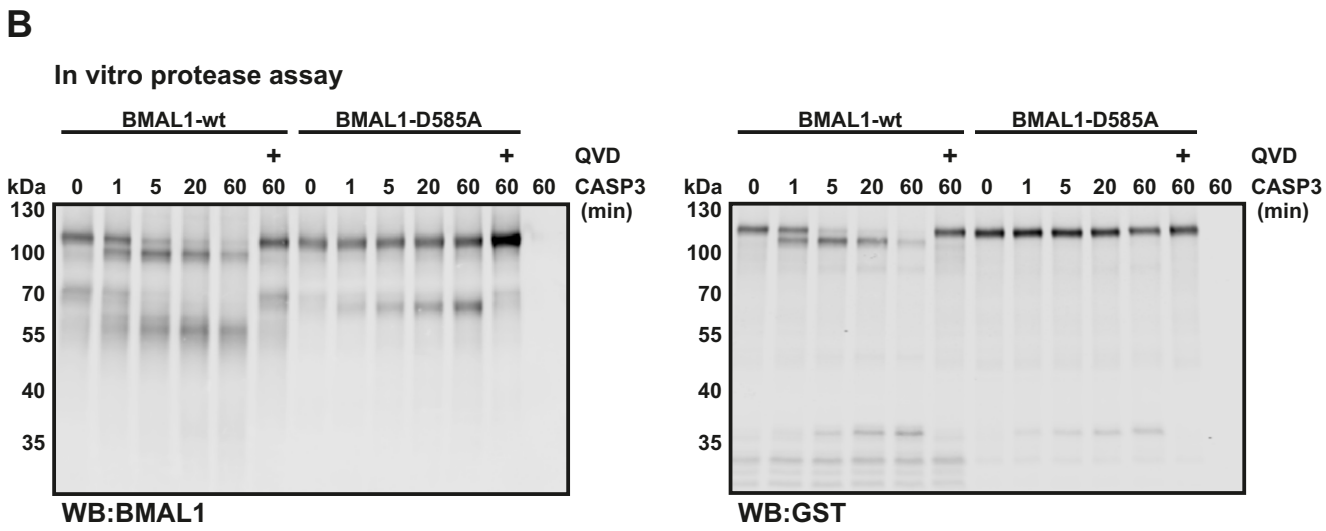
B
In vitro protease assay
BMAL1-wt
BMAL1-D585A
QVD
CASP3
(min)
kDa
0 1 5 20 60 60 0 1 5 20 60 60 60
130
100
70
55
40
35
WB:BMAL1
BMAL1-wt
BMAL1-D585A
QVD
CASP3
(min)
kDa
0 1 5 20 60 60 0 1 5 20 60 60 60
130
100
70
55
40
35
WB:GST

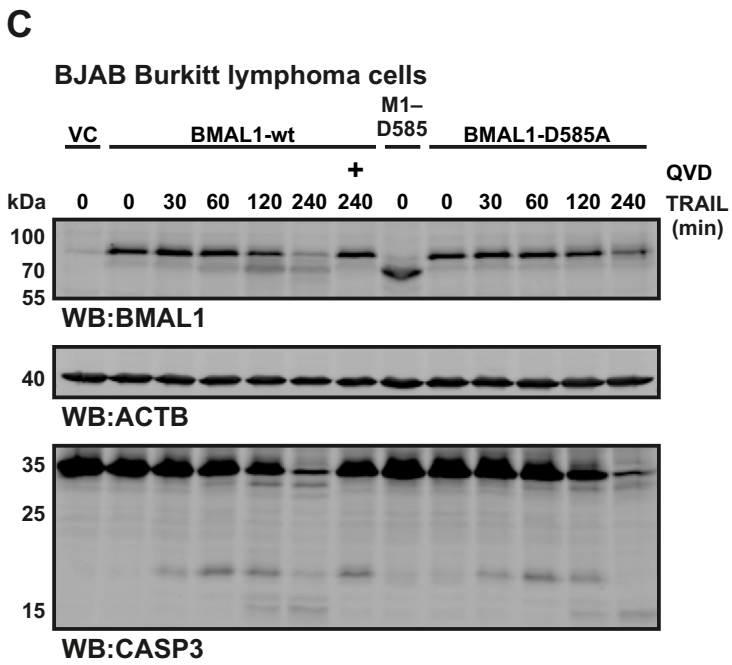
C
BJAB Burkitt lymphoma cells
VC
BMAL1-wt
M1–
D585
BMAL1-D585A
QVD
TRAIL
(min)
kDa
0 0 30 60 120 240 240 0 0 30 60 120 240
100
70
55
WB:BMAL1
40
WB:ACTB
35
25
15
WB:CASP3

Figure 3

A

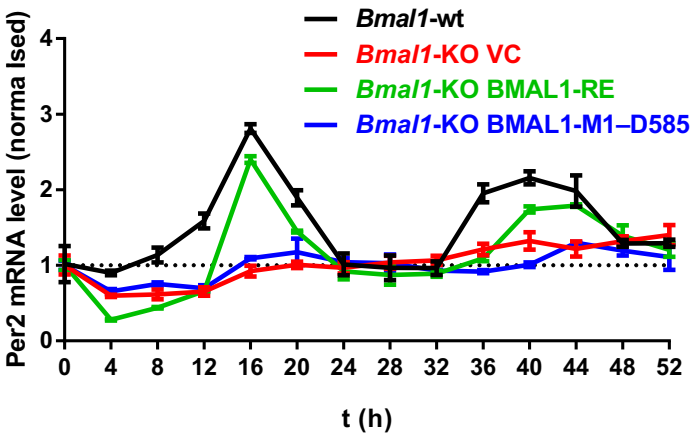
Bmal1-wt
Bmal1-KO VC
Bmal1-KO BMAL1-RE
Bmal1-KO BMAL1-M1–D585
Per2 mRNA level (norma lsed)
0
1
2
3
4
0 4 8 12 16 20 24 28 32 36 40 44 48 52
t (h)

B

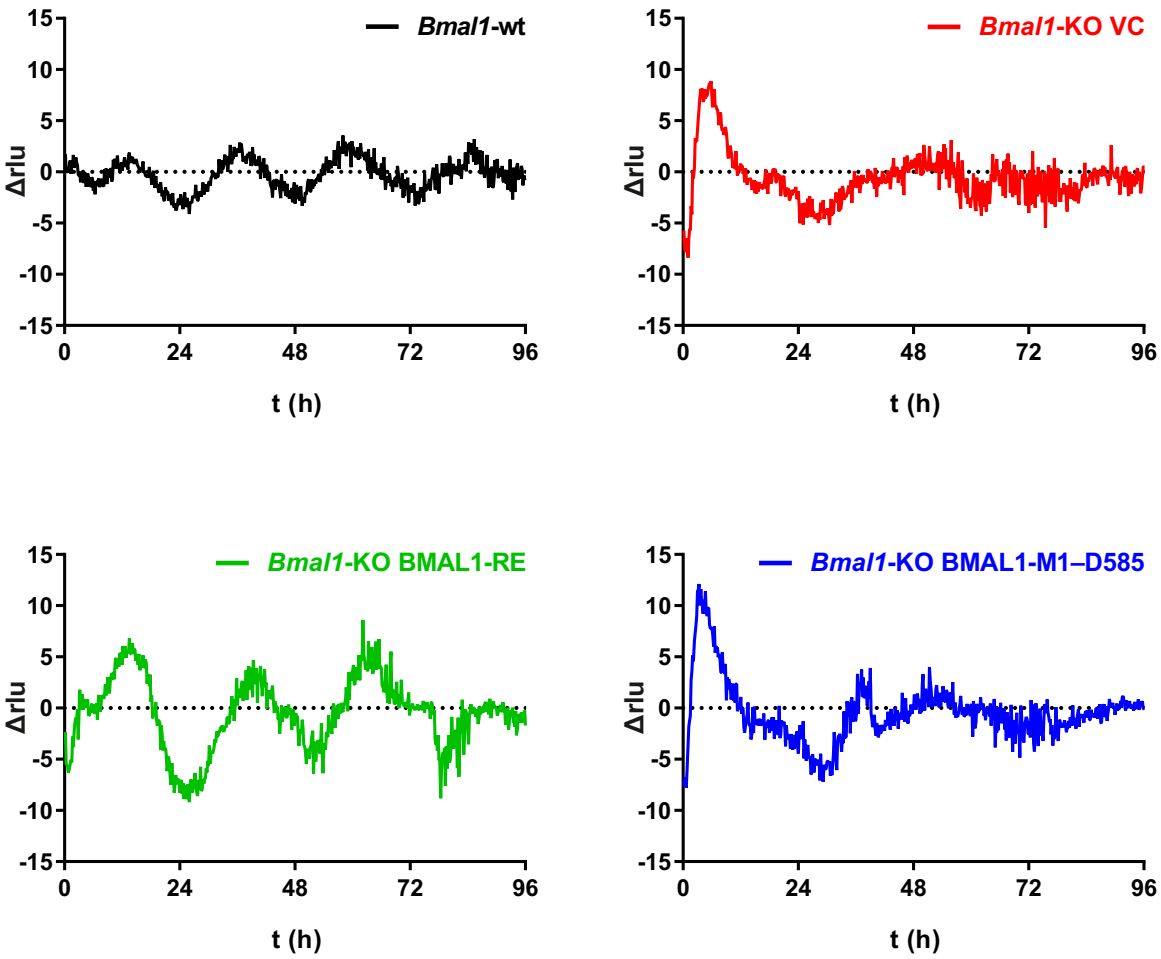
Bmal1-wt
Bmal1-KO VC
Bmal1-KO BMAL1-RE
Bmal1-KO BMAL1-M1–D585
Δrlu
15
10
5
0
-5
-10
-15
0 24 48 72 96
t (h)

Ich versichere an Eides Statt, dass die Dissertation von mir selbständig und ohne unzulässige fremde Hilfe unter Beachtung der „Grundsätze zur Sicherung guter wissenschaftlicher Praxis an der Heinrich-Heine-Universität Düsseldorf“ erstellt worden ist.

Philip Böhler

Düsseldorf, den 30.06.2019